UNIVERSITÀ
DEGLI STUDI
DI PADOVA

Sede Amministrativa: Università degli Studi di Padova

Dipartimento di Ingegneria Civile, Edile e Ambientale

SCUOLA DI DOTTORATO DI RICERCA IN : Scienze dell'Ingegneria Civile e Ambientale
INDIRIZZO: Meccanica computazionale ed ingegneria strutturale
CICLO: XXV

3D NONLINEAR COUPLED MODELLING OF GEOMATERIALS USING THE UNCONVENTIONAL SUBLOADING SURFACE APPROACH

Direttore della Scuola: Ch.mo Prof. Stefano Lanzoni

Supervisori: Dott. Ing. Valentina Salomoni
Ch.mo Prof. Carmelo Majorana

Dottorando: Riccardo Fincato

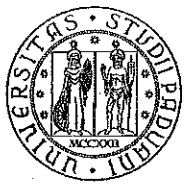

UNIVERSITÀ
DEGLI STUDI
DI PADOVA

Sede Amministrativa: Università degli Studi di Padova

Dipartimento di Ingegneria Civile, Edile e Ambientale

SCUOLA DI DOTTORATO DI RICERCA IN : Scienze dell'Ingegneria Civile e Ambientale
INDIRIZZO: Meccanica computazionale ed ingegneria strutturale
CICLO: XXV

3D NONLINEAR COUPLED MODELLING OF GEOMATERIALS USING THE UNCONVENTIONAL SUBLOADING SURFACE APPROACH

Direttore della Scuola: Ch.mo Prof. Stefano Lanzoni

Supervisori: Dott. Ing. Valentina Salomoni
Ch.mo Prof. Carmelo Majorana

Dottorando: Riccardo Fincato

Acknowledgements

This work wouldn't have been possible without the encouragement and help of so many people that is difficult to count all of them in these acknowledgments.

I would like to thank my family for the continuous support in all the choices that I've made, the serenity, the encouragement in going on with the studies and for 'having learned' how to use skype when we were distant.

A special thanks goes to Prof. V. Salomoni, who first believed in my capabilities and convinced me to start this Ph.D., for her patience in teaching me, for being a guide and constant incitement to be curious in the scientific research. I also would like to place on record my gratitude to Prof. C.E. Majorana for his precious advices and fundamental support.

I would like to express my deepest appreciation to Prof. K. Hashiguchi for all the time he spent teaching me about plasticity, for the inspiring discussion and his kindness. My gratitude also goes to Prof. T. Okayasu for his patience and time dedicated to me at Kyushu University, for the amazing laboratory parties and for his precious help. I would also thank Prof M. Ueno for the beautiful time I spent at the Ryukyus University in the Okinawa Island.

A sincere and huge thanks must go to Giovanna for being a good friend, a great colleague and a continuous support in all these years. Nevertheless I've to thanks a lot Gianluca for having helped me so much in my work, for the constructive discussions and for being a great friend. I cannot forget to express my gratitude to Daniele for being a friend before a colleague and to Beatrice for the good time spent working together which makes the studies less "hard" than they really are.

Last but not least I would like to thank the amazing people I've met in my experience in Japan: all the guys in the Kyushu University; Marika and my "chinese family" (Han Ping, Su Ping, Shi Run) for making me feel more like "at home" and Giulia for the great talks and the beautiful time together.

Abstract

The purpose of the work presented in this thesis is aimed to investigate the nonlinear behaviour of porous media, in detail soils, by means of an unconventional plasticity model named *subloading surface*.

The main feature of this model is the abolition of the neat distinction between elastic and plastic domains by assuming that plastic deformations occur whenever a change in the stress state is induced. Inside the conventional yield surface a new surface is create by means of a similarity transformation. This new surface, named subloading surface, expands or contracts depending on the stress evolution, leading to a gradual and smooth development of permanent deformations in the granular material.

Besides the more realistic answer of the simulations this theory allows a simpler numerical computation without the recourse of special techniques to define if the stress lies or not on the yield surface. In fact the subloading surface is such to pass always to the current stress point assuming the role of driving and measuring how the stress evolves in the analysis.

Many unconventional plasticity models can be found in literature but, except for the present, they all show some defects which may be relevant in cyclic plastic analyses where the accumulation of errors can produce a significant mistake in the forecast of the simulations.

As it will be shown in the following chapters the *simple subloading surface* model and the *extended subloading surface* one have been implemented in a fully coupled hydro-(thermo)-mechanical three dimensional F.E. research code, PLASCON 3D, in several scenarios dealing with: consolidation problems, subsidence at regional scale, numerical triaxial tests, tensile strength for particular soils and finally cyclic plasticity investigations. All the results show a good accordance with experimental data proving the reliability both of the theoretical model and of its implementation in the F.E. code.

Abstract (Italian)

Lo scopo di questo elaborato è quello di analizzare il comportamento non lineare di mezzi porosi, nel dettaglio terreni, tramite un modello di plasticità non convenzionale chiamato *subloading surface*.

La principale caratteristica di questo modello è l'abolizione della distinzione in un dominio elastico ed uno plastico assumendo che le deformazioni plastiche si producano ogni qualvolta venga introdotta una variazione nello stato tensionale nel materiale. All'interno della superficie plastica convenzionale si crea una nuova superficie tramite una trasformazione di similitudine. Questa nuova superficie, chiamata subloading surface, si espande o si contrae a seconda dell'evoluzione dello stato di stress, producendo un graduale e regolare sviluppo delle deformazioni plastiche nei materiali.

Al di là della risposta più realistica del modello nelle simulazioni, questa teoria permette un calcolo numerico "più snello" senza dover ricorrere a speciali tecniche numeriche per verificare se lo stress giaccia o meno sulla superficie plastica ed eventualmente riportarlo su di essa. Infatti la superficie di subloading è costruita in modo tale da passare sempre per il punto di stress attuale assumendo il ruolo di guidare e misurare come lo stato tensionale evolva nelle analisi.

In letteratura si trovano numerosi esempi di modelli plastici non convenzionali ma, ad eccezione del presente, tutti mostrano qualche lacuna che può risultare rilevante in analisi cicliche dove l'accumulo di errori è in grado di produrre uno scostamento notevole dalla risposta reale.

Come verrà mostrato nei capitoli successivi il modello *simple subloading surface* e quello *extended subloading surface* sono stati implementati in un codice di ricerca igro-(termo-)meccanico pienamente accoppiato, chiamato PLASCON 3D, per simulare diversi scenari: problemi di consolidazione, prove triassiali, resistenza a trazione per alcune tipologie di terreni ed infine per analisi di plasticità con carichi ciclici. Tutti i risultati ottenuti mostrano una buona capacità di riprodurre dati sperimentali provando l'affidabilità sia del modello teorico che della sua implementazione nel codice ad elementi finiti.

Introduction

Every material, under a load, produces continuous deformations in time which depend on several aspects: the entity of the load, the boundary conditions and the nature of the material itself and its properties. Soils structures can usually be defined by the dimension of elementary units (i.e. the grains), by their geometric relations during the settlement and by the presence and the dimension of the pores, nevertheless the fluid parts inside them.

It can be easily understood the degree of complexity of such a structure, which has represented a real challenge for many authors in the past who tried to catch the more realistic answer of the soil subjected to different loading conditions. The results of the investigations led to several rheological models aimed to define a constitutive bond useful in engineering applications and constructions. A first attempt was that of Terzaghi's primary consolidation theory [1], followed by the Biot [2-7] who tried to catch the three dimensional effects of consolidation problems and to find a relation between the solid and fluid phases.

Nowadays the use of computers and the more sophisticated numerical techniques allow to solve complex problems and, even more importantly, to take into account a nonlinear behaviour of the skeleton together with a variation of permeability. The theoretical problem has been enriched with other considerations such as fluid compressibility by Ghaboussi and Wilson, the grains change of volume by Zienkiewicz [8] and even the first attempt to deal with soil plasticity by Small [9] or Siriwardane and Desai [10]. All these authors consider displacements and pore pressure as basic variables of the model from which derive the fluid flows or stresses and strains.

The attention of the research therefore has been shifted to focus on a more realistic modelling of the physics nature of the phenomena, rather than the simplification of the equations that govern it, aiming to produce a reliable numerical code which can be used in different cases with predictive purposes.

The work shown in this thesis represents the sum of theoretical equations and hypothesis for simulation of geomaterials behaviour and numerical techniques necessary to run finite elements code. The fully coupled research code PLASCON 3D has been implemented to take into account the nonlinear response of soil in several simulations. In the following chapters different topics will be expounded, at first the theoretical bases and the assumptions considered and then the numerical results of the code.

Chapter 1 reports the equations governing the solid and the fluid phases of the porous media starting from a dissertation from the different theories that have been developed in the past and pointing out all the assumptions that have been made.

Chapter 2 deals with the finite elements formulation of the problem, showing the discretization in space and time of the set of equations written in the previous chapter and explaining the coupling strategies for the solution of the whole system.

Chapter 3 introduces the non-linear mechanical response for soils comparing the conventional elastoplastic constitutive equations with the ones proper of the *simple subloading surface* and of the

extended subloading surface models, underlining the differences and the advantages for the unconventional plasticity.

In *Chapter 4* the numerical code PLASCON 3D is explained, pointing out the new contributes and the modifications improved respect to the original form.

Chapter 5 reports the numerical analyses starting from the validation of the code and its application to several problems such as: consolidation, subsidence scenarios, triaxial tests, tensile strength of sands and cyclic loading case.

In the *Appendix* an upgraded version of the F.E. research code NEWCON3D describing concrete as a porous medium has been developed so to innovatively couple creep (via the Maxwell-chain model assuming model B3 [11] for the compliance function), shrinkage and damage (via the Mazars' damage model [12]) with the *simple subloading surface* model in order to obtain a visco-elasto and plastic constitutive law.

References

[1] Terzaghi K., (1923), "Die Berechnung der Durchlässigkeitsziffer des Tones aus dem Verlauf der hydrodynamischen Spannungserscheinungen", Ak. der Wissenschaften in Wien, Sitzungsberichte mathematisch-naturwissenschaftliche Klasse, part IIa, 132 (3/4), pp. 125-38.

[2] Biot M.A., (1941a), "General theory of three-dimensional consolidation", *J. Appl. Phys*., **12**, pp. 155-64.

[3] Biot M.A., (1941b), "Consolidation settlement under a rectangular load", *J. Appl. Phys.*, **12**, pp. 426-30.

[4] Biot M.A., (1955), "Theory of elasticity and consolidation for a porous anisotropic solid", *J. Appl. Phys.*, **26**, pp. 182-85.

[5] Biot M.A., (1956a), "General solution of the equation of elasticity and consolidation for a porous material", *J. Appl. Mech.*, **23**, pp. 91-96.

[6] Biot M.A., (1956b), "Theory of deformation of a porous viscoelastic anisotropic solid", *J. Appl. Phys*., **27**, pp. 459-67.

[7] Biot M.A., (1963), "Theory of stability and consolidation of a porous medium under initial stress", *J. Math. Mech.*, **12**, pp. 521-41.

[8] Zienkiewicz O.C., Humpheson C., Lewis R.W., (1977), “A unified approach to soil mechanics including plasticity and visco-plasticity”, Ch.4 in *Finite Elements in Geomechanics*, ed. G. Gudehus, Wiley, London.

[9] Small J.C., Booker J.R, Davis E.H., (1976), “Elastoplastic consolidation of soil”, *Int. J. Solids and Struct.*, **12**, pp. 431-438.

[10] Desai C.S., Siriwardane T.H.J., (1979), “Subsidence due to consolidation including nonlinear behaviour”, Evaluation and Prediction of Subsidence, ed S.K. Saxena, ASCE, New York, pp. 500-515.

[11] Bažant, Z. P., Baweja, S., (2000), “Creep and shrinkage prediction model for analysis and design of concrete structures: Model B3”, in Adam *Neville Sym.: Creep and Shrinkage – Structural Design Effects*, ACI SP – 194, 1-83.

[12] Pijaudier-Cabot, G., Mazars, J., Pulikowski, J., (1991), “Steel-concrete bond analysis with non local continuous damage”, *J. Str. Engrg.*, **117**(3), pp. 862-8

1. Hydro-(thermo-)mechanical modelling of porous media

1.1. Introduction

In this chapter the partial differential equations governing the mechanical behaviour of the saturated and partially saturated porous media will be discussed. As it will be shown the three-phases mixed flow case is the general one, including the saturated-non saturated and the one-phase problems.

All the equations have been developed according to the Biot [1-5] theory. The solid phase is considered as composed by a set of particles (i.e. specifically for soil the grains) forming a porous rigid skeleton surrounded by one or more fluid phases (for instance gas, vapour, water, oil). The shear stress in the fluid phase is smaller than in the solid one, so it can be neglected in the former.

In the present work infinitesimal strains theory has been assumed, so it is possible to apply the Darcy's law in terms of total fluid velocity rather than relative velocity between the grain and the fluid. In fact Gambolati [6] demonstrated that is not necessary to consider the relative movements of the two phases if the grains displacement is smaller than the 5% of the total compaction of the soil. This condition is generally satisfied especially for subsidence at regional scale, connected with shrinkage and underground flows problems as it will be shown later.

1.2. Solid phase behaviour

A "pure" fluid pressure (external and internal), named p, is responsible for the uniform volume change due to grains compression and the main contribute to the total deformation is caused by the solid skeleton deformation depending on the so called *effective stress σ'*. The relationship between p and σ' can be expressed, in incremental form, according to the following formula, where tensile strength is considered as positive whereas compression negative:

$$\dot{\boldsymbol{\sigma}}' = \dot{\boldsymbol{\sigma}} - \mathbf{I}\dot{p}_w \tag{1.1}$$

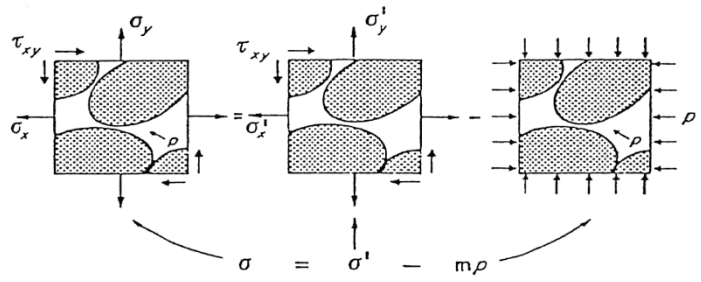

Figure 1 – Total and effective stresses in the porous media.

$\boldsymbol{\sigma}$ is the total stress, **I** is the identity matrix with unitary values on the diagonal components and zero for all the others. Equation (1.1) can be obtained by static considerations that allow to decompose the total stress vector into the sum of two contributes, well known in literature as “Principle of effective stress” and formulated for the first time by Terzaghi [7].

The constitutive equations which relate this effective stress with the deformations of the solid skeleton are independent from the pore pressure and, in general, for a nonlinear material can also be written in order to include plasticity as will be shown in following chapters. If creep contribute is present the expression appears as:

$$\dot{\boldsymbol{\sigma}}' = \mathbf{D}_T \left(\dot{\boldsymbol{\varepsilon}} - \dot{\boldsymbol{\varepsilon}}_c - \dot{\boldsymbol{\varepsilon}}_u - \dot{\boldsymbol{\varepsilon}}_0 \right) \tag{1.2}$$

where $\dot{\boldsymbol{\varepsilon}}$ represents the total deformation of the skeleton,

$$\dot{\boldsymbol{\varepsilon}}_c = \mathbf{c}\, dt \tag{1.3}$$

is the creep contribute,

$$\dot{\boldsymbol{\varepsilon}}_u = -\mathbf{I} \left(\frac{\dot{\mathbf{p}}}{3K_S} \right) \tag{1.4}$$

is the deformation caused by the uniform compression of the particles by means of the pore fluid pressure, where K_s is the compressibility modulus for the solid phase. In soils this last term is generally not relevant thus it can be neglected, however this is not possible in rocks mechanics, where the compressibility of the solid grains is comparable to the skeleton one.

At least, $\dot{\boldsymbol{\varepsilon}}_0$ represents all the other deformations which cannot be directly associated to a stress variation (i.e. swelling, thermal, chemical, etc.) and named “autogeneous deformations”.

$\mathbf{D}_T$ matrix and the creep function $\mathbf{c}$ depend on the effective stress and, if deformation effects are take into account, on the total deformation of the skeleton $\dot{\boldsymbol{\varepsilon}}$.

The equilibrium equation, relating the total stress with the body forces (**b**) and the forces applied on the boundaries (**f**), is formulated in terms of unknown displacements. In detail, using the *principle of virtual work*, the equilibrium can be written as

$$\int_{\Omega} \delta\boldsymbol{\varepsilon}\, \boldsymbol{\sigma}\, d\Omega - \int_{\Omega} \delta\mathbf{u}\, \mathbf{b}\, d\Omega - \int_{\Gamma} \delta\mathbf{u}\, \mathbf{f}\, d\Gamma = 0 \tag{1.5}$$

Equation (1.5) is a weak form of the equilibrium equation incorporating the boundary conditions, whereas the local form of the linear momentum balance can be summarized as follows:

$$\nabla \dot{\boldsymbol{\sigma}} = 0 \tag{1.6}$$

obviously the (1.5) is valid even in the incremental form, which can be easily obtained as:

$$\int_{\Omega} \delta\boldsymbol{\varepsilon}\, d\boldsymbol{\sigma}\, d\Omega - \int_{\Omega} \delta\mathbf{u}\, d\mathbf{b}\, d\Omega - \int_{\Gamma} \delta\mathbf{u}\, d\mathbf{f}\, d\Gamma = 0 \tag{1.7}$$

substituting eq. (1.1) inside eq. (1.7):

$$\int_{\Omega} \delta\boldsymbol{\varepsilon}\; d\boldsymbol{\sigma}'\, d\Omega - \int_{\Omega} \delta\boldsymbol{\varepsilon}\; \mathbf{I} d\mathbf{p}\, d\Omega - d\tilde{f} = 0 \tag{1.8}$$

where

$$d\tilde{f} = \int_{\Omega} \delta\mathbf{u}\; d\mathbf{b}\, d\Omega + \int_{\Gamma} \delta\mathbf{u}\; d\mathbf{f}\, d\Gamma \tag{1.9}$$

takes into account the variation of the external forces due to load on the outside and inside of the domain.

In addition, remembering the constitutive law expressed by eq. (1.2), and dividing by time variation *dt*, it can be obtained:

$$\begin{aligned} &\int_{\Omega} \delta\boldsymbol{\varepsilon}\; \mathbf{D}_{\mathbf{T}} \frac{\partial\boldsymbol{\varepsilon}}{\partial t} d\Omega - \int_{\Omega} \delta\boldsymbol{\varepsilon}\; \mathbf{I} \frac{\partial\mathbf{p}}{\partial t} d\Omega + \int_{\Omega} \delta\boldsymbol{\varepsilon}\; \mathbf{D}_{\mathbf{T}}\, \mathbf{I} \frac{\partial\mathbf{p}}{\partial t} \frac{1}{3K_s} d\Omega - \\ &\int_{\Omega} \delta\boldsymbol{\varepsilon}\; \mathbf{D}_{\mathbf{T}}\, \mathbf{c} d\Omega - \int_{\Omega} \delta\boldsymbol{\varepsilon}\; \mathbf{D}_{\mathbf{T}} \frac{\partial\boldsymbol{\varepsilon}_0}{\partial t} d\Omega - \frac{d\tilde{\mathbf{f}}}{dt} = 0 \end{aligned} \tag{1.10}$$

If the pore pressure is known (note that if a multi phase fluid is consider, an average value has to be chosen) then displacements and stresses of the whole system can be computed with this equation. However, in general, the pressure field is coupled together with variations of deformation so is necessary to use another set of equations as it will be shown in the next paragraph.

In the numerical analyses, reported in the present work, the final equation (1.10) has been simplified because some contributes have not been taken into account, for instance creep, autogeneous deformations and the grain compressibility due to fluid pressure.

1.3. Fluid phase behaviour

The complexity of the geometry of a porous media requires a particular approach to study the velocity of the fluid part, because it is almost impossible an analytical definition for that. In order to avoid this problem an average value of filtration velocity, also known as *Darcy's velocity* or *volume velocity*, has been considered:

$$q = -\frac{1}{\mu}\mathbf{k}\nabla(p + \rho g h) \tag{1.11}$$

Where **k** is the absolute permeability matrix which is different for every material considered, μ is the dynamic viscosity of the fluid, *g* is the gravity factor and *h* is the depth at which the data are referred to [8].

When a multi-phase fluid is taken into account (for instance with oil, hydrocarbon gasses or liquid, water, vapour) each fluid influences the behaviour of the other inside the pore and then a more complex mathematical model is necessary.

The portion of the pore occupied by a certain substance is defined as *saturation* S_π, where π is the generic phase considered. It is assumed that the permeability of each phase is directly proportional to its saturation, in fact experimental studies showed that the multi-phase flow reduces material permeability both for the whole mix and for each individual fluid [9]. This is the reason why a relative permeability functions $k_{r\pi}(S_\pi)$ are introduced to modify the permeability matrix in the eq. (1.11). Although their expressions can be obtained by analytical relations [10], [11] an experimental value is generally preferred [12], [13].

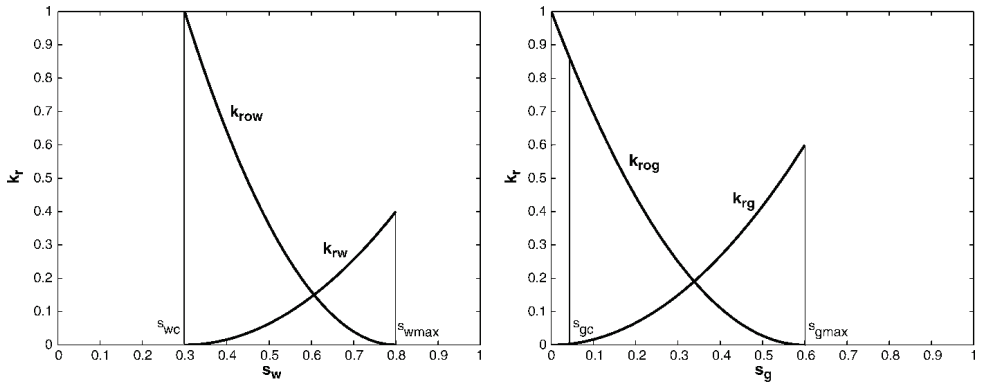

Figure 2 – typical permeability curves for water-oil and oil-gas.

Figure 2 shows two typical permeability curves for a water-oil system and for a oil-gas one, the saturation degree for both the phases has been obtained from the relations between the suction and the saturation degree.

In case of three-phase fluid (e.g. oil, gas, water) the functions can be estimated starting from the data for a two-phase one that means, for instance, to consider at first the relation between water-oil and then the one for oil-gas [14] for computing the values of all the relative permeability k_{rg}, k_{rw}, k_{ro}.

The numerical analyses presented in chapter 5 consider a one-phase fluid in order to simplify the computation and reduce the number of variables in the simulation. In this particular case the continuity flow equation must satisfied the following expression:

$$\{\text{fluid accumulation velocity}\} + \nabla\{\rho_w \mathbf{q}\} = 0 \tag{1.12}$$

Which, combined with the *Darcy's velocity* in eq.(1.11), becomes:

$$\{\text{fluid accumulation velocity}\} + \nabla\left\{-\frac{\rho_w \mathbf{k}}{\mu}\nabla\left(p_w + \rho_w g h\right)\right\} = 0 \tag{1.13}$$

When gas, liquid hydrocarbon and water are contemporary present the only two phases that cannot mix are oil and water. The gas solution in both of them changes the physic property of the fluids. It becomes necessary to introduce some parameters to take into account this aspect: at first a *volume*

factor $B_\pi(p_\pi)$ must be defined such to express the ratio between the volume occupied by the π phase at the p_π pressure with the volume occupied in the *stock tank conditions* (STC) [15]. The reference volume for gas state hydrocarbons is the one at the surface condition. The definition of the volume factor depends on wet or dry phase. In this second case it can be formulated as follows:

$$B_\pi(p_\pi) = \frac{V_\pi(p_\pi)}{V_{\pi STC}} \tag{1.14}$$

where V_π is the volume of a unitary mass of π phase at p_π pressure and $V_{\pi STC}$ is the volume of a unitary mass of the same phase at ST conditions. For the wet case the phase is composed by two terms, one is the wet term while the other is the dissolved dry one:

$$B_\pi(p_\pi) = \frac{V_\pi(p_\pi) + \bar{V}_\pi(p_\pi)}{V_{\pi STC}} \tag{1.15}$$

In this second definition it is required that the volume of an unitary mass, in the ST condition for the dissolved dry part, is equal to zero.

The other parameter that should be introduced is the *solution ratio* in order to take into account the solubility of gas into oil and water. Hydrocarbon in the gas state can exist in three different forms:

- free gas;
- gas solved into water;
- gas solved into oil;

the solution ration for computing the exact amount of gas solved into a liquid is defined as

$$R_{S\pi} = \frac{V_{dgSTC}}{V_{\pi STC}} \tag{1.16}$$

where V_{dgSTC} is the volume occupied by a dissolved gas in a unitary mass of the phase considered at STC, whereas $V_{\pi STC}$ is the volume of the phase at the same conditions.

Incorporating these two parameters inside a three-phase system the continuity equation for oil can be rewritten as:

$$\nabla\left\{\mathbf{k}\frac{k_{ro}(S_o)\rho_o}{\mu_o B_o(p_o)}\nabla(p_o + \rho g h)\right\} = \text{fluid accumulation velocity} \tag{1.17}$$

The right hand of eq. (1.17) is the sum of many different contributes [16]:

- total deformation velocity change

$$\frac{\partial \boldsymbol{\varepsilon}_V}{\partial t} = \mathbf{I}\frac{\partial \boldsymbol{\varepsilon}}{\partial t} \tag{1.18}$$

- velocity of volume change of grains due to fluid pressure change

$$\frac{(1-\phi)}{K_s}\frac{\partial \bar{p}}{\partial t} \tag{1.19}$$

where ϕ is the porosity and p dashed is the average value for the fluid part, in general this parameter is a function of the saturation of the three phases and it can be formulated as

$$\bar{p} = S_o p_o + S_w p_w + S_g p_g \tag{1.20}$$

- Saturation velocity change (here for a generic phase)

$$\phi \frac{\rho_\pi}{B_\pi}\frac{\partial S_\pi}{\partial t} \tag{1.21}$$

- Velocity change of fluid density (here for a generic phase)

$$\phi S_\pi \frac{\partial}{\partial t}\left(\frac{\rho_\pi}{B_\pi}\right) \tag{1.22}$$

- Grains volume change due to variation of effective stress in time

$$-\frac{1}{3K_S}\mathbf{I}\frac{\partial \boldsymbol{\sigma}'}{\partial t} \tag{1.23}$$

Inserting eq. (1.23) into eq. (1.2) it holds

$$-\frac{1}{3K_s}\mathbf{I}\mathbf{D}_\mathbf{T}\left(\frac{\partial \boldsymbol{\varepsilon}}{\partial t}+\frac{1}{3K_s}\mathbf{I}\frac{\partial \bar{p}}{\partial t}-\mathbf{c}\right) \tag{1.24}$$

Finally the continuity equations for the oil (1.25) and the water (1.26) are written as:

$$\begin{aligned}&-\nabla^T\left\{\mathbf{k}\frac{k_{ro}(S_o)\rho_o}{\mu_o B_o(p_o)}\nabla(p_o+\rho g h)\right\}+\phi\frac{\rho_o}{B_o}\frac{\partial S_o}{\partial t}+\phi\frac{\partial}{\partial t}\left(\frac{\rho_o}{B_o}\right)+\\&+\rho_o\frac{S_o}{B_o}\left\{\left(\mathbf{I}-\frac{1}{3K_s}\mathbf{I}\mathbf{D}_\mathbf{T}\right)\frac{\partial \boldsymbol{\varepsilon}}{\partial t}+\frac{1}{3K_s}\mathbf{I}\mathbf{D}_\mathbf{T}\,\mathbf{c}+\left(\frac{(1-\phi)}{K_s}-\frac{1}{(3K_s)^2}\mathbf{I}\mathbf{D}_\mathbf{T}\mathbf{I}\right)\frac{\partial \bar{p}}{\partial t}\right\}=0\end{aligned} \tag{1.25}$$

$$\begin{aligned}&-\nabla^T\left\{\mathbf{k}\frac{k_{rw}(S_w)\rho_w}{\mu_w B_w(p_w)}\nabla(p_w+\rho g h)\right\}+\phi\frac{\rho_w}{B_w}\frac{\partial S_w}{\partial t}+\phi\frac{\partial}{\partial t}\left(\frac{\rho_w}{B_w}\right)+\\&+\rho_w\frac{S_w}{B_w}\left\{\left(\mathbf{I}-\frac{1}{3K_s}\mathbf{I}\mathbf{D}_\mathbf{T}\right)\frac{\partial \boldsymbol{\varepsilon}}{\partial t}+\frac{1}{3K_s}\mathbf{I}\mathbf{D}_\mathbf{T}\,\mathbf{c}+\left(\frac{(1-\phi)}{K_s}-\frac{1}{(3K_s)^2}\mathbf{I}\mathbf{D}_\mathbf{T}\mathbf{I}\right)\frac{\partial \bar{p}}{\partial t}\right\}=0\end{aligned} \tag{1.26}$$

Instead the continuity equation for the gas, counting possible sources and the solution ratio R_{Rs}becomes

$$\begin{aligned}
&-\nabla^T\left\{\mathbf{k}\rho_g\left[\frac{k_{rg}}{\mu_g B_g}+\frac{k_{ro}R_{so}}{\mu_o B_o}+\frac{k_{rw}R_{sw}}{\mu_w B_w}\right]\nabla(p_g+\rho g h)\right\}+\\
&+\phi\frac{\partial}{\partial t}\left(\rho_g\left[\frac{S_g}{B_g}+\frac{S_o R_{so}}{B_o}+\frac{S_w R_{sw}}{B_w}\right]\right)+\\
&+\rho_g\left[\frac{S_g}{B_g}+\frac{S_o R_{so}}{B_o}+\frac{S_w R_{sw}}{B_w}\right]\\
&\left\{\left(\mathbf{I}-\frac{1}{3K_s}\mathbf{I}\mathbf{D}_\mathbf{T}\right)\frac{\partial\boldsymbol{\varepsilon}}{\partial t}+\frac{1}{3K_s}\mathbf{I}\mathbf{D}_\mathbf{T}\,\mathbf{c}+\left(\frac{(1-\phi)}{K_s}-\frac{1}{(3K_s)^2}\mathbf{I}\mathbf{D}_\mathbf{T}\mathbf{I}\right)\frac{\partial\bar{p}}{\partial t}\right\}=0
\end{aligned}\tag{1.27}$$

In eq. (1.25), (1.26), (1.27) the relative permeability of the single phase is function of the saturation of the phase itself whereas the volume factor is a function of the pore pressure. A last important condition that must be fulfilled is that the sum of the saturations must have a unitary value:

$$S_o+S_w+S_g=1 \tag{1.28}$$

The set of equations (1.10), (1.25), (1.26), (1.27) must be solved together to compute the displacement and pressure fields and the same time.

1.3.1. Flow equation for a single phase fluid

As reminded before the simulations carried out for this thesis consider a single phase fluid, specifically water, with the only exception of the subsidence at regional scale phenomena, where a locally partially saturated porous media is take into account. In the most simple case it has been consider the pores fully occupied by water, i.e. saturation parameter assumes unitary value, which leads to a simplification of the eq. (1.26). Starting from the definition of the velocity change of the fluid density (eq. (1.22)), imposing the volume factor equal to one and multiply and divide for the water density, it can be obtained:

$$\phi\frac{1}{\rho_w}\frac{\partial\rho_w}{\partial t}=\phi\frac{1}{\rho_w}\frac{\partial\rho_w}{\partial\bar{p}}\frac{\partial\bar{p}}{\partial t}=\frac{\phi}{K_w}\frac{\partial\bar{p}}{\partial t} \tag{1.29}$$

Where the average pressure of the fluid mix *p dashed* is exactly the water pressure, and K_w is its compressibility modulus. Finally, through some substitutions and simplifications eq. (1.26) becames [17], [18]:

$$\begin{aligned}
&-\nabla^T\left\{\frac{\mathbf{k}}{\mu_w}\nabla(p_w+\rho_w g h)\right\}+\left(\mathbf{I}-\frac{1}{3K_s}\mathbf{I}\mathbf{D}_\mathbf{T}\right)\frac{\partial\boldsymbol{\varepsilon}}{\partial t}+\\
&\frac{1}{3K_s}\mathbf{I}\mathbf{D}_\mathbf{T}\,\mathbf{c}+\left(\frac{(1-\phi)}{K_s}+\frac{\phi}{K_s}-\frac{1}{(3K_s)^2}\mathbf{I}\mathbf{D}_\mathbf{T}\mathbf{I}\right)\frac{\partial p_w}{\partial t}=0
\end{aligned}\tag{1.30}$$

A last passage is the one for change the absolute permeability matrix **k** in the more well known *permeability* or *hydraulic conductivity matrix*, which coefficients have a space/time dimension.

$$-\nabla^T\left\{\mathbf{K}\nabla\left(\frac{p_w}{\rho_w g}+h\right)\right\}+\left(\mathbf{I}-\frac{1}{3K_s}\mathbf{ID_T}\right)\frac{\partial\boldsymbol{\varepsilon}}{\partial t}+$$
$$\frac{1}{3K_s}\mathbf{ID_T}\,\mathbf{c}+\left(\frac{(1-\phi)}{K_s}+\frac{\phi}{K_s}-\frac{1}{(3K_s)^2}\mathbf{ID_T}\mathbf{I}\right)\frac{\partial p_w}{\partial t}=0 \tag{1.31}$$

1.4. Coupled solution for displacements and pressure for reservoirs

An interesting application of the formulation for the saturated porous media is the investigation of the settlements and the pore pressure distribution in a control volume comprehensive of one or more reservoirs from which a fluid phase is extracted.

The procedure developed should be considered valid under few hypothesis: at first the horizontal extension of the tank results smaller than the counter volume cross section considered, its height should be smaller than the total depth of the sample [19] and finally, in case of more than one point of extraction, the withdrawal velocity should be the same for each reservoirs. This last condition is important for creating a uniform decrease of pressure inside the domain. Another additional, but fundamental, requirement is that the pore pressure should be such to satisfy in every moment the cumulative balance equation for the material [20], [21]:

$$W_e = N_p(B_o - R_{so}B_g)+G_pB_g+W_pB_w-N(B_t-B_{ti})-$$
$$-G(B_g-B_{gi})-F-\frac{1}{(1-S_{wi})}(C_f-S_wC_w)(\bar{P}_i-\bar{P}) \tag{1.32}$$

where all the terms involved are reported in Box 1 below.

The cumulative balance equation for the material is basically a volume balance at reservoir conditions for:

- The fluids initially contained inside the tank;
- The portion of the fluid part which stays inside the reservoir;
- The water inflow coming from adjacent zones;
- The water and gas amount extracted or injected.

The above mentioned equation represents the more complex case in which a multi-phase fluid has been considered, counting the volume factor and the solution ratio presented in the equations (1.14) and (1.16). For sake of simplicity the problem described in the numerical chapter considers only a gas phase within a fully saturated porous media.

The continuity equation for the gas phase becomes:

$$GB_{gi} = \left(G - G_p\right)B_g + W_e - W_p B_w \tag{1.33}$$

C_f = effective compressibility of rock
C_w = compressibility of water
B_g = gas volume factor
B_o = oil volume factor
B_w = water volume factor
B_t = total volume factor
F = total flui injection inside the domain
G = initial free gas in the pores
G_p = total gas extraction
N = initial oil in situ
N_p = total oil extraction
$\bar{P}$ = average pressure in the reservoir
R_{so} = initial solution ratio gas-oil
S_w = average water saturation
W_e = water inflow from near the tank
W_p = total water extraction
i = initial conditions

Box 1 – List of variables for equation (1.32).

which can be also written in its incremental form as:

$$\left(G - G_p\right)\Delta B_g + \Delta W_e = \Delta G_p B_g + B_w \Delta W_p + \Delta B_w W_p \tag{1.34}$$

the volumetric formation factor for the gas phase can be obtained from the ideal gas law:

$$B_g = \frac{p_{sc}}{T_{sc}}\frac{Z\ T}{P} \tag{1.35}$$

$$\Delta B_g = \frac{p_{sc}}{T_{sc}}\left(\Delta Z\frac{T}{P} - \frac{ZT}{P^2}\Delta P + \frac{p_{sc}}{T_{sc}}Z\Delta T\right) \tag{1.36}$$

Where *Z(T,P)* is the compressibility factor, *T* the absolute temperature and the subscript *sc* indicates the surface conditions. The equations (1.33) and (1.35) furnish the gas pore pressure p_g, once the water inflow and gas production are known, which is used as boundary condition for the reservoirs (through an internal numerical procedure used in the finite elements). At this point the solution in terms of displacements and pore pressure for the whole domain is obtained by means of the coupled equations explained in the previous paragraph.

References

[1] Biot M.A., (1941a), "General theory of three-dimensional consolidation", *J. Appl. Phys*., **12**, pp. 155-64.

[2] Biot M.A., (1941b), "Consolidation settlement under a rectangular load", *J. Appl. Phys.*, **12**, pp. 426-30.

[3] Biot M.A., (1955), "Theory of elasticity and consolidation for a porous anisotropic solid", *J. Appl. Phys.*, **26**, pp. 182-85.

[4] Biot M.A., (1956a), "General solution of the equation of elasticity and consolidation for a porous material", *J. Appl. Mech.*, **23**, pp. 91-96.

[5] Biot M.A., (1963), "Theory of stability and consolidation of a porous medium under initial stress", *J. Math. Mech.*, **12**, pp. 521-41.

[6] Gambolati G. (1973), "Equation for one-dimensional vertical flow of groundwater, 2, Validity range of the diffusion equation", *WAT. Res. Research*, **9**(5), 1385-95.

[7] Terzaghi K., (1943), "Theoretical Soil Mechanics", Wiley, New York.

[8] De Wiest R.J.M., (1969), "Flow through porous media", *Academic Press*, New York.

[9] Plummer F.B., (1937), "American Petroleum Institute Drilling Production and Practice", *American Petroleum Institute*.

[10] Leverett M.C., (1941), "Capillary behaviour in porous media", *Petr. Trans*., AIME, **142**, 341-58.

[11] Corey A.T., (1954), "The interrelation between gas and oil relative permeabilities", *Producers Monthly*, **19**, 38-41.

[12] Buckley S.E., Leverett M.C., (1942), "Mechanisms of fluid displacements in sands", *Trans. AIME*, **146**, pp. 108-116

[13] Scheidegger A., (1957), "The physics of flow through porous media", *Univ. of Toronto Press*

[14] Crichlow H.B., (1977), "modern Reservoir Engineering – a Simulation Approach", *Pretience Hall*, Englewood Cliffs.

[15] Collins R.E., (1961), " Flow of Fluids Trough Porous Materials", *Reinhold*, New York.

[16] Lewis R.W., Schrefler B.A., (1982), "A finite element simulation of the subsidence of a gas reservoir undergoing a waterdrive", in *Finite elements in Fluids*, Vol. 4, ed. R.H. Gallagher et al., Wiley, London, pp. 179-200.

[17] Lewis R.W., Roberts G.K., Zienkiewicz O.C., (1976), "A non-linear flow deformation analysis of consolidation problems", *Proc. Sec. Int. Conf. Num. Meth. In Geomechanics*, ASCE, pp. 1006-88.

[18] Lewis R.W., Schrefler B.A., (1978), "A fully coupled consolidation model of the subsidence of Venice", *Wat. Res. Research*, **14**, 223-30.

[19] Lewis R.W., Schrefler B.A., (1998), "The Finite Element Method in Static and Dynamic Deformation and Consolidation in Porous Media", *J. Wiley and Sons*.

[20] Craft B.C., Hawkins M.F., (1969), *"*Applied petroleum reservoir engineering*"*, *Prentice-Hall*, Eglewood Cliffs.

[21] Crichlow H.B., (1977), "Modern reservoir engineering-a simulation approach", *Prentice-Hall*, Englewood Cliffs.

[22] Schrefler B.A., Lewis R.W., Majorana C.E., (1981), "Subsidence above volumetric and waterdrive gas reservoir", *Int. J. Num. Meth. Fluids*, **1**, 101-15.

2. Solving procedures

The equations system composed by eq. (1.10), (1.25), (1.26), (1.27) can be solved in many ways, in general there are two main classes of procedures:

- Coupled solutions
- Uncoupled solutions

The first strategy has been adopted in the present work for finite elements analyses on a single phase fully saturated porous media (with the exception of the subsidence at regional scale case). This solving procedure, explained in the following paragraph, is valid also for a two-phases flow with not mixable substances or for a saturated not-saturated flow in a porous media. The latter has been proved to be formally identical to the single phase case. Furthermore all of these techniques developed can be extended for the more complicated multi-phase flow.

Uncoupled solution procedures will be briefly commented in the next paragraph.

2.1. Uncoupled solutions

The continuity equation for the fluid part and the equilibrium equation of the solid skeleton can be uncoupled under the hypothesis that the total stress remains constant in time. The changes of the fluid pressure become exactly equal and opposite to the volumetric changes of the effective stress, decreasing the number of unknowns of the problem. This basic assumption has been used in different ways in the uncouple strategies as described afterward.

A first attempt for the one-phase case can be obtained ignoring the deformation of the solid part as shown by Morgan [1].

Another one consists in the uncoupling of the fluid-solid system of equations assuming that horizontal displacements are negligible. This of course is valid for particular cases where vertical deformations are dominant respect to the other two and so limits the applicability of the method to few cases but can be applied, for instance, to subsidence problems. Furthermore, due to constant load, volumetric deformations can be directly linked to pressure increments [2].

For an elastic material

$$\varepsilon_V = \varepsilon_z = \lim_{\Delta z \to 0} \frac{\delta(\Delta z)}{\Delta z} = m_V d\overline{p} \tag{2.1}$$

where $m_V = \frac{(1-2\upsilon)(1+\upsilon)}{E(1-\upsilon)}$ is the variation volume coefficient, E is the Young's modulus and υ is the Poisson's modulus. Necessary conditions for this assumption can be expressed as follows:

$$\frac{\partial u_x}{\partial x} + \frac{\partial u_y}{\partial y} \ll \frac{\partial u_z}{\partial z} \tag{2.2}$$

$$\frac{\partial \sigma_z}{\partial t} = 0 \tag{2.3}$$

This approach has been used by Finol and Farouq Ali [3].

For the single phase fluid Gambolati [4], [5] obtained the uncoupled solution for an axial-symmetric case in a subsidence model for Venice. The flow equation has been solved by means of finite elements using a pressure distribution variable in time. The analysis of the deformation has been subsequently developed considering a one dimensional finite differences model for the elastic skeleton. In this case the modelling of the fluid phase and the solid has been realized with a different discretization of the domain where the nodes, in which the solution is computed, can be different as well as the parameters used during the simulation.

Generally speaking this kind of strategy has been widely adopted because allows to separate in two different steps the solution of the equations system previously shown. On the other hand it means that only one of the unknowns, depending on which one between the fluid and the solid phases is solved at first, is an independent variable the other one is computed as a consequence of the fulfilment of the equilibrium or continuity equations. This numerical techniques is very attractive because speeds up the computational time and allows to change the mesh on the domain depending on the phase considered but the solution is strongly affected by the fact that pressure and displacements cannot be solved contemporary producing a mistake in both of them.

A more detailed review about uncoupled solution methods can be found in the references of this chapter at number [6].

2.2. Coupled solutions

The discussion about the coupled solution strategies will be explained dealing with the equations for a single phase saturated porous media since it is the simplest case, whereas the more general multi-phase one can be obtained by this introducing the parameters shown in paragraph 1.3 (i.e. volume factor B_π, the solution ratio R_π) together with eq. (1.25), (1.26), (1.27), (1.28). As previously stated when a partially saturate porous media is taken into account the set of equations is exactly the same for the saturated single phase one with the only exception of the pressure value that should be considered, later on this aspect will be discussed in detail.

The two formulas (1.10) and (1.30) characterize the equations that govern soil and fluid mechanics according to Biot's theory [7], [8] and are here reported again for sake of completeness.

$$\int_{\Omega} \delta\boldsymbol{\varepsilon}\, \mathbf{D_T} \frac{\partial \boldsymbol{\varepsilon}}{\partial t} d\Omega - \int_{\Omega} \delta\boldsymbol{\varepsilon}\, \mathbf{I} \frac{\partial \mathbf{p}}{\partial t} d\Omega + \int_{\Omega} \delta\boldsymbol{\varepsilon}\, \mathbf{D_T}\, \mathbf{I} \frac{\partial \mathbf{p}}{\partial t} \frac{1}{3K_s} d\Omega - \int_{\Omega} \delta\boldsymbol{\varepsilon}\, \mathbf{D_T}\, \mathbf{c} d\Omega - \int_{\Omega} \delta\boldsymbol{\varepsilon}\, \mathbf{D_T} \frac{\partial \boldsymbol{\varepsilon}_0}{\partial t} d\Omega - \frac{d\tilde{\mathbf{f}}}{dt} = 0 \tag{2.4}$$

$$\bar{\mathrm{A}} = -\nabla^T \left\{ \frac{\mathbf{k}}{\mu_w} \nabla (p_w + \rho_w g h) \right\} + \left(\mathbf{I} - \frac{1}{3K_s} \mathbf{I} \mathbf{D_T} \right) \frac{\partial \boldsymbol{\varepsilon}}{\partial t} + \frac{1}{3K_s} \mathbf{I} \mathbf{D_T}\, \mathbf{c} + \left(\frac{(1-\phi)}{K_s} + \frac{\phi}{K_s} - \frac{1}{(3K_s)^2} \mathbf{I} \mathbf{D_T} \mathbf{I} \right) \frac{\partial p_w}{\partial t} = 0 \tag{2.5}$$

2.2.1. Solution of the boundary value

A boundary problem requires that all the equations must be fulfilled in each point of the domain Ω and the boundary conditions should be satisfied on the border Γ of that domain.

If we look at equation (2.4) it can be noticed that boundary conditions are here already incorporated so the attention is focused on continuity equation. In this case it should be take into account

- The continuity of the flux on the border (Neumann condition)

$$\bar{\mathrm{B}} \equiv -\mathbf{n}^T \frac{\mathbf{k}}{\mu} \nabla (p + \rho g h) - \mathbf{q} = 0 \tag{2.6}$$

  Where the vector **n** is the unitary vector normal to the boundary, whereas **q** is the exit velocity flow per unit of area of the border surface.

- Prescribed pore pressure (Dirichlet condition)

$$p = p^b \tag{2.7}$$

Considering that eq. (2.5) must be fulfilled in Ω and eq. (2.6) on Γ it is possible to write the following condition

$$\int_{\Omega} a^T \bar{\mathrm{A}}\, d\Omega + \int_{\Gamma} b^T \bar{\mathrm{B}}\, d\Gamma = 0 \tag{2.8}$$

Where *a* and *b* are arbitrary functions due to the fact that $\bar{\mathrm{A}}$ and $\bar{\mathrm{B}}$ are automatically satisfied in their domains. On the contrary, if eq. (2.8) is valid for every arbitrary value of *a* and *b*, the differential equations (2.5) and (2.6) must be satisfied for every point of the domain and of the boundary respectively.

Only few cases can be solved analytically using the set of equations for the skeleton and for the fluid phase presented before; in general for complicated problem is common practice to use the finite elements method for finding a solution with a good approximation. In the next paragraphs space and time discretization for the above mentioned system will be shown.

2.2.2. The Finite Elements Method

The finite elements method will be applied to the equations (2.4) and (2.8) in term of displacements and pore pressure. In the second formula the presence of a second derivative of the term ($p+\rho gh$) requires the application of the Green theorem (where the $\mathbf{n}_x$ is the cosine director, along the x direction, of the outward normal to the border)

$$\int_{\Omega} \phi \frac{\partial \Psi}{\partial x} d\Omega = -\int_{\Omega} \Psi \frac{\partial \phi}{\partial x} d\Omega + \int_{\Gamma} \phi \Psi \mathbf{n}_x d\Gamma \tag{2.9}$$

for having the weak form

$$\begin{aligned} \int_{\Omega} \Bigg\{ & (\nabla \mathrm{a})^T \frac{\mathbf{k}}{\mu} \nabla (p + \rho gh) + \mathrm{a}^T \left(\mathbf{I} - \frac{1}{3K_s} \mathbf{I}\mathbf{D}_\mathbf{T} \right) \frac{\partial \boldsymbol{\varepsilon}}{\partial t} + \mathrm{a}^T \frac{1}{3K_s} \mathbf{I}\mathbf{D}_\mathbf{T} \mathbf{c} + \\ & + \mathrm{a}^T \left(\frac{1-\phi}{K_s} + \frac{\phi}{K_w} - \frac{1}{(3K_s)^2} \mathbf{I}\mathbf{D}_\mathbf{T} \mathbf{I} \right) \frac{\partial p}{\partial t} \Bigg\} d\Omega - \int_{\Gamma} \Big\{ \mathrm{a}^T \mathbf{n}^T \frac{\mathbf{k}}{\mu} \nabla (p + \rho gh) + \\ & + \mathrm{b}^T \mathbf{n}^T \frac{\mathbf{k}}{\mu} \nabla (p + \rho gh) + \mathrm{b}^T \mathbf{q} \Big\} d\Gamma = 0 \end{aligned} \tag{2.10}$$

Since *a* and *b* have been chosen such that to be arbitrary functions it is possible to write down

$$\mathrm{b} = -\mathrm{a} \tag{2.11}$$

and thus simplify the previous equation as

$$\begin{aligned} \int_{\Omega} \Bigg\{ & (\nabla \mathrm{a})^T \frac{\mathbf{k}}{\mu} \nabla (p + \rho gh) + \mathrm{a}^T \left(\mathbf{I} - \frac{1}{3K_s} \mathbf{I}\mathbf{D}_\mathbf{T} \right) \frac{\partial \boldsymbol{\varepsilon}}{\partial t} + \mathrm{a}^T \frac{1}{3K_s} \mathbf{I}\mathbf{D}_\mathbf{T} \mathbf{c} + \\ & + \mathrm{a}^T \left(\frac{1-\phi}{K_s} + \frac{\phi}{K_w} - \frac{1}{(3K_s)^2} \mathbf{I}\mathbf{D}_\mathbf{T} \mathbf{I} \right) \frac{\partial p}{\partial t} \Bigg\} d\Omega + \int_{\Gamma} \mathrm{a}^T \mathbf{q} \, d\Gamma = 0 \end{aligned} \tag{2.12}$$

Now the approximation to finite elements is applied to eq. (2.4) and eq. (2.12). Displacements and pore pressure are computed in a series of points of the domain; this implies that the body should be divided in a series of elements in which nodes the values of $\bar{u}$ and $\bar{p}$ are found. The number of these points and their distribution depend on the problem considered and on the degree of approximation of the solution, as well as on the potential of the computer used in the analysis.

Obviously in the other points of the domain, different from the mesh nodes, the solution is determined by means of the shape functions of the elements, thus it is important to place the nodes in critical points where the attention is focused. The shape functions are relate on the type of element and the number of nodes per element used in the mesh, in this short description a generic symbol **N** will be used without discussing the details:

$$\begin{aligned} \mathbf{u} &= \mathbf{N}\bar{\mathbf{u}} \\ p &= \bar{\mathbf{N}}\bar{p} \\ \boldsymbol{\varepsilon} &= \mathbf{B}\bar{\mathbf{u}} \end{aligned} \tag{2.13}$$

The number and position of the nodes for the displacements vector and the pressure may not be the same, that's the reason why in eq. (2.13) two different symbols for the shape functions have been used. The F.E. discretization gives the following expressions:

$$\begin{aligned} &\int_\Omega \delta\bar{\mathbf{u}}^T \mathbf{B}^T \mathbf{D}_T \mathbf{B}\, d\Omega \frac{d\bar{\mathbf{u}}}{dt} - \int_\Omega \delta\bar{\mathbf{u}}^T \mathbf{B}^T \mathbf{I}\,\bar{\mathbf{N}}\, d\Omega \frac{d\bar{p}}{dt} + \\ &+ \int_\Omega \delta\bar{\mathbf{u}}^T \mathbf{B}^T \mathbf{D}_T \frac{1}{3K_s} \mathbf{I}\,\bar{\mathbf{N}} d\Omega \frac{d\bar{p}}{dt} - \int_\Omega \delta\bar{\mathbf{u}}^T \mathbf{D}_T \mathbf{B}\,\mathbf{c}\, d\Omega - \\ &- \frac{1}{dt}\int_\Omega \delta\bar{\mathbf{u}}^T \mathbf{D}_T \mathbf{B}\, d\boldsymbol{\varepsilon}_\mathbf{0}\, d\Omega - \int_\Omega \delta\bar{\mathbf{u}}^T \mathbf{B}^T \frac{d\mathbf{b}}{dt} d\Omega - \\ &- \int_\Gamma \delta\bar{\mathbf{u}}^T \mathbf{N}^T \frac{d\mathbf{f}}{dt} d\Gamma = 0 \end{aligned} \tag{2.14}$$

$$\begin{aligned} &\int_\Omega (\nabla \mathrm{a})^T \frac{\mathbf{k}}{\mu} \nabla\bar{\mathbf{N}}\, d\Omega\, \bar{p} + \int_\Omega \mathrm{a}^T \left(\mathbf{I} - \frac{1}{3K_s} \mathbf{I}\mathbf{D}_\mathbf{T} \right) \mathbf{B}\, d\Omega \frac{\partial\bar{\mathbf{u}}}{\partial t} + \\ &+ \int_\Omega \mathrm{a}^T \frac{1}{3K_s} \mathbf{I}\mathbf{D}_\mathbf{T}\mathbf{c} + \int_\Omega \mathrm{a}^T \left(\frac{1-\phi}{K_s} + \frac{\phi}{K_w} - \frac{1}{(3K_s)^2} \mathbf{I}\mathbf{D}_\mathbf{T}\mathbf{I} \right) \bar{\mathbf{N}} d\Omega \frac{\partial\bar{p}}{\partial t} \\ &+ \int_\Gamma \mathrm{a}^T \mathbf{q}\, d\Gamma + \int_\Omega \mathrm{a}^T \frac{\mathbf{k}}{\mu} \nabla\rho g h = 0 \end{aligned} \tag{2.15}$$

Equation (2.14) is valid for every arbitrary value of the virtual displacement, thus it is possible to get rid of this $\delta\bar{\mathbf{u}}$ and write the expression in a different manner, suitable for being introduce in a matrix system as shown later:

$$\mathbf{K}\frac{d\bar{\mathbf{u}}}{dt} + \mathbf{L}\frac{d\bar{\mathbf{p}}}{dt} - \mathbf{C} - \frac{d\tilde{\mathbf{f}}}{dt} = 0 \tag{2.16}$$

where the terms are

$$\begin{aligned}
\mathbf{K} &= \int_{\Omega} -\mathbf{B}^T \mathbf{D}_T \mathbf{B}\ d\Omega \\
\mathbf{L}^T &= \int_{\Omega} \mathbf{B}^T \mathbf{I}\, \bar{\mathbf{N}} d\Omega - \int_{\Omega} \mathbf{B}^T \mathbf{D}_T\ \frac{1}{3K_S} \mathbf{I} \bar{\mathbf{N}} d\Omega \\
\mathbf{C} &= -\int_{\Omega} \mathbf{B}^T \mathbf{D}_T\, \mathbf{c}\ d\Omega \\
d\tilde{\mathbf{f}} &= -\int_{\Omega} \mathbf{B}^T \mathbf{D}_T\, d\boldsymbol{\varepsilon}_o d\Omega - \int_{\Omega} \mathbf{N}^T d\mathbf{b}\ d\Omega - \int_{\Gamma} \mathbf{N}^T d\mathbf{f}\ d\Gamma = 0
\end{aligned} \tag{2.17}$$

It has to be noticed that the form of function *a* in equation (2.15) is still arbitrary and must be specified before solving the equation. It is better to choose a form for *a* that increases accuracy of the solution. In order to do that in the present work has been adopted the Galerkine's weighted residual method which means that among all the available functions exactly the shape functions have been considered. In the solution of the problem this technique has the advantage to origin symmetric matrix, which is suitable for numerical computation.

The equation (2.15) becomes

$$\mathbf{H}\,\bar{\mathbf{p}} + \mathbf{S}\frac{d\bar{\mathbf{p}}}{dt} + \mathbf{L}^T \frac{d\bar{\mathbf{u}}}{dt} - \bar{\mathbf{f}} = 0 \tag{2.18}$$

where

$$\begin{aligned}
\mathbf{H} &= \int_{\Omega} (\nabla \bar{\mathbf{N}})^T \frac{\mathbf{k}}{\mu} \nabla \bar{\mathbf{N}} d\Omega \\
\mathbf{S} &= \int_{\Omega} \bar{\mathbf{N}}^T \left[\frac{(1-\phi)}{K_S} + \frac{\phi}{K_w} - \frac{1}{(3K_S)^2} \mathbf{I}\, \mathbf{D}_T\, \mathbf{I} \right] \bar{\mathbf{N}}\ d\Omega \\
\mathbf{L} &= \int_{\Omega} \bar{\mathbf{N}}^T \left(\mathbf{I} - \frac{1}{3K_S} \mathbf{I}\, \mathbf{D}_T \right) \mathbf{B}\, d\Omega \\
\bar{\mathbf{f}} &= -\int_{\Gamma} \bar{\mathbf{N}}^T \mathbf{q}\, d\Gamma - \int_{\Omega} \bar{\mathbf{N}}^T \frac{1}{3K_S} \mathbf{I} \mathbf{D}_T c d\Omega - \int_{\Omega} \bar{\mathbf{N}}^T \nabla^T \frac{\mathbf{k}}{\mu} \nabla \rho g h\, d\Omega
\end{aligned} \tag{2.19}$$

It can be easily proved that these equations are symmetric if the matrix $\mathbf{D_T}$ remains symmetric.

The numerical integration is usually realized using computational techniques, for instance Gauss quadrature, Newton-Cotes quadrature [9], where the integral function is evaluated in a series of specific points inside the domain and on the border and then it is weighted and added up.

All the procedure has been developed in local coordinates ξ, η, ζ which can have positive or negative value depending on the reference system adopted. The global coordinates **x** are always expressed in terms of nodal coordinates **X** by means of a relation

$$\mathbf{x} = W\,\mathbf{X} \tag{2.20}$$

where *W* are weight functions depending on the local coordinate system.

Considering that the shape functions **N** or **N**-dashed are themselves functions expressed by the ξ, η, ζ coordinates it is possible to use these ones as weight functions, falling within the family of the so called *isoparametric elements*.

For sake of simplicity the equations system formed by (2.16) and (2.18), which represents the spatial discretization of differential equations, can be expressed in the condensed form:

$$\begin{bmatrix} 0 & 0 \\ 0 & \mathbf{H} \end{bmatrix} \begin{Bmatrix} \bar{\mathbf{u}} \\ \bar{\mathbf{p}} \end{Bmatrix} + \begin{bmatrix} \mathbf{K} & \mathbf{L} \\ \mathbf{L}^{\mathbf{T}} & \mathbf{S} \end{bmatrix} \frac{d}{dt} \begin{Bmatrix} \bar{\mathbf{u}} \\ \bar{\mathbf{p}} \end{Bmatrix} = \begin{Bmatrix} \frac{d\tilde{\mathbf{f}}}{dt} + \mathbf{C} \\ \bar{\mathbf{f}} \end{Bmatrix} \tag{2.21}$$

The values of displacements and pore pressure, in different time, can be obtained by solving the (2.21) set with an appropriate time-stepping algorithm as explained in the following paragraph.

2.2.3. Time discretization

The time discretization method can be regarded as one-dimensional finite element scheme, different from the spatial one.

The time domain is subdivided in a series of elements, as known as time steps, for each of them the solution of the system reported in the (2.21) is computed to get the variation of the unknowns: displacements and fluid pressure. The step-by-step integration can be added up in the end in order to understand the total evolution of the variables.

It has to be noticed that time integration has nothing different from the spatial one, thus the same integration form has been used for the system (2.21), giving the following

$$\begin{aligned} \int_{t_k}^{t_k+\Delta t_k} \bar{g} \begin{bmatrix} 0 & 0 \\ 0 & \mathbf{H} \end{bmatrix} \begin{Bmatrix} \bar{\mathbf{u}} \\ \bar{\mathbf{p}} \end{Bmatrix} dt + \int_{t_k}^{k+\Delta t_k} \bar{g} \begin{bmatrix} \mathbf{K} & \mathbf{L} \\ \mathbf{L}^{\mathbf{T}} & \mathbf{S} \end{bmatrix} \frac{d}{dt} \begin{Bmatrix} \bar{\mathbf{u}} \\ \bar{\mathbf{p}} \end{Bmatrix} = \\ = \int_{t_k}^{t_k+\Delta t_k} \bar{g} \begin{Bmatrix} \frac{d\mathbf{f}}{dt} + \mathbf{C} \\ \bar{\mathbf{f}} \end{Bmatrix} dt \end{aligned} \tag{2.22}$$

where Δt_k is the length of the k-time step chosen for the simulation whereas g is a time arbitrary function exactly as it has been done for spatial weak form of equation (2.10).

The first derivative of displacements and pore pressure in time can be approximated assuming a linear variation of the two unknowns in each time step (this approach is commonly used, reducing the computational effort and giving a good accordance with the results)

$$\begin{Bmatrix} \bar{\mathbf{u}} & \bar{\mathbf{p}} \end{Bmatrix} = \begin{Bmatrix} 1-\alpha & \alpha \end{Bmatrix} \begin{bmatrix} \mathbf{u}^t & \mathbf{p}^t \\ \mathbf{u}^{t+\Delta t} & \mathbf{p}^{t+\Delta t} \end{bmatrix} \tag{2.23}$$

where α is a parameter given as follows

$$\alpha = \frac{(t - t_k)}{\Delta t_k} \tag{2.24}$$

from the (2.22) and taking into account the (2.23) and the (2.24) it can be written

$$\begin{bmatrix} \mathbf{K} & \mathbf{L} \\ \mathbf{L}^{\mathbf{T}} & \mathbf{S} + \alpha \mathbf{H} \Delta t_k \end{bmatrix}_{k,\alpha} \begin{Bmatrix} \bar{\mathbf{u}} \\ \bar{\mathbf{p}} \end{Bmatrix}_{t_k + \Delta t_k} = \begin{bmatrix} \mathbf{K} & \mathbf{L} \\ \mathbf{L}^{\mathbf{T}} & \mathbf{S} - (1-\alpha)\mathbf{H} \Delta t_k \end{bmatrix}_{k,\alpha} \begin{Bmatrix} \bar{\mathbf{u}} \\ \bar{\mathbf{p}} \end{Bmatrix}_{t_k} + \begin{Bmatrix} \frac{d\mathbf{f}}{dt} + \mathbf{C} \\ \bar{\mathbf{f}} \end{Bmatrix}_{k,\alpha} \Delta t_k \tag{2.25}$$

The system (2.25) is the final form solved by the research F.E. code PLASCON 3D at every time step. It has to be noticed that, if the material behaves in a linear-elastic manner and if the permeability maintains constant, the matrix **K**, **L**, **S** and **H** do not change, meaning that they should be computed once in the first step of the simulation and no more, with a great saving of time in the analyses. On the contrary, for nonlinear material, matrix **K**, which deals with the solid skeleton, has to be estimated (locally for each element and then assembled in the global matrix) and updated in the system in each time step. The same has to be done for the contributes of permeability in **H** and the porosity in **S**, generating a more complicate model and slowing down the computation time.

The last point that should be discussed is the α parameter. The range of values available for this term varies between 0 to 1 and for each of them a different scheme is generated:

- α = 0 Euler explicit
- α = 0.5 Crank-Nicolson
- α = 1 Backward difference (Euler implicit)

In these three cases the algorithm gives the same result for the standard finite differences: foreword differences (Euler), central differences (Crank-Nicolson), and backward differences respectively. In the analyses presented in this work the Crank-Nicolson method has been adopted, since it guarantees a unconditionally stable solution for each size of the time discretization and because it generates a second-order convergence rate.

Other values for alpha can give different schemes which will be not discussed in this thesis, some detailed informations can be found in references [10], [11].

References

[1] Morgan K, Lewis R.W., White I.R., (1982) “The mechanism of ground surface subsidence above compacting multiphase reservoirs and their analysis by the finite element method”, *App. Math. Modelling*, **4**, pp. 217-24.

[2] Gambolati G. (1973), “Equation for one-dimensional vertical flow of groundwater, 2, Validity range of the diffusion equation”, *WAT. Res. Research*, **9**(5), pp. 1385-95.

[3] Finol A., Farouq Ali S.M., (1975), *“*Numerical simulation of oil production with simultaneous ground subsidence*”*, *S.P.E.J.*, **15**, pp. 411-24.

[4] Gambolati G., Freeze R.A., (1973) “Mathematical simulation of the subsidence of Venice, 1, theory”, *Wat. Res. Rresearch*, **9**, pp. 563-77.

[5] Gambolati G., Gatto P., Freeze R.A., (1974), “Mathematical simulation of the subsidence of Venice, 1, theory”, *Wat. Res. Research*, **10**, pp.563-77.

[6] Corapcioglu M.Y., (1984) “Land subsidence – a state of art review” in *Fundamentals of Trasport Phenomena in Porous Media*, ed J. Bear and M.Y. Corapcioglu, Nato A.S.I. Series, E 82, Nijhoff, Dordrecht, pp. 369-444.

[7] Biot M.A., (1941a), "General theory of three-dimensional consolidation", *J. Appl. Phys*., **12**, pp. 155-64.

[8] Biot M.A., (1955), "Theory of elasticity and consolidation for a porous anisotropic solid", *J. Appl. Phys.*, **26**, pp. 182-85.

[9] Zienkiewicz O.C., Taylor R.L., (1982), “*The Finite Element Method – Vol. I the Basis*”, Fifth Edition, McGraw-Hill ed.

[10] Sandhu R.S., (1968), “ Fluid flow in saturated porous elastic media”, PhD Thesis, University of California, Berkeley.

[11] Hwang C.T. Morgenstern N.R., Murray D.W., (1971), “On solution of lane strain consolidation problems by finite element methods”, *Can. Geot. J.*, **8**, pp.108-18.

3. Elastoplasticity

In many laboratory tests it has been observed that, beyond a particular stress level, different materials produce irreversible deformations. If this behaviour can be neglected under certain circumstances it is definitely untrue for others. Elasticity theory is based on the concept that the alteration of the particles is temporary and all the deformations induced by a certain loading condition can be fully recovered once the forces are removed.

In detail a direct and inverse bond between deformation and stress can always be defined leading to a one-to-one correspondence. This is very attractive computationally speaking, because it generates a really easy scheme to solve due to the fact that stiffness matrix of the system never changes as already mentioned in the previous chapter.

Some complications arise for instance in porous media when the stress reaches a level (*yield stress*) which causes the slippage of the grains in addition to their own deformation and, in some cases, the entity of the former is way more relevant than the latter. This relative movement causes a rearrangement among particles that is unique and cannot be brought back to the original configuration even if the load is removed, producing the so called plastic deformations. It has to be pointed out that the same behaviour can be observed even in metals which are definitely not granular material, in this case other considerations due to the crystal solid structure modification are involved, but they are not investigated in this thesis.

This lost of one-to-one correspondence implies that it is necessary to formulate the constitutive equations in term of stress and strain rates because the loading history and the evolution of the stresses must be taken into account. Only if the analysis is carried out from the current point to the next one the answer of the model can be defined correctly.

The elastoplastic constitutive equations that will be described in this chapter can be used for modelling a general material (metals, granular material etc.), however all the applications will be focused on the description of soils as shown in the following chapters. In many engineering problems it is admissible to neglect the more or less pronounced time dependence of soil deformation and consider it as rate-independent material. Starting from the pioneer work of Coulomb and passing through the Cam-Clay model, new elastoplastic theories have been developed with increasing complexity and variables involved in order to represent soil behaviour in the most realistic way.

The first part of this chapter is focused on dealing with *conventional* elastoplastic constitutive equations, where the classification in conventional frame was due to Drucker [1]. The second part introduces instead *unconventional* models treating in detail with the subloading surface which has been proposed by Proff. Hashiguchi and Ueno in the ’70 [2].

The choice to use this specific model has to be searched in its simple formulation together with its capacity of predicting realistically soil behaviour both in a monotonic loading and under cyclic loading-unloading analyses. The introduction of a second surface, additionally to the classical yield surface, creates the possibility of a very efficient and numerically easy computation. Furthermore the solid

mathematic derivation of the constitutive bond guarantees the fulfilment of all the mechanical requirements for the material and the possibility to use an associative flow rule, implying the symmetry of the stiffness matrix **K**, with all the advantages connected.

Although a formulation in finite strains for the subloading surface model already exists, the theory described here is limited to the infinitesimal strains case, remanding to the bibliographical references for a more detail explanation.

A last aspect that should be highlighted is that no reference will be made on the fluid phase in this chapter, assuming that the plastic behaviour of the solid phase affects directly only the skeleton, whereas the fluid part is interested indirectly by means of the coupling solution as will be shown in the numerical analyses chapter. Under this hypothesis the *idrostatic* component of the stress mentioned in the following paragraphs refers to the effective stress only and, despite of the name, is not relate strictly to the fluid pressure.

3.1. Conventional Elastoplasticity

3.1.1. Uniaxial case

The purpose of this paragraph is to show the basic equations regulating the elastoplastic answer of a general material. Since it has already mentioned the necessity to proceed in an incremental form the stress and strain symbols written in the following formula should be intended in a rate form, which for sake of simplicity will be omitted.

In textbooks is common to start dealing with the elastoplasticity from the definition of the one dimensional bond, which is quite easy to explain and to be understood. In addition the behaviour of the uniaxial case sums up some of the most important features of the general case and all the numerical analyses in this thesis have been firstly investigated by one dimensional simulations as shown later.

Observing Figure 3 the point moves, from the origin of the graph, in a line which tangent is exactly the value of the elastic modulus E of the material and the answer is purely linear elastic, giving a one-to-one correspondence expressed by Hooke's law $\sigma = E\varepsilon$. When it reaches the value σ_0 for the stress in the point A the behaviour suddenly changes and some irreversible deformations are induced. From point B ($\sigma = \sigma_{01}$) the sample is unloaded and some of the deformations produced in the loading path are recovered. When the unloading is complete (point C) the intersection with the deformations axes is not in the origin of the space, meaning that the whole process has altered the structure of the material by means of some reorganization of the particles which can be proved by a residual deformation equal to $(\varepsilon_B - \sigma_{01})/E$.

The segment BC can be considered elastic, meaning that inside this field stress variations $\Delta\sigma$ correspond to reversible deformation variations $\Delta\varepsilon$ linked together by the Young's modulus. For sake

of completeness the tangent E is not exactly the same for the two interval 0A and BC, but in the common practice it is assumed to be the equal.

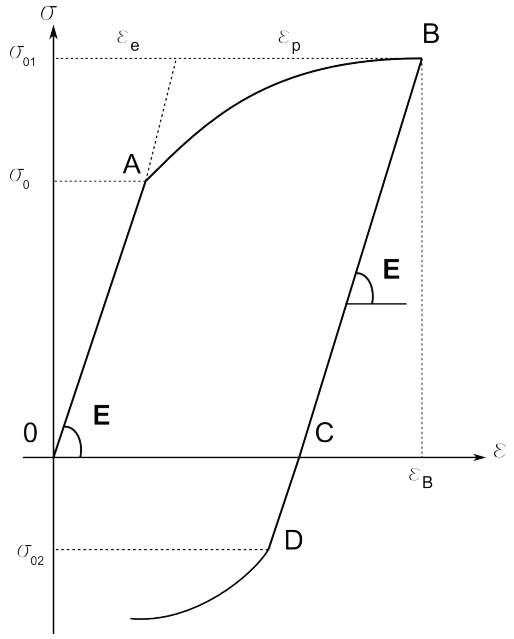

Figure 3 – Uniaxial elastoplastic behaviour.

This brief description points out the necessity to distinguish in separate contributes, one *elastic* and reversible ε_e and one permanent and *plastic* ε_p, for an analytical formulation of the elastoplastic bond. Under the hypothesis of infinitesimal strains this two terms additively form the total deformation ε:

$$\varepsilon = \varepsilon_e + \varepsilon_p \tag{3.1}$$

Furthermore this let us to write the linear elastic relationship as

$$\sigma = E(\varepsilon - \varepsilon_p) \tag{3.2}$$

The irreversible nature of the plastic deformations implies that, the elastoplastic bond should depend on the loading history and, as reminded before, it must be written in an incremental form. It has to be specified that the stress and strain rates are time independent (for theoretical considerations at this point creep phenomena is not considered, it will be introduced for a numerical application in the *Appendix*), so it means that time plays the rule of creating an order between subsequent loading and unloading phases and nothing more.

The control of the loading history is really important because the boundaries of the so called elastic domain depend on it. If the incremental process starts from a point inside the instantaneous elastic domain (every point inside the line 0A ore BD, with the only exception of the point A, B and D themselves) the answer will be purely elastic with a one-to-one correspondence. On the contrary when the process starts from one of the extremes then some plastic deformations will be induced. If we chose to analyze the behaviour from the point B two different mechanisms can take place depending on the sign of the deformation rate.

$$\begin{aligned} \sigma &= E_{ep}\varepsilon \quad \text{for } \varepsilon \succ 0 \\ \sigma &= E\varepsilon \quad \text{for } \varepsilon \prec 0 \end{aligned} \tag{3.3}$$

Where the term E_{ep} indicates the tangent of the curve AB at the point B. Generally speaking the elastic domain can be defined, in terms of stress, by the following inequality:

$$\sigma_{02} \leq \sigma \leq \sigma_{01} \tag{3.4}$$

Where the extremes depend, once again, on the loading history of the sample and on the type of material. It is quite easy to understand that the direct bond, express for example in the eq. (3.3), can be always defined because the answer in term of stress can be univocally determined if the strain rate is known (some exceptions hold in case of critical softening or subcritical softening, but they're very rare), on contrary in certain situations (i.e. perfect plasticity, softening) the inverse bond is undetermined or not admissible.

The condition (3.4) can be expressed in a different form which is more suitable for the definition of the bond. The plastic deformations can cumulate in tensile stress or compression (for ductile material the limit of the instantaneous elastic domain coincide, for fragile materials or other geomaterials this is generally not true) so it is important to define a way to take them into account.

$$\varepsilon_p = \begin{bmatrix} 1 & -1 \end{bmatrix} \begin{bmatrix} \lambda_1 \\ \lambda_2 \end{bmatrix} = \mathbf{N}\boldsymbol{\lambda}_{tot} \tag{3.5}$$

The vector [1 -1] is usually expressed as **N** and indicates the normalized normal to the plastic surface (in uniaxial case the whole surface coincides with σ_{01} or σ_{02} respectively), whereas the parameter λ_i is named *positive proportionality factor* and is such to be not-negative and not-decreasing:

$$\boldsymbol{\lambda} \geq 0 \tag{3.6}$$

(note that the positive proportionally factor is here expressed in matrix form and rate one is implied). The case when λ_i is positive or null should be now discussed. As stated before a plastic deformation can be produced only if the point lies on the boundaries of the elastic domain (i.e. point A, B and D), so it is logical to consider that the positive proportionally factor will assume a non null value in case the point stays on the extremes whereas it will be zero for all the other points. The idea is to introduce new parameters which give an idea of how far is the point from the edge of the elastic domain and if it will maintain there during the simulation or it will go back inside the elastic field. These new variables are called *plastic functions* and they're function of the σ_{01} or σ_{02} stresses:

$$\begin{bmatrix} \varphi_1 \\ \varphi_2 \end{bmatrix} = \begin{bmatrix} 1 \\ -1 \end{bmatrix} \sigma_{tot} - \begin{bmatrix} \sigma_{01} \\ \sigma_{02} \end{bmatrix} \leq 0 \quad \text{or} \quad \boldsymbol{\varphi} = \mathbf{N}^T \sigma_{tot} - \boldsymbol{\sigma}_0 \leq 0 \tag{3.7}$$

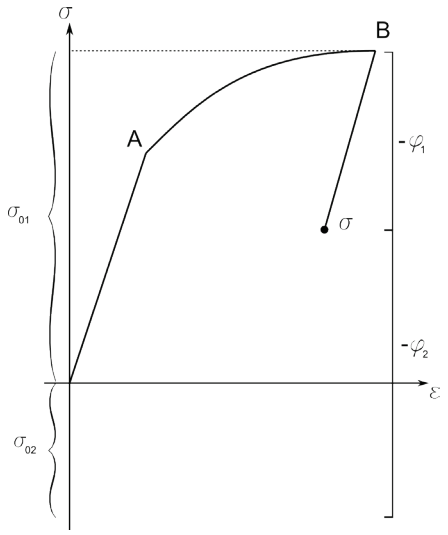

Figure 4 – representation of the plastic functions.

When, for example, the point lies on the AB curve the plastic function φ_1 becomes zero until the point B is reached and then the elastic unload starts. This means that proportionally factor and the plastic functions are strictly connected one to each other giving the well known *Kuhn-Tucker conditions:*

$$\boldsymbol{\varphi} \le 0, \quad \boldsymbol{\lambda} \ge 0, \quad \boldsymbol{\varphi}\boldsymbol{\lambda} = 0 \tag{3.8}$$

It has to be noticed that the extremes of the elastic domain depend on the proportionally factor which plays the rule of keeping memory of all the loading history and also assumes the meaning of internal variable for the elastoplastic problem.

$$\boldsymbol{\sigma}_0 = f(\boldsymbol{\lambda}) \tag{3.9}$$

This aspect is very important when different mechanisms such as perfect plasticity, linear hardening, non-linear hardening, etc. should be take into account because a modification of the (3.7) becomes necessary:

$$\boldsymbol{\varphi} = \mathbf{N}^T \sigma - \mathbf{H}\boldsymbol{\lambda} \tag{3.10}$$

where matrix **H** is called hardening matrix, which terms are the partial derivatives of the functions of the extremes respect to the internal variables:

$$\mathbf{H} = \begin{pmatrix} \dfrac{\partial \sigma_{01}}{\partial \lambda_1} & \dfrac{\partial \sigma_{01}}{\partial \lambda_2} \\ \dfrac{\partial \sigma_{02}}{\partial \lambda_1} & \dfrac{\partial \sigma_{02}}{\partial \lambda_2} \end{pmatrix} \tag{3.11}$$

At this point the uniaxial elastoplastic bond can be defined

$$\sigma = E(\varepsilon - \varepsilon_p) \qquad \varepsilon_p = \mathbf{N}\boldsymbol{\lambda}_{tot}$$
$$\boldsymbol{\varphi} = \mathbf{N}^T \sigma_{tot} - \boldsymbol{\sigma}_0(\boldsymbol{\lambda}_{tot}) \qquad \dot{\boldsymbol{\varphi}} = \mathbf{N}^T \sigma - \mathbf{H}\boldsymbol{\lambda} \tag{3.12}$$
$$\boldsymbol{\varphi} \le 0 \quad \boldsymbol{\lambda} \ge 0 \quad \boldsymbol{\varphi}^T \boldsymbol{\lambda} = 0 \quad \dot{\boldsymbol{\varphi}}^T \boldsymbol{\lambda} = 0$$

Note that the Kuhn-Tucker (as known as *consistency requirement*) has been modified including the condition on the rate form of the plastic functions, meaning that irreversible deformations are induced only if the point keeps lying on the edge of the elastic domain, this last check is named *persistency conditions* [3].

Considering now the case in which the point lies on one of the two extremes of the instantaneous elastic domain, for instance the point B of Figure 4, and keeps on it during the process (i.e. fulfilment of both the consistency requirement and persistency conditions) it is possible to write:

$$\sigma = E(\varepsilon - 1\lambda_1) \tag{3.13}$$

$$\dot{\varphi}_1 = 1\sigma - H_{ii}\lambda_1 \tag{3.14}$$

$$\varphi_1 \le 0 \quad \lambda_1 \ge 0 \quad \varphi\lambda = 0 \quad \dot{\varphi}_1 \lambda_1 = 0 \tag{3.15}$$

the equations (3.13), (3.14) and (3.15) allow to explicit the direct and inverse bond when it is possible. Eliminating the σ by substitution of the (3.13) into (3.14), where obviously the term N_i^2 is equal to 1^2 and then still 1, it is possible to write:

$$\dot{\varphi}_1 = 1E\dot{\varepsilon} - \left(H_{ii} + E\right)\lambda_1 \tag{3.16}$$

Considering the definition of the proportionality factor, expressed in eq. (3.6), and assuming a positive value of *(H_{ii} + E)* then the value of the plastic function rate cannot exceed the value of the first term of the (3.16). If this is negative or null eq. (3.15) requires that λ_1 = 0; on the contrary if this is positive the rate of the plastic function must be null and in this case is possible to compute λ_1 without ambiguity. In both cases it is possible to explicit the direct bond as:

$$\text{if } 1E\dot{\varepsilon} \le 0 \qquad \lambda_1 = 0, \quad \dot{\varphi}_1 = 1E\dot{\varepsilon} \le 0 \qquad \text{and} \quad \sigma = E\varepsilon \tag{3.17}$$

$$\text{if } 1E\dot{\varepsilon} \succ 0 \qquad \text{if } 1E\dot{\varepsilon} \le 0 \quad \dot{\varphi}_1 = 0, \quad \lambda_1 = \frac{1}{H_{ii} + E} 1E\dot{\varepsilon} \succ 0 \qquad \text{and} \quad \sigma = E\frac{H_{ii}}{H_{ii} + E}\varepsilon \tag{3.18}$$

Under the condition that

$$H_{ii} \succ -E \tag{3.19}$$

The inverse relation between strain and stress can be written in an analogous way as shown for the (3.17) and (3.18), but in this case the condition that is required is that H_{ii} must be positive because, only in that case, the proportionality factor can be defined univocally.

$$\begin{aligned} &\text{if } \ 1\sigma \le 0 \qquad \lambda_1 = 0, \quad \dot{\varphi}_1 = 1\sigma \le 0 \\ &\text{and} \qquad \varepsilon = \frac{1}{E}\sigma \end{aligned} \tag{3.20}$$

$$\begin{aligned} &\text{if } \ 1\sigma \succ 0 \qquad \dot{\varphi}_1 = 0, \quad \lambda_1 = \frac{1}{H_{ii}}\partial\sigma \succ 0 \\ &\text{and} \qquad \varepsilon = \frac{1}{E}\frac{H_{ii}+E}{H_{ii}}\sigma \end{aligned} \tag{3.21}$$

Observing eq. (3.18) the tangent of the curve in the plastic domain (i.e. the branch AB in Figure 3) can easily identified:

$$E_{ep} = E\frac{H_{ii}}{H_{ii}+E} \tag{3.22}$$

This is the expression for the elastoplastic modulus in one dimensional elastoplasticity and, as it will be clear later, the formulation is quite simple compared to the three dimensional case but it is still useful to define different types of plasticity and also because it is exactly the form that has been used in all the test programs for the F.E. code.

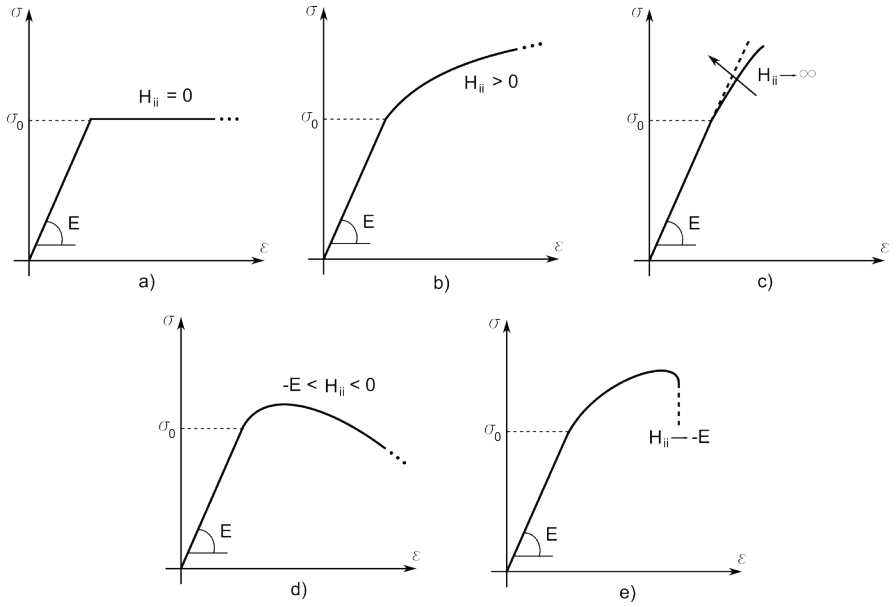

Figure 5 – a) perfect plasticity, b) hardening, c) almost linear-elastic, d) softening, e) critical softening.

If H_{ii} is null then the curve in the elastoplastic branch becomes flat, case b) of Figure 5 corresponds to the hardening case in which material is still capable of sustain a stress increment after the value of σ_0 has been past. If H_{ii} tends to infinite then the curve approaches to the linear elastic line and in this

case the material behaves almost like an elastic one. On the contrary cases d) and f) show a material which cannot sustain an increment of stress after the yielding, creating a softening branch which can be push up to the critical state when H_{ii} tends to the limit value of $-E$.

It should be point out that in cases b) and c) is always possible to define the inverse relation between stress and strain explicited in the (3.21) however it is impossible in a) due to the null denominator of the fraction, it becomes null in e) because the numerator is zero, whereas for case d) it cannot be determined if the answer is an elastic unloading or a plastic softening.

Uniaxial case is a really simple case where it is quite easy to compute the normal vectors to the plastic surface (which here coincides with the yielding stress) because they can be just +1 or -1 depending on extension or compression. This is very useful in computational simulation, speeding up the computational time and reducing many numerical errors as it will be shown for the simulations in the return mapping case.

3.1.2. General conventional elastoplastic constitutive law

This paragraph reformulates all the equations seen before in a general tensorial way where all the components of the stress tensor **σ** should be considered. Obviously some complications arise because the yield surface is now represented by a three dimensional surface and doesn't coincide anymore with a point as in the previous case. This leads to a more complex mathematical treatment for the derivative of the plastic potential respect to the stress tensor in order to compute the normal vector.

Here no indications have been made to relate the constitutive law with a precise type of material, it means that the shape of the yield surface will be not defined at this point as well as the nature of hardening rule, giving a simple general introduction to a elasto-plastic rheology model as described by Drucker [1].

The analysis is limited to the infinitesimal strains theory and thus we can confuse the reference and the actual configurations, it is possible to write the velocity gradient for example as:

$$\mathbf{L} = \frac{\partial \mathbf{v}}{\partial \mathbf{x}} \tag{3.23}$$

Where **v** is the velocity vector, whereas **x** are the points coordinate. Using a property of the second-order tensors, well known as the Cartesian decomposition, the velocity gradient tensor is split in two parts: a symmetrical one **ε** (the strain rate) and the skew symmetric one **W** (the continuum spin). In detail:

$$\boldsymbol{\varepsilon} = \frac{1}{2}(\mathbf{L} + \mathbf{L}^T) \quad \text{and} \quad \mathbf{w} = \frac{1}{2}(\mathbf{L} - \mathbf{L}^T) \tag{3.24}$$

It is also assumed that the total strain rate **ε** can be additively decomposed into an elastic part $\boldsymbol{\varepsilon}^e$ and into a plastic one $\boldsymbol{\varepsilon}^p$, i.e. in a component:

$$\boldsymbol{\varepsilon}_{ij} = \boldsymbol{\varepsilon}_{ij}^{e} + \boldsymbol{\varepsilon}_{ij}^{p} \tag{3.25}$$

The elastic contribution is given using the fourth-order elastic tensor as shown below:

$$\boldsymbol{\sigma}_{ij} = \mathbf{E}_{ijkl} \cdot \boldsymbol{\varepsilon}_{kl}^{e} \tag{3.26}$$

Finally re-writing the previous relationship and including the additive property of the total strain rate we obtain exactly the same results obtained for the one dimensional case for eq.(3.2)

$$\boldsymbol{\sigma}_{ij} = \mathbf{E}_{ijkl}(\boldsymbol{\varepsilon}_{kl} - \boldsymbol{\varepsilon}_{kl}^{p}) \tag{3.27}$$

As just mentioned in a three dimensional stress space it is necessary to define a yield surface to distinguish an elastic domain from the plastic one. In this case no kinematic or rotational hardening has been considered so it is possible to assume that the expansion or contraction of the plastic potential in the stress space is regulated by a simple isotropic hardening.

$$f(\boldsymbol{\sigma}) = F(H) \tag{3.28}$$

where *F* is the so called hardening function which regulates the dimension of the surface and it depends on the *H* named *isotropic hardening/softening variable*. Observing the previous equation it can be notice that, if we take to the left side of the equal all the terms, we obtain exactly the plastic function defined in the previous paragraph (eq. (3.7)) in the particular case in which the point lies on the yield surface

$$\boldsymbol{\varphi} = f(\boldsymbol{\sigma}) - F(H) = 0 \tag{3.29}$$

It is assumed that the stress function (i.e. the left term of eq. (3.28)) depends only on stress invariants and it is a homogeneous function of degree-one of $\boldsymbol{\sigma}$

$$f(s\boldsymbol{\sigma}) = s f(\boldsymbol{\sigma}) \tag{3.30}$$

where *s* is an arbitrary positive scalar. This allows to write

$$tr\left(\frac{\partial f(\boldsymbol{\sigma})}{\partial \boldsymbol{\sigma}}\boldsymbol{\sigma}\right) = f(\boldsymbol{\sigma}) \tag{3.31}$$

by means of the *Euler's theorem* for homogeneous function in degree-one (for additional details see Appendix 3 of reference [2]):

$$\sum_{i=1}^{n} \frac{\partial f(x)}{\partial x_i} x_i = k\, f(x) \qquad \forall\, x \in A \tag{3.32}$$

Using eq. (3.28) and (3.31) it holds

$$\frac{\partial f(\boldsymbol{\sigma})}{\partial \boldsymbol{\sigma}} = \frac{tr\left(\frac{\partial f(\boldsymbol{\sigma})}{\partial \boldsymbol{\sigma}}\boldsymbol{\sigma}\right)}{tr(\mathbf{N}\boldsymbol{\sigma})}\mathbf{N} = \frac{\partial f(\boldsymbol{\sigma})}{tr(\mathbf{N}\boldsymbol{\sigma})}\mathbf{N} = \frac{F}{tr(\mathbf{N}\boldsymbol{\sigma})}\mathbf{N} \tag{3.33}$$

Where **N** is the normalized outward vector to the yield surface and as reminded before it has to be derived directly from the mathematical expression of the plastic potential, in general form

$$\mathbf{N} \equiv \frac{\partial f(\boldsymbol{\sigma})}{\partial \boldsymbol{\sigma}} \Big/ \left\| \frac{\partial f(\boldsymbol{\sigma})}{\partial \boldsymbol{\sigma}} \right\| \tag{3.34}$$

Using the expression (3.28) for the yield surface it keeps a similar shape and orientation respect to the origin of the stress space by taking into account the homogeneity of the function and also because any shift induced by a kinematic or rotational hardening has been ignored.

Using a time differentiation the consistency condition can be written as

$$tr\left(\frac{\partial f(\boldsymbol{\sigma})}{\partial \boldsymbol{\sigma}} \overset{\circ}{\boldsymbol{\sigma}}\right) = F' \overset{\bullet}{H} \tag{3.35}$$

where

$$F' \equiv \frac{dF}{dH} \tag{3.36}$$

Indicates the total derivative of function F respect to the isotropic/softening variable, *tr* is the trace, ($\overset{\circ}{\boldsymbol{\sigma}}$) represents the co-rotational rate (becoming simply the time derivative under the hypothesis of small strain) and at last the symbol ($\bullet$) over the H stands for the time material derivative (i.e. $\frac{DH}{Dt} = \frac{\partial H}{\partial t} + \mathbf{v}\cdot\nabla H$). $\dot{H}$ is assumed to be function of the stress, *internal variables*, and plastic strain rate

$$\dot{H} = h(\boldsymbol{\sigma}, H_i, \boldsymbol{\varepsilon}^p) \tag{3.37}$$

the symbol H_i stands for a generic internal variable with the index *i* that varies from 1, 2, etc. *h* is a homogeneous function of degree-one of the plastic deformation rate which means, as well for the yield condition,

$$h(\boldsymbol{\sigma}, H_i, s\boldsymbol{\varepsilon}^p) = s\,h(\boldsymbol{\sigma}, H_i, \boldsymbol{\varepsilon}^p) \tag{3.38}$$

This assumption is true only for rate-independent deformation behaviour, whereas *h* becomes a nonlinear equation of $\boldsymbol{\varepsilon}^p$ in general.

Once defined the yield function, which let distinguish among points inside and outside the elastic domain, it has also to be specified a *flow rule* that governs the increments of plastic deformation. Depending on how this formula is obtained we can distinguish between *associate* and *non-associate*

flow rule. The former type is the most common and it is also used in this work deriving the expression of the yield function respect to the stress tensor for a certain point. It is named *associated flow* or *normality rule* because the vector is "associated" and normal to a plastic potential surface that is exactly the yield surface. The latter type is obtained defining a further surface called potential plastic surface $g(\boldsymbol{\sigma})$ from which, once again, the derivative respect to the actual stress is taken:

$$\mathbf{M} \equiv \frac{\partial g(\boldsymbol{\sigma})}{\partial \boldsymbol{\sigma}} \Bigg/ \left\| \frac{\partial g(\boldsymbol{\sigma})}{\partial \boldsymbol{\sigma}} \right\| \tag{3.39}$$

For sake of generality the expression of the flow rule will be given using this **M** vector, however in the numerical analyses carried out eq. (3.34) has been used instead of (3.39) imposing $f(\boldsymbol{\sigma}) = g(\boldsymbol{\sigma})$

$$\boldsymbol{\varepsilon}^p = \lambda \mathbf{M} \tag{3.40}$$

where λ is the proportionality factor already introduced for the uniaxial case in eq. (3.5). Substituting the equations (3.33) and (3.40) into the consistency condition ((3.35)) it holds

$$tr(\mathbf{N}\overset{\circ}{\boldsymbol{\sigma}}) = \frac{F'}{F} tr(\mathbf{N}\boldsymbol{\sigma})\ \lambda\ h(\boldsymbol{\sigma}, H_i, \mathbf{M}) \tag{3.41}$$

From the previous expression it is possible to derive three important parameters of the elastoplastic problem: the proportionality factor, the plastic strain rate, and the plastic modulus

$$\lambda = \frac{tr(\mathbf{N}\overset{\circ}{\boldsymbol{\sigma}})}{M^p} \tag{3.42}$$

$$\boldsymbol{\varepsilon}^p = \frac{tr(\mathbf{N}\overset{\circ}{\boldsymbol{\sigma}})}{M^p}\mathbf{M} \tag{3.43}$$

$$M^p = \frac{F'}{F} tr(\mathbf{N}\boldsymbol{\sigma})\ h(\boldsymbol{\sigma}, H_i, \mathbf{M}) \tag{3.44}$$

remembering that, under the hypothesis of infinitesimal strains, we can consider that the elastic deformation and the plastic one additively form the total $\boldsymbol{\varepsilon}$ we can reformulate eq. (3.25) as:

$$\boldsymbol{\varepsilon} = \mathbf{E}^{-1}\overset{\circ}{\boldsymbol{\sigma}} + \frac{tr(\mathbf{N}\overset{\circ}{\boldsymbol{\sigma}})}{M^p}\mathbf{M} \tag{3.45}$$

The proportionality factor λ can also be written in term of the strain rate by using the symbol Λ and by substituting into eq. (3.41) the expression (3.27)

$$tr(\mathbf{NE}(\boldsymbol{\varepsilon}-\boldsymbol{\varepsilon}^p)) = \frac{F'}{F} tr(\mathbf{N}\boldsymbol{\sigma})\ \lambda\ h(\boldsymbol{\sigma},H_i,\mathbf{M})$$

$$\text{but } \boldsymbol{\varepsilon}^p = \frac{tr(\mathbf{N}\overset{\circ}{\boldsymbol{\sigma}})}{M^p}\mathbf{M},\ \lambda = \frac{tr(\mathbf{N}\overset{\circ}{\boldsymbol{\sigma}})}{M^p} \quad \text{and } M^p = \frac{F'}{F} tr(\mathbf{N}\boldsymbol{\sigma})\ h(\boldsymbol{\sigma},H_i,\mathbf{M}) \tag{3.46}$$

then

$$tr(\mathbf{NE}\boldsymbol{\varepsilon}) - tr(\mathbf{NE}\lambda\mathbf{M}) = \lambda M^p$$

Changing the expression of λ into Λ and solving for the latter

$$\Lambda = \frac{tr(\mathbf{NE}\boldsymbol{\varepsilon})}{\left[M^p + tr(\mathbf{NEM})\right]} \tag{3.47}$$

In conclusion, using the inverse relationship between stress and strain expressed in the (3.45), it holds

$$\overset{\circ}{\boldsymbol{\sigma}} = \mathbf{E}\boldsymbol{\varepsilon} - \frac{tr(\mathbf{NE}\boldsymbol{\varepsilon})}{M^p + tr(\mathbf{NEM})}\mathbf{EM} \tag{3.48}$$

$$\overset{\circ}{\boldsymbol{\sigma}} = \left\{\mathbf{E} - \frac{(\mathbf{EM})\otimes(\mathbf{NE})}{M^p + tr(\mathbf{NEM})}\right\}\boldsymbol{\varepsilon} \tag{3.49}$$

$$\mathbf{E}^{ep} = \mathbf{E} - \frac{(\mathbf{EM})\otimes(\mathbf{NE})}{M^p + tr(\mathbf{NEM})} \tag{3.50}$$

The content of the brackets in the previous formula is the so called *elastoplastic matrix* and plays an analogous role of the one for the uniaxial case in (3.22). It has to be noticed that in this general case the form of the matrix is not-symmetrical, this is due to the fact that a different plastic potential from the yield surface has been chosen. To symmetrise eq.(3.50) it is necessary to assume that plastic deformations are induced outward-normally the yield function so the previous formula becomes

$$\mathbf{E}^{ep} = \mathbf{E} - \frac{(\mathbf{EN})\otimes(\mathbf{NE})}{M^p + tr(\mathbf{NEN})} \tag{3.51}$$

3.1.3. On associative flow rule

A brief explanation on the associative flow rules and postulates lying at the base of this concept will be given in this paragraph.

The two well known postulates, one by Drucker [6] and the other one by Ilyushin [4], both lead to the normality of the plastic strain increment respect to the yield surface in the stress space.

- Drucker stated that *"the work done during the stress cycle by external agency is positive"* and it can be translated by the following formula as:

$$W_D = \oint_{\sigma} \left(\sigma_{ij} - \sigma_{ij}^0 \right) d\varepsilon_{ij} \geq 0 \tag{3.52}$$

σ_{ij}^0 is a generic initial state in the stress space where the cycle begins and ends. Starting from the (3.52), and assuming that the inside the yield surface is the elastic domain, then is possible to write the inequality

$$\left(\boldsymbol{\sigma}_y - \boldsymbol{\sigma}_0 \right) d\boldsymbol{\varepsilon}^p \geq 0 \tag{3.53}$$

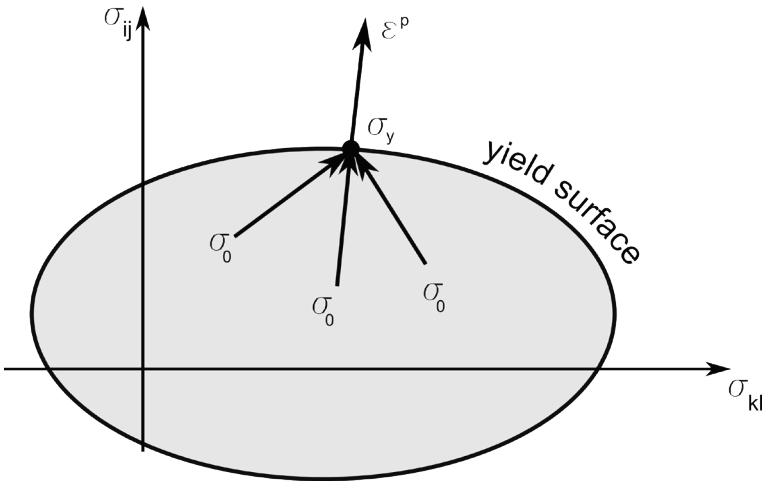

Figure 6 – Normality rule.

where σ_y is a point lying on the yield surface. To fulfill eq. (3.53) some assumptions must hold:

a) The plastic strain rate is directed outward normal the yield surface as shown in Figure 6, leading to associate flow rule where the flow direction depends only on the current stress and not on the stress rate;

b) The yield surface must be convex. This is an important assumption and can be easily explained looking at the vector displayed in Figure 6. If the surface is concave it can happen that vector ($\boldsymbol{\sigma}_y - \boldsymbol{\sigma}_0$) form an obtuse angle with the vector of the plastic strain rate and then violates the postulate.

- Ilyushin defined a class of material for which the net work in an arbitrary strain cycle is non-negative,

$$W_1 = \oint \sigma_{ij} d\varepsilon_{ij} \geq 0 \tag{3.54}$$

and also demonstrated that $W_1 > W_D$ so proving that the class of materials obeying Ilyushin's postulate is wider than that following the Drucker's one. It is easy to imagine that a strain cycle is always realizable, however the stress cycle cannot be made in softening case due to the fact that the stress cannot go back to the initial value. In fact an arbitrary deformation can be always given instead the stress is limited by the material resistance.

Additionally it has to be pointed out that the hypothesis, in which the interior of the yield surface is a purely elastic domain, holds only for the Drucker's postulate, whereas is not essential for the validity of the positivity of the second-order plastic relaxation work which states that the purely elastic deformation is induced at the moment of the unloading. This last assumption is fundamental for the introduction of the subloading surface method as it will be clear later.

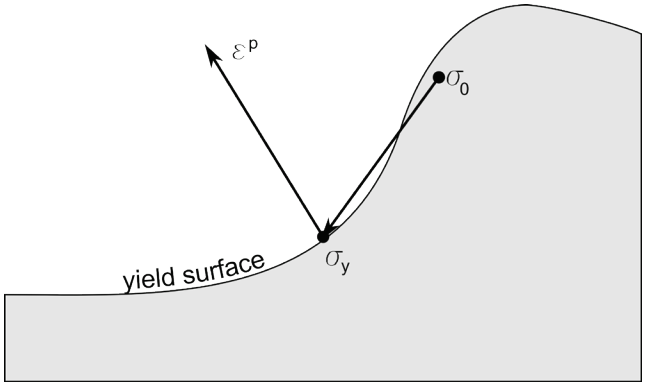

Figure 7 – example of violation of Drucker's postulate.

If Drucker's postulate is restricted to stress cycle that involve only infinitesimal additional plastic straining, the inequality expressed by eq. (3.52) becomes, considering an elastic recovery in closed stress cycles,

$$W_D = (\sigma_{ij} - \sigma_{ij}^0) d\varepsilon_{ij}^p + \frac{1}{2} d\sigma_{ij} d\varepsilon_{ij}^p \geq 0 \tag{3.55}$$

when the stress σ_{ij}^0 is well inside the current yield surface or on the yield surface far away from the current stress point σ_{ij} the second term of the (3.55) goes to zero if $d\varepsilon_{ij}^p$ tends to zero and leads to the (3.53), this is often referred as *the principle of the maximum plastic work* [6], [7].

3.2. The subloading surface model

The conventional elastoplastic models, treated generally in the previous chapter, assume that the interior of the yield surface is purely elastic. This has allowed in the past, and even currently, to a more or less accurate description of materials behaviour. However the passage from one domain to another is sudden and this aspect reflects on the abrupt change on the stress-strain curve. The smooth transition shown by experimental curves cannot be obtained properly by using these models but more importantly it seriously affects the ability of prediction softening response.

In addition conventional models cannot catch properly the accumulation of plastic deformations due to cyclical loading-unloading condition. As it will be reminded in the following chapters more in detail, if a small stress amplitude from the edge of the yield surface to the inside of the elastic domain is induced in the material, the answer of the model will be a pure elastic deformation with a full recovery once the

simulation is over. In reality, during a repeated cycle, for instance from the yield limit to null stress, plastic strains cumulate until the sample goes to failure.

In the following paragraph the *simple subloading surface* and the *extended subloading surface* model will be introduced. The latter is the evolution of the former to adjust the ability of predicting the correct amount of irreversible strains in cyclic loading-unloading cases, whereas both of them can produce smooth stress-strain transition curves and catch a realistic softening behaviour.

3.2.1. Simple subloading surface model

The problem with the conventional plasticity models is that they violate the continuity and the smoothness conditions although they correctly fulfill other mechanical requirements such as thermodynamic restrictions or objectivity for the constitutive equations.

The first two will be briefly explain before dealing with the constitutive equations of the model, for a more detailed explanation see references [8-11].

- Experimentally it is observed that the stress rate changes continuously for a continuous change of the strain rate. It means that for a small change in the strain rate the stress must behave regularly, without producing jumps or abrupt change of values. This concept was firstly introduced by Prager [12] but only Hashiguchi [8-11] furnished a mathematical expression for this as

$$\lim_{\delta\boldsymbol{\varepsilon}\to 0} \overset{\circ}{\boldsymbol{\sigma}}(\boldsymbol{\sigma}, H_i, \boldsymbol{\varepsilon}+\delta\boldsymbol{\varepsilon}) = \overset{\circ}{\boldsymbol{\sigma}}(\boldsymbol{\sigma}, H_i, \boldsymbol{\varepsilon}) \tag{3.56}$$

  The (3.56) is valid for the conventional elastoplastic models except for point on the frontier of the elastic domain where this principle is violated. In addition the Prager's formulation was expressed for the continuity of the strain rate, exactly the opposite of the one given above, and can be ambiguous in softening or perfect plasticity cases.

- The smoothness condition can be stated as "the stress rate induced by identical strain rate changes continuously for a continuous change of stress rate". Analogously as before

$$\lim_{\delta\boldsymbol{\sigma}\to 0} \overset{\circ}{\boldsymbol{\sigma}}(\boldsymbol{\sigma}+\delta\boldsymbol{\sigma}, H_i, \boldsymbol{\varepsilon}) = \overset{\circ}{\boldsymbol{\sigma}}(\boldsymbol{\sigma}, H_i, \boldsymbol{\varepsilon}) \tag{3.57}$$

  Introducing the elastoplastic modulus which is function of the stress and the internal variables and regulates the mechanical response the eq. (3.57) becomes

$$\lim_{\delta\boldsymbol{\sigma}\to 0} \mathbf{E}^{ep}(\boldsymbol{\sigma}+\delta\boldsymbol{\sigma}, H_i) = \mathbf{E}^{ep}(\boldsymbol{\sigma}, H_i) \tag{3.58}$$

  The violation of this condition reflects on the capability of predicting softening behaviour correctly.

In the subloading surface model [2], [13-15] the conventional yield surface is renamed *normal-yield* surface just to remark what already stated in the introduction of this chapter, which is that there is no longer separation between elastic and plastic domains but irreversible deformations are induce whenever a change in the stress state is induced. The yield surface becomes only a reference to draw the subloading one, which is such to pass always through the current stress point and keeps a similar shape and a similarity ratio in its approach to the normal-yield surface.

It is thus possible to list the following geometrical properties:

- All lines connecting an arbitrary point on or within the subloading surface and its conjugate point on or within the normal-yield surface connect to a unique point, called similarity-centre;
- All ratios of length of an arbitrary line-element connecting two points on or inside the subloading surface to that of an arbitrary conjugate line-element connecting two conjugate points on or inside the normal-yield surface are identical. The ratio is called the similarity-ratio, which coincides with the ratio of the size of these surfaces.

In detail the above mentioned similarity ratio can assume every real value included between 0 and 1:

- R = 0 means that the stress state is zero, in the stress space the subloading surface degenerates into a point which belongs to the origin of the axes;
- 0 < R < 1 means that the stress state is included inside the normal-yield surface;
- R = 1 means that the subloading surface and the normal-yield surface perfectly overlap.

The state when R = 0 is purely elastic (the elastic domain degenerates in a single point), when 0 < R < 1 (0 < *f* < F) the stress lies on the so called *sub-yield state* and finally for R = 1 the point is on the normal yield surface and in the homonymous state. It should be noticed that the subloading surface is not an independent surface but it is related to the normal one which is the only independent surface exactly like in the conventional elastoplastic models, moreover when R = 1 the two surfaces collide and become one. In other unconventional models plural independent surfaces have been assumed with a defect on the smoothness condition.

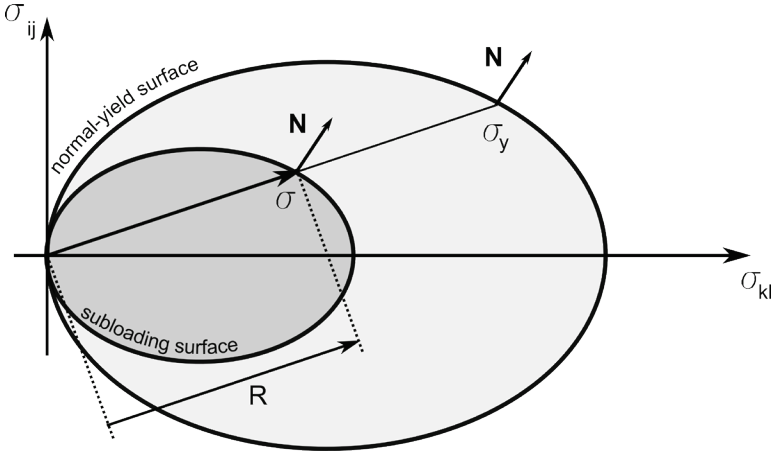

Figure 8 – Normal-yield surface and subloading surface.

Once defined the similarity-ratio evolution and its field of existence it is possible to obtain the analytical form for the subloading surface, which is quite similar of that reported in eq. (3.28):

$$f(\boldsymbol{\sigma}) - RF(H) = 0 \tag{3.59}$$

As already seen for the conventional elastoplastic constitutive equations, the function *f* should be assumed homogeneous of degree-one respect to the stress

$$tr\left(\frac{\partial f(\boldsymbol{\sigma})}{\partial \boldsymbol{\sigma}}\boldsymbol{\sigma}\right) = f(\boldsymbol{\sigma}) \tag{3.60}.$$

It has to be noticed that functions product rule in derivation has to be used in the second term of the (3.59) to arrive correctly at the following form:

$$tr\left(\frac{\partial f(\boldsymbol{\sigma})}{\partial \boldsymbol{\sigma}}\overset{\circ}{\boldsymbol{\sigma}}\right) = \dot{R}F + RF'\dot{H} \tag{3.61}$$

Theoretically speaking if the stress moves from a generic state to a non null one the R value consequently increases (or decreases depending on the entity of the stress in the final point respect to the first) and the same does the subloading surface, which expands (or contracts) and comes near (shrinks far away) the normal-yield surface. It's thus necessary to define an evolution law for the similarity ratio that regulates the behaviour of R respect to the evolution of the stress in the stress space.

The choice for the functions depends on some assumptions that $\dot{R}$ must fulfill in the loading case, in other words when irreversible strains are induced.

- First of all $\dot{\bar{R}} / \left\| \boldsymbol{\varepsilon}^p \right\| \to \infty$ for $\bar{R} < R_e$ where R_e is a material constant describing the elastic limit as indicated in Figure 9. For soil it can be set equal to zero, for some metals R_e > 0.2 [16].

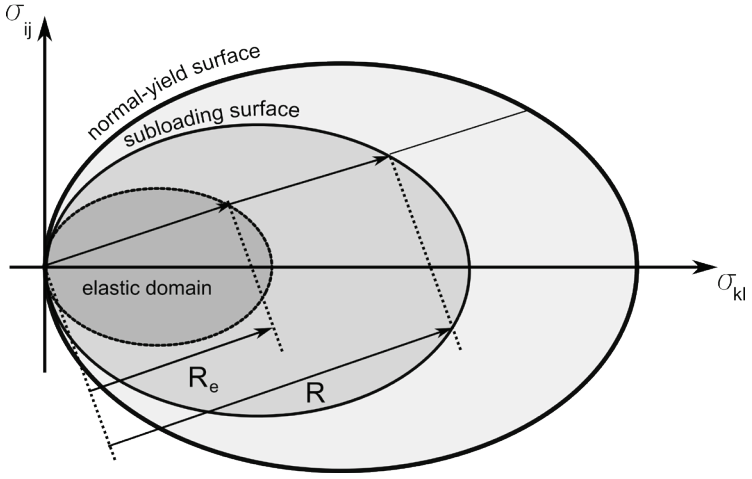

Figure 9 - Inner elastic domain governed by R_e parameter.

- When instead the ratio is between the limit elastic and the normal-yield then it must be $\dot{\bar{R}} / \left\| \boldsymbol{\varepsilon}^p \right\| > 0$.
- The $\dot{\bar{R}} / \left\| \boldsymbol{\varepsilon}^p \right\|$ term should decrease monotonically for increasing value of R, in fact when the stress increases, and the point moves in the stress space, the entity of the plastic deformations increase proportionally to the expansion of the subloading surface.
- $\dot{\bar{R}} / \left\| \boldsymbol{\varepsilon}^p \right\|$ should maintain on null value whenever the subloading surface reaches the normal-yield R = 1.
- All the equations defined for the conventional plasticity must hold when the similarity ratio reaches unitary value because subloading surface coincides with the normal-yield one.
- If the ratio R becomes greater than 1 then $\dot{\bar{R}} / \left\| \boldsymbol{\varepsilon}^p \right\|$ must be negative so to bring back the stress to lie on the conventional yield surface. This point is really important computationally speaking as it will be shown later.

To satisfy all the requests listed above it has been chosen the following expression

$$\dot{R} = U \left\| \boldsymbol{\varepsilon}^p \right\| \quad per \quad \boldsymbol{\varepsilon}^p \neq 0 \tag{3.62}$$

Where *U* is a decreasing monotonic function of R that obeys to the following system of equations, in which small *u* it's a material parameter obtained experimentally and on which value depends the smoothness of the stress-strain curve. The choice of the function is not arbitrary but it must be such to satisfied the ability to attract the stress on the normal-yield surface whenever R > 1

$$U = u \cot\left(\frac{\pi}{2} \frac{\langle R - R_e \rangle}{1 - R_e} \right) \tag{3.63}$$

$\langle \ \rangle$ are the McCauley's brackets which give for an arbitrary scalar value *a*

$$\langle a \rangle = \frac{\left(a + |a| \right)}{2} \rightarrow \begin{cases} \langle a \rangle = a & \text{for } a \geq 0 \\ \langle a \rangle = 0 & \text{for } a < 0 \end{cases} \tag{3.64}$$

U(R) function evolution can be summarized by the following expression and its pattern can be seen in Figure 10.

$$U(R) \begin{cases} \rightarrow +\infty & for \quad 0 \leq R \leq R_e & \text{(quasi-elastic state)} \\ > 0 & for \quad R_e < R < 1 & \text{(sub-yield state)} \\ = 0 & for \quad R = 1 & \text{(normal-yield state)} \\ < 0 & for \quad R > 1 & \text{(over normal-yield state)} \end{cases} \tag{3.65}$$

Note that if R_e has null value as happens for instance in soils then the curve depicted in Figure 10 must be shifted backward to the origin of the axes.

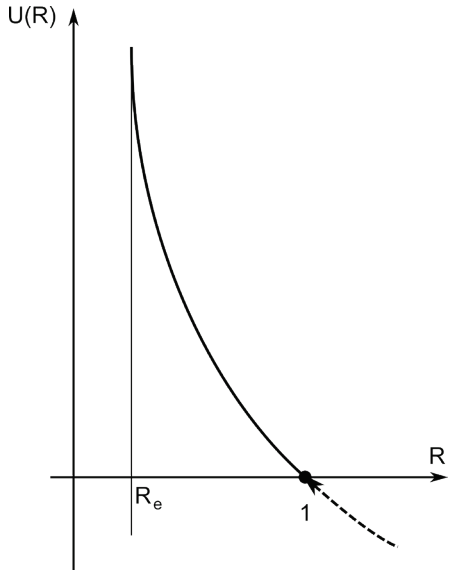

Figure 10 – Graphical representation of the function U(R).

The expression (3.63) has been preferred to the logarithmic form, previously used by Hashiguchi [15], because it can be integrated and an equation for the similarity ration depending on the plastic deformation can be found

$$R = \frac{2}{\pi}(1-R_e)\cos^{-1}\left\{\cos\left(\frac{\pi}{2}\frac{R_0-R_e}{1-R_e}\right)\exp\left(-u\frac{\pi}{2}\frac{\varepsilon^p-\varepsilon^0}{1-R_e}\right)\right\}+R_e \tag{3.66}$$

$$\varepsilon^p-\varepsilon^0 = \frac{2}{\pi}(1-R_e)\ln\frac{\cos\left(\frac{\pi}{2}\frac{R_0-R_e}{1-R_e}\right)}{\cos\left(\frac{\pi}{2}\frac{R-R_e}{1-R_e}\right)} \tag{3.67}$$

under the initial conditions that $\varepsilon^p = \varepsilon_0^p$ and $R = R_0$, where the term ε^p is the integration in time of the modulus of the plastic deformations

$$\varepsilon^p = \int \left\| \boldsymbol{\varepsilon}^p \right\| dt \tag{3.68}$$

Substituting the R evolution law (3.62) inside the time differentiation of the subloading surface formula (3.61), the extended consistence condition can be obtained as follows:

$$tr\left(\frac{\partial f(\boldsymbol{\sigma})}{\partial \boldsymbol{\sigma}}\overset{\circ}{\boldsymbol{\sigma}}\right) = U\left\| \boldsymbol{\varepsilon}^p \right\| F + RF'\dot{H} \tag{3.69}$$

Using an associative flow rule for the material the plastic strains are assumed to develop normally to the yield surface defined in the (3.59)

$$\boldsymbol{\varepsilon}^p = \bar{\lambda}\mathbf{N} \tag{3.70}$$

Where $\bar{\lambda}$ once again is the positive proportionality factor, whereas **N** is the normalized outward-normal of the subloading surface (it's exactly the same vector of the normal-yield, but now is applied to the internal surface). The function *f* in the subloading surface equation is such to be homogeneous function of degree-one wih regard to the stress tensor which means that, as seen before, it is possible to apply the *Euler Theorem*, leading to a similar form saw in the (3.33) with the only add of the similarity ratio from eq. (3.59):

$$\frac{\partial f(\boldsymbol{\sigma})}{\partial \boldsymbol{\sigma}} = \left\| \frac{\partial f(\boldsymbol{\sigma})}{\partial \boldsymbol{\sigma}} \right\| \mathbf{N} = \frac{tr\left(\dfrac{\partial f(\boldsymbol{\sigma})}{\partial \boldsymbol{\sigma}} \boldsymbol{\sigma} \right)}{tr\,(\mathbf{N}\boldsymbol{\sigma})} = \frac{RF}{tr\,(\mathbf{N}\boldsymbol{\sigma})}\mathbf{N} \tag{3.71}.$$

Substituting into eq. (3.69) the equations (3.70) and (3.71) it can be obtained

$$\frac{RF}{tr(\mathbf{N}\boldsymbol{\sigma})} tr(\mathbf{N}\overset{\circ}{\boldsymbol{\sigma}}) = RF'\,\bar{\lambda}\, h(\boldsymbol{\sigma}, H_i, \mathbf{M}) + U(R)\bar{\lambda} F \tag{3.72}.$$

Consequentially we can define the plastic modulus, the proportionally factor and finally the plastic strain rate:

$$\bar{M}^p \equiv \left(\frac{F'}{F} h + \frac{U}{R} \right) tr\,(\mathbf{N}\boldsymbol{\sigma}) \tag{3.73}$$

$$\bar{\lambda} = \frac{tr\,(\mathbf{N}\overset{\circ}{\boldsymbol{\sigma}})}{\bar{M}^p} \tag{3.74}$$

And

$$\boldsymbol{\varepsilon}^p = \frac{tr\,(\mathbf{N}\overset{\circ}{\boldsymbol{\sigma}})}{\bar{M}^p}\mathbf{N} \tag{3.75}$$

Analogously as seen before it is now possible to explicit the inverse relationship between stress and strain by substituting in eq. (3.25) the value obtained for the elastic strain rate and the plastic one depending on the stress

$$\boldsymbol{\varepsilon} = \mathbf{E}^{-1}\overset{\circ}{\boldsymbol{\sigma}} + \frac{tr\,(\mathbf{N}\overset{\circ}{\boldsymbol{\sigma}})}{\bar{M}^p}\mathbf{N} \tag{3.76}.$$

Eq. (3.76) is exactly the same as (3.45) with the only exception of the dashed plastic modulus that contains the similarity ratio. It means that plastic part of the strain rate developed proportionally to the distance of the subloading to the normal-yield surface as it was expected. For writing the direct bond is

necessary to transform the dashed λ in a form which depends on the strains, as done in the (3.46) and (3.47):

$$\bar{\Lambda} = \frac{tr(\mathbf{NE\varepsilon})}{\bar{M}^p + tr(\mathbf{NEN})} \tag{3.77}$$

Finally

$$\overset{\circ}{\sigma} = \mathbf{E\varepsilon} - \mathbf{E}\frac{tr(\mathbf{NE\varepsilon})}{\bar{M}^p + tr(\mathbf{NEN})}\mathbf{N} \tag{3.78}$$

$$\overset{\circ}{\sigma} = \left\{\mathbf{E} - \frac{(\mathbf{EN})\otimes(\mathbf{NE})}{\bar{M}^p + tr(\mathbf{NEN})}\right\}\boldsymbol{\varepsilon} \tag{3.79}$$

Again the term inside the brackets represents the *elastoplastic matrix* but it has to point out that differently from conventional models, in which it is defined only when the stress reaches the yield surface, and before that a constant elastic matrix is used, here in all the numerical computations the matrix should be updated step by step (with the only exception when R_e is defined different from zero).

The evolution of the subloading surface in the stress plane depends on the sign of the elastoplastic matrix (3.79), when it is greater than zero it is the case of subloading hardening, null value corresponds to subloading nonhardening case and eventually if it is lower than zero subloading softening happens.

The normal yield surface instead depends on the time derivate of the hardening function *F*: when it is greater than zero it generates normal-isotropic hardening case, null value corresponds to normal-isotropic nonhardening and finally if it is lower than zero normal-isotropic softening happens [17].

3.2.2. On loading criteria

Considering a conventional plasticity model the answer to a loading path can be duplex, both elastic and plastic depending on where the point lies respect to the yield-surface. In the subloading surface model plastic deformations are always induced in a monotonic loading process because of the abolition of the inner elastic domain, however, as in the conventional theory, once the load has been removed only elastic strain can be produced. Thus in both cases is important to create a judgment which allows to understand if a reversible or irreversible process is going on.

A standard judgment is the *loading criterion,* for which Hashiguchi [11] provides a mathematical expression.

- First of all it is required that, in the loading process, when plastic deformation are induced ($\boldsymbol{\varepsilon}^p \neq 0$)

$$\lambda = \Lambda > 0 \tag{3.80}$$

- In the unloading case ($\boldsymbol{\varepsilon}^p = 0$), when elastic deformations are induced it has to be

$$tr(\mathbf{N}\overset{\circ}{\boldsymbol{\sigma}}) \leq 0 \tag{3.81}$$

This also allows to transform the expression (3.47) for conventional plasticity (here is taken a general expression for a non associative flow rule) into

$$\Lambda = \frac{tr(\mathbf{NE}\boldsymbol{\varepsilon})}{M^p + tr(\mathbf{NEM})} = \frac{tr(\mathbf{NE}\boldsymbol{\varepsilon}^e)}{M^p + tr(\mathbf{NEM})} = \frac{tr(\mathbf{N}\overset{\circ}{\sigma})}{M^p + tr(\mathbf{NEM})} \tag{3.82}$$

- The plastic modulus M^p can assume both the signs, instead the elastic matrix **E** is a positive definite tensor and then $tr(\mathbf{NEM}) \gg M^p$, and, considering that the plastic relaxation does not proceed to infinite, the denominator of the (3.82) can be considered positive or eventually tending to zero in critical softening case.

Observing the definition for the proportionality factor, the plastic strain rate and the expression just written (3.82), in the unloading case the following series of inequality can be defined

$$\begin{aligned} &\lambda \leq 0; \quad \Lambda \leq 0 \quad \text{when} \quad M^p > 0 \\ &\lambda \to -\infty \text{ or indetermined}; \quad \Lambda \leq 0 \quad \text{when} \quad M^p = 0 \\ &\lambda \geq 0; \quad \Lambda \leq 0 \quad \text{when} \quad M^p < 0 \end{aligned} \tag{3.83}.$$

Loading	M^p	$tr(\mathbf{N}\overset{\circ}{\boldsymbol{\sigma}})$	$tr(\mathbf{NE}\boldsymbol{\varepsilon})$	λ	Λ
hardening	**+**	**+**	**+**	**+**	**+**
non hardening	**0**	**0**	**+**	**+**	**+**
softening	**-**	**-**	**+**	**+**	**+**

Table 1 – sign of the parameters during the loading case.

Unloading	M^p	$tr(\mathbf{N}\overset{\circ}{\boldsymbol{\sigma}})$	$tr(\mathbf{NE}\boldsymbol{\varepsilon})$	λ	Λ
hardening	**+**	**-**	**-**	**+**	**-**
non hardening	**0**	**-**	**-**	***I***	**-**
softening	**-**	**-**	**-**	**-**	**-**

Table 2 – sign of the parameters during the elastic unloading.

The sign of the proportionality factor in term of stress factor is not necessarily negative at the moment of the elastic unloading so it cannot be used as a benchmark to understand which process (elastic or plastic) is involved at the moment. On the contrary its definition in term of strain keeps negative sign during elastic unloading, whereas is always positive when plastic deformations are induced. This allows to write the loading criterion univocally as:

$$\begin{aligned} &\boldsymbol{\varepsilon}^p \neq 0 : f(\boldsymbol{\sigma}) - F(H) = 0 \text{ and } \Lambda > 0 \\ &\boldsymbol{\varepsilon}^p = 0 : \text{ otherwise} \end{aligned} \tag{3.84}$$

Formula in (3.84) is valid in the general case of conventional plasticity, however it can be further simplified when using subloading surface. According to this unconventional theory plastic strains are induced whenever a change in the stress state appears, so an internal surface (i.e. the subloading one) has been created such as to pass always through the current stress point thanks to the similarity transformation. This means that the fulfilment of the first condition of the (3.84) is no longer necessary, therefore it is possible to write:

$$\begin{aligned} &\boldsymbol{\varepsilon}^p \neq 0 : \ \bar{\Lambda} > 0 \\ &\boldsymbol{\varepsilon}^p = 0 : \ \text{otherwise} \end{aligned} \tag{3.85}$$

This simplification, which may appear irrelevant, is fundamental for a big improvement in fast numerical computation.

3.2.3. Comparison between the two theories

A first main difference existing in these two models is the form of the loading criteria. In the conventional elasto-plastic model it's necessary to satisfy two conditions for having permanent deformations, whereas in the unconventional theory the subloading surface is such to pass always through the current stress point. This makes the consistency condition always valid so it is only necessary to observe if Λ is positive or negative to decide if plastic strains will be produced or not.

Moreover stress is automatically pulled back to the normal-yield surface even if it goes outside from that surface because of similarity ratio evolution law analytical form:

$$\begin{cases} \dot{R} > 0 \quad for \quad R < 1 \quad \text{(sub - yield state)} \\ \dot{R} < 0 \quad for \quad R > 1 \quad \text{(over normal - yield state)} \end{cases} \tag{3.86}$$

This leads to a computational advantage that speeds up the calculation process. In fact it's no more necessary to use some pull-back algorithm with a large number of sub-steps for checking the convergence during the process for bringing the stress to lie on the yield-surface.

One other big difference is that the yield stress is not a characteristic of the material itself, but it depends on loading conditions. Vice versa in the classical plastic theory the yield surface is unique and depends only on the considered material, without pay any attention on how the load is applied.

As reminded in the introduction of this chapter the adoption of an associate flow rule makes the stiffness matrix for the solid skeleton **K** symmetric, which simplified a lot the numerical implementation of the algorithm and its use.

It has to be remarked that the conventional plasticity models can be seen as a particular case of the simple subloading one. In fact if the *u* parameter is set to tends to infinite, or the R_e is imposed to have unitary value, then the two theories coincide.

The violation of the continuity and of the smoothness conditions shown in eq. (3.56) and (3.57) leads to a rough representation of the stress-strain curves and, in case of softening, even a overestimation of the peak phase.

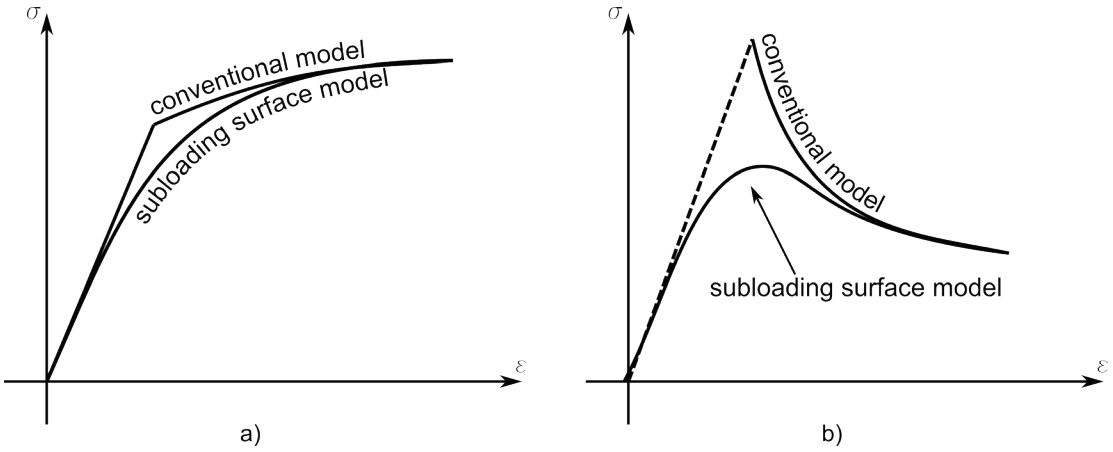

Figure 11 – Prediction of hardening and softening behaviour for conventional and for subloading surface models.

3.2.4. Return Mapping

Elastoplastic model are generally formulated in incremental form because the answer at a certain stress level depends on the loading history experienced by the material in time.

Calculations performed at each step are subjected to some kind of errors using the Euler method, which depend on the size of step itself, because the elastoplastic constitutive equations do not fulfill the complete integrability conditions. This means that calculation carried out with affecting the stiffness matrix at each time step contains an error which is directly proportional to the dimension of the strain rate or stress rate give as input for the model. In fact the tangent modulus set up at the *n* iteration point is used to predict the material behaviour at the *n+1*, if the two points are closed one to each other then the approximation is quite good and errors propagation does not affect the final result, on the contrary the gap increases appreciably when two consecutive points are separated by a large step.

In order to achieve precise results even using large steps computation different numerical algorithm have been proposed, one of them is the *return mapping* [19] which has been developed as a general case of previous particular ones [20], [21] and since then it has been widely adopted.

The idea at the base of this numerical technique is quite simple; it is supposed that everything is known at the *n* iteration, where the stress and all the internal plastic variables have been already founded. For the next computational step *n+1* it is assumed to initially freeze the plastic strain and to perform a pure elastic (*trial*) step to which corresponds a fake stress value. This fictitious state depends uniquely on the initial condition computed at the *n* step $\boldsymbol{\varepsilon}_n$, $\boldsymbol{\varepsilon}_n^p$, H_n, and on the increment of the strain $\Delta\boldsymbol{\varepsilon}_n$ chosen as size of the iteration.

It is possible to use the same procedure applying a stress increment as input value for the algorithm, however it has to be remarked once again that the direct bond in a non linear problem can always be

defined, whereas the inverse may not, depending on the answer of the material (hardening, perfect plasticity, softening). In fact in general it is always possible to impose a certain deformation to a body but not all the stress are admissible, moreover in the F.E. implementation of the return mapping the stresses are a derived variable from the strains so it is easy to implement the first form rather than the second.

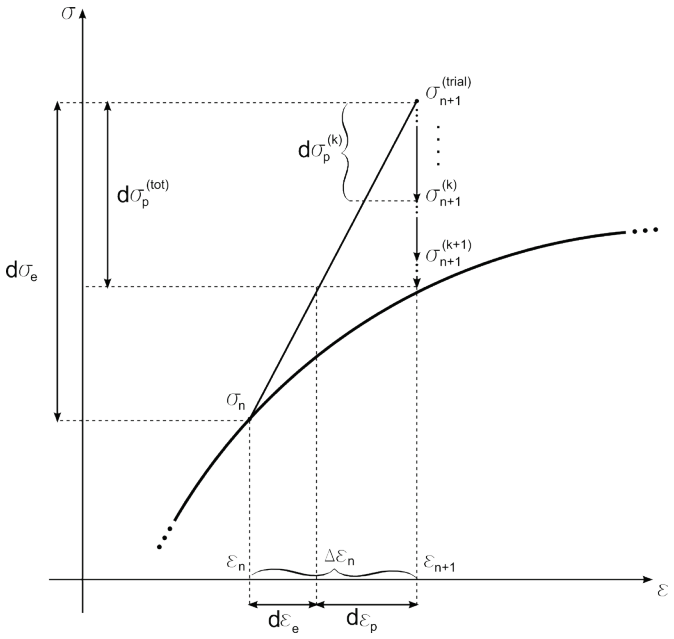

Figure 12 – Geometric interpretation of the return mapping algorithm for a general hardening case.

Observing Figure 12 it should be clear that the trial state may not, and in general it will not, be an admissible state for the material because in most of the cases it will overestimate the stress level.

After the elastic stress has been computed two scenarios are possible: the plastic function is lower than zero or it is greater/equal to zero. In the first case the point belongs to the inside the elastic domain (assuming to dealing with a conventional plasticity model) and it is directly the solution of the problem, in the second case it violates the condition expressed on the plastic functions (3.7) and a sort of correction should be carried out to bring back the stress to lie on the correct plastic surface. This operation is called *plastic relaxation* of the trial state and can be performed by subtracting to the $\boldsymbol{\sigma}_{n+1}^{(trial)}$ the *plastic corrector* $d\boldsymbol{\sigma}_p^{(k)}$ which is function of the proportionality factor $\Delta\lambda$ of the step.

The amount of deformation of the step $\Delta\boldsymbol{\varepsilon}_n$, which has been initially assumed to be formed by only elastic deformation, maintains the same magnitude but varies its composition. In fact the plastic deformation increases during the relaxation process whereas decreases the elastic one until the stress goes back to the correct curve and a final composition of $d\boldsymbol{\varepsilon}_p$ and $d\boldsymbol{\varepsilon}_e$ is then reached as it can be seen in Figure 12.

The way of how this plastic relaxation is performed will be described in the following lines directly for the unconventional subloading surface model but a clear and detailed explanation for the conventional approach can be found in reference [22], [23].

There are mainly two different types of return mapping: *the closest projection method* (*CPPM*) and the *cutting plane algorithm* (*CPA*).

The CPPM [24-26] is a complete implicit method which, considering a strain increment as an input, allows to compute all the variables of the system in order to satisfy the set of equations composed by the yield condition and the evolution law of the internal variables. This technique is based on the concept of the consistent linearization and the asymptotic quadratic rate of convergence on the solution makes the CPPM really attractive to use.

Despite its quadratic convergence rate and its solid mathematical implant the constitution of the local matrix requires the second order derivatives of the yield function respect to the stress which can be a high computational effort, especially dealing with soils.

The CPA [25], [27] is an incomplete implicit method and thus is not possible to compute a consistent tangent modulus as the CPPM. However here is no more necessary to compute the second order derivatives of the plastic potential and then computation is considerably simplified and its application should be regarded especially for materials which yield surface form has a complicated formulation.

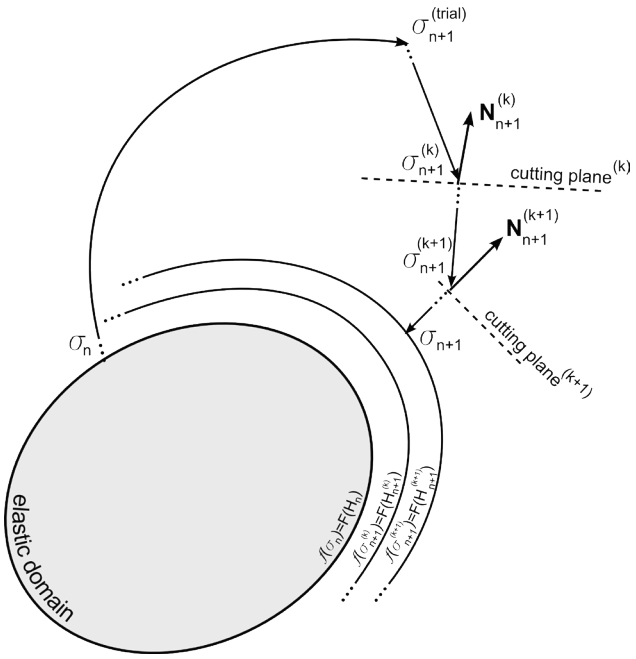

Figure 13 – Cutting-plane return mapping for a conventional hardening plasticity.

Basically the cutting plane return mapping algorithm can be seen as an iterative procedure where the linear approximation to the plastic consistency equation is solved at every iteration. The stress and the internal variables don't converge directly to the yield surface in the stress space, as happens for the CPPM, in the CPA the convergence is realized on a plane (i.e. cutting plane) in the stress space which represents the linearised consistency equation. The rate of convergence for this second algorithm is quadratic as well for the first one despite of the simple formulation of its constitutive equations. A

geometrical interpretation for a simple plastic hardening case, in a two dimensional representation in the stress space, is furnished by Figure 13.

3.2.4.1. Cutting-plane algorithm for the subloading surface model

In the present paragraph the formulas of return mapping algorithm for the subloading surface are given, for more detail dissertation is possible to consult references [17], [28].

The first control, when using return mapping algorithm, concerns the judgment if plastic deformation can be produced or not. Considering a generic step *n* and adding to the stress $\boldsymbol{\sigma}_n$ the elastic trial rate, a new stress state $\boldsymbol{\sigma}_{n+1}^{(trial)}$ is obtained. At this point is necessary a check to understand if perform a plastic relaxation or not. This condition can be explicited as follows:

$$\begin{aligned} &f(\boldsymbol{\sigma}_{n+1}^{(trial)}) \le R_n F(H_n) \quad \text{then} \quad \boldsymbol{\varepsilon}_{n+1}^{p} = 0 \text{ and } \boldsymbol{\sigma}_{n+1}^{(trial)} = \boldsymbol{\sigma}_{n+1}^{(final)} \\ &f(\boldsymbol{\sigma}_{n+1}^{(trial)}) > R_n F(H_n) \quad \text{then} \quad \boldsymbol{\varepsilon}_{n+1}^{p} \neq 0 \text{ and } \boldsymbol{\sigma}_{n+1}^{(trial)} \neq \boldsymbol{\sigma}_{n+1}^{(final)} \end{aligned} \tag{3.87}$$

Equation (3.87) can be geometrically interpreted as a verification if the point stays over or under the stress-strain curve of Figure 12.

Starting from the definition of the consistency condition saw in equation (3.59) is possible to define a new function *g(**σ**,* F, R) as

$$g(\boldsymbol{\sigma},F,R) = f(\boldsymbol{\sigma}) - RF(H) \tag{3.88}$$

From this condition the previous formula is rearranged using the Taylor expansion series:

$$\begin{aligned} g(\boldsymbol{\sigma}+d\boldsymbol{\sigma},F+dF,R+dR) = g(\boldsymbol{\sigma},F,R) + tr\left(\frac{\partial g(\boldsymbol{\sigma},F,R)}{\partial \boldsymbol{\sigma}} d\boldsymbol{\sigma}\right) + \\ + tr\left(\frac{\partial g(\boldsymbol{\sigma},F,R)}{\partial F} dF\right) + tr\left(\frac{\partial g(\boldsymbol{\sigma},F,R)}{\partial R} dR\right) \end{aligned} \tag{3.89}$$

Where in the (3.89) second order derivative terms have been neglected. Now substituting in (3.89) the expression of the *g* function formulate in the (3.88):

$$g(\boldsymbol{\sigma}+d\boldsymbol{\sigma},F+dF,R+dR) = f(\boldsymbol{\sigma}) - RF + tr\left(\frac{\partial f(\boldsymbol{\sigma})}{\partial \boldsymbol{\sigma}} \overset{\circ}{\boldsymbol{\sigma}}\right) - FdR - RdF = 0 \tag{3.90}.$$

Note that if the subloading surface is satisfied then term $tr\left(\frac{\partial f(\boldsymbol{\sigma})}{\partial \boldsymbol{\sigma}} \overset{\circ}{\boldsymbol{\sigma}}\right) - FdR - RdF$ is null and so the remaining expression is identical to the time differentiation expressed in (3.61). It has to be reminded that function *f* has been chosen such to be homogeneous of degree-one of the stress tensor, this allows us to write expression (3.71) which for sake of completeness is reported once again

$$\frac{\partial f(\boldsymbol{\sigma})}{\partial \boldsymbol{\sigma}} = \left\| \frac{\partial f(\boldsymbol{\sigma})}{\partial \boldsymbol{\sigma}} \right\| \mathbf{N} = \frac{tr\left(\frac{\partial f(\boldsymbol{\sigma})}{\partial \boldsymbol{\sigma}} \overset{\circ}{\boldsymbol{\sigma}} \right)}{tr(\mathbf{N}\boldsymbol{\sigma})} = \frac{RF}{tr(\mathbf{N}\boldsymbol{\sigma})}\mathbf{N} \tag{3.91}.$$

Substituting the right part of the (3.91) into the consistency condition (3.61) it is possible to write

$$\begin{aligned} &\left(\frac{\partial f(\boldsymbol{\sigma})}{\partial \boldsymbol{\sigma}} : \overset{\circ}{\boldsymbol{\sigma}} \right) - dRF - RdF = \left(\frac{RF}{\mathbf{N} : \boldsymbol{\sigma}} \mathbf{N} \right) : \overset{\circ}{\boldsymbol{\sigma}} - dRF - RdF = \\ &= \frac{RF}{\mathbf{N} : \boldsymbol{\sigma}} \left[\mathbf{N} : \overset{\circ}{\boldsymbol{\sigma}} - \frac{(\mathbf{N} : \boldsymbol{\sigma})}{RF} (dRF + RdF) \right] = \frac{RF}{\mathbf{N} : \boldsymbol{\sigma}} \left[\mathbf{N} : \overset{\circ}{\boldsymbol{\sigma}} - (\mathbf{N} : \boldsymbol{\sigma}) \left(\frac{dR}{R} + \frac{dF}{F} \right) \right] = 0 \end{aligned} \tag{3.92}$$

Remembering now the evolution law for the similarity ratio *R*, considering an associate flow rule and substituting eq. (3.93) and (3.94) inside the (3.92), it holds:

$$\dot{R} = dR = U(R) \left\| \boldsymbol{\varepsilon}^p \right\|; \qquad \boldsymbol{\varepsilon}^p = \lambda \mathbf{N} \tag{3.93}$$

$$\dot{F} = dF = F' \dot{H}; \quad F' = \frac{dF}{dH}; \quad \dot{H} = \lambda h \tag{3.94}$$

$$\frac{RF}{\mathbf{N} : \boldsymbol{\sigma}} \left[\mathbf{N} : \overset{\circ}{\boldsymbol{\sigma}} - (\mathbf{N} : \boldsymbol{\sigma}) \left(\frac{\lambda U}{R} + \frac{F' \lambda h}{F} \right) \right] = \frac{RF}{\mathbf{N} : \boldsymbol{\sigma}} \left[\mathbf{N} : \overset{\circ}{\boldsymbol{\sigma}} - \lambda M^p \right] \tag{3.95}$$

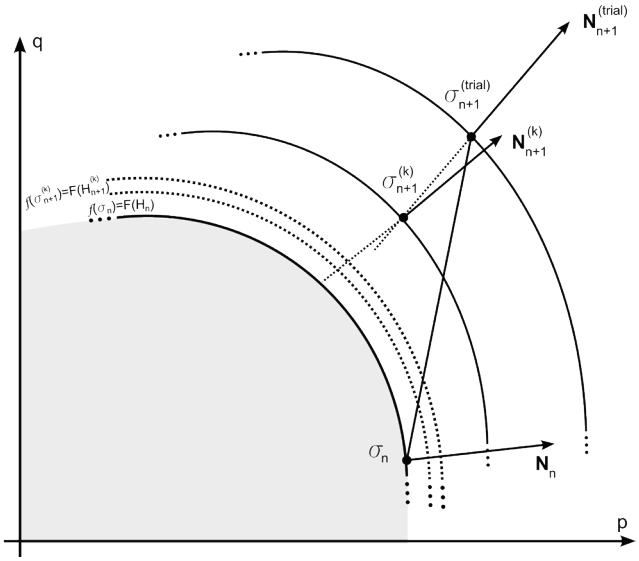

Figure 14 – Geometric interpretation of the return mapping algorithm in the deviatoric-idrostatic plane.

If we use the expression just found together with the consistency condition derived with the Taylor's serie we have

$$f(\boldsymbol{\sigma}) - RF + \frac{RF}{\mathbf{N} : \boldsymbol{\sigma}} \left[\mathbf{N} : \overset{\circ}{\boldsymbol{\sigma}} - \lambda M^p \right] = f(\boldsymbol{\sigma}) - RF + \frac{f(\boldsymbol{\sigma})}{\mathbf{N} : \boldsymbol{\sigma}} \left[\mathbf{N} : \overset{\circ}{\boldsymbol{\sigma}} - \lambda M^p \right] = 0 \tag{3.96}$$

Then solving the previous equation respect to the proportionality factor we can obtain the scalar value that multiplied for the normal **N** gives back the plastic strain rate that compete to the *n+1* step for a generic total strain rate $\Delta\boldsymbol{\varepsilon}_n$:

$$\lambda = \frac{\mathbf{N}:\boldsymbol{\sigma}}{f(\boldsymbol{\sigma})}\frac{f(\boldsymbol{\sigma})-RF}{M^p+\mathbf{N}:\mathbf{E}:\mathbf{N}} \tag{3.97}.$$

Finding the value of λ through equation (3.97) or satisfying the condition expressed by the (3.88) is exactly the same thing, in fact the proportionally factor expresses the quantity of plastic strain rate which is connected to the plastic corrector $d\boldsymbol{\sigma}_p$ such that to bring back the stress to lie on the yield surface from the elastic trial.

Referring to Figure 14 an geometric interpretation of the return mapping algorithm in the idrostatic deviatoric plane is given. After the computation of the trial elastic state the normal vector to the surface is computed and used as direction along which perform the plastic correction of the elastic stress state. At the same time the internal variables are updated, for instance the *isotropic hardening variable H* passes from the value H_n to the value H_{n+1} leading to the consequent expansion of the subloading surface or the normal-yield one depending on the position of the $\boldsymbol{\sigma}_n$.

In the following box the procedure to follow for every step is reported. As it can be seen this is an iterative procedure where every time step is subdivided in *k* sub-steps corresponding to the number of the cutting plane necessary to get the fulfilment of eq. (3.90).

I. Setting variable for the trial state

$$\boldsymbol{\sigma}_{n+1}^{(0)} \equiv \boldsymbol{\sigma}_{n+1}^{(trial)}; \quad \Delta\lambda^{(0)} = 0; \quad H_{n+1}^{(0)} = H_n; \quad F_{n+1}^{(0)} = F_n$$

II. Computing subloading surface parameters

$$f(\boldsymbol{\sigma}_{n+1}^{(k)}) = p\left(1+\chi^2\right); \quad U(R) = u\cot\left(\frac{R_{n+1}^{(k)}-R_e}{1-R_e}\right)$$

$$\tilde{\mathbf{N}}_{n+1}^{(k)} = \frac{\partial f(\boldsymbol{\sigma}_{n+1}^{(k)})}{\partial \boldsymbol{\sigma}_{n+1}^{(k)}}; \quad \mathbf{N}_{n+1}^{(k)} = \frac{\partial f(\boldsymbol{\sigma}_{n+1}^{(k)})}{\partial \boldsymbol{\sigma}_{n+1}^{(k)}} \Bigg/ \left|\frac{\partial f(\boldsymbol{\sigma}_{n+1}^{(k)})}{\partial \boldsymbol{\sigma}_{n+1}^{(k)}}\right|; \quad h_{n+1}^{(k)} = -tr\mathbf{N}$$

$$M_p = \left(\mathbf{N}_{n+1}^{(k)}:\boldsymbol{\sigma}_{n+1}^{(k)}\right)\left[\frac{F'^{(k)}_{n+1}}{F_{n+1}^{(k)}}h_{n+1}^{(k)} + \frac{U_{n+1}^{(k)}}{R_{n+1}^{(k)}}\right]$$

III. Compute the magnitude of the proportionality factor

$$\lambda_{n+1}^{(k)} = \frac{\left(\mathbf{N}_{n+1}^{(k)}:\boldsymbol{\sigma}_{n+1}^{(k)}\right)}{f(\boldsymbol{\sigma}_{n+1}^{(k)})}\left[\frac{f(\boldsymbol{\sigma}_{n+1}^{(k)}) - R_{n+1}^{(k)}F_{n+1}^{(k)}}{M_p + \mathbf{N}_{n+1}^{(k)}:\mathbf{E}:\mathbf{N}_{n+1}^{(k)}}\right]$$

IV. Plastically relax the k-state stress

$$\boldsymbol{\sigma}_{n+1}^{(k+1)} = \boldsymbol{\sigma}_{n+1}^{(k)} + d\boldsymbol{\sigma}_{n+1}^{p(k+1)} = \boldsymbol{\sigma}_{n+1}^{(k)} - \mathbf{E}:\lambda_{n+1}^{(k)}\mathbf{N}_{n+1}^{(k)}$$

V. Update variables

$$H_{n+1}^{(k+1)} = H_{n+1}^{(k)} + h_{n+1}^{(k)}\lambda_{n+1}^{(k)}; \quad f(\boldsymbol{\sigma}_{n+1}^{(k+1)}); \quad R_{n+1}^{(k+1)}$$

If $\left[g(\boldsymbol{\sigma}_{n+1}^{(k+1)}) = (f(\boldsymbol{\sigma}_{n+1}^{(k+1)}) - R_{n+1}^{(k+1)} F_{n+1}^{(k+1)}) / F_{n+1}^{(k+1)} \leq TOLL \right]$ then

Exit

Else **GO TO** II

Box 2 – Return mapping procedure for the simple subloading surface model.

3.2.5. Extended subloading surface

Conventional plasticity models show some defects when try to model non linear materials such as the violation of the smoothness and continuity conditions. Despite these aspects, which can be accepted if the gap from the real behaviour is not so big, there is another problem concerning the neat distinction between an elastic and plastic domain.

When cyclic loading case is investigated there is no possibility to predict correctly the permanent deformations due to a continue load and unload of the sample. This concept can be immediately clarified observing Figure 15 where a stress-strain curve is plotted together with the yield surface in the idrostatic-deviatoric plane.

First of all it should be pointed out that the shape of the yield functions does not affect the general behaviour that will be described (here in the image a classical plastic surface for a soil has been drawn). When the yielding stress has been reached (point A) it is possible to admit that material exhibits a reserve of strength shifting the limit of the elastic domain from point A to point B with the consequential expansion of the linear elastic domain, as pictured on the right of Figure 15. From point B an elastic unloading is performed until point C, inside the elastic domain. If a cycle of loading and unloading of fixed amplitude (i.e. from stress $\boldsymbol{\sigma}_C$ to $\boldsymbol{\sigma}_B$) is performed then no irreversible deformations are cumulated underestimating the real behaviour of the sample.

For that reason, starting from the 1960s, many unconventional plasticity models have been proposed and all of them do not consider a neat distinction in two different domains, elastic and plastic. They all go under the name of cyclic plasticity models for their nature of investigating material answer subjected to cyclic loading. In the following part of this paragraph a brief mention to some of these have been provided, for a more detail and complete treatment of the argument see reference [9].

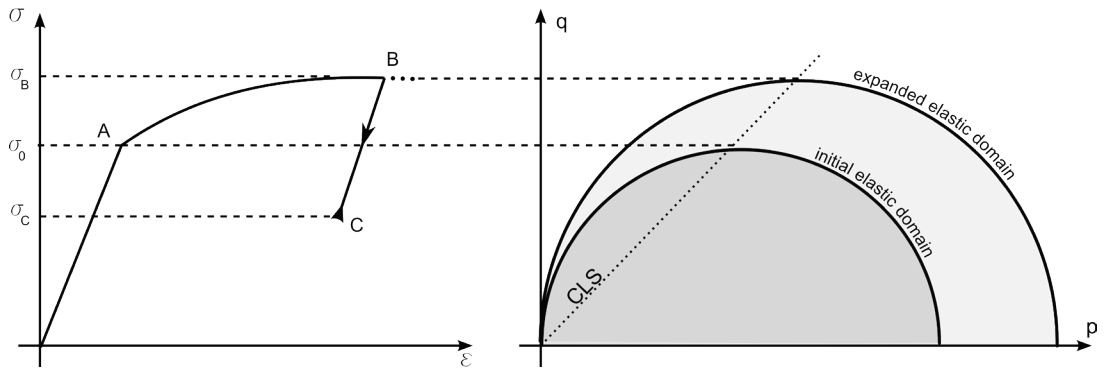

Figure 15 – cyclic loading investigation on conventional plasticity models.

All of these models introduce a small yield surface (or even named loading surface) inside the conventional one that, depending on the author, has been renamed: *limiting surface* [29], *bounding surface* [30], *normal-yield surface* [31]. Besides the terminology other differences should rather be pointed out. First of all two classes of unconventional plasticity models can be distinguished: the first one, derived from the Mroz [32] and Iwan [33] work, is based on the concept of the translation of the subyield surface (or surfaces), the other consider the expansion/contraction of the subyield surface and it has been proposed by Hashiguchi and Ueno [2].

The Multi-Surface Model [32], [33], the Infinite-Surface Model [34] and the Two-surface Model [30] belong to the first class, but if the multi-surface and the infinite-surface use a linear kinematic hardening rule the latter is developed with a nonlinear one. All of these models have been largely used in many different applications, however they contain some mechanical imprecisions partially due to the fact that the translation of the subyield surface has been assumed a priori without any mathematical justification for that [35].

The Multi-Surface Model for instance shows a non smooth stress-strain transition or it cannot predict plastic strains accumulation under the smallest subyield surface which includes a pure elastic domain, moreover a singularity point is created whenever two subyield surfaces with different plastic moduli contact at one point and few others lacks are proper of its formulation. Infinite-Surface Model partially corrects all the problems described above but still some of them remain as well as for the Two-Surfaces Model. In particular an important aspect that should be taken into account is the computational inefficiency based on the judgment "where the stress lies" for the Multi-Surface Model and the Two-surface Model and the memorization of all the stresses in a decreasing stress amplitude event for the Infinite-Surface Model, which slows down the calculation time and makes these models unattractive for numerical simulations.

Although the smoothness and continuity equations, together with the unnecessary recurs to the judgment "where the stress lies", even the simple subloading surface cannot catch the right behaviour of a sample subjected to cyclic loading. The similarity transformation with a fix similarity centre produces the same stress-strain curves during loading and reloading for a perfect plasticity material (for hardening case the curves are improved but still some defects remain, for instance open hysteresis loops) and also doesn't allow to produce any irreversible deformations during unloading. This creates an excessively strong mechanical ratcheting effect leading to an unrealistic plastic

accumulation in cycles together with the absence of *Masing* effect in the unloading-reverse loading curves.

The improvement to the simple subloading surface comes with the extended subloading surface where all the mechanical requirements are fulfilled and moreover the similarity centre is no more fixed in the stress origins but moves with the plastic strains rate [15], [36].

It can be concluded that none of the proposed theory except the extended subloading surface can described properly the behaviour of material under cyclic loading case.

3.2.5.1. Extended subloading surface: the equations

As just stated the innovative point of the extended subloading surface, respect to the simple one, lies on the introduction of the movement of the similarity centre driven by the plastic strain rate.

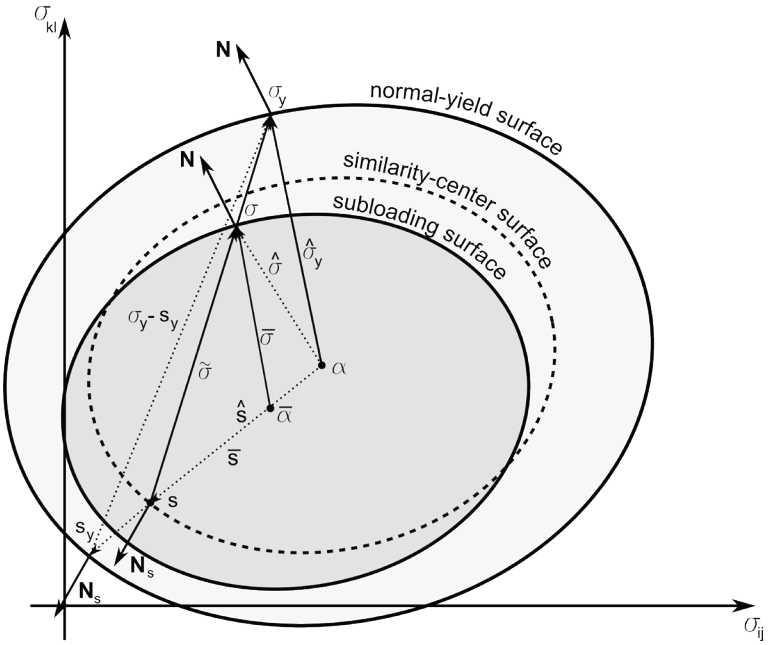

Figure 16 – Schematic representation of the surfaces of the extended subloading model.

This means that in the initial model the normal-yield surface and the subloading one commonly touch each other exactly in the origin of the stress space and the only movement allowed is the contraction or expansion of the subloading surface. Here another variable is added to the formulation and the inner surface can expand and translate in the stress space requiring an new evolution law for the movement. The current stress point assumes a different name depending if it's observed form the origin of the stress space or from the similarity centre **s** or moreover for the back stress **α**. In order to clarify all the variables the scheme of the new model is pictured in Figure 16 and the relation existing among all the them are described in equations (3.101), (3.102), (3.103).

The normal yield surface can be written as usual as

$$f(\hat{\boldsymbol{\sigma}}) = F(H) \tag{3.98}$$

where the name and symbol used are exactly the same seen for the simple subloading model with the only exception that the hardening/softening isotropic function is now a function of the stress

$$\hat{\boldsymbol{\sigma}} = \boldsymbol{\sigma} - \boldsymbol{\alpha} \tag{3.99}$$

The extended subloading surface equation is similar to the (3.59) but is reformulated as

$$f(\bar{\boldsymbol{\sigma}}) = RF(H) \tag{3.100}$$

where

$$\begin{aligned} &\bar{\boldsymbol{\sigma}} = \boldsymbol{\sigma} - \boldsymbol{\alpha} = R\hat{\boldsymbol{\sigma}}_y \\ &\hat{\boldsymbol{\sigma}}_y \equiv \boldsymbol{\sigma}_y - \boldsymbol{\alpha} \\ &\boldsymbol{\sigma}_y = \tilde{\boldsymbol{\sigma}}_y + \mathbf{s} \\ &\tilde{\boldsymbol{\sigma}} = \boldsymbol{\sigma} - \mathbf{s} = R\tilde{\boldsymbol{\sigma}}_y \\ &\hat{\mathbf{s}} = \mathbf{s} - \boldsymbol{\alpha} \end{aligned} \tag{3.101}$$

Substituting in the first equation of the (3.101) all the values reported in the below expression it is possible to rewrite the dashed stress as

$$\begin{aligned} &\bar{\boldsymbol{\sigma}} = R\hat{\boldsymbol{\sigma}}_y = R\boldsymbol{\sigma}_y - R\boldsymbol{\alpha} = R\left(\tilde{\boldsymbol{\sigma}}_y + \mathbf{s}\right) - R\boldsymbol{\alpha} = \\ &= R\tilde{\boldsymbol{\sigma}}_y + R\left(\mathbf{s} - \boldsymbol{\alpha}\right) = \tilde{\boldsymbol{\sigma}} + R\hat{\mathbf{s}} \end{aligned} \tag{3.102}$$

s is the vector unifying the origin of the stress space with the centre of similarity between the normal-yield surface and the subloading surface. $\bar{\boldsymbol{\alpha}}$ is the conjugate point on the subloading surface of the back stress for the normal-yield on and can be rewritten as a function of the similarity centre (and vice versa) as

$$\begin{aligned} &\bar{\boldsymbol{\alpha}} = \mathbf{s} - R\hat{\mathbf{s}} \\ &\bar{\mathbf{s}} = \mathbf{s} - \bar{\boldsymbol{\alpha}} = R\hat{\mathbf{s}} \end{aligned} \tag{3.103}$$

$\boldsymbol{\sigma}_y$ is the conjugate point on the normal-yield surface of the current stress on the subloading surface **σ**.

The result founded in the (3.102) is fundamental for numerical simulations because it allows to compute the similarity ratio R by solving an iterative procedure which substitutes the expression of the (3.102) into the (3.100)

$$f(\tilde{\boldsymbol{\sigma}} + R\hat{\mathbf{s}}) = RF(H) \tag{3.104}$$

The material time derivative of the previous equation leads to the same expression obtained in the (3.61) with the addition of a term derived from the presence of the back stress **α**:

$$-\frac{\partial f(\bar{\boldsymbol{\sigma}})}{\partial \bar{\boldsymbol{\sigma}}} : \overset{\circ}{\bar{\boldsymbol{\alpha}}} \quad \text{where} \quad \overset{\circ}{\bar{\boldsymbol{\alpha}}} = R\overset{\circ}{\boldsymbol{\alpha}} + (1-R)\overset{\circ}{\mathbf{s}} - \dot{R}\hat{\mathbf{s}} \tag{3.105}$$

As happened in the simple model the elastic domain collides on a single point but, if in the previous model this point is the origin of the stress space, in this case it is the similarity centre. **s** is free to move in the stress space and it is driven by the plastic strain rate moving following the current stress **σ**, however some limitations must be imposed. The similarity centre cannot approach directly to the normal yield because this would mean that the elastic domain can touch the normal-yield surface or even go beyond it just following the plastic flow. Moreover, if the mathematical formulation for the subloading surface is observed, it is impossible to define the subloading surface uniquely when the stress coincides with the similarity centre on the normal-yield surface.

To avoid all thess problems a coherent evolution law for the similarity centre is given by introducing a new surface named *similarity-centre surface*, depicted in Figure 16 with a dashed line. This new geometrical figure is create by means of a similarity transformation to the normal-yield surface but in this case respect to the back stress **α** (so that to keep the same shape and orientation in the stress space) and it always passes through the similarity centre point. Basically this surface behaves in the same way as the subloading one and in fact its analytical formulation is entirely similar to that with the exception of a different definition for the ratio R

$$f(\hat{\mathbf{s}}) = R_s F(H) \tag{3.106}$$

Theoretically speaking it is admissible to think that the similarity centre yield ratio range can varies from null to unitary value but for the previous statements it should be limited to be less than one. A material parameter χ is introduced with the constrain to be $\chi < 1$, so to transform the eq. (3.106) in the following inequality

$$f(\hat{\mathbf{s}}) \le \chi F(H) \tag{3.107}$$

Once defined the field of existence for the similarity ratio an evolution for this should be given in order to understand how it moves inside the normal-yield surface. Time-differentiating the (3.106) for the limit conditions that $R_s = \chi$, and keeping in mind all the relation expressed in the (3.101) and (3.103) it holds

$$\begin{aligned} \frac{\partial f(\hat{\mathbf{s}})}{\partial \hat{\mathbf{s}}} : \overset{\circ}{\mathbf{s}} - \frac{\partial f(\hat{\mathbf{s}})}{\partial \hat{\mathbf{s}}} \overset{\circ}{\boldsymbol{\alpha}} - \left(\frac{\partial f(\hat{\mathbf{s}})}{\partial \hat{\mathbf{s}}} : \hat{\mathbf{s}} \right) \frac{\dot{F}}{F} \le 0 \\ \frac{\partial f(\hat{\mathbf{s}})}{\partial \hat{\mathbf{s}}} : \left(\overset{\circ}{\mathbf{s}} - \overset{\circ}{\boldsymbol{\alpha}} - \hat{\mathbf{s}} \frac{\dot{F}}{F} \right) \le 0 \end{aligned} \tag{3.108}$$

The second inequality expressed in the (3.108) can be seen as a scalar product between two vectors where the left one is exactly the $\mathbf{N_s}$ depicted in Figure 16, so it is possible to assume the following equation satisfying the (3.108)

$$\overset{\circ}{\mathbf{s}} - \overset{\circ}{\boldsymbol{\alpha}} - \hat{\mathbf{s}} \frac{\dot{F}}{F} = c \left\| \boldsymbol{\varepsilon}^p \right\| \left(\boldsymbol{\sigma}_y - \boldsymbol{\alpha} - \frac{R_s}{\chi} (\mathbf{s}_y - \boldsymbol{\alpha}) \right) \tag{3.109}$$

where the left side of the (3.109) is a vector that can varies between two limits: $R_s = \chi$ or $R_s = 0$:

$$\boldsymbol{\sigma}_y - \boldsymbol{\alpha} - \frac{R_s}{\chi}(\mathbf{s}_y - \boldsymbol{\alpha}) \begin{cases} \boldsymbol{\sigma}_y - \boldsymbol{\alpha} = \dfrac{\boldsymbol{\sigma} - \mathbf{s}}{R} & \text{for} \quad R_s = 0 \\ \boldsymbol{\sigma}_y - \mathbf{s}_y & \text{for} \quad R_s = \chi \end{cases} \tag{3.110}$$

And where the term $\mathbf{s}_y$ is the conjugate point on the normal-yield surface for the $\mathbf{s}$ on the similarity-centre surface respect to the back stress.

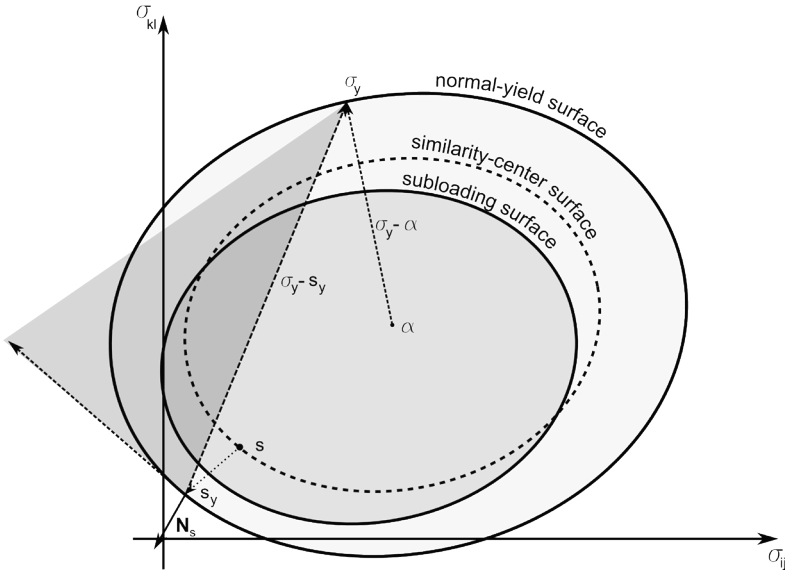

Figure 17 – field of existence for the vector (3.110) to satisfy the relation (3.108)

Figure 17 intuitively representes the field of possibility for the choice of the vectors that satisfy equation (3.108), it is sufficient that $\mathbf{N_s}$ vector forms an obtuse angle with the other to get the fulfilment of the so called *enclosing condition of the similarity centre*.

It is possible to write the evolution for the similarity centre starting from the previous equation (3.101) and (3.109)

$$\overset{\circ}{\mathbf{s}} = c\left\|\boldsymbol{\varepsilon}^p\right\|\left(\frac{\tilde{\boldsymbol{\sigma}}}{R} - \left(\frac{1}{\chi} - 1\right)\hat{\mathbf{s}}\right) + \overset{\circ}{\boldsymbol{\alpha}} + \hat{\mathbf{s}}\frac{\dot{F}}{F} \tag{3.111}$$

Inserting the (3.111) into the second of equation (3.105) it can be obtained

$$\overset{\circ}{\bar{\boldsymbol{\alpha}}} = \overset{\circ}{\boldsymbol{\alpha}} + (1-R)\left(c\left\|\boldsymbol{\varepsilon}^p\right\|\left(\frac{\tilde{\boldsymbol{\sigma}}}{R} - \left(\frac{1}{\chi} - 1\right)\hat{\mathbf{s}}\right) + \hat{\mathbf{s}}\frac{\dot{F}}{F}\right) - \dot{R}\hat{\mathbf{s}} \tag{3.112}$$

Assuming the associated flow rule, as done for the simple subloading model, eq. (3.112) is substituted backward into the time differentiation of the consistency condition getting

$$\frac{\partial f(\bar{\boldsymbol{\sigma}})}{\partial \bar{\boldsymbol{\sigma}}} : \overset{\circ}{\boldsymbol{\sigma}} - \frac{\partial f(\bar{\boldsymbol{\sigma}})}{\partial \bar{\boldsymbol{\sigma}}} : \overset{\circ}{\boldsymbol{\alpha}} - \dot{R}F - R\dot{F} = 0 \quad \text{where} \quad \left\| \frac{\partial f(\bar{\boldsymbol{\sigma}})}{\partial \bar{\boldsymbol{\sigma}}} \right\| \bar{\mathbf{N}} : \bar{\boldsymbol{\sigma}} = \frac{\partial f(\bar{\boldsymbol{\sigma}})}{\partial \bar{\boldsymbol{\sigma}}} : \bar{\boldsymbol{\sigma}} = RF$$
$$\left\| \frac{\partial f(\bar{\boldsymbol{\sigma}})}{\partial \bar{\boldsymbol{\sigma}}} \right\| \left[\bar{\mathbf{N}} : \overset{\circ}{\boldsymbol{\sigma}} - \bar{\mathbf{N}} : \left(\overset{\circ}{\boldsymbol{\alpha}} - \left(\frac{\dot{F}}{F} + \frac{\dot{R}}{R} \right) \bar{\boldsymbol{\sigma}} \right) \right] = 0 \tag{3.113}$$

Remembering that

$$\dot{F} = F' \dot{H} = F' h \lambda \quad \text{and} \quad \dot{R} = U \lambda \tag{3.114}$$

We can write

$$\left\| \frac{\partial f(\bar{\boldsymbol{\sigma}})}{\partial \bar{\boldsymbol{\sigma}}} \right\| \left[\bar{\mathbf{N}} : \overset{\circ}{\boldsymbol{\sigma}} - \bar{\mathbf{N}} : \left(\overset{\circ}{\boldsymbol{\alpha}} - \left(\frac{F' h \lambda}{F} + \frac{U \lambda}{R} \right) \bar{\boldsymbol{\sigma}} \right) \right] = 0 \tag{3.115}$$

If we call

$$\bar{\mathbf{a}} = \overset{\circ}{\bar{\boldsymbol{\alpha}}} / \lambda = \mathbf{a} + (1 - R) \left(c \left(\frac{\tilde{\boldsymbol{\sigma}}}{R} - \left(\frac{1}{\chi} - 1 \right) \hat{\mathbf{s}} \right) + \hat{\mathbf{s}} \frac{F' h}{F} \right) - U \hat{\mathbf{s}} \tag{3.116}$$

equation (3.115) can be rewritten as

$$\left\| \frac{\partial f(\bar{\boldsymbol{\sigma}})}{\partial \bar{\boldsymbol{\sigma}}} \right\| \left[\bar{\mathbf{N}} : \overset{\circ}{\boldsymbol{\sigma}} - \bar{\mathbf{N}} : \left(\bar{\mathbf{a}} - \left(\frac{F' h}{F} + \frac{U}{R} \right) \bar{\boldsymbol{\sigma}} \right) \lambda \right] = 0$$
$$\left\| \frac{\partial f(\bar{\boldsymbol{\sigma}})}{\partial \bar{\boldsymbol{\sigma}}} \right\| \left[\bar{\mathbf{N}} : \overset{\circ}{\boldsymbol{\sigma}} - \lambda \bar{M}^p \right] = 0 \tag{3.117}$$

In fact

$$\bar{\mathbf{a}} - \left(\frac{F' h}{F} + \frac{U}{R} \right) \bar{\boldsymbol{\sigma}} = \mathbf{a} + (1 - R) \left(c \left(\frac{\tilde{\boldsymbol{\sigma}}}{R} - \left(\frac{1}{\chi} - 1 \right) \hat{\mathbf{s}} \right) + \hat{\mathbf{s}} \frac{F' h}{F} \right) - U \hat{\mathbf{s}} - \left(\frac{F' h}{F} + \frac{U}{R} \right) \bar{\boldsymbol{\sigma}} =$$
$$= \frac{F' h}{F} \hat{\boldsymbol{\sigma}} + \mathbf{a} + \frac{\tilde{\boldsymbol{\sigma}}}{R} U + c (1 - R) \left[\frac{\tilde{\boldsymbol{\sigma}}}{R} - \left(\frac{1}{\chi} - 1 \right) \hat{\mathbf{s}} \right] \tag{3.118}$$

So the plastic modulus can be found as

$$\bar{M}^p = \mathbf{N} : \left\{ \frac{F' h}{F} \hat{\boldsymbol{\sigma}} + \mathbf{a} + \frac{\tilde{\boldsymbol{\sigma}}}{R} U + c (1 - R) \left[\frac{\tilde{\boldsymbol{\sigma}}}{R} - \left(\frac{1}{\chi} - 1 \right) \hat{\mathbf{s}} \right] \right\} \tag{3.119}$$

The definition of the other variables are exactly the same as the one seen for the simple subloading surface model, so the only variable that changes is the plastic modulus, that takes into account the presence of the evolution of the similarity ratio

$$\lambda = \frac{tr(\mathbf{N} \overset{\circ}{\boldsymbol{\sigma}})}{\bar{M}^p}; \quad \boldsymbol{\varepsilon}^p = \frac{tr(\mathbf{N} \overset{\circ}{\boldsymbol{\sigma}})}{\bar{M}^p} \mathbf{N} \tag{3.120}$$

$$\bar{\Lambda} = \frac{tr(\bar{\mathbf{N}}\mathbf{E}\boldsymbol{\varepsilon})}{\bar{M}^p + tr(\bar{\mathbf{N}}\mathbf{E}\bar{\mathbf{N}})} \tag{3.121}$$

$$\overset{\circ}{\sigma} = \left\{\mathbf{E} - \frac{(\mathbf{E}\bar{\mathbf{N}}) \otimes (\bar{\mathbf{N}}\mathbf{E})}{\bar{M}^p + tr(\bar{\mathbf{N}}\mathbf{E}\bar{\mathbf{N}})}\right\}\boldsymbol{\varepsilon} \tag{3.122}$$

The loading criterion also remains unaltered

$$\begin{aligned} &\boldsymbol{\varepsilon}^p \neq 0: \quad \bar{\Lambda} > 0 \\ &\boldsymbol{\varepsilon}^p = 0: \quad \text{otherwise} \end{aligned} \tag{3.123}$$

In general in soil the back stress is always null so the definition of the similarity centre evolution, or the one of the plastic modulus, are less complicated. In addition it has to be noticed that in the previous series of equations nothing has been said about anisotropy. In this case the function describing the normal-yield surface (3.98) and consequently the one for the subloading (3.100) should be modified in the following form

$$\begin{aligned} f(\hat{\boldsymbol{\sigma}}, \boldsymbol{\beta}) &= F(H) \\ f(\hat{\boldsymbol{\sigma}}, \boldsymbol{\beta}) &= RF(H) \end{aligned} \tag{3.124}$$

where $\boldsymbol{\beta}$ is the second order tensor describing the rotation of the yield surface. The representation of the deviatoric stress ratio tensor thus becomes:

$$\frac{\boldsymbol{\sigma}'}{p} \rightarrow \frac{\boldsymbol{\sigma}'}{p} - \boldsymbol{\beta} \tag{3.125}.$$

with the one called *rotational hardening variable* [37], which is fundamental in soil analysis. It is obvious that all the equations, starting from the time-material derivation, contains some additive terms for the inclusion of this contribution.

Until now nothing has been said about the behaviour of the similarity centre in the evolution of the plastic deformations. Figure 18 shows a uniaxial loading-unloading simulation for a generic soil as it can be seen by the section shape of the yield surface in the stress space.

a) At the beginning of the simulation the similarity centre and the conjugate back stress both lie at beginning of the origin, together with the null stress so the subloading surface collides in a single point.

b) During the loading of the sample the subloading surface expands, the similarity centre and the back stress move in the same direction on the loading axis with different velocity. The similarity centre shows an evolution similar to the stress, whereas the conjugate back stress reaches the maximum before the other two variables and it goes to zero when the other two reach the maximum.

c) In the unloading case the subloading surface shrinks until the stress reaches the similarity centre. It has to be noticed, looking at the stress-strain curves, that no irreversible

deformations are induced; this means that the similarity centre doesn't move during the unloading process. On the other side the conjugate back stress increases again.

d) Once the stress has passed the similarity centre the subloading surface starts to expand again producing new plastic deformations but in this case in the opposite direction. The similarity centre, which always follows the plastic flow, starts to decrease and also does the conjugate back stress. In case of soil, the unloading is pushed until the stress reaches null value, however it has to be clear that for that point the similarity centre is not zero and neither the conjugate back stress.

e) If a further loading is carried out an hysteresis loop is created as shown in the picture, but the plastic deformation does not occur until the stress reaches again the similarity centre as happened in the case of the unloading.

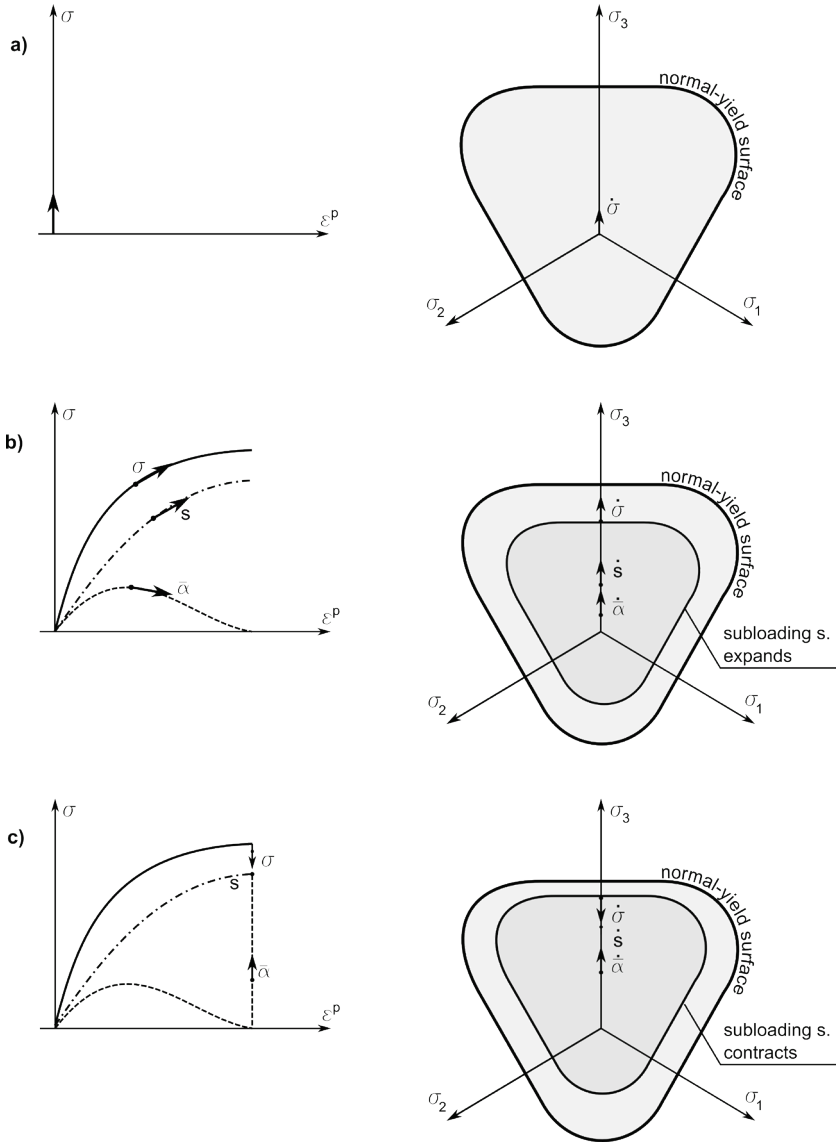

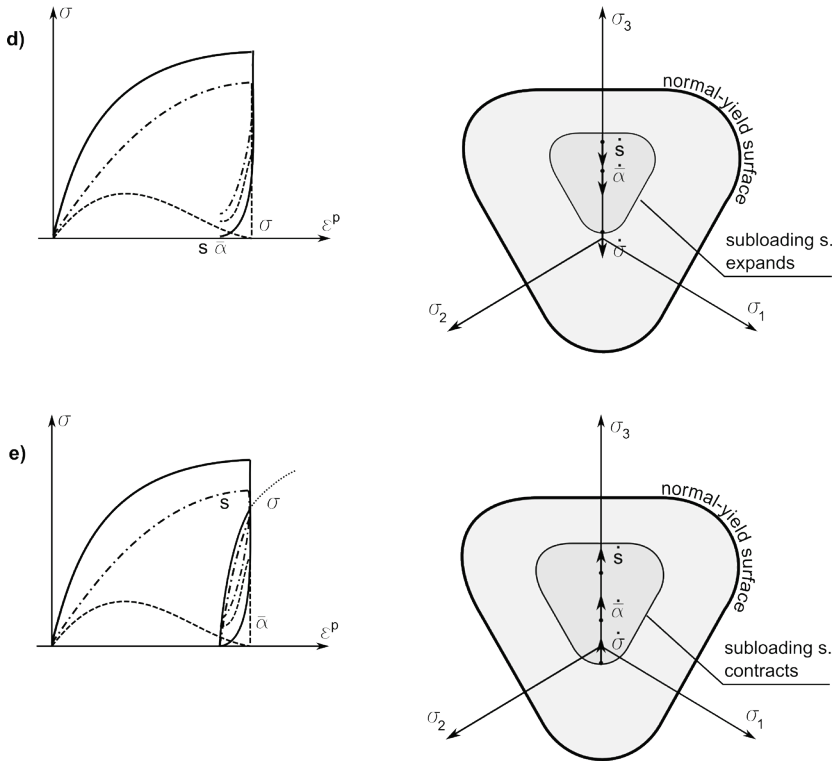

Figure 18 – Similarity centre and back stress evolution for as uniaxial loading-unloading analysis for soil.

3.2.5.2. The reloading curve

The relation expressed by equation (3.67) connects the strain rate with the evolution of the similarity ratio and vice-versa under the initial condition in the monotonic loading process. The model answer, in terms of strain rate, is independent from the process but it is strictly dependent on the R changes. For instance, after an unloading, the consequent load curve tends to move on the previous monotonic one with an unrealistic prediction of the plastic deformations.

It has to be noticed that this lack is not proper of the nature of the model and in fact it can be correct by a simple modification of the reloading curve behaviour as it will show in the numerical analyses chapter and explained in the following lines according to [17] .

It has to be noticed that:

a) The *Masing rule* [38] defining the curvature of the reloading and inverse loading curves should be respected.

b) The similarity-centre approaches to the normal-yield surface, together with the formation of irreversible deformation, governed by the similarity-centre ratio.

c) The material parameter *u* affects the shape of the stress strain curve in the sense that if it increases the curve becomes stiffer. In fact it regulates the monotonic function *U(R)* in a direct proportionally way.

d) In accordance to the previous statements the value of *u* should be connected with the value of similarity-centre ratio, for increasing value of R_s the difference between *u* in reloading curve and inverse loading should increase.

e) Finally as a measurement of the degree of reloading it can be chosen the measure of "*how the stress the stress is directed outward from the similarity-centre surface when it is observed from the similarity centre*" [17].

According to the last statement it is possible to judge the degree of reloading by the scalar product of two vectors assumed as benchmark of the process: the normalized outward-normal to the similarity-centre surface ($\mathbf{N}_s$) and the direction vector $\tilde{\boldsymbol{\sigma}}'/\|\tilde{\boldsymbol{\sigma}}'\|$, which is formed by the deviatoric part of the stress tensor on the subloading surface observed by the similarity centre as shown in Figure 16.

$$S_\sigma = \mathbf{N}_s : \frac{\tilde{\boldsymbol{\sigma}}_r}{\|\tilde{\boldsymbol{\sigma}}_r\|} = tr\left(\mathbf{N}_s \frac{\tilde{\boldsymbol{\sigma}}'}{\|\tilde{\boldsymbol{\sigma}}'\|}\right) \qquad (-1 < S_\sigma < 1)$$
$$= \begin{cases} \dfrac{\pm\sqrt{3}\tilde{\sigma}_m}{\|\tilde{\boldsymbol{\sigma}}\|}\left(= \pm\dfrac{\tilde{\sigma}_m}{\|\tilde{\sigma}_m\|} \text{ for } \tilde{\boldsymbol{\sigma}}' = 0\right) & \text{for } \mathbf{N}_s = \pm\dfrac{1}{\sqrt{3}}\mathbf{I} \\ tr\left(\mathbf{N}_s \dfrac{\tilde{\boldsymbol{\sigma}}'}{\|\tilde{\boldsymbol{\sigma}}'\|}\right) & \text{for } \mathbf{N}_s = 0 \end{cases} \tag{3.126}$$

Where

$$\tilde{\boldsymbol{\sigma}}_r = \tilde{\boldsymbol{\sigma}}' + \left|\frac{1}{3} tr\,\mathbf{N}_s\right| \mathbf{I}\tilde{\sigma}_m = \begin{pmatrix} \tilde{\boldsymbol{\sigma}} & \text{for } \mathbf{N}_s = \pm\dfrac{1}{\sqrt{3}}\,\mathbf{I} \\ \tilde{\boldsymbol{\sigma}}' & \text{for } \mathbf{N}_s = 0 \end{pmatrix} \tag{3.127}$$

$$\mathbf{N}_s = \frac{\partial f(\hat{\mathbf{s}})}{\partial \mathbf{s}} \Big/ \left\| \frac{\partial f(\hat{\mathbf{s}})}{\partial \mathbf{s}} \right\| \tag{3.128}$$

At this point, once defined a parameter evaluating the degree of reloading, a law that allows to modify the *U(R)* should be found depending on S_σ, Hashiguchi [17] proposed the following formula:

$$u = u_0 \exp(u_s R_s S_\sigma) = \begin{cases} u_0 \exp(u_s) & \text{for } R_s = 1 \text{ and } S_\sigma = 1 \\ u_0 & \text{for } R_s = 0 \text{ and } S_\sigma = 0 \\ u_0 \exp(-u_s) & \text{for } R_s = 1 \text{ and } S_\sigma = -1 \end{cases} \tag{3.129}$$

Where u_0 is the *u* parameter in the initial monotonic loading curve, u_s is a material parameter. Thanks to eq. (3.129) the *u* increases during the reloading whereas decreases in the inverse loading curve respecting the Masing effect and leading to a more realistic description of the accumulation of the plastic deformation as shown in Figure 19 b).

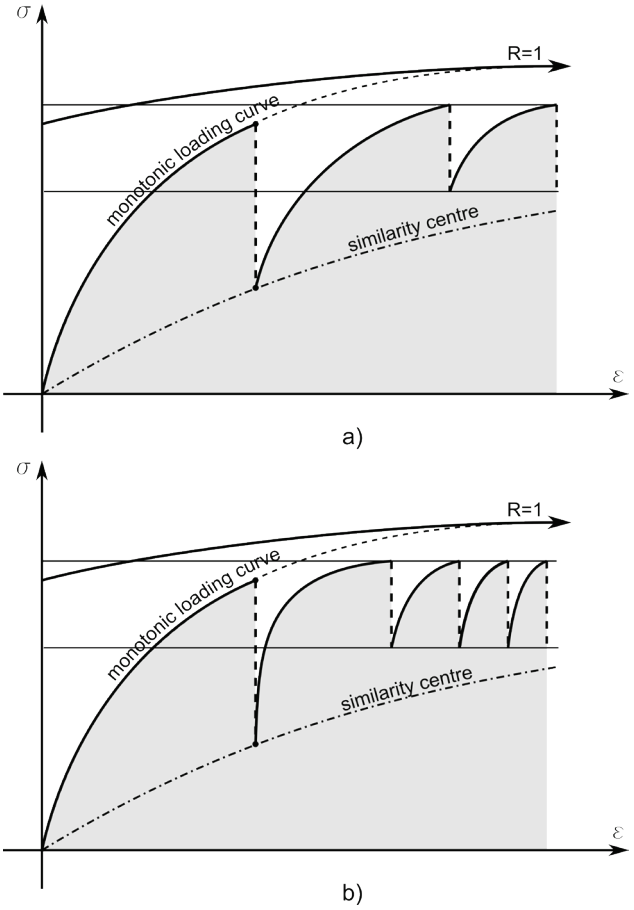

Figure 19 – representation of the answer of the extended subloading surface in terms of stress-strain curve for: a) original formulation, b) modification of the reloading curve.

Some simulations will be shown in the numerical analyses chapter for a uniaxial and three dimensional cases considering a comparison between using or not the modification of the reloading curve.

3.3. Soils

The study of soil acquired a lot of importance with the development of engineeristic constructions involving foundations, slides, tunnels, dams and many other applications. The first attempt to model granular materials is due to Coulomb, who elaborates the Mohr's circle theory for the definition of the first yield surface for geomaterials.

However the behaviour of soils cannot merely be described by this simplistic approach because presents some characteristics that lead to complications for certain stress level:

- The applied load and the pore pressure interact each other and determine the effective stress which controls the mechanics response of the material as shown in eq. (1.1);

- Soils compression and volume changes are regulated by the reorganization of particles composing the solid skeleton and by the consequential rearrangement of the voids;
- Shear resistance behaviour is frictional and then it is deeply influenced by the stress state and by confining pressure. Stiffness also increases with the confining pressure and so with the depth from the surface in natural condition;
- From the previous statements it can be concluded that resistance and stiffness are inversely proportional to the pore pressure and the water content;
- Volumetric deformations and distortions are not reversible in general. Soil cannot be properly describe by a pure elastic theory because of the nature of its granular composition.

After the definition of the first yield surface by Coulomb many other models have been proposed by fitting the laboratory tests with a simple or more complicated function, or using some theoretical assumptions proper of the behaviour of granular materials.

A simple and elegant formulation was proposed by researchers of Cambridge University in the 60', well known as Cam-Clay model [39], and then modified afterwards (i.e. Modified Cam-Clay model [40]). Starting from this point similar models have been developed, however all them use a form of the yield function that can be expressed like:

$$f(\boldsymbol{\sigma}) = p g(\chi) \tag{3.130}$$

where p is the isotropic pressure and:

$$\chi = \frac{\|\boldsymbol{\eta}\|}{M}, \quad \boldsymbol{\eta} = \frac{\boldsymbol{\sigma}'}{p} \tag{3.131}.$$

In the critical state line the M parameter is exactly equal to the $\|\boldsymbol{\eta}\|$ and for this reason it is called *critical state stress ratio*. An analytical form for it was proposed as follows by Hashiguchi [11]:

$$\begin{aligned} M(\cos 3\theta_{\boldsymbol{\sigma}}) &= \frac{14\sqrt{6}\sin\phi_c}{(3-\sin\phi_c)(8+\cos 3\theta_{\boldsymbol{\sigma}})} \\ \cos 3\theta_{\boldsymbol{\sigma}} &= \sqrt{6}\, tr\, \boldsymbol{\tau}^3, \quad \boldsymbol{\tau} = \frac{\boldsymbol{\sigma}'}{\|\boldsymbol{\sigma}'\|} \end{aligned} \tag{3.132}$$

ϕ_c is the frictional angle of the soil in the critical state for the tri-axial compression. The surface section in the stress space is the one schematically seen in the picture Figure 18 and, how it can be clearly seen, it respects the convexity condition reported in the eq. (3.53) and explained in paragraph 3.1.3., for the detailed demonstration see [17].

For justifying the shape of the yield function generally expressed in the (3.130) some conditions must be explicated before:

- It should involve not only positive but also negative pressure (i.e. tensile strength resistance). It has to be noticed that this aspect will solve a problem connected with the nature of the simple subloading surface which is the singularity point of the plastic modulus when the stress is null. In the extended model this problem doesn't exist because the similarity centre is not forced to be zero;

- the yield-surface expands and contracts in the stress space keeping similar shape with regard to the origin of the stress space (considering a type of anisotropy that doesn't affect the shape of the plastic surface, i.e. rotational, kinematic), and so the expansion and contraction happen in all the directions in the stress space simultaneously;

- the yield condition is split in two part, the first one is the function dealing with the stress and internal variables (back-stress, anisotropy) and the other one is the function involving the isotropic hardening/softening variable.

To fulfill the first condition many attempts have been made [41-43] however for them some defects have been pointed out, finally Hashiguchi and Mase [44] proposed the following expression:

$$f(p,\chi)=F,\quad f(p,\chi)=\begin{cases} p\left(1+\left(\dfrac{\chi}{p}\right)^2\right) & \text{for } \xi=0 \\ \dfrac{1}{\hat{\xi}}\left(p_\chi-\bar{\xi}p\right) & \text{for } \xi\neq 0 \end{cases} \tag{3.133}$$

where

$$\hat{\xi}=2(1-\xi)\xi,\quad \bar{\xi}=(1-2\xi),\quad p_\chi=\sqrt{p^2+2\hat{\xi}\chi^2} \tag{3.134}$$

ξ is a material constant that should be imposed as input for the model and, due to a stronger resistance in compression rather than extension, it must be:

$$0\le\xi\le\frac{1}{2} \tag{3.135}$$

It has to be noticed that the previous formula (3.133) has to be changed in case anisotropy is taken into account. The definition of the (3.131) can be substituted using a different definition of the deviatoric stress by incorporation of the rotational hardening variable $\boldsymbol{\beta}$:

$$\begin{aligned} \hat{\boldsymbol{\sigma}}' &= \boldsymbol{\sigma}' - p\boldsymbol{\beta} \\ \hat{\chi} &= \frac{\left\|\hat{\boldsymbol{\sigma}}'\right\|}{\hat{M}} \\ M(\cos 3\theta_{\hat{\sigma}}) &= \frac{14\sqrt{6}\sin\phi_c}{(3-\sin\phi_c)(8+\cos 3\theta_{\hat{\sigma}})} \end{aligned} \tag{3.136}$$

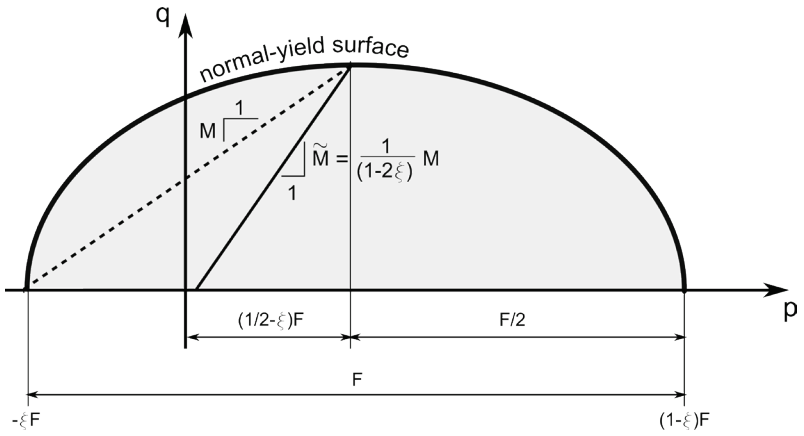

Figure 20 – Shift of the yield surface.

The equation (3.133) fulfills all the conditions exposed previously, in fact by means of the ξ it can take into account negative pressure (i.e. material extension) and, if the rotational hardening parameter is constant, expansion/contraction occurs keeping similar shape respect to the origin of the stress space. Some examples will be shown in numerical analyses chapter.

3.3.1. Isotropic hardening/softening function

The isotropic hardening/softening for a soil is connected with the volumetric expansion or contraction and affects only the dimension of the yield-surface surface without inducing any modification in its orientation.

Hardening/softening behaviour varies depending on the type of material considered, in general clays and sands can be described with a completely different mechanisms as it will be shown in the following equations.

First of all a definition for the isotropic hardening/softening function must be given and then a different evolution for the H variable, based on the different type of material, will be introduced. Starting from some considerations about the volumetric plastic expansion of soils and introducing the parameter p_e, that is a material constant prescribing the pressure at which the volume becomes infinite, it is possible to write:

$$F(H) = \left(F_0 + \frac{p_e}{1-\xi} \right) \exp \frac{H}{\rho - \gamma} - \frac{p_e}{1-\xi}$$
$$F' = \frac{dF}{dH} = \frac{1}{\rho - \gamma} \left(F + \frac{p_e}{1-\xi} \right) \tag{3.137}$$

At this point the only other thing to define is the evolution of the hardening/softening variable which is different if a clay or a sand is taken into account:

- Considering a shift of the normal-yield in the stress plane it is possible to write the formulas applicable for the clays:

$$\dot{H} = -D_v^p - \zeta \left\| \mathbf{D}^{p'} \right\| \langle -p \rangle, \quad h = -tr\,\bar{\mathbf{N}} - \zeta \left\| \bar{\mathbf{N}} \right\| \langle -p \rangle \tag{3.138}.$$

The previous expression can be divided in two: the volumetric strain is the main variable to take into account for hardening/softening of soil, whereas in case of negative regime of idrostatic pressure (i.e. shift of the yield surface in the tensile strength) the deviatoric part of the plastic strain rate tensor is responsible for the softening answer of the model. ζ is a material constant.

- For sand it is necessary to use a different formulation, as it has been point out by [45-47], depending on how dense is the material considered, as shown in Figure 21.

  The isotropic hardening and softening are due to both the volumetric plastic strain rate and by the deviatoric part when the stress is higher and lower than a certain threshold M_d proper of every material.

$$\dot{H} = -D_v^p + \mu_d \left\| \mathbf{D}^{p\,\prime} \right\| \frac{\left\| \boldsymbol{\sigma}' \right\| - M_d p}{F} \tag{3.139}$$

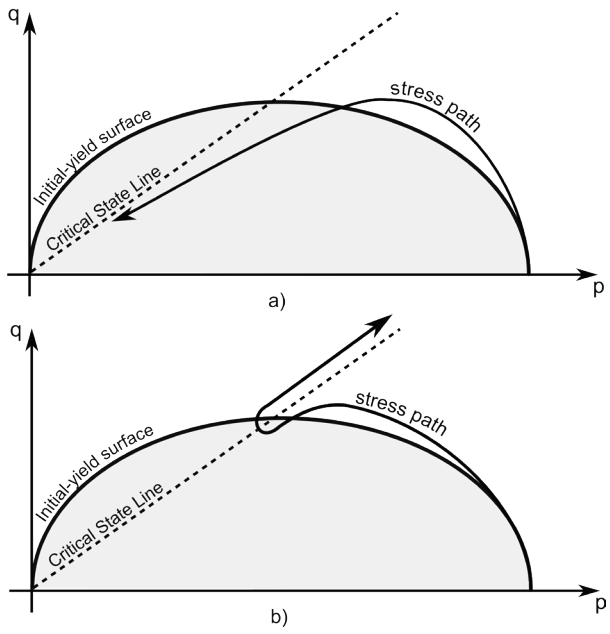

Figure 21 – Stress path under undrained triaxial test for: a) loose sand, b) dense sand.

References

[1] Drucker D.C., (1988), "Conventional and unconventional plastic response and representation", *Appl. Meek. Rev.*, ASME, **41**, pp. 151-167.

[2] Hashiguchi K., Ueno M., (1977), "Elastoplastic constitutive laws of granular materials, Constitutive Equation of Soils", in Murayama S., Schofield A.N. eds., *Proc. 9th Int. Conf. Soil Mech. Found. Eng.*, Spec. Ses. 9, Tokyo, JSSMFE, pp. 73-82.

[3] Simo J.C., Huges T.J.R., (1998), "Computation Inelasticity", Springer, Heidelberg.

[4] Drucker D.C., (1951), "A more fundamental approach to plastic stress-strain relations", in: *Proc. 1st U.S. National Congress App. Mech.*, (ASME), vol.1, pp. 487-491

[5] Ilyushin A.A., (1961), "O the postulate of plasticity", *Prik. Mat Mekh,* **25**, p.503.

[6] Hill R., (1950), "The mathematical Theory of Plasticity", *Oxford Press University*, Oxford, p.66.

[7] Lubliner J., (1990), "Plasticity Theory", Macmillan Publ. Comp., New York, p.117.

[8] Hashiguchi K., (1993a), "Fundamental requirements and formulation of the elastoplastic constitutive equations with tangential plasticity", *Int. J. of Plasticity*, **9**, pp. 525-549.

[9] Hashiguchi K., (1993b), "Mechanical requirements and structures of cyclic plasticity model", *Int. J. of Plasticity*, **9**, pp. 721-748.

[10] Hashiguchi K., (1997), "The extended flow rule in plasticity", *Int. J. of Plasticity*, **13**, pp. 37-58.

[11] Hashiguchi K., (2000), "Fundamentals in constitutive equation: continuity and smoothness conditions and loading criterion", *Soil and Foundations*, **40**(3), pp.155-161.

[12] Prager W., (1949), "Recent development in the mathematical theory of plasticity", *J. Appl. Mech.*, ASME, **20**, pp.235-241.

[13] Hashiguchi K., (1978), "Plastic constitutive equations of granular materials", In: Cowin, S.C., Satake, M. (eds.) *Proc. US-Japan Seminar on Continuum Mech. Stast Appr. Mech. Granular Materials*, Sendai, pp.321-329.

[14] Hashiguchi K., (1980), "Constitutive equations of elastoplastic materials with elastic-plastic transition", *J. Appl. Mech.* (ASME) **47**, pp.266-272.

[15] Hashiguchi K., (1989), Subloading surface model in unconventional plasticity. *Int. J. Solids Structures*, **25**, pp. 917-945.

[16] Tsutsumi S., Toyosada M., Hashiguchi K., (2006), "Extended subloading surface model incorporating elastic limit concept", in: *Proc. Plasticity 2006*, Halifax, pp.217-219.

[17] Hashiguchi K.,(2009), "Elastoplasticity theory - Lecture notes in applied and computational mechanics". In: F Pfeiffer, P Wriggers (Eds.), Springer, Berlin, **42**, 393 pp.

[18] Hill R., (1958), "A General Theory of Uniqueness and Stability in Elastic-Plastic Solids", *J. Mech. Phys. Solids*, **6**, pp.236.

[19] Simo J.C., Taylor R.L., (1986), "A Return Mapping Algorithm for Plane Stress Elastoplasticity", *Int. J. Numer. Meth. Engng*, **22**, pp. 649–670.

[20] Wilkins M.L., (1964), "Calculation of Elasto-plastic Flow", In: *Alder, B. et al. (Ed.), Methods of Computational Physics*, Vol. 3, New York, Academic Press.

[21] Krieg R.D., Krieg D.B., (1977). "Accuracies of Numerical Solution Methods for the Elastic-perfectly Plastic Model", *J. Pressure Vessel Tech.*, **99**, pp. 510‑515.

[22] Simo J.C., Huges T.J.R., (1998), "Computation Inelasticity", Springer, Heidelberg.

[23] De Souza E.N., Peric D., Owen D.J.R., (2008), "Computational Methods for Plasticity". *John Wiley and Sons*, Chichester.

[24] Simo J.C., Taylor R.L., (1985), "Consistent tangent operators for rate-independent elastoplasticity", *Comput. Methods Appl. Mech. Eng.*, **48** (3), pp. 101-118.

[25] Simo J.C., Ortiz M., (1985), "A unified approach to finite deformation elastoplasticity based on the use of hyperelastic constitutive equations", *Compt. Meth. Appl. Mech. Eng.*, **49**, pp. 221-245.

[26] Ortiz M., Popov E.P., (1985), "Accuracy and Stability of Integration Algorithms for Elastoplastic Constitutive Relations", *Int. J. Numer. Meth. Engng*, **21**, pp. 1561‑1576.

[27] Ortiz M., Simo J.C., (1986), "An Analysis of a New Class of Integration Algorithms for Elastoplastic Constitutive Relations", *Int. J. Numer. Meth. Engng*, **23**, pp. 353‑366.

[28] Hashiguchi K., (2011), "Subloading Surface Model and its Return-mapping Formulation", *Proc. 60th Nat. Cong. Of Theoretical & Applied Mechanics*.

[29] Krieg R.D., (1975), "A Pratical Two Dimensional Plasticity Theory", *J.Appl. Mech.*, ASME, **42**, p.641.

[30] Dafalias Y.F., Popov E.P., (1975), "A Model of Nonlinearly Hardening Maetrials for Complex Loading", *Acta Mech.*, **23**, p.173.

[31] Hashiguchi K., (1985) "Macrometric Approaches –Static- Intrinsically Time –Independent", in Murayama S., (ed.), *Constitutive Laws of Soils*, (Proc. 11th Int. Conf. Soil Mech. Found. Eng., Discussion Session IA, San Francisco), JSSMFE, Tokyo, p.25.

[32] Mroz Z., (1967), "On the Description of Anisotropic Hardening", *J. Mech. Phys. Solids*, **15**, p.163.

[33] Iwan W.D., (1967) "On a Class of Models for the Yielding Behaviour of Continuous and Composite Systems", *J. Appl. Mech.*, ASME, **34**, p.612.

[34] Mroz Z., Norris V.A., Zienkiewicz O.C., (1981), "An anisotropic, critical state model for soils subject to cyclic loading", *Geotechnique*, **31**, pp.451-469.

[35] Hashiguchi K., (1985), "Subloading Surface Model of Plasticity", *Constitutive Laws of Soils* (Proc. 11th Int. Conf. Soil Mech. Found. Eng., Discussion Session IA, San Francisco), JSSMFE, Tokyo, p.127.

[36] Hashiguchi K., (1986), “Elastoplastic constitutive model with a subloading surface”, in: *Proc. Int. Conf. Comput. Mech.*, pp. IV65-IV70.

[37] Sekiguchi H., Otha H., (1977), “Induced anisotropy and its time dependence in clays, Constitutive Equations of Soils”, in: *Proc. Spec. Session 9, 9th ICSFME*, Tokyo, pp. 229-238.

[38] Masing G., (1926), “Eigenspannungen und Verfestigung beim Messing”, in: *Proc. 2nd Int. Congr. Appl. Mech.*, Zurich, pp. 332-335.

[39] Schofield A.N., Wroth C.P., (1968), “Critical State Soil Mechanics”, *McGraw-Hill*, London.

[40] Roscoe K.H., Burland J.B., (1968), “On the generalized stress-strain behaviour of ‘wet’ clay”, in: *Engineering Plasticity*, J Heyman and F.A. Leckie (eds.), Cambridge University Press, Cambridge.

[41] Vrech S.M., Este G., (2006), “Geometrical localization analysis of gradient-dependent parabolic Drucker-Prager elastoplasticity”, *Int. J. Plasticity*, **22**, pp.943-964.

[42] Alonso E.E., Gens A., Josa A., (1990), “ A constitutive model for partially saturated soils”, *Geotechnique*, **40**, pp. 405-430.

[43] Yasufuku, Nakata Y.,Hyodo M., Murata M., (1994), “An isotropic hardening model for sand considering the bonding effects”, in: *Proc. Pre-Failure Deformation of Geomaterials*, Balkema, pp. 445-450.

[44] Hashiguchi K., Mase T., (2007), “Extended yield condition of soils with tensile yield strength and rotational hardening”, *Int. J. Plasticity*, **23**, pp. 1939-1956.

[45] Nova R., (1977), “On the hardening of soils”, *Arch. Mech. Stos.*, **29**, pp. 445-458.

[46] Wilde P., (1977), “Two invariants depending models of granular media”, *Arch Mech. Stos.*, **29**, pp. 799-809.

[47] Hashiguchi K., Chen Z.P., (1998), “Elastoplastic constitutive equations of soils with the subloading surface and the rotational hardening”, *Int. J. Numer. Anal. Meth. Geomech.*, **22**, pp. 197-227.

4. The numerical code

The numerical code used for the analyses is a fully coupled F.E. research code dealing with a u-p-T formulation (i.e. *u* stands for displacements, *p* for pressure and *T* for temperature) and named PLASCON 3D. The theory at the bases of the model equations has already been explained in the previous Chapters 1 and 2, here some indications about the implementation of the routine updated for non linear material are described. The complete manual for PLASCON 3D can be found in the references [1], [2].

Before dealing with the F.E. code some paragraphs will be spent in the description of small programs created for checking the reliability of the numerical implementation of the constitutive equations shown in the Chapter 3.

All the codes have been written in FORTRAN language and are here described starting from the most simple uniaxial plasticity case to the three dimensional F.E. boundary problem passing through the three dimensional single Gauss point case. The output results are not reported in this chapter but they will be discussed in the next one.

4.1. One dimensional program

A one dimensional program has been developed to check the accuracy of the return mapping algorithm and also to verify the implementation of the constitutive equations of the simple subloading surface and of the extended subloading surface models. These three theories have been translated in a programming language and inserted in the main code in three different subroutines in order to allow the user to switch from one to another depending on the type of the analysis required. A small description for each of them is here provided together with the numerical code adopted.

The MAIN routine is common for all the subroutines and basically manage the call to all the different parts of the program such as the one responsible for the reading of the input file or the one for the plotting of the results, moreover let the user decide which mechanism consider (i.e. simple subloading model, extended subloading or the return mapping algorithm).

Respect all the other parts of the code rewritten in the following chapter, there is no algorithm dedicated to the computation of the normal vectors to the plastic surface for the one dimensional problem because, as mentioned in the paragraph 3.1.1, the yield surface collides in one point and the direction of the plastic flow maintains obviously constant.

4.1.1. Simple subloading surface routine

All the simulations realized in this present work deal with modelling of soils, which are well known to be an assembly of particles which can bear quite well compression but have a weak or null stress tensile resistance.

All the simulation realized with the uniaxial algorithm are compression cases and this explain why in the code, reported in the Box 3, the normal unitary vector **N** is simply indicated as -1, by consent of the convention where the compression is negative while the traction is positive.

```
    subroutine subSURF (stressTp,stressP,stressE,plasticT,young,i)
    use SUBS

! --- defining normal yield and normal yield ratio
     F = F0 * dexp((acca)/(rho-gmm))
     R = abs(stressTp)/F
     dfdh = F/(rho-gmm)
     hplm = 1

! --- definition of the monotonic function U
     if ((R-Re).ge.0) then
        Ufun = pu*(1.0d0/(dtan((pi/2.0d0)*((R-Re)/(1.0d0-Re)))))
     else
        Ufun = 1.0e+12
     end if

! --- defining the plastic modulus
     Pm  = (dfdh/F + Ufun/R)*(-stresstp)
     PmtrN = Pm + young

! --- computing the new modulus
     EPD = young*pm/(PmtrN)
     stressP = EPD * epsil

    trNEMD = young*(-1)*epsil

! --- checking the loading conditions
     if (trNEMD .gt. 0.D0) then
         plastic = stressP/pm
         plasticT = plasticT + plastic
        stressTp = stressTp + stressP
        plastic = stressP/pm
        plm = trNEMD/PmtrN
        acca = acca + plm*hplm
    else
        stressTp = stressTp + stressE
    end if

    return
    end
```

Box 3 – One dimension simple subloading surface algorithm.

The present routine sets up the elastoplastic matrix as seen in the formula (3.22) but according with the formulation seen for the simple subloading surface in the creation of the plastic modulus.

At the beginning the yield function *F* is founded (in this case $F = \sigma_0$) as function of the hardening/softening variable H (i.e. *acca* in the code) then the similarity-ratio *R* is calculated from the

ratio between the current total stress point, which is an input from the MAIN of the code, and the actual position of the yield stress.

To define the monotonic function *U* an *if* condition is imposed, because numerically the cotangent cannot assume infinite value so, if the similarity ratio is smaller than the R_e parameter, a value equal to 10^{+12} is attributed.

The plastic modulus is evaluated by means of the (3.73) and subsequently is possible to build the elastoplastic matrix

$$E^{ep} = E\frac{M^p}{E + M^p} \tag{4.1}$$

The stress rate is then computed by multiplying the total strain rate (given as an input of the problem) for the elastoplastic matrix just found. Obviously the input can also be given in terms of stress rate and in this case the inverse bond expressed in (3.21) should be used. The convenience to use strain rate input is that the control of loading and unloading condition (i.e. the loading criteria) can be directly explicited by the multiplication on the Young's modulus for the normal vector and the input condition for the actual step.

If term trNEMD is bigger than zero it means that irreversible deformations are induced (i.e. loading case), the internal isotropic hardening/softening variable is updated and in the next step it will influence the expansion or contraction of the yield surface. On the other hand if trNEMD is negative nothing is updated and linear elastic stress rate is added to the total stress.

4.1.2. Return mapping routine

The present routine allows to investigate the nonlinear response of the material without creating the elastoplastic matrix. The trial elastic is performed with the Young's modulus and then stress state is corrected by using the proportionality factor compute according to eq. (3.97).

The algorithm is exactly the same presented in Box 2 with the only difference that the tensorial quantities degenerate in simple scalar values. Input parameters necessary for the computation are the total stress, which is already comprehensive of the elastic trial (i.e. imagine to input a constant $\Delta\varepsilon$, the elastic $\Delta\sigma$ proper of the step can be immediately estimated in the MAIN), and the Young's modulus for the plastic relaxation.

As it can be seen two other parameters are passed from the MAIN: the maxsteps and the toll. The first one is necessary to prevent infinite loops whereas the second is the tolerance defined by the user.

```
subroutine RetMap(stressTp,toll,maxsteps,young,i)

  use SUBS

! routine for the implementation of the return mapping on a uniaxial
! case for the subloading surface algorithm
! ----------------------------------------------------------------
```

```
  dpl = 0.0d0
  counter = 0
! ------------------------------------------------------------------
  control0 = abs(stressTp) - RM*F
  write(7,9) counter, control0

  if (abs(stressTp) >= RM*F) then

! --- The cycle is under a conditioned DO CYCLE (old repeat_until cond)
!    to avoid infinite loop maxsteps parameter must be fixed in the input
!    data file

    do
     counter = counter + 1

! --- definition of the monotonic function U
      if ((R-Re).ge.0.d0) then
        Ufun = pu*(1.0d0/(dtan((pi/2.0d0)*((R-Re)/(1.0d0-Re)))))
      else
        Ufun = 1.0e+12
      end if

      dfdh = F/(rho-gmm)
      hplm =  1

      pm = (dfdh/f + Ufun/R)*(-stresstp)
      trNEN = (1)*young*(1)
      pmtrN = pm + trNEN
      Epd = young*pm/pmtrN

! --- definition of the plastic increment dlambda and integral value dpl
      dlambda = (+1)*(-stressTp-R*F)/pmtrN
      dpl = dpl + dlambda

! --- plastic correction
      dstrain = dLambda * (-1)
      dstress = young * dstrain

      stressTp = stressTp - dstress

! --- update variable
      if (RM-Re <= 0.0d0) then
        cosin = 1.0d0
      else
        cosin = dcos((pi/2.0d0)*(RM - Re)/(1.0d0-Re))
      endif
      espR  = dexp(-(pi/2.0d0)*pu*dpl/(1.0d0-Re))
      acca  = acca + dLambda*hplm

      R = (2.0d0/pi)*(1.0d0-Re)*dacos(cosin*espR) + Re
      F = F0 * dexp(acca/(rho-gmm))
```

```
      control = (abs(stressTp) - R*F) /(RF)
      write(7,9) counter, control

      if ((counter == maxsteps) .or. (control <= toll)) exit
    end do
    RM = R
    write(7,*) '-----------------------------------'
  end if
  return
end
```

Box 4 – Code for the uniaxial return mapping algorithm.

The first control that should be made, once inside the routine applying the return mapping method, is if the point belongs to the inside of the previous subloading surface or to the outside. As explained in the paragraph 3.2.4, this condition is reported in eq. (3.87) and translated in the FORTRAN language in the Box 4.

If the plastic relaxation is required a DO cycle performs all the substeps necessary to satisfy the tolerance imposed by the user. The target of the algorithm is the computation of the proportionality factor λ (i.e. lambda in the code) of the *n* step according to the formula (3.97) which allows to calculate the correct plastic relaxation.

In order of appearance the monotonic *U* function, the plastic modulus and the scalar value **N:E:N** are estimated and introduced in eq. (3.97). Then the plastic correction is carried out by subtracting to the total stress the one obtained multiplying the $\Delta\boldsymbol{\varepsilon}^p$ for the Young's modulus

$$\begin{aligned} \boldsymbol{\sigma}_{n+1}^{(k+1)} &= \boldsymbol{\sigma}_{n+1}^{(k)} - \mathbf{E} : \lambda \mathbf{N} \\ \boldsymbol{\sigma}_{n+1}^{(k+1)} &= \boldsymbol{\sigma}_{n+1}^{(k)} - \mathbf{E} : \Delta\boldsymbol{\varepsilon}^{p} \\ \boldsymbol{\sigma}_{n+1}^{(k+1)} &= \boldsymbol{\sigma}_{n+1}^{(k)} + \boldsymbol{\sigma}^{p} \end{aligned} \tag{4.2}$$

Where, if $k = 0$ then

$$\boldsymbol{\sigma}_{n+1}^{(0)} = \boldsymbol{\sigma}_{n+1}^{(trial)} \tag{4.3}$$

After stress correction has been carried out the internal isotropic hardening/softening variable *H*, together with the similarity ratio and the yield surface *F* are updated. It must be noticed that similarity ratio is obtained directly from the inelastic strain rate using the equation (3.66).

In the end a further check if the new stress state lies or not on the updated yield surface is performed. The *control* variable is normalized using the value of the new yield surface for having a dimensionless parameter to compare with the impose tolerance. If the last inequality is not satisfied a new sub-cycle is carried out starting from the definition of the *U* function and, subsequently to all the other variables, until convergence.

4.1.3. Extended subloading routine

```
subroutine extended (stressTp,stressP,stressE,plasticT,young,direction,controlU,i)

   use SUBS
!-----------------------------------------------------------------------
! routine for external subloading surface

! --- normal yield-evolution
      F = F0 * dexp((acca)/(rho-gmm))
      dfdh = F/(rho-gmm)

      if (direction == 1) then
          on = -1
          hplm = -on
      else
         on = +1
         hplm = -on
      end if

! --- computing sigmaT
      sigma  = stressTp
      sigmaT = sigma - esse

! --- coputing the similarity ratio Rd
      R = abs(sigmaT)/(F-esse)
      sigmaD = sigmaT+R*esse
      alphaD = (1-R)*esse

! --- definition of the monotonic function U
      Rs = abs(esse)/F
      if (direction == 1) then
         Ssigma = +1
      else
         Ssigma = -1
      end if

      if ((controlU == 0).and.(abs(sigma)>=abs(esse)))then
          uvar = pu
      end if
      if ((controlU == 1).and.(abs(sigma)>=abs(esse)))then
          uvar = pu
      end if
      if ((controlU == 1).and.(abs(sigma)<=abs(esse)))then
          uvar = pu*dexp(us*Rs*Ssigma)
      end if
      if (controlU == 2) then
          uvar = pu*dexp(us*Rs*Ssigma)
      end if

     if ((R-Re).ge.0) then
```

```
        Ufun = uvar*(1.0d0/(dtan((pi/2.0d0)*((R-Re)/(1.0d0-Re)))))
      else
        Ufun = 1.0e+12
      end if

! --- definition of the plastic modulus
       part1 = on*(dfdh/F*hplm*sigma)
       part2 = on*Ufun*sigmaT/R
       part3 = on*ccentr*(1.0d0-R)*(sigmaT/R-(1.0d0/chiS-1.0d0)*esse)
       pm = part1+part2+part3
       PmtrN = Pm + young

! --- computing the new modulus
       EPD = young*pm/(PmtrN)
       stressP = EPD * epsil

       trNEMD = young*(on)*(epsil)
      if  (trNEMD <= 0.0d0) then
          plm = trNEMD/PmtrN
          plastic = stressP/pm
          stressTp = stressTp + stressP
          plasticT = plasticT + plastic
          s1 = ccentr*abs(plastic)*(sigmaT/r)
          s2 = -ccentr*abs(plastic)*esse*(1.0d0/chiS-1.0d0)
          s3 = (dfdh/F)*hplm*plm*esse
          esseI = s1 + s2+ s3
          esse = esse + esseI
          acca = acca + plm*hplm
      end if
      if (trNEMD >= 0.0d0) then
          plm = trNEMD/PmtrN
          plastic = stressP/pm
          stressTp = stressTp + stressP
          plasticT = plasticT + plastic
          s1 = ccentr*abs(plastic)*(sigmaT/r)
          s2 = -ccentr*abs(plastic)*esse*(1.0d0/chiS-1.0d0)
          s3 = (dfdh/F)*hplm*plm*esse
          esseI = s1 + s2+ s3
          esse = esse + esseI
          acca = acca + plm*hplm
      end if
      return
end
```

Box 5 - Code for the uniaxial extended subloading surface.

The extended subloading surface routine is created translating in FORTRAN language the equations contained in paragraph 3.2.5.1. The only upgrade respect to the simple subloading surface consists in the definition of the similarity-centre and its evolution which enters in the definition of the plastic modulus *pm*.

Differently from the simple subloading model the extended one can produce irreversible deformations even during the unloading phase. In fact whenever the stress state passes through the similarity centre, the inner surface starts to expand again inducing plastic strains. A check on the normal vector direction is then necessary for the correct interpretation of the algorithm, on the other hand in the simple code the normal on the yield surface keeps the same sign (i.e. plastic deformations are induced only in loading case) so no check is required.

A comparison between the simple and the extended uniaxial models is reported in the numerical analyses chapter for a cyclic loading-unloading case.

4.2. Three dimensional single Gauss point program

The three dimensional single Gauss point program has been written as a preparation test for the finite elements modelling because boundary conditions are added as input in the code and thus the simulations can be more "user controlled" for the verification of the implementation.

Differently from the uniaxial case six initial values should be given as input in term of stress rate or strain one or mixed conditions. The solution of the system is performed using a direct *Gauss elimination method* where the matrix should be split in two (i.e. upper triangular matrix and lower triangular matrix) by means of a Cholesky decomposition. This allows to solve the system as

$$\left.\begin{aligned}\mathbf{K}\mathbf{x}&=\mathbf{f}\\ \mathbf{K}&=\mathbf{L}\mathbf{L}^{\mathbf{T}}\end{aligned}\right\}\rightarrow\begin{cases}\mathbf{L}\mathbf{y}=\mathbf{f}\\ \mathbf{L}^{\mathbf{T}}\mathbf{x}=\mathbf{y}\end{cases} \tag{4.4}$$

where at first the direct solution is performed and then the so called back substitution is carried out. It is important to notice that the stiffness matrix of the system coincides exactly with the elastic (**E**) or elastoplastic ($\mathbf{E}^{ep}$) matrices so assembly procedure is not required for the solution.

The single Gauss point problem allows to neglect the boundary conditions in terms of imposed displacements or forces and considers directly stress and strain rates with a perfect parallelism. Looking at the system of eq. (4.5) is it easy to imagine that the procedure for the solution is exactly the same adopted for F.E.M. with the exception of different terminology.

$$\begin{bmatrix}E_{11}&E_{12}&E_{13}&\cdots&\cdots&0\\ E_{21}&E_{22}&E_{23}&&&\vdots\\ E_{31}&E_{32}&E_{33}&&&\vdots\\ \vdots&&&E_{44}&&\vdots\\ \vdots&&&&E_{55}&\vdots\\ 0&\cdots&\cdots&\cdots&\cdots&E_{66}\end{bmatrix}\begin{bmatrix}\varepsilon_{11}\\ \varepsilon_{22}\\ \varepsilon_{33}\\ \varepsilon_{12}\\ \varepsilon_{23}\\ \varepsilon_{13}\end{bmatrix}=\begin{bmatrix}\sigma_{11}\\ \sigma_{22}\\ \sigma_{33}\\ \sigma_{12}\\ \sigma_{23}\\ \sigma_{13}\end{bmatrix} \tag{4.5}$$

If a prescribed strain rate component is given as input, the system solved is smaller than the one depicted in eq. (4.5) because the row and column with the imposed Dirichlet condition should be eliminated. As an alternative it is possible to use *penalty method* which consists in multiplying the

diagonal term on the stiffness and the correspondent one on the right hand of the system, associated to the known strain rate value, for a scalar value of big magnitude (i.e. $10^{+12} \sim 10^{+15}$). When the system will be solved all the extra diagonal terms can be considered as negligible and the prescribed value of the strain rate will be found. This method is very attractive to use especially for big sparse stiffness matrix because the error commited in using a scalar multiplier is contained by the fact that a large number of coefficients is null.

$$\begin{bmatrix} E_{11} & E_{12} & E_{13} & \cdots & \cdots & 0 \\ E_{21} & E_{22} & E_{23} & & & \vdots \\ E_{31} & E_{32} & a\cdot 1 & & & \vdots \\ \vdots & & & E_{44} & & \vdots \\ \vdots & & & & E_{55} & \vdots \\ 0 & \cdots & \cdots & \cdots & \cdots & E_{66} \end{bmatrix} \begin{bmatrix} \varepsilon_{11} \\ \varepsilon_{22} \\ \bar{\varepsilon}_{33} \\ \varepsilon_{12} \\ \varepsilon_{23} \\ \varepsilon_{13} \end{bmatrix} = \begin{bmatrix} \sigma_{11} \\ \sigma_{22} \\ a\bar{\varepsilon}_{33} \\ \sigma_{12} \\ \sigma_{23} \\ \sigma_{13} \end{bmatrix} \tag{4.6}$$

The stiffness matrix, in a quadrature point program, is quite small (i.e. a 6x6 matrix) so is not necessary to use the penalty method and a traditional solver has been used as reported in Box 6.

```
subroutine solver(M,s,e,cond)

    implicit none
    integer i, ii, j
    real*8 M, s, e, calc, y, L, MC,cond
    dimension M(6,6), s(6), e(6), y(6)
    dimension cond(6), L(6,6), MC(6,6)

    do i = 1, 6
      do j = 1, 6
        MC(i,j) = M(i,j)
      end do
    end do

    do i = 1, 6
      if (cond(i) == 1)then
        do j = 1, 6
          if (i == j) then
            MC(i,j) = 1.0d0
          else
            MC(i,j) = 0.0d0
          end if
        end do
      else
        do j = 1, 6
          if (cond(j) == 1) then
            MC(i,j) = 0.0d0
          end if
        end do
      end if
    end do
```

```
33 format (e15.6,1x,e15.6,1x,e15.6,1x,e15.6,1x,e15.6,1x,e15.6)
    do i = 1, 6
      write(47,33) (Mc(i,j), j = 1, 6)
    end do
    write(47,*)

! --- routine for the direct solution of a linear system
!    |A|x = B --> |LU|x = B --> |L|y = B, |U|x = y

     call cholesky (MC,L)
! --- solution of the first |L|y = B

     y(1) = s(1)/L(1,1)

     do i = 2, 6
       calc = 0.0d0
       do j = 1, i-1
         calc = calc + L(i,j)*y(j)
       end do
       y(i) = (s(i)- calc)/L(i,i)
     end do

! --- solution of the second |Lt|x = y

     e(6) = y(6)/L(6,6)

     do i = 5, 1, -1
       calc = 0.0d0
       do j = 6, i+1, -1
         calc = calc + L(j,i)*e(j)
       end do
       e(i) = (y(i)- calc)/L(i,i)
     end do

      return
end

subroutine Cholesky (A,L)

     use SUBS

     integer i,j,k
     real*8 A,L, sum
     dimension a(6,6), L(6,6)

     L = 0.0d0

     L(1,1) = dsqrt(A(1,1))
     do i = 2,6
       do j = 1, i
         sum = 0.0d0
```

```
        if (i/= j) then
          do k = 1, j-1
            sum = sum + L(i,k)*L(j,k)
          end do
          L(i,j) = (A(i,j)-sum)/L(j,j)
        else
          do k = 1, i-1
            sum = sum + L(i,k)**2.0d0
          end do
          L(i,i) = dsqrt(A(i,i)-sum)
        end if
      end do
    end do

    if (counter == 1) then
      do i = 1, 6
        write(42,33) (L(i,ii), ii = 1, 6)
      end do
    end if
    return
 end

subroutine pre (A,se,ep,cond)
    use SUBS

    implicit none
    integer i, j
    real*8 A, cond,se,ep
    dimension A(6,6), cond(6),se(6),ep(6)

    do i = 1, 6
      if (cond(i) == 0) then
        do j = 1, 6
          if (cond(j) == 1) then
            se(i) = se(i) - A(i,j)*ep(j)
          end if
        end do
      else
        se(i) = ep(i)
      end if
    end do

    return
 end

subroutine post (A,se,e,cond)
    use SUBS
    implicit none
    integer i, j
    real*8 A, cond,se,e
    dimension A(6,6), cond(6),se(6),e(6)
```

```
    do i = 1, 6
      if (cond(i) == 1) then
      se(i) = 0.0d0
        do j = 1, 6
          se(i) = se(i) + A(i,j)*e(j)
        end do
      end if
    end do

    return
end
```

Box 6 – solver routine for the three dimensional single Gauss point code.

In order to give mixed stress strain rates input a vector called *cond* has been set up such as its components can assume unitary or null value. If *cond(i)* is equal to one the input condition is registered as a strain rate otherwise as a stress rate. This vector is passed through the solver from the MAIN because it is essential for the elimination of the rows and columns correspondent to a known strain rate.

The three dimensional code has been divided for convenience in two different programs: one for the implementation of the return mapping and one for the simple and extended subloading model maintaining the same solver structure.

4.2.1. Return mapping implementation

The three dimensional structure is similar to the one saw in Box 4, when the elastic trial is performed in the MAIN of the program and then the stress is passed in the subroutine, with the exception that now the normal-yield and the subloading surface have a different definition leading to a more complex computation for the normal vector in the associate flow rule (3.75).

The analytical formulation of the normal vector and of the other terms used in the numerical code will not be given, however for a complete list of all the variables is possible to consult the reference number [3].

In the following pages only two subroutines will be reported. The MAIN routine will be omitted, because its role is limited to few functions such as the reading of the input data and to perform the elastic trial.

```
subroutine retMap(stressTp,kk,cond,maxsteps,epsilE)

    use SUBS


    if (kk == 0) then
      stressTpS  = 0.0d0
      stressTpSd = 0.0d0
      plasticC   = 0.0d0
    end if
! --- set to zero value some variable
```

```
      counter  = 0
      dpl = 0.0d0
      ctr = 0
      dLambda = 0.0d0
      control1 = 0

! --- store previous normal vector

      call DRV
      call idrodev(stressTp)
      fun = Pmed*(1.0d0 + exe**2.0d0)
      controlto = fun - RM1*F

! ------------------------------------------------------------------------------
! --- first IF CONDITION, if the new stress is inside the previous
!     subloading surface the compute elastic unloading

     if (fun <= RM1*F) then
! ----------------------------------------------ELASTIC UNLOADING -- START
       epsilRM = epsil
       stressRM = stress
       call pre(D,stressRM,epsilRM,cond)

       call solver (D,stressRM,epsilRM,cond)
       stressRM = stress
       call post(D,stressRM,epsilRM,cond)

        do i = 1, 6
          strainTp(i) = strainTp(i) + epsilRM(i)
        end do
       R   = fun/F
       RM1 = R
! ----------------------------------------------ELASTIC UNLOADING -- END
     else
! ----------------------------------------------RET MAPPING CORE  -- START
! --- The cycle is under a conditioned DO CYCLE (old repeat_until cond)
!    to avoid infinite loop maxsteps parameter must be fixed in the input
!    data file

       do
         counter = counter + 1
! --- definition of the monotonic function U
        if ((R-Re).ge.0.d0) then
          Ufun = pu*(1.0d0/(dtan((pi/2.0d0)*((R-Re)/(1.0d0-Re)))))
        else
          Ufun = 1.0e+12
        end if

! --- definition of the plastic modulus Pm
        dfdh = F/(rho-gmm)
        hplm = - trN
        Nsigma = 0.0d0
```

```
        do i = 1,6
           Nsigma = Nsigma + on(i)*stressTp(i)
        end do
        Pm = (Nsigma)*(dfdh*hplm/F + Ufun/R)

! --- definition of tnNEN
        trNEN = 0.0d0
        do j = 1, 6
          EN(j) = 0.0d0
          do k = 1, 6
            if (k <= 3) then
               EN(j) = EN(j) + D(j,k) * on(k)
            else
               EN(j) = EN(j) + D(j,k) * 2.0d0*on(k)
            end if
          end do
          if (j <= 3) then
             trNEN = trNEN + EN(j) * on(j)
          else
             trNEN = trNEN + EN(j) * 2.0d0*on(j)
          end if
        end do

        PmtrN = Pm + trNEN

! --- definition of dLambda
        dLambda  = (Nsigma/fun)*(fun - R*F)/(Pm + trNEN)
        dpl = dpl + dLambda
        plasticC = plasticC + dLambda

! --- computation of the strain correction
        do i = 1, 6
          dstrain(i) = dLambda*on(i)
        end do

! --- definition of the plastic corrector, update of the
!     total stress
        do i = 1, 6
          dstress(i) = 0.0d0
            do j= 1, 6
              dstress(i) = dstress(i) + D(i,j)*dstrain(j)
            end do
        end do

        stressTp(i) = stressTp(i) - dstress(i)

        call DRV
        call idrodev(stressTp)

!-------------------------------------------------------------------------
! --- definition of the new Ratio and Normal-yield function F
      if (RM1-Re <= 0.0d0) then
```

```
        cosin = 1.0d0
      else
        cosin = dcos((pi/2.0d0)*(Rini - Re)/(1.0d0-Re))
      endif
      espR  = dexp(-(pi/2.0d0)*pu*plasticC/(1.0d0-Re))
      plm = trNEMD/PmtrN
      acca  = acca + dLambda*hplm
      fun   = Pmed*(1.0d0 + exe**2.0d0)

      R = (2.0d0/pi)*(1.0d0-Re)*dacos(cosin*espR) + Re
      F = F0 * dexp(acca/(rho-gmm))
      control = fun - R*F

      if ((counter == maxsteps) .or. (control <= toll)) exit
      end do
      if  (counter == maxsteps) then
          write(*,*) 'warning: no equilibrium has been found'
      end if
!-----------------------------------------UPDATE PARAMETER & PRINT
       do i = 1, 6
            do ii = 1, 6
              EPD(i,ii) = D(i,ii) - EN(i)*EN(ii)/(PmtrN)
            end do
       end do
       do i = 1,6
          stressRMP(i) = stressTp(i) - stressTpS(i)
       end do

       strainRMP = epsil
       store = stressRMP
       call pre(EPD,stressRMP,strainRMP,cond)

       call solver (EPD,stressRMP,strainRMP,cond)
       stressRMP = store
       call post(EPD,stressRMP,strainRMP,cond)

       do i = 1, 6
           strainTp(i)  = strainTp(i) + strainRMP(i)
           stressTpS(i) = stressTp(i)
       end do
       call DRV

! --- updating the RM1 step for the next iteration
        RM1 = R
!---------------------------------------------------------------------
     end if
     return
end
```

Box 7 – Three dimensional single Gauss point return mapping subroutine.

Finally the subroutine for the computation of the normal vector is reported in Box 8. It has to be noticed that some secondary subroutines have not been included in the previous boxes for sake of brevity, however the main core for the implementation of the three dimensional return mapping is present in the previous code line.

```
subroutine DRV

      use SUBS

! ----- set all comulative variable to 0
       dfdss = 0.0d0
       trN   = 0.0d0

! ----- Computing the outward normal and its norm
!  -->  dfds  =   df/dsigma
!  -->  dfdsm = ||df/dsigma||
!  -->  on    =   dfds/dfdsm

      do i = 1, 6
        if (i <= 3) then
          dfds(i) = -(1.0d0 - exe**2.0d0)/3.0d0 + 2.0d0*exe*sdsdm(i)/cm
        else
          dfds(i)= 2.0d0*exe*sdsdm(I)/cm
        end if
      end do

      do i = 1, 6
        if (i <= 3) then
           dfdss = dfdss + dfds(i)**2.0d0
        else
           dfdss = dfdss + 2.0d0*dfds(i)**2.0d0
        end if
      end do

      if (dfdss == 0.d0) then
         dfdsm = 0.D0
      else
         dfdsm = DSQRT(dfdss)
      end if

      do i = 1, 6
          if (i <= 3) then
             on(i) = dfds(i)/dfdsm
          else
             on(i) = dfds(i)/dfdsm
        end if
      end do

      do i = 1,3
        trn = trn + on(i)
      end do
```

```
    return
end
```

Box 8 – Computation of the normal unitary vector to the yield surface.

Observing the derivative of the normal-yield respect to the stress tensor it can be noticed that the shape of the surface is not the one traced in Figure 18 but in this case its cross section in the stress space is circular. This simplification can be easily improved to a more realistic one just modifying few line in the Box 8.

A control parameter (i.e. *maxsteps)*, for the max number of iterations necessary to get convergence, has been introduce in Box 7 in order to prevent infinite loops. In fact the if condition "if ((counter == maxsteps) .or. (control <= toll)) exit" is satisfied whenever one of the two conditions is true but, if the second one is verified the correct convergence point is found in the other case a warning pointing out that no equilibrium has been reached in the *k-substeps* must appear.

The first variable computed is the normal vector to the surface passing to the trial state along which plastic relaxation is performed. The definition of the *U* function is similar to the one in the uniaxial case whereas for plastic modulus it is necessary to compute the trace between the normal vector and the stress tensor: $tr(\mathbf{N}\boldsymbol{\sigma})$. The plastic relaxation is realized by multiplying the proportionality factor for the normal vector **N** and subtract this contribute from the total stress state.

Once updated the internal hardening/softening variable *H* the plastic surface is evaluated and subsequently the similarity ratio too. If the distance, between the new stress and the yield surface just introduced, is minor than a tolerance defined by the user, the program exits from the internal DO cycle and convergence is satisfied. The similarity ratio value is stored in the *RM1* variable to perform the check, expressed in eq.(3.87), for the next *n+1* step.

4.2.2. The simple and extended subloading surface

The simple and extended subloading surface codes have being realized using the constitutive equations proposed in paragraphs 3.2.1 and 3.2.5.1. Furthermore a procedure for taking into account the shift of the yield-surface and the anisotropy induced by rotational hardening has been added.

As seen before, in paragraph 4.1.2, also here only few subroutines will be reported, leaving some comments for the numerical analyses chapter.

```
subroutine SSrotational(strainTp,stressTp,EPD,i,cond,beta,zeta,pe,chi)

! ------------------------------------------------------------------
! this routine perform the setting up of the elasto plastic matrix for
! textile yield stress and rotational hardening

    use SSextended
    use SUBS
    parameter (pi = 3.1415926535897932)
! ------------------------------------------------------------------
```

```
!    setting variable to 0
     EPD = 0.0D0
     call AverDev(stressTp,Pmed,sd)
     call Norm(sd,sdm)

! ---------------------------------------------------------------------
!    computation of the cos(3*Lode) and function M (note that M and M-hat
!    are the same function)

     do j = 1,6
       sigmaDH(j) = sd(j) - Pmed*beta(j)
     end do
     call Norm(sigmaDH,sigmaDHNorm)

! --- case if the initial tensional state is on the idrostatic axis
     if (sigmaDHNorm == 0.0d0) then
        TauH = 0.0d0
     else
        do j = 1,6
          tauH(j) = sigmaDH(j)/sigmaDHNorm
        end do
     end if
     trTauH = 0.0d0

     call prod(tauH,tauH,tauH2)
     call prod(tauH2,tauH,tauH3)

     do j = 1,3
       trTauH = trTauH + tauH3(j)
     end do

     cosLode = dsqrt(6.0d0)*trTauH
     MH = (14.0d0*dsqrt(6.0d0)*dsin(fic))/((3.0d0-dsin(fic))*(8.0d0+cosLode))
! ---------------------------------------------------------------------
     exeH  = sigmaDHNorm/MH
     zetaH = 2.0d0*(1.0d0-zeta)*zeta
     zetaD = (1.0d0-2.0d0*zeta)
     pchi  = dsqrt((Pmed**2.0d0)+(2.0d0*zetaH*exeH**2.0d0))
     write(333,*)pmed,pchi,sdm
! --- defining normal yield and normal yiel ratio in this case
!     the similarity centre is in the origin of the stress spaces

      F = (F0 + pe/(1.0d0-zeta)) * dexp((acca)/(rho-gmm))- pe/(1.0d0-zeta)
      dfdh = 1.0d0/(rho-gmm)*(F + pe/(1.0d0-zeta))

     if (shift == 0) then
! --- case zeta = 0
        fun = Pmed*(1.0d0+(exeH/Pmed)**2.0d0)
! --- case not zeta = 0
     else
         fun = (1.0d0/zetaH)*(pchi-zetaD*Pmed)
     end if
```

```
! --- computation of the similarity ratio R
      R = fun/F

! --- definition of the monotonic function U
      if ((R-Re).ge.0) then
          Ufun = pu*(1.0d0/(dtan((pi/2.0d0)*((R-Re)/(1.0d0-Re)))))
      else
         Ufun = 1.0e+12
      end if

      MrH = (14.0d0*dsqrt(6.0d0)*dsin(fir))/((3.0d0-dsin(fir))*(8.0d0+cosLode))
! --- computation of the outwar normal to the yield surface
      call DXDS(DexDS,MH,TauH,cosLode)
      call DRVrotational(exeH,pchi,zetaD,zetaH,beta,DexDS)
      call AverDev(on,onAv,onDev)
      call Norm(onDev,onDNorm)

! --- internal variable h
       if (cOs == 1) then
! --- 1) clay
         if (-Pmed >= 0.0d0) then
            hplm = -trN - chi*onDNorm*(-Pmed)
         else
            hplm = -trN
         end if
      else
! --- 2) sand
          MdH = (14.0d0*dsqrt(6.0d0)*dsin(fid))/((3.0d0-dsin(fid))*(8.0d0+cosLode))
          hplm = -trN + mud*onDNorm*((sigmaDHNorm-MdH*pmed)/F)
      end if

! --- b tensor
       if (rotH == 1) then
          do j = 1,6
             bi(j) = br*onDNorm*(mrH*tauH(j)-beta(j))
          end do
      end if
! ----------------------------------------------------------plastic modulus start
! computation of the plastic modulus , first call to the routine
! DXDS for computing Dexe-hat/Dsigma-hat

     if (rotH == 1) then
        call DfDbeta(dfdb,exeH,DexDS,Pmed,pchi)
     end if

     trace = 0.0d0
      do j = 1,6
       if (j <=3) then
          trace = trace + dfdb(j)*bi(j)
       else
          trace = trace + 2.0d0*dfdb(j)*bi(j)
```

```
      end if
    end do

    trNS = 0.0d0
    do j = 1,6
      if (j <= 3) then
        trNS = trNS + on(j)*stressTp(j)
      else
        trNS = trNS + 2.0d0*on(j)*stressTp(j)
      end if
    end do

    if (rotH == 1) then
! --- WITH ROTATIONAL HARDENING
       pm = (trNS)*(dfdh/F*hplm - (1.0d0/(R*F))*trace + Ufun/R)
    else
! --- WITHOUT ROTATIONAL HARDENING
       pm = (trNS)*(dfdh/F*hplm + Ufun/R)
    end if

! ----------------------------------------------------------plastic modulus end
    trNEN  = 0.0d0
    do j = 1, 6
      EN(j) = 0.0d0
      do k = 1, 6
        EN(j) = EN(j) + D(j,k) * on(k)
      end do
       trNEN = trNEN + EN(j) * on(j)
    end do

    PmtrN = Pm + trNEN
! ----------------------------------------------------------ELASTO PLASTIC MATRIX
    do j = 1, 6
      do k = 1, 6
        EPD(j,k) = D(j,k) - EN(j)*EN(k)/(PmtrN)
      end do
    end do
! ------------------------------------------------------------------------
    strainP = epsil
    stressP = stress

    call pre(EPD,stressP,strainP,cond)
    call solver (EPD,stressP,strainP,cond)
    stressP = stress
    call post(EPD,stressP,strainP,cond)

   trNEMD = 0.0d0
     do j = 1, 6
        trNEMD = trNEMD + EN(j)*strainP(j)
     end do

 ! --- checking the loading conditions
```

```
      if (trNEMD <= 0.D0) then
        strainSE  = epsil
        stressSE = stress
        call pre(D,stressSE,strainSE,cond)
        call solver (D,stressSE,strainSE,cond)
        stressSE = stress
        call post(D,stressSE,strainSE,cond)

        do j = 1, 6
          strainTp(j) = strainTp(j) + strainSE(j)
          stressTp(j) = stressTp(j) + stressSE(j)
        end do
      else
! ----------------------------------------------------------------
! update parameters beta, H, alpha-dash and compute the new solution
       plm = trNEMD/PmtrN

! --- computing vector Dp, its deviatoric component and norm
        trNS2 = 0.0d0
        do j = 1,6
         if (j <= 3) then
            trNS2 = trNS2 + stressP(j)*on(j)
         else
            trNS2 = trNS2 + 2.0d0*stressP(j)*on(j)
         end if
       end do
       do j = 1,6
         Dp(j) = (trNS2/pm)*on(j)
       end do
       call AverDev(Dp,DpAv,DpDev)
       call Norm(DpDev,DpDNorm)

! ------------------------------------------------------- UPDATE INETRNAL VAR. start

! --- update H parameter, different formulation if 1)clay or 0)sand
       if (cOs == 1) then
! --- 1) clay
          if (-Pmed >= 0.0d0) then
             acca = acca - plm*trN - chi*DpDNorm*(-Pmed)
          else
             acca = acca + plm*hplm
          end if
       else
! --- 2) sand
          acca = acca + plm*hplm + mud*DpDNorm*((sigmaDHNorm-MdH*Pmed)/F)
       end if
! --- update beta tensor
       if (rotH == 1) then
          do j = 1,6
                    beta(j) = beta(j) + br*DpDNorm*(mrH*tauH(j)-beta(j))
          end do
        end if
```

```
        do j = 1, 6
          strainTp(j) = strainTp(j) + strainP(j)
          stressTp(j) = stressTp(j) + stressP(j)
        end do
        call AverDev(strainTp,StrainTpAv,StrainTpDev)
        call Norm(strainTpDev,strainTpDevNorm)
       end if
   return
end
```

Box 9 – Simple subloading surface algorithm for tensile strength and rotational hardening of soil.

```
subroutine ExtendedSS(strainTp,stressTp,EPD,i,cond,beta,esse,zeta,pe,chi)

  use SUBS
  use SSextended

! ---------------------------------------------------------------------
 ! set avriable to zero value when necessary
    trEsDB    = 0.0d0
    trSTDB    = 0.0d0
    trSTDEsD  = 0.0d0
    counter   = 0
    sigma = stressTp
    limit = limit
 ! ---------------------------------------------------------------------
 ! --- defining normal yield and normal yiel ratio
       F = (F0 + pe/(1.0d0-zeta)) * dexp((acca)/(rho-gmm))- pe/(1.0d0-zeta)
      dfdh = 1.0d0/(rho-gmm)*(F + pe/(1.0d0-zeta))
      zetaT = 2.0d0*(1.0d0-zeta)*zeta
      zetaD = (1.0d0-2.0d0*zeta)
      call AverDev(sigma,sigmaAv,sigmaDev)
      call Norm(sigmaDev,sdm)
      Pmed = sigmaAv

 ! ------------------------------------------------------------ R COMPUTATION START
 ! computation of RD (R-dashed) ratio between extended subloading surface
 ! and normal-yield ratio by means of an iterative procedure

    do j = 1,6
       sigmaT(j) = sigma(j) - esse(j)
    end do

 ! --- computiation of average sigma tilde and average esse and their deviatoric
 !    tensor with AverDev routine

    call AverDev(sigmaT,sigmaTAv,sigmaTDev)
    call AverDev(esse,esseAv,esseDev)
    sigmaTAv = - sigmaTAv
    esseAv = - esseAv

 ! --- norma of the deviatoric sigma-tilde and esse tensor using the routine Norm
```

```
    call Norm(sigmaTDev,sigmaTDNorm)
    call Norm(esseDev,esseDNorm)
    call Norm(beta,betaNorm)

! --- computing tr(esseDev-beta)[trEsDB], tr(sigmaTDev-beta),[trSTDB]
!     tr(sigmaTDev-esseDev)[trSTDEsD]; note that the result should be
!     a scalar term and that the tensor are expressed in engineering form

   do j = 1,6
    if (j <= 3) then
       trEsDB   = trEsDB   + esseDev(j)*beta(j)
       trSTDB   = trSTDB   + sigmaTDev(j)*beta(j)
       trSTDEsD = trSTDEsD + sigmaTDev(j)*esseDev(j)
    else
       trEsDB   = trEsDB   + 2.0d0*esseDev(j)*beta(j)
       trSTDB   = trSTDB   + 2.0d0*sigmaTDev(j)*beta(j)
       trSTDEsD = trSTDEsD + 2.0d0*sigmaTDev(j)*esseDev(j)
    end if
   end do

! --- ITERATIVE INTERNAL PROCEDURE ---
!     assign value for R-dashed term for the iteration n-1 to perform
!     an iterative loop for convergence

     if (i == 1) then
! --- 1) average M-dashed/arc value for trial
       MDA = 2.0d0*dsqrt(6.0d0)*dsin(fic)/3.0d0
     end if

     do
       counter = counter + 1
       RdM1 = Rd

! --- 2) computation of coefficient A, B, C of formula 11.77 Hashiguchi's
!       Elastoplasticity Theory
       call Coeff(coeffA,coeffB,coeffC,esseAv,esseDnorm,betaNorm,sigmaTAv,&
              sigmaTDNorm,trSTDB,trEsDB,trSTDEsD,zetaT,zetaD)

! --- 3) computation of the R-Dashed ratio with formula 11.77 (see point 2)

       Rd = (dsqrt((coeffB**2.0d0)-(4.0d0*coeffA*coeffC))-coeffB)/(2.0d0*coeffA)
       if (Rd < 0.0d0) then
          Rd = (-dsqrt((coeffB**2.0d0)-(4.0d0*coeffA*coeffC))-coeffB)/(2.0d0*coeffA)
       end if
!
! --- 4) computing Tau-Dashed-Arc [TauDA] from the sigma deviatoric-dashed-arc [sigmaDADev]
       do j = 1,6
         sigmaDADev(j) = sigmaTDev(j)+Rd*esseDev(j)+(sigmaTAv+Rd*esseAv)*beta(j)
       end do
       call Norm(sigmaDADev,sigmaDADevNorm)
       if (sigmaDADevNorm == 0) then
```

```
          tauDA = 0.0d0
        else
          do j = 1,6
            tauDA(j) = sigmaDADev(j)/sigmaDADevNorm
          end do
        end if

! --- 5) new calculation of the M-dashed/arc value (formula 11.79)thanks to the R-dashed
!       ratio just found
        trTDA = 0.0d0
        call prod(tauDA,tauDA,tauDA2)
        call prod(tauDA2,tauDA,TauDA3)

        do j = 1,3
          trTDA = trTDA + tauDA3(j)
        end do

        cosTLa = dsqrt(6.0d0)*trTDA
        write(58,*) cosTLa

        if (i /= 1) then
          MDA = (14.0d0*dsqrt(6.0d0)*dsin(fic))/((3.0d0-dsin(fic))*(8.0d0+cosTLa))
        end if

        controlR = RdM1-Rd
        write(333,*)counter,controlR
! --- 6) exit condition
        if (i == 1) then
        exit
        end if
        if ((abs(RdM1-Rd) <= tollR).or.(counter == maxsteps)) then
        exit
        end if

      end do
! ------------------------------------------------------------- R COMPUTATION END

! --- computing the X-dashed-arc and p-dashed
     exeDA = sigmaDADevNorm/MDA
     pD    = - (sigmaTAv+Rd*esseAv)
     pchi  = dsqrt((pD**2.0d0)+(2.0d0*zetaT*(exeDA**2.0d0)))
! ------------------------------------------------------------- DERIVATION START
! --- computing D X-dashed-arc/ Dsigma-dashed-arc-deviatoric
      call DXDS(DexDS,MDA,TauDA,cosTLa)
! --- computing Df/Dsigma
      call DfDsigma(DexDS,beta,pD,pchi,exeDA,zetaT,zetaD)
! --- computing Df(sigma)/Dbeta
      call DfDbeta(dfdb,exeDA,DexDS,pD,pchi)
! --- computing Df(esse)/Dbeta
      call DfDesse(dfdes,esseAV,esseDev,beta,zetaT,esse,pDs,pchiS,exeAes,dexdes)
! ------------------------------------------------------------- DERIVATION END
```

```
! ------------------------------------------------------------- FUNCTIONS start
      call functions(funS,pD,pchi,exeDA,zetaT,zetaD)
      call functions(funES,pDs,pchiS,exeAes,zetaT,zetaD)
      Rs = funEs/F
      write(66,*) pDS, esseDNorm
      write(67,*) pd,  sigmaDADevNorm
! ------------------------------------------------------------- FUNCRIONS end
!     if (cyclicN == 0) then
        call u(uReloaded,Rs,sigmaTav,sigmaTdev,sigmaTDNorm,dexdes,pDs,pchiS,exeAes,j)
        write(68,*) i, uReloaded
!     else
!       uReloaded = pu
!       write(68,*) i, uReloaded
!     end if

! --- definition of the U function of R-dashed
      if ((Rd-Re).ge.0) then
         Ufun = uReloaded*(1.0d0/(dtan((pi/2.0d0)*((Rd-Re)/(1.0d0-Re)))))
      else
        Ufun = 1.0e+10
      end if

! --- computing the outward normalized normal by means of the Df/Dsigma
!     computed before
      call Norm(dfds,dfdsN)
      do j = 1,6
        if (j <= 3) then
          onD(j) = dfds(j)/dfdsN
        else
          onD(j) = dfds(j)/dfdsN
        end if
      end do

      call AverDev(onD,onDAv,onDDev)

! --- computing Mr parameter
      MAr = (14.0d0*dsqrt(6.0d0)*dsin(fir))/((3.0d0-dsin(fir))&
          *(8.0d0+cosTLa))
      write(53,*) MAr
! --- computing b tensor
      if (rotH == 1) then
        do j = 1,6
          bi(j)= br*(MAr*TauDA(j)-beta(j))
        end do
      end if

! --- computing internal variable h = f(sigma,H,N-dashed)
      trN = 0.0d0
      do j = 1,3
         trN = trN + onD(j)
      end do
! --- internal variable h - DIFFERENTIATION FOR CLAYS OR SANDS
```

```
      call Norm(onDDev,onDDNorm)

    if (cOs == 1)then
! --------CLAY
       if (- pD >= 0.0d0) then
          hplm = -trN - chi*onDDNorm*(-pd)
       else
          hplm = -trN
       end if
    else
! --------SAND
       MdH = (14.0d0*dsqrt(6.0d0)*dsin(fid))/((3.0d0-dsin(fid))*(8.0d0+cosTLa))
       hplm = -trN+mud*onDDNorm*((sigmaDADevNorm-MdH*pD)/F)
    end if
! ------------------------------------------------------------- Plastic Modulus START
    do j = 1,6
      alphaD(j) = (1-Rd)*esse(j)
      sigmaD(j) = sigmaT(j)+Rd*esse(j)
    end do
    call AverDev(alphaD,alphaDAv,alphaDDev)

    call PlasticModulus(Mp,onD,sigmaT,onDDNorm,dfdb,bi,sigmaD,dfdes,esse,sigma)
! ------------------------------------------------------------- Plastic Modulus END
    trNEN  = 0.0d0
    do j = 1, 6
      EN(j) = 0.0d0
      do k = 1, 6
        if (k <= 3) then
          EN(j) = EN(j) + D(j,k) * onD(k)
        else
          EN(j) = EN(j) + D(j,k) * 2.0d0*onD(k)
        end if
      end do
      if (j <= 3) then
        trNEN = trNEN + EN(j) * onD(j)
      else
        trNEN = trNEN + EN(j) * 2.0d0*onD(j)
      end if
    end do

    PmtrN = Mp + trNEN
! ------------------------------------------------------------- ELASTO-PLASTIC MATRIX
    do j = 1, 6
      do k = 1, 6
        EPD(j,k) = D(j,k) - EN(j)*EN(k)/(PmtrN)
      end do
    end do
! ---------------------------------------------------------------------------
   strainP = epsil
   stressP = stress
   call pre(EPD,stressP,strainP,cond)
   call solver (EPD,stressP,strainP,cond)
```

```
      stressP = stress
      call post(EPD,stressP,strainP,cond)
      trNEMD = 0.0d0
      do j = 1, 6
        trNEMD = trNEMD + EN(j)*strainP(j)
      end do
!-----------------------------------------------------------------------
! the solution shoul be correctly updated in dependence on the case
! - if it is loading case then update and computed parameter correlated
!   with plastic deformation
! - in unloading case it must be distinguished if the stress state is
!   less than similarity centre state ----> plastic update
!   on the contrary                    ----> elastic unload
      if (trNEMD >= 0.0d0) then
         plm = trNEMD/PmtrN
         cas = 1
         call  update(esse,beta,onD,stressP,Mp,chi,pD,sigmaDADevNorm,&
                  MdH,TauDA,dfdes,sigmaT,Mar,i)
         do j = 1, 6
            strainTp(j) = strainTp(j) + strainP(j)
            stressTp(j) = stressTp(j) + stressP(j)
         end do
       end if
      if (trNEMD <= 0.0d0) then
         plm = 0.0d0
         cas = 2
         call  update(esse,beta,onD,stressP,Mp,chi,pD,sigmaDADevNorm,&
                  MdH,TauDA,dfdes,sigmaT,Mar,i)
         strainSE  = epsil
         stressSE = stress
         call pre(D,stressSE,strainSE,cond)
         call solver (D,stressSE,strainSE,cond)
         stressSE = stress
         call post(D,stressSE,strainSE,cond)

         do j = 1, 6
           strainTp(j) = strainTp(j) + strainSE(j)
           stressTp(j) = stressTp(j) + stressSE(j)
         end do
      end if

    return
end
```

Box 10 – Extended subloading subroutine.

```
subroutine DfDsigma(DexDS,beta,pD,pchi,exeDA,zetaT,zetaD)

! ------------------------------------------------------------
! routine for computation of Dfunction(f,xi)/Dsigma

    use SSextended
```

```
    use SUBS

    trace = 0.0d0
    call prod(DexDS,beta,DEDSbeta)

    do i = 1,6
      sub(i) = DexDS(i)- DEDSbeta (i)
      if (i <= 3) then
        trace = trace + sub(i)
      end if
     end do

! --- computation of the derivation
      if (pD == 0.0d0) then
        do i = 1,6
          if (i <= 3) then
          dfds(i) = -(1.0d0/3.0d0)
        else
          dfds(i) = 0.0d0
        end if
       end do
    else

      if (shift == 0)then
        do i = 1,6
          if (i <= 3) then
            dfds(i) = -(1.0d0/3.0d0)*(1.0d0-(exeDA/pD)**2.0d0)&
                  +2.0d0*(exeDA/pD)*(DexDS(i)-trace/3.0d0)
          else
            dfds(i) = 2.0d0*(exeDA/pD)*DexDS(i)
          end if
        end do
      else
        do i = 1,6
          if (i <= 3) then
            dfds(i) = -(1.0d0/3.0d0)*(1.0d0/zetaT)*(pD/pchi-zetaD)+&
                   2.0d0*(exeDA/pchi)*(DexDS(i)-trace/3.0d0)
          else
            dfds(i) = 2.0d0*(exeDA/pchi)*DexDS(i)
          end if
         end do
      end if
    end if
    return
end
```

Box 11 – Subroutine for the evaluation of the normalized vector to the normal-yield surface.

The subroutine for the computation of the normalized normal vector to the yield surface contained in Box 11 can be used for the evaluation of the same quantity both for the extended subloading surface routine in Box 10 and for the simple one in Box 9. For the simple algorithm an ‘ad hoc’ routine has

been created but it has to be clear that many of the variables contained in Box 11 just disappear when a fixed similarity centre on the origin of the stress space is considered.

In the previous Boxes some parameter should be commented a part:

- *rotH*: this parameter can assume unitary o null value depending on the user choice. If 1 is set on the input data file then anisotropy is activated and rotational hardening is taken into account together with the isotropic one. The second order tensor $\boldsymbol{\beta}$ affects the rotation of the normal-yield and the subloading surface and enters in the evolution of the similarity centre and plastic modulus equations.

- *Shift*: this variable regulates the shift of the yield surface in the deviatoric-idrostatic plane towards the positive (i.e. tensile strength) stress regime. If zero is set in the input file then the normal-yield surface is tangent the deviatoric axis exactly at the origin, whereas if unitary value is set then the parameters defining the shift are read form the input file according to the formulation exposed in the paragraph 3.3 (eq. (3.133)).

- *cOs*: this parameter, as well the others, can assume just 0 or 1 value. It allows to consider two different classes of soil: clays or sands. The effective behaviour of the specific material is then define by the proper parameters such as density, specific weight, small u, initial normal-yield surface etc. but depending on the value of *cOs* different algorithms are activated for the isotropic hardening/softening variable evolution as shown in paragraph 3.3.1.

4.3. The F.E. code: PLASCON 3D

The F.E. code Plascon3D solves the set of equations presented in the second chapter of this thesis, and in detail the system (2.25). Here is presented the flow chart with all the routines included in the algorithm (i.e. Figure 22) but just the main of them are briefly commented. In detail the new parts, responsible for the non linear computation of the solid skeleton will be described more deeply.

As reminded before the fluid phase will not be interested by any modification of the **H** matrix of the permeability, but indirectly the water in the saturated porous media will experience the influence of the non linear behaviour of the solid phase through the coupling of the equations. As future further development the change of permeability with the deformation should be investigated.

The algorithm in Figure 22 is divided in principal and secondary routines. All starts from the MAIN which handles the calling to the subroutines Gdata and Master:

- *Gdata*: is the routine responsible for the reading of the geometry of the sample. The geometry can be created with an automatic meshing procedure or using an external software as a pre-processor. In general this second solution is preferred because more complicate and big meshes can be created. Another reason for this preference lies in the fact that nodes number re-ordering is possible, generating a more compact skyline in the stiffness matrix speeding up

the computational time. Initial boundary conditions are read in *bound* subroutine and can be modified in the ongoing process by input file.

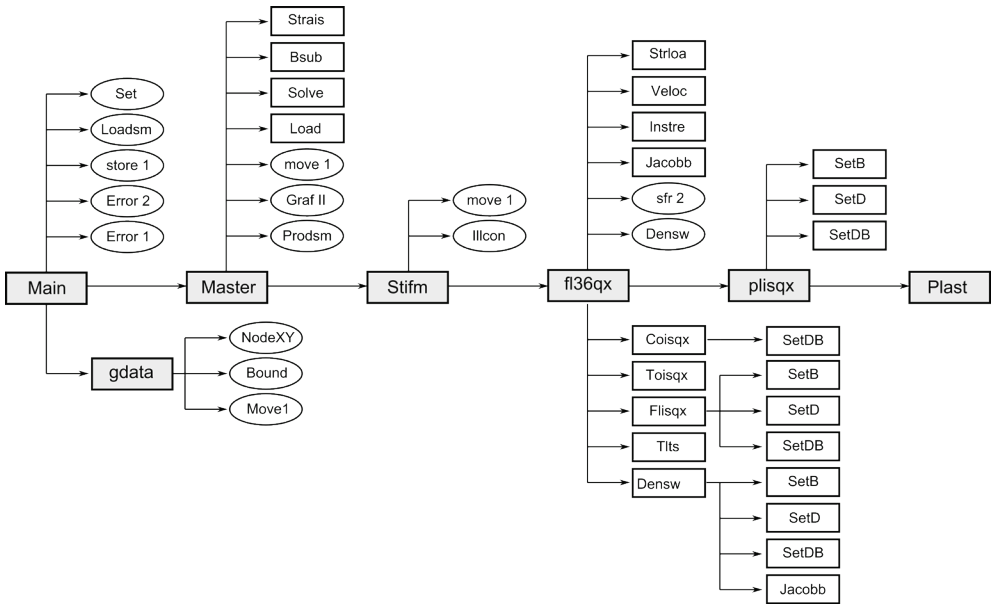

Figure 22 – PLASCON3D flow chart.

- *Master*: this routine executes the call to the derivate subroutines in every time step of the simulation and, after the setting up of all the matrices in (2.22) the system is solved by means of *solve* and *bsub*, which perform the Gauss elimination method explained in the paragraph 4.2 (after the right hand side of the system is formed by *load*). Inside this routine there is also a check to verify if the boundary conditions are changed, in affirmative case *bound* is called again. Routine *strais* is dedicated to the computation of the strain and stress rates. The finite elements method allows to compute the solution in certain points (i.e. the nodes of the mesh) just in terms of displacements and pore pressure so it means that strains and stresses are derived unknowns and must be computed after the system of equation has been solved (i.e. $\boldsymbol{u}$ at the current time step has been found). The problem is that strains and stresses cannot be calculated on the node because of their nature and connection with the main variable $\boldsymbol{u}$ and thus they are found on the Gauss points of each element using the following procedure:

$$\begin{aligned} \boldsymbol{\varepsilon} &= \mathbf{B}\mathbf{u} \\ \boldsymbol{\sigma} &= \mathbf{D}\mathbf{B}\mathbf{u} \end{aligned} \tag{4.7}$$

- *Stifm*: is the routine responsible for the call to the other two routines (i.e. fl36qx and plisqx) where the capacity matrix **H** and the stiffness one **K** are set up. The algorithm at this level is focused on the Gauss points contributes meaning that only local matrices are created, the assembly part for the global equation system is made elsewhere.

- *setD*, *setB*, *setDB* are, in the order, depicted for building the constitutive elastic matrix **D**, the shape function derivative matrix **B** and the **DB** one. The last two are exactly the ones used in the eq. (4.7) for the calculation of stress and strain starting from the displacement in the

subroutine *strais*. It has to be mentioned that routine *setD* is also called for the setting up of the capacity matrix, in this case, instead of the Young and Poisson's modulus, the permeability in the three main directions is passed from the main routine.

- *Jacobb*: this routine is called for each elements and compute, as the name suggest, the Jacobian matrix and its determinant. The Jacobian is inverted for the calculation of the Cartesian derivatives of the shape functions, from their local derivatives, for use them in the above mentioned *setB* routine.

In the flow chart of Figure 22 the last routine *plast* doesn't really exist but it has been introduced only for indicating that in that part of the algorithm the local constitutive matrix **D** should be modified if a nonlinear behaviour for the solid skeleton has to be taken into account.

```
!-----------------------------------------------------SUBLOADING SURF. CALL

      do i = 1, ics1a
        STRESSp(i) = 0.d0
        if (nstep .eq. 1) then
          STRESSp(i) = SINI(mat,i)
        else
          STRESSp(i) = Taux(i,igjg,nel)
        end if
      end do

! --- all for return mapping - start

      if ((nstep .eq. 1).and.(PARAM(MAT,1).ne. 0)) then
          call readSS
          call idrodev(stressp)
          call DRV(igjg,nel)
          fun = Pmed*(1.0d0 + exe**2.0d0)
          R(igjg,nel)   = fun/F0
          RM1(igjg,nel) = R(igjg,nel)
       end if
! --- all for return mapping - end

!     if(R(igjg,nel).gt.0.97) then
       if (PARAM(MAT,1).ne. 0) then
! --------- call to the simple subloading surface
!             call subsurface(A,STRESSp, MTOT, a(n1), A(N50))

! --------- call to the shift simple subloading surface with rot. hardening
              call Ssrotational(A, STRESSp, MTOT, a(n1), A(N50))

! --------- call to the extended subloading surface
!            call ExtendedSS(A,STRESSp, MTOT, a(n1), A(N50))
       end if
!    end if
!-----------------------------------------------------SUBLOADING SURF. CALL
```

Box 12 – Selection of the nonlinear routine.

Different routines can be selected in the call for the nonlinear computation depending on the type of analyses chosen (i.e. simple subloading model, extended one, simple subloading with shift of the yield surface and rotational hardening). The Box 12 show a part of the finite elements code where the choice of the routine for the setting up of the nonlinear local stiffness matrix is made. This difference is simply due to different implementation in time of the algorithm, the first routine realized was the simple subloading model, then the simple subloading with the shift and rotational hardening and finally the extended subloading surface model. For sake of simplicity they have been all maintained and to use one specific of them is sufficient to comment the other two.

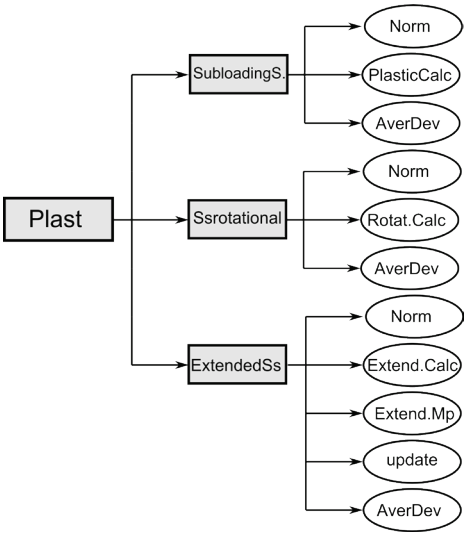

Figure 23 – Flow chart for the elastoplastic routines.

Two routines commonly used in the code are *Norm* and *AverDev* which respectively compute the Euclidean norm of a given vector as follows:

$$\mathbf{a} = \begin{pmatrix} a_1 & a_2 & \cdots & a_n \end{pmatrix}; \quad \|\mathbf{a}\| = \sqrt{\sum_{i=1}^{n} a_i^2} \tag{4.8}$$

and the second one the idrostatic and deviatoric part of the stress tensor as follows:

$$p = \frac{1}{3} tr(\boldsymbol{\sigma}); \quad \boldsymbol{\sigma}' = \begin{bmatrix} \sigma_{11} - p & \sigma_{12} & \sigma_{13} \\ \sigma_{21} & \sigma_{22} - p & \sigma_{23} \\ \sigma_{31} & \sigma_{32} & \sigma_{33} - p \end{bmatrix} = \boldsymbol{\sigma} - \mathbf{I}p \tag{4.9}$$

- *SubloadingS*: is the routine that is responsible for the implementation of the simple subloading surface according to the theory exposed in the paragraph 3.2.1. A secondary call is made to *plasticCalc* for the computation of the outward normalized normal vector to the plastic surface.

- *Ssrotational*: is basically similar to the previous one with the exception that parameter ξ in eq. (3.133) can be different from zero value so the shift of the yield surface in the q-p plane can be taken into account. Subroutine *Rotat.Calc* is called for the creation of the outward normalized normal vector to the plastic surface as seen before. In this routine anisotropy is also

introduced with the modification of the main variables for considering the rotation of the normal yield surface on the q-p plane.

- *ExtendedSs*: it is the routine depicted for the evaluation of the extended subloading surface model. This is the more complex routine and it represents the sum of all the other cases exposed before. In *Extend.Calc* the outward normalized normal vector to the plastic surface is computed according to the formulas reported in Chapter 11.6 of [3]. Due to the complexity of the algorithm and to the increase number of variables it has been preferred to split the computation of the plastic modulus and the update of the conjugate back stress and similarity centre in ad hoc subroutines, respectively *Extend.Mp* and *Update*. The latter is activated only if the term ***tr(NEε)*** in the loading criteria is greater than zero, elsewhere no modification is produced on the similarity centre position according to the theory. It has to be pointed out that in the extended subloading surface is not possible to compute directly the similarity ratio *R* but an iterative procedure solving a second degree order equation is necessary. In this elaborate the mathematical passages will be neglected, for the full dissertation see reference [3].

A different explanation is reserved to the return mapping algorithm. The subloading surface model is provided with the *U* function that automatically brings back the stress to lie on the normal-yield surface if it goes outside, however nothing has been said about the subyield state. In this case no control has been performed so nothing can be said on the accuracy of the results if a large steps analysis has carried out. The formulation proposed by Hashiguchi [3], [4], supplies this lack and defines the algorithm of return mapping that should be used until the stress point is included in the subyield state.

In Box 12 a check on the value assumed by the similarity ratio is performed to verified if the subloading surface has reached the normal-yield one or is still smaller. In the former case no return mapping procedure is necessary and the evolution of the test is guided by the monotonic function *U*, in the latter case the local elastic matrix **D** is not affected and the return mapping procedure is activated.

The elastic trial will be performed elastically, whereas the plastic relaxation takes place only after the stresses and strains are computed by the routine *strais* in *Master*. At this point the stress level found to get the convergence of the local return mapping algorithm is not balanced with the external global forces applied to the sample because the constitutive law (i.e. linear elastic) used to find the solution is no more fulfilled and the equilibrium cannot be guarantee.

To avoid this kind of problems a global iterative procedure should be introduced to have both global and local convergence of the algorithm. As it shown in Figure 24 the first step allows to find a solution in terms of displacements and then computes stresses and strains by means of *strais* subroutine. The elastic trial is subsequently relaxed by using the return mapping algorithm performing *k* local iterations for each Gauss point of every element. As said before in general equilibrium will not be fulfilled, especially if a large steps analysis has been carried out, thus a new routine *Int.forces* constructs the vector of the internal forces through a series of cycles on the Gauss points of the elements (i.e. Figure 25) to make a comparison with the external forces vector applied on the sample. If the difference between the two vectors is greater than a given tolerance the residue will be imposed as the right hand side term of the solving system and operations from the solver will be execute one more time.

It is important to remind that the solution indicated in Figure 24 as $\boldsymbol{\sigma}^1$ is already incremental so the $\Delta\boldsymbol{\sigma}^1$ has a complete different meaning, it is a sort of correction of the first solution found by applying the return mapping procedure. Before performing the check on the internal and external vector forces the correct stress rate has to be update to take into account the correction:

$$\boldsymbol{\sigma}^{2,p} = \boldsymbol{\sigma}^{1,p} + \Delta\boldsymbol{\sigma}^{1,p} \tag{4.10}$$

where the $\boldsymbol{\sigma}^{2,p}$ indicates that the stress state has already been corrected (i.e. second global iteration), whereas the apex *p* means that a plastic relaxation has been performed respect to the point found using the purely elastic matrix.

Once the check condition has been satisfied the stress fulfils the boundary conditions, thus the equilibrium is guarantee and a new time step will be computed.

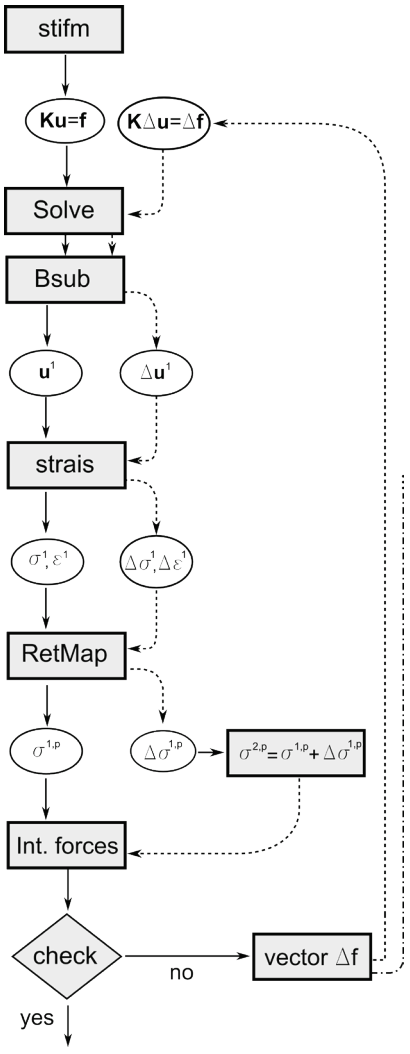

Figure 24 – Global iterative procedure for return mapping algorithm in F.E. method.

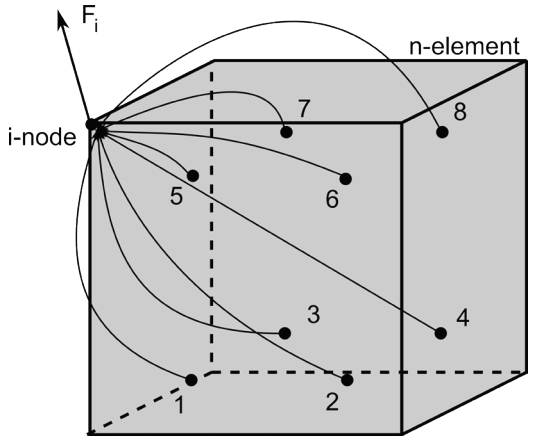

Figure 25 - sketch for the computation of the internal forces.

References

[1] Majorana C.E., (1987) "Two-dimensional non-linear thermo-elastoplastic consolidation program Plascon", In: RW Lewis, BA Schrefler, *The finite element method in the deformation and consolidation of porous media*, Chapter 9. Wiley, Chichester.

[2] Befi M., (1993), "Modelli tridimensionali per l'analisi termomeccanica di geomateriali", *graduation thesis*, Department of Civil, Environmental and Architectural Engineering, University of Padua, pp. 271, (Italian).

[3] Hashiguchi K.,(2009), "Elastoplasticity theory - Lecture notes in applied and computational mechanics". In: F Pfeiffer, P Wriggers (Eds.), Springer, Berlin, **42**, 393 pp.

[4] Hashiguchi K., (2011), "Subloading Surface Model and its Return-mapping Formulation", *Proc. 60th Nat. Cong. Of Theoretical & Applied Mechanics*.

5. The numerical analyses

In this chapter the numerical results obtained by means of uniaxial code, three dimensional single Gauss point problem code and the F.E. PLASCON 3D code are reported for different types of analyses.

At first some graphs for the a subsidence problem at regional scale will be described using the formulation for the cumulative mass balance equation explained in the paragraph 1.4. A preliminary work of calibration and validation will be shown reproducing some cases in literature [1].

The second paragraph of this chapter reports the implementation of the return mapping algorithm. Uniaxial case will be shown using the code in Box 4 and then using a three dimensional single Gauss point program. Particular attention will be focused on the errors committed by the algorithm when soils are considered due to the mathematical formulation of the yield-surface and its normal vector. A preliminary work in the research finite elements code for the return mapping will be reported in the last part of the paragraph.

Another application realized by the modification of few lines of the FORTRAN code is the shift of the yield function for modelling the tensile strenght of some cemented sands. Additionally the stress path on the deviatoric-idrostatic plane (i.e. p-q plane) has been drawn to check the results obtained.

The last part of this chapter is dedicated to the investigation of soil response to cyclic loading and unloading. Many diagrams are reported for simple compression case, the small number of elements involved in the simulations is due to the preliminary level of the study and because the attention is focused on the correct application of the algorithm and evolution of the parameters rather than the prediction of a real case.

5.1. Subsidence at regional scale

The coupled hydro-mechanical state in soils coming from consolidation/subsidence processes and undergoing plasticity phenomena is here evaluated by means of the simple subloading surface model. The 3D model has been first calibrated and validated against examples taken from literature [1], and then subsidence analyses at regional scales due to gas extractions have been developed to predict the evolution of settlements and pore pressure in soils for long-term scenarios.

Surface subsidence due to withdrawal of underground fluids occurs in many parts of the world, see for instance the case book of Poland [2]. Underground fluids involved are either water from superficial aquifers or gas and oil from usually deeper reservoirs. Such surface settlement is a particular threat if it is experienced in low lying areas, close to the sea, e.g. Groningen in the Netherlands (gas), Venice (water) and Ravenna (water and gas) in Italy, Wilmington (oil) in the USA. Surface subsidence of this kind is almost exclusively understood in terms of drop of pressure in the aquifers or in the reservoir: i.e. withdrawal of these underground fluids results in a reduction of their pressure downhole; this in

turn increases the part of the overburden carried by the skeleton of the reservoir rocks causing compaction. The compaction manifests itself, through deformation of the overlying strata, as surface settlement.

In case of a single fluid (water) involved, compaction can easily be explained by the principle of Terzaghi [3] which states that the compression of a porous medium is controlled by changes of effective stresses, i.e. variations of the difference between total stresses and the pressure of the fluid in the pores. However, when more fluids are involved or more phases of the same fluid, the Terzaghi traditional expression of effective stress alone is not sufficient to completely justify measured compaction and the concepts of unsaturated soil mechanics with appropriate stress measures (e.g. Bishop stress [4], generalized Bishop stress [5], [6] or the net stress [7]) and elastoplasticity concepts are needed. Drop of reservoir pressure is not the only mechanism leading to reservoir compaction and suction effects must also be accounted for at least for some types of extracted fluids and some reservoir rocks. This additional mechanism has been suggested for oil reservoirs in the case of the Ekofisk field (chalk) [8 - 11]. For the influence of capillary effects in oil reservoirs, see also [12], [13]. A brief survey of constitutive models for the mechanical behaviour of partially saturated soils is given in [14].

It is then proposed in [15], [16] that capillary effects and structural collapse cannot be ruled out as significant factors in the development of subsidence occurring above gas fields. These phenomena seem to provide sound explanations for continuing surface settlements when reservoir pore pressures stabilise and for additional settlements occurring even after the end of gas production. However, it is to be said that for the investigated area here considered, undergoing subsidence, there is no direct experimental evidence on samples from the field to show the key effect of capillarity on subsidence itself and hence any additional consideration could be largely speculative with many assumptions that are not justified enough.

Again, the discussion about the contribution of capillary effects when performing reservoir compaction and subsidence analyses at regional scale is out of scope for the present work. The idea is to make use of unconventional plasticity by means of the subloading surface model for predicting softening behaviour of soil as well as reducing computational efforts when performing fully coupled hydro-mechanical subsidence analyses in three-dimensional domains [18], as demonstrated below.

It is to be said that, from a computational point of view, strain-softening may be associated to numerical procedures affected by a lack of convergence and the solution may depends strongly on the mesh adopted. Several techniques have been reported in literature, essentially when dealing with shear band formation and strain localization [19], [20], employed to obtain mesh size-independent shear banding (e.g. [21]). Mesh size-dependent hardening modulus procedures have been proposed by Pietruszczak and Mroz [22] and employed by a number of authors (e.g. [23], [24]); enrichments or enhancements of the continuum models can be alternatively found in literature which include the non-local formulation proposed by Eringen [25] and Kroner [26] and developed extensively by Bažant and Cedolin [27]. A complete review of softening plasticity models with internal variables regularized by non-local averaging of integral type can be found in [28], where it is stated that the appropriate choice of the regularization operator and of the internal variables to model a non-local continuum need to be

dealt with a combination of micromechanical analysis and experimental investigations; probably only experimental investigations can provide the validation of one choice or of the other.

However, as evidenced in [29], the accuracy and the convergence property of the subloading surface model (even if there incorporated into a stress-update algorithm for the Cam-Clay one), when e.g. used to reproduce over-consolidated soils experiencing softening, has been demonstrated for a single finite element and a plane mesh of 2460 eight-noded quadratic elements as well; in the latter situation different mesh sizes have not been considered. The robustness of the model has been there proved by increasing the number of loading steps only, even when considering dilation with a decrease in deviatoric stress.

Hence at present, essentially considering the main objectives of this paragraph as outlined before and in line with [29], it seems reasonable to prove the accuracy of the calculations presented here by comparing the numerical solutions for different mesh sizes and time steps as well, referring to the 3D subsidence analysis on regional scale.

All the analyses have been carried out referring to the theory reported in the paragraph 1.3.1, 1.4, 3.2.1 and for sake of brevity all the equations will not be written again in this chapter.

5.1.1. Calibration and validation tests

The numerical model has been first calibrated and subsequently validated against the results obtained by Siriwardane and Desai [1], the first dealing with the consolidation of a column of soil under a uniformly distributed load, the second with the consolidation of a soil strip in plane strain. The former has allowed for defining a value for the plastic variables necessary to the subloading surface model (see below) so to reproduce the same behaviour as the one evidenced in [1] accounting for conventional plasticity.

The reason for referring to the Drucker-Prager model within the validation test, as indicated in the following, is twofold: a) it is proved that the DP model, together with the subloading surface one, is able to reproduce test data for drained and undrained triaxial compression of overconsolidated soils [30]; b) the approach is in line with what presented again in [30], so evidencing here (numerically) a material behaviour already experimentally found there. The main objective here is not to compare the material response by assuming conventional or unconventional plasticity models but, on one side, to numerically confirm the capability of the subloading surface model in predicting softening behaviours and, on the other side, to be able to explain, *via* such a model, ongoing surface subsidence (observed in reality) after shutdown of the wells. In fact, it has already been proved in [16] that conventional plasticity alone is not fully able to reproduce such a phenomenon.

5.1.1.1. The calibration – One dimensional consolidation

The modelled soil column is shown in Figure 26, impermeable and constrained at the bottom and laterally. The load has been applied through two fictitious rigid elements, reproducing the condition of a distributed pressure on the top. In the context of linear elasticity, the one-dimensional consolidation [31] has an exact solution [32] for both pressure and vertical displacements:

$$p(Z,T_V) = \sum_{m=1}^{\infty} \frac{2p_0}{M} \sin(MZ) e^{-M^2 T_V} \tag{4.11}$$

$$u(T_V) = -\frac{\bar{H} p_0}{b} \left[1 - 2 \sum_{m=1}^{\infty} \frac{e^{-M^2 T_V}}{M^2} \right] \tag{4.12}$$

where p_0 is the applied load at t = 0, $\bar{H}$ the length of drainage path for one-way vertical drainage, T_v the non-dimensional time factor

$$T_V = \frac{c_V \cdot t}{\bar{H}^2} \tag{4.13}$$

(c_V being the consolidation factor equal to 0.0514 m^2/day in our case and t the time), Z the non-dimensional longitudinal coordinate [33], b the volume compressibility coefficient, and M is a parameter defined by

$$M = \frac{2m-1}{2}\pi \tag{4.14}$$

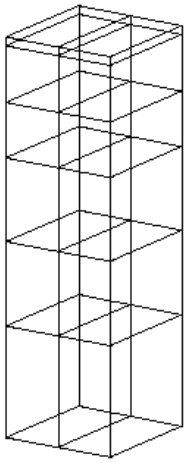

Figure 26 – sketch of the mesh for the one-dimensional consolidation analysis.

Additional numerical results are also available for the same problem [34], [35]. The material data adopted in the elastic and elasto-plastic analyses are shown in Table 3; m_c is the critical state slope on the *q-p* plane, e_0 is the void index and k_i the permeabilities along *i* (x, y, z) direction; isothermal conditions apply.

E [KN/m^2]	287.4
υ	0.4
ρ'	0.14
γ	0.05

m_c	1.05
e_0	0.90
k_i [m/day]	$1.22 \cdot 10^{-6}$
u	15
F_0 [N/m^2]	180

Table 3 – Material data for the one-dimensional consolidation.

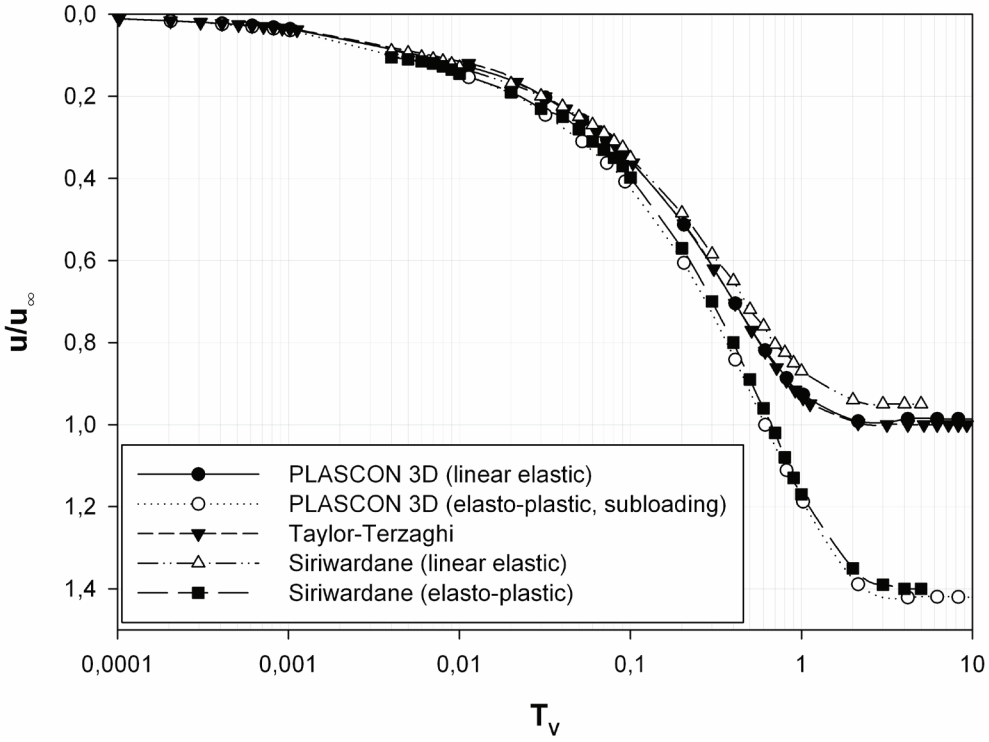

Figure 27 – One dimensional consolidation: surface settlements versus time.

As evidenced by Figure 27, depicting the evolution of surface settlements with respect to u_∞ (the ultimate settlement predicted by Terzaghi's theory) the results show excellent agreement with the analytical solution, as well as with the 2D elastic and elasto-plastic results of Siriwardane and Desai.

The same conclusions apply when considering the pore pressure evolution, non dimensionalized with respect to the initially applied load (Figure 28, referring to a node closed to the column base), and its distribution along the sample's height

(Figure 29; "S" stands for subloading model's results): the inclusion of plastic effects delay the dissipation of pore water pressure and decreases the magnitude of dissipation for almost the whole time span. Hence the predicted values of pore pressure are higher than those of the elastic case, with lower effective stresses and higher deformations (Figure 30) as well.

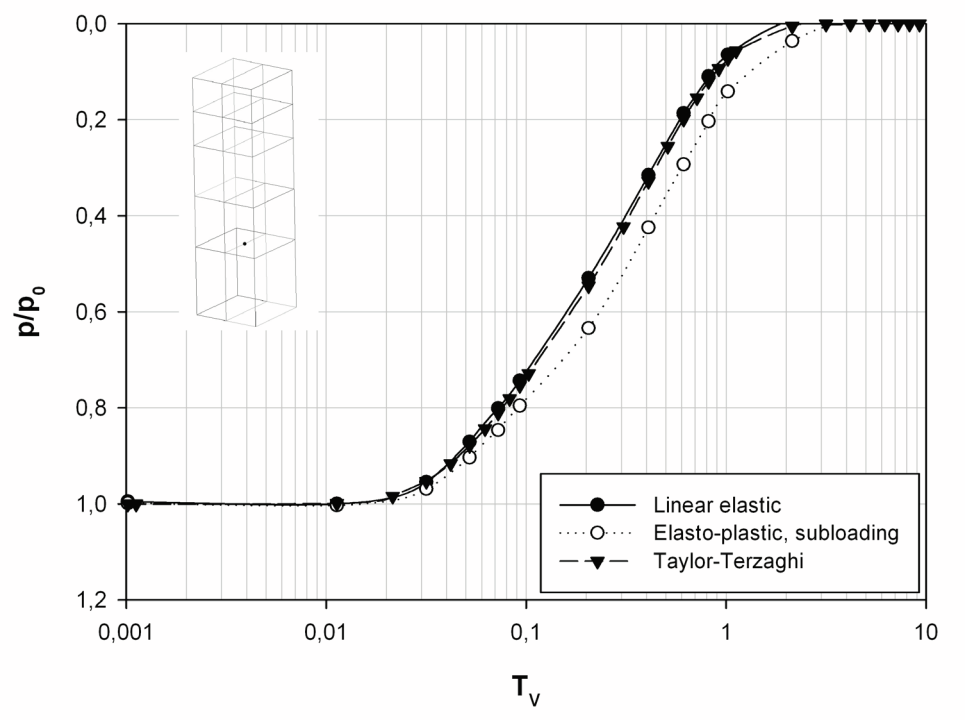

Figure 28 – One dimensional consolidation: pore pressure versus time.

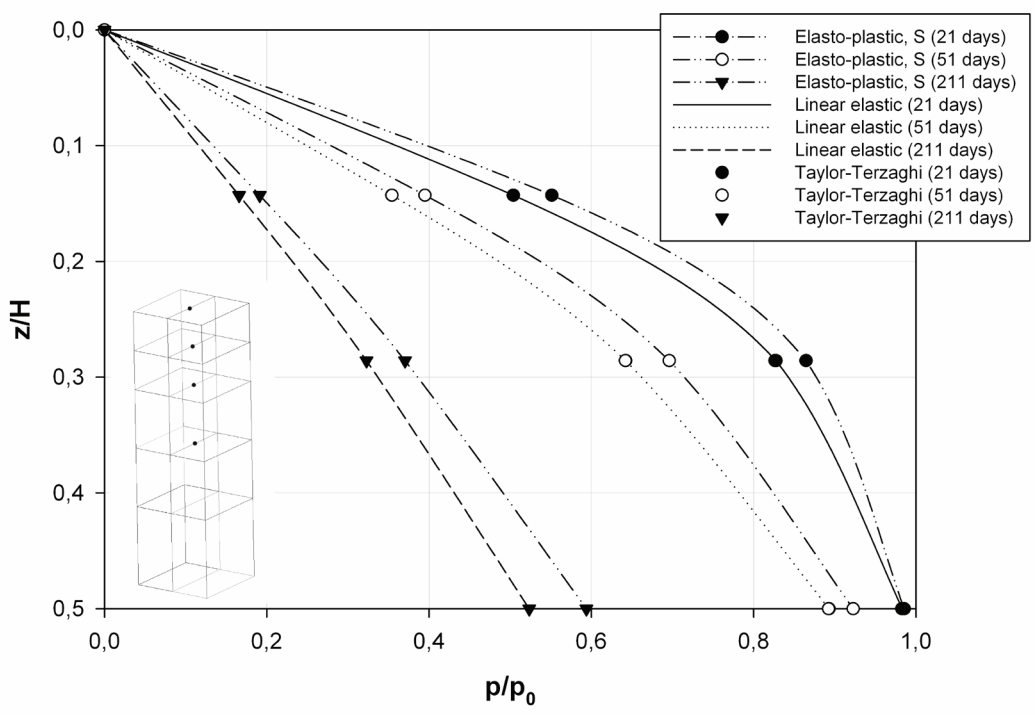

Figure 29 – Pore pressure distribution along vertical axis.

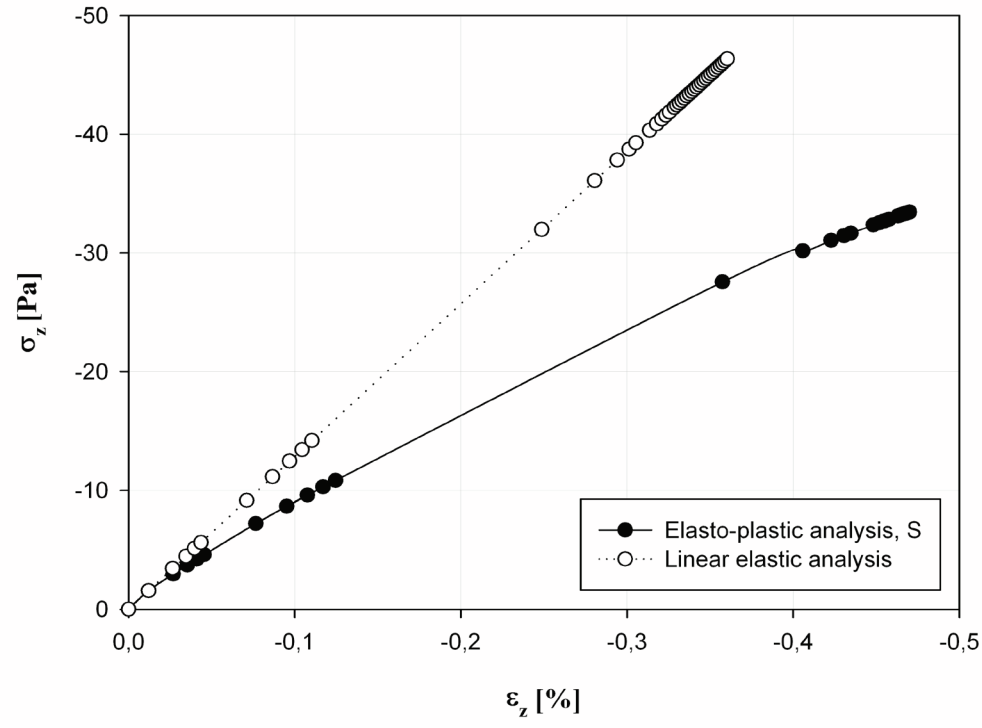

Figure 30 – Stress-strain curves.

5.1.1.2. *The validation* – Consolidation of a soil strip in plane strain state

The model has been validated against the results of the consolidation of a soil strip (6B long and 2B high) in plane strain state [1], Figure 31; the mesh is constrained on all edges except at the top surface (as to simulate plane strain conditions), free flux is allowed on the top and on the bottom, as well as on the vertical border close to the load. The load (applied on a length B) varies in time reaching its maximum value at T_v = 0.07. The material data adopted in the elastic and elasto-plastic analyses are shown in

E [KN/m^2]	622.7
υ	0.4
ρ'	0.14
γ	0.05
m_c	1.05
e_0	0.90
k_i [m/day]	$1.22 \cdot 10^{-5}$
u	15
F_0 [N/m^2]	180

Table 4 – Material data for validation test.

Vertical displacements have been evaluated both for linear elastic and elastoplastic constitutive models, and the results are shown in Figure 32 and Figure 33, respectively. The comparison with Siriwardane and Desai's curves evidences slight differences, essentially due to three-dimensional effects; such discrepancies are anyway reduced if considering the results by Shafiqu [36] and Supangkat [37] (not reported here for sake of brevity).

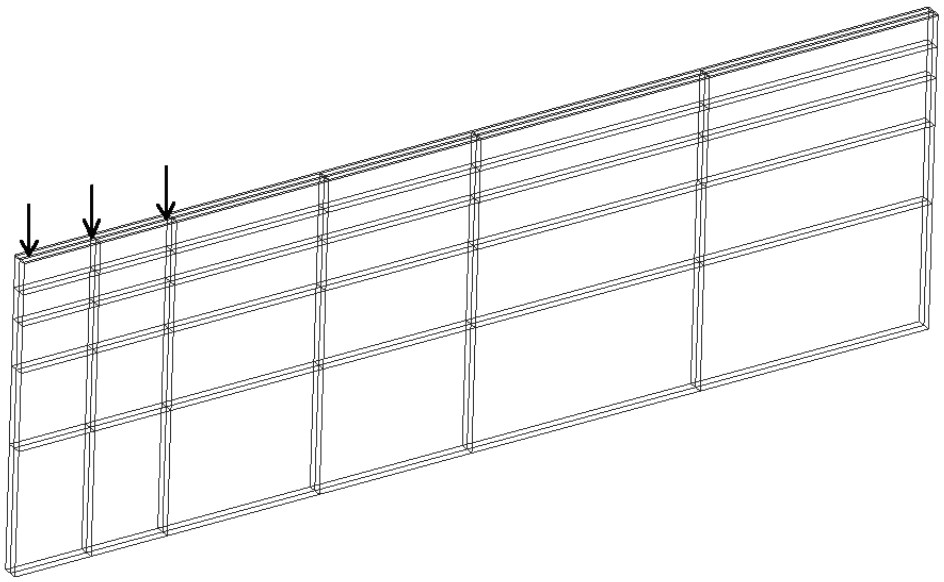

Figure 31 – Sketch of the finite element mesh for the 2D consolidation.

Additionally, the normal yield surface, an initial and the final subloading surfaces have been calculated for a representative point close to the loaded area and they are shown in Figure 35 in the (q, p) plane; the critical state line and the initial yield surface for the Drucker-Prager model are reported as well. By assuming that the DP yield surface passes through the stress at the critical state of the normal yield surface (which is not always the case but it is considered here as an example), it is obtained that the possible failure stresses are higher than 7.4 kPa but lower than 18.8 kPa. The stress path is additionally evidenced: the subloading surface model describes a smooth stress-strain curve (until softening occurs, branch AB); a positive term U/R in the plastic modulus in eq. (3.73) leads to $\bar{M}^p > 0$ even when the stress reaches the critical state line in the subyield state and thus enables the stress to increase over the critical state line. The curve deviatoric stress-volumetric strain then shows an inflection point (A) when the deviatoric stress exhibits the maximum value; a short softening response is shown, until unloading starts (B).

The obtained numerical results confirm (in terms of prediction of soil deformation behaviour) the experimental-analytical ones reported in [30]; additionally, such a capability of describing softening behaviour seems to provide sound explanation for continuing surface settlements when performing subsidence analyses.

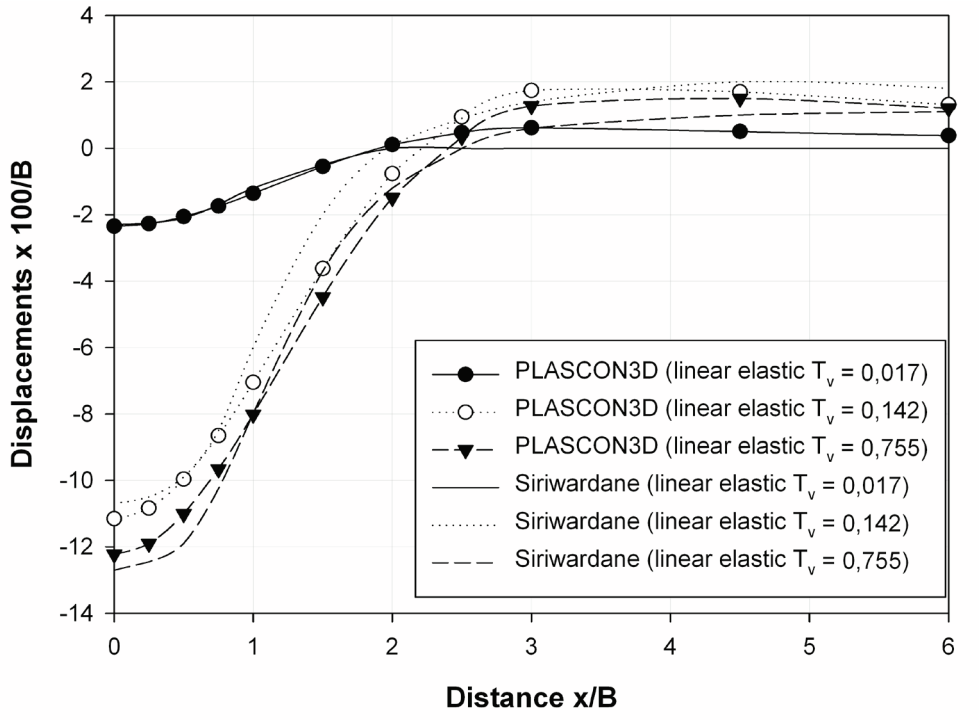

Figure 32 – Two dimensional consolidation: vertical displacements (linear elastic analysis).

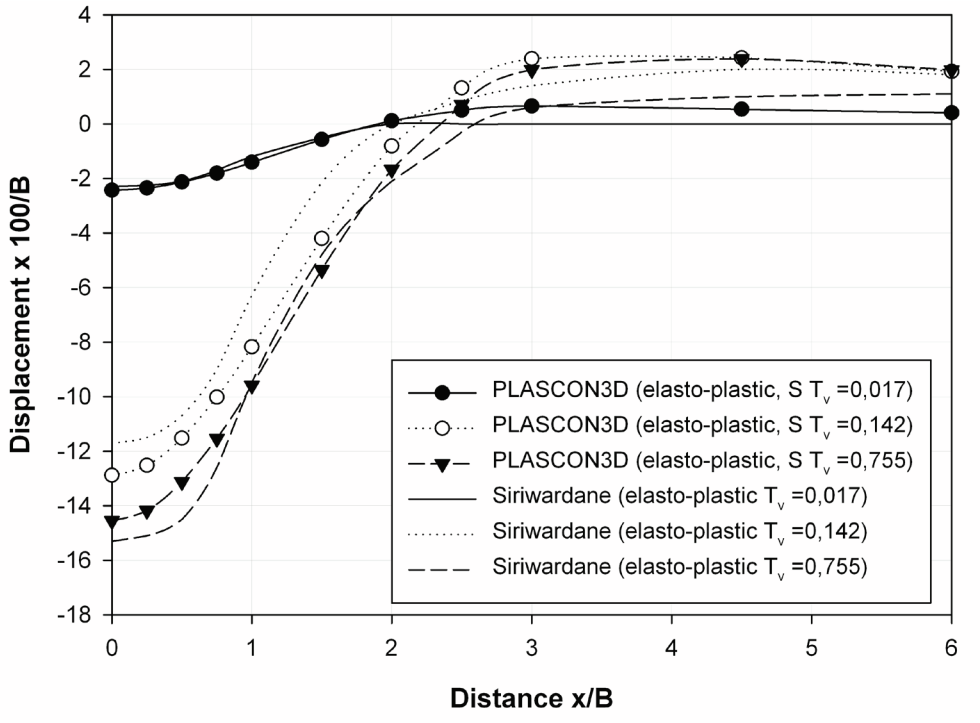

Figure 33 – Two dimensional consolidation: vertical displacements (elasto-plastic analysis).

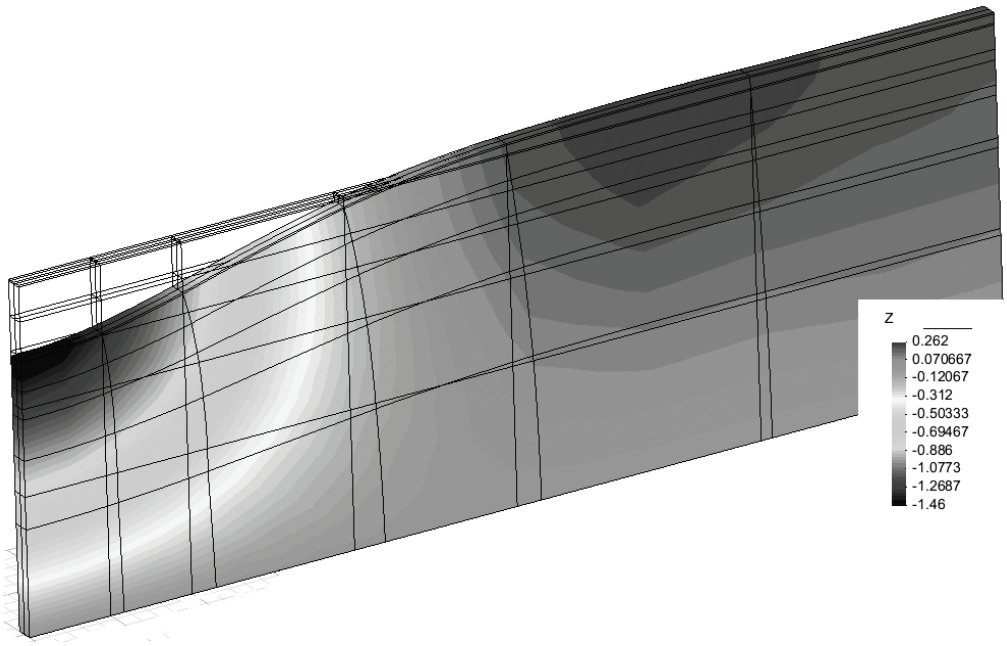

Figure 34 – Two dimensional consolidation: deformed (amplified) mesh at $T_v = 0.755$ (elasto-plastic analysis).

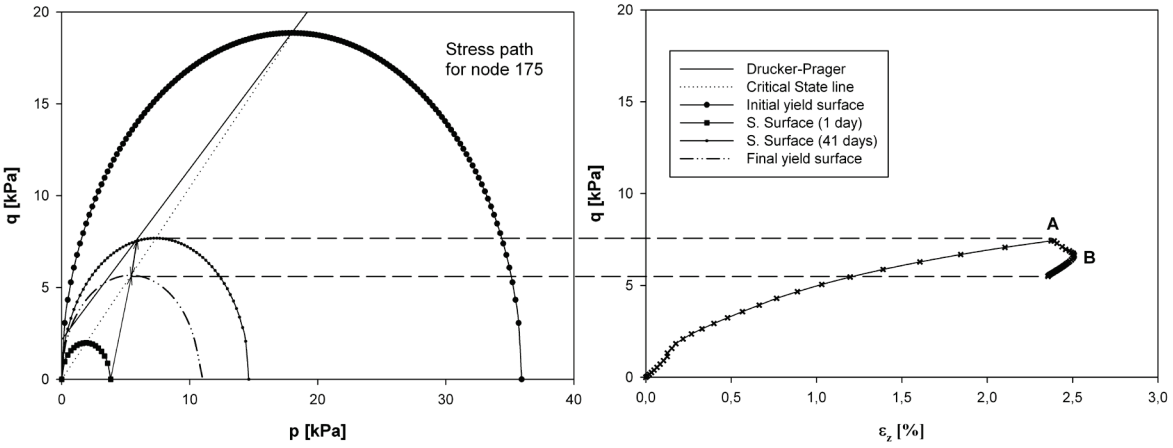

Figure 35 – stress path for the two dimensional consolidation test.

5.1.2. 3D subsidence analyses

Surface subsidence due to extraction of underground fluids (water, hydrocarbons) plays an important role in reservoir engineering. For decades a great deal of attention has been directed towards modelling this phenomenon, also because it affects historical cities, like Venice and Ravenna in Italy ([15-17],[38-43]). Subsidence analyses are computationally intensive by involving problems of regional scale and very long time spans: e.g. in the case of the Groningen gas field, subsidence predictions for the year 2050 have been made from the year 1973 on. The subsidence surfaces have been obtained with different models and codes, e.g. in [44] with ECLIPSE ; in [45] with a quasi three-dimensional

hydrologic model and a three-dimensional uncoupled structural model and in [10], [41] with a fully coupled consolidation model.

Apart from exceptions (as e.g. in [9]), three-dimensional subsidence models have assumed a linear elastic response for the solid skeleton and not much has been done for modelling possible interactions in case several reservoirs at different levels are distributed over a large area, as it is the case of the Northern Adriatic region, Italy [46](Figure 36). Here the pools' depth of burial ranges between 900 and 4000 m and the horizontal area involved is about 19000 Km^2. In addition, the different pools are not scheduled to be put in production at the same time [47], which complicates the situation further.

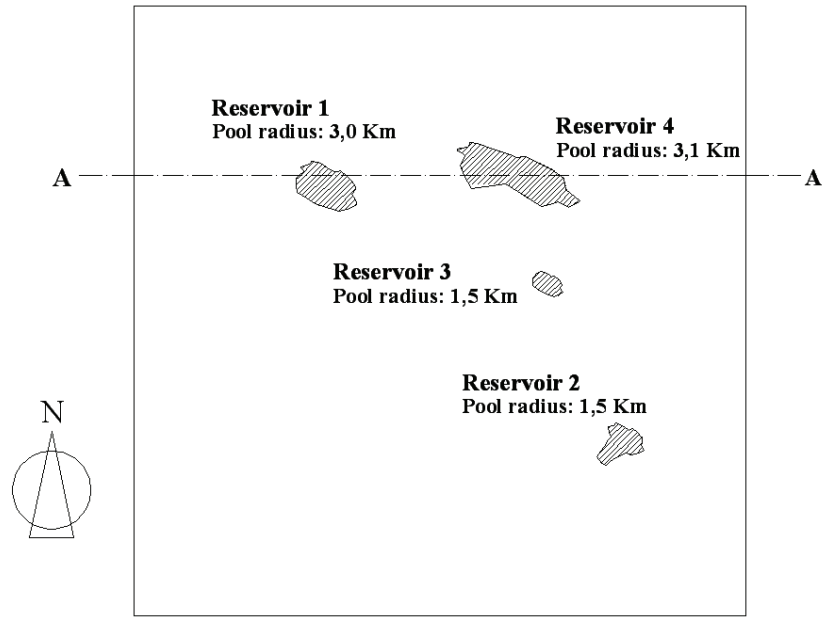

Figure 36 – Schematic representation of the reservoirs.

The Northern Adriatic basin belongs to the easternmost part of the wide sedimentary Po river basin [46]. The subsurface system consists of a sequence of stratified deposits laid down during the Quaternary and the Upper Pliocene in different environments, from continental, lagoonal, and deltaic in the upper zone, to littoral and marine in the lower zone. Some uncertainties exist on the geomechanical parameters characterizing the subsoil behaviour, but our results demonstrate that the chosen order of magnitude for the necessary data gives results in line with those available in literature.

Subsidence due to gas withdrawals can be a matter of great concern if the field is located below or close to low-lying and densely urbanized coastal areas. A ground elevation loss of only a few centimetres in these areas can enhance the ingress of sea water inland and expose the shore to flooding during the tides and severe storm events. Rock compaction in response to gas withdrawal may continue long after the cessation of pumping due to a dynamically active aquifer surrounding the reservoir where pore pressure decline also continues after field production has ceased. Hence, near abandoned gas or oil fields, a "residual" delayed land subsidence may result, an unexpected event that can prove difficult to relate to the original source.

At present, creep, plasticity [46] and capillary effects [15-17] are envisaged among the possible processes yielding a retarded sinking over the reservoir; as already explained before, the choice here is to refer to an unconventional elastoplastic model, also being its potentialities independent on the specific application case treated here.

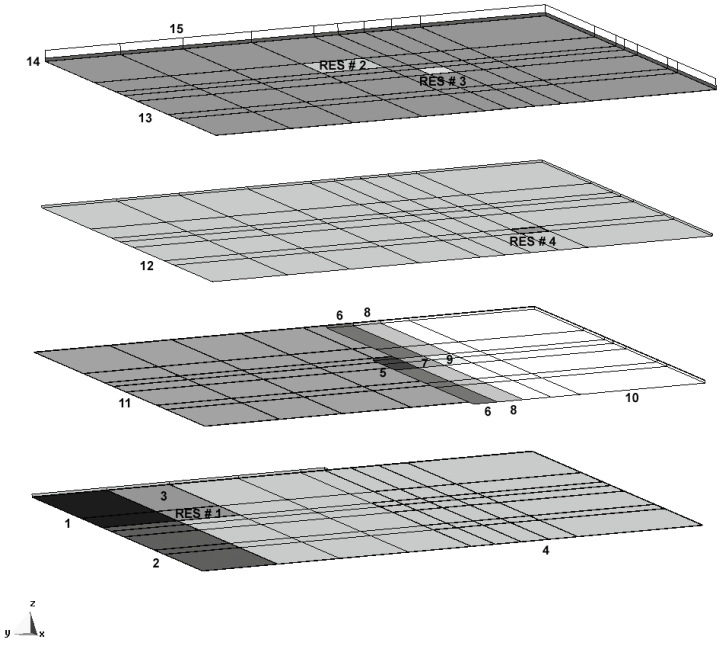

Figure 37 - Schematic representation of the soil strata distribution: macro-levels are superimposed from surface (top) to bottom (see **Table 5**).

The effects of the exploitation of four of the gas reservoirs shown in Figure 36, located at three different depths and undergoing different production histories [47], are here analysed; the region covers an area of 40×40 km^2 and has a depth of 1300 m; it is discretized by about 500 20-node isoparametric elements. Free flux on the horizontal and vertical boundaries of the investigated area is assumed. The main material parameters are shown in Table 5 [39], [47]; the grains are assumed to be incompressible and the clayey layers to behave in agreement with the subloading surface model when accounting for plasticity effects. The geomechanical data have been obtained through analysis of master-logs at our disposal, which are representative of the investigated area, whereas the plastic variables have been taken from the previous examples, appropriately scaled to take into account the effect of depth.

As evidenced by Table 5 and Figure 37, some planimetric variability for the soil strata has been additionally introduced just to be closer to the real configuration of the subsoil, e.g. considering the available seismic section of [47]; so 7 *macro-levels* are present, including 15 different soil strata. The horizontal projection of the investigated pools can be seen in Figure 36, together with the mean radius of their productive levels. The exploitation points (wells) are assumed to be equally distributed above each reservoir such as to allow for the assumption of a constant drop of pressure inside it. The pressure histories (Figure 38), obtained from previous reservoir simulators (starting from available gas production records developing in 10 years) are applied as boundary conditions to the nodes of each

pool. A computationally more expensive alternative would be to apply the outflow given from the production schedule (if available).

Soil stratum #	E [MPa]	υ	k_i [m/day]	Depths [m]
1	$1.13 \cdot 10^4$	0.17	0.2208	1300÷1254
2	$1.00 \cdot 10^4$	0.17	$0.865 \cdot 10^{-4}$	1300÷1254
3 & Reservoir # 1	$1.13 \cdot 10^4$	0.17	0.2208	1300÷1254
4	$1.00 \cdot 10^4$	0.17	$0.865 \cdot 10^{-4}$	1300÷1254 & 1300÷1070
5, 7, 9	$1.14 \cdot 10^4$	0.30	0.7985	1254÷1070
6, 8, 10	$0.322 \cdot 10^4$	0.38	$0.865 \cdot 10^{-4}$	1254÷1070
11 & Reservoir # 4	$1.14 \cdot 10^4$	0.30	0.7985	1070÷1027
12	$0.322 \cdot 10^4$	0.38	$0.865 \cdot 10^{-4}$	1027÷860
13 & Reservoirs # 2, 3	$0.898 \cdot 10^4$	0.15	0.9752	860÷848
14	$0.555 \cdot 10^4$	0.37	$0.865 \cdot 10^{-4}$	848÷600
15	$0.224 \cdot 10^4$	0.39	$0.865 \cdot 10^{-4}$	600÷0

Table 5 – Material data for the subsidence analysis.

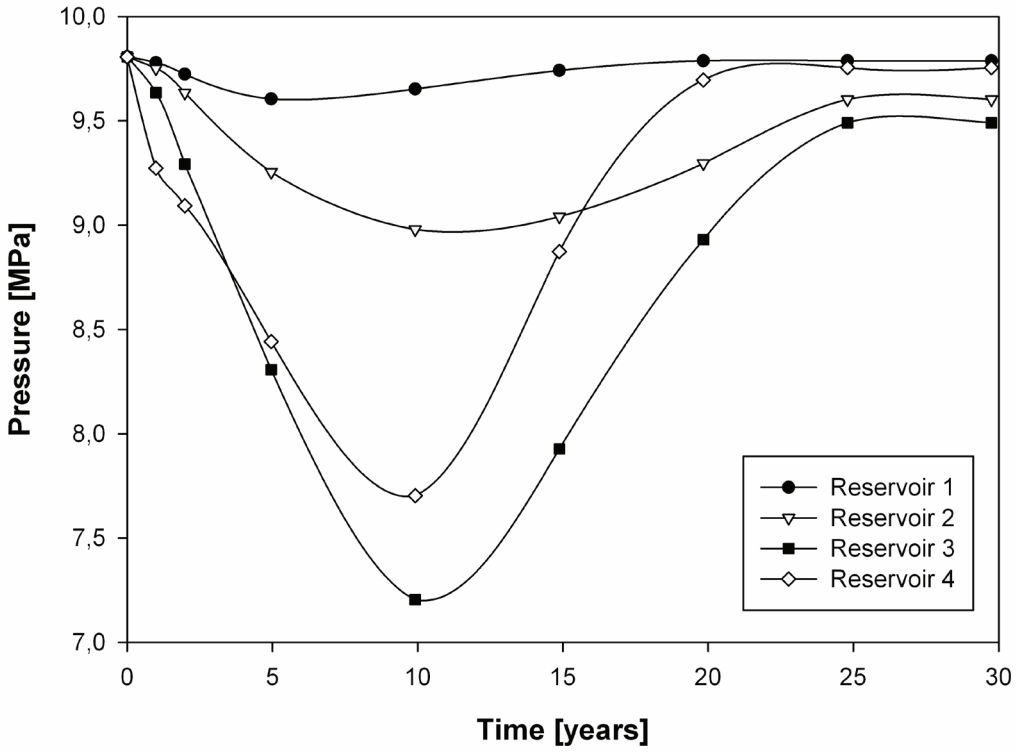

Figure 38 – Reservoirs' pressure histories.

The analysis has been pushed up to 30 years from the beginning of exploitations, when a general pressure recovery has already been attained (Figure 38); the results in terms of surface subsidence above each reservoir are shown in Figure 39, accounting for linear elasticity and unconventional elasto-plasticity as well. The effect of interaction among the different reservoirs can be seen from the shifting in time of the maximum value of subsidence as compared with the minimum of reservoir pressure: this phenomenon is also to be partly ascribed to the presence of clay layers confining the

pools, but it is particularly evident when plasticity is introduced: as an extreme situation, maximum subsidence cannot be reached even after 30 years; a “residual” delayed land subsidence has clearly appeared, so confirming the usefulness of the proposed unconventional plasticity model for modelling continuing surface settlements when reservoir pore pressures stabilize and for additional settlements occurring even after the end of gas production.

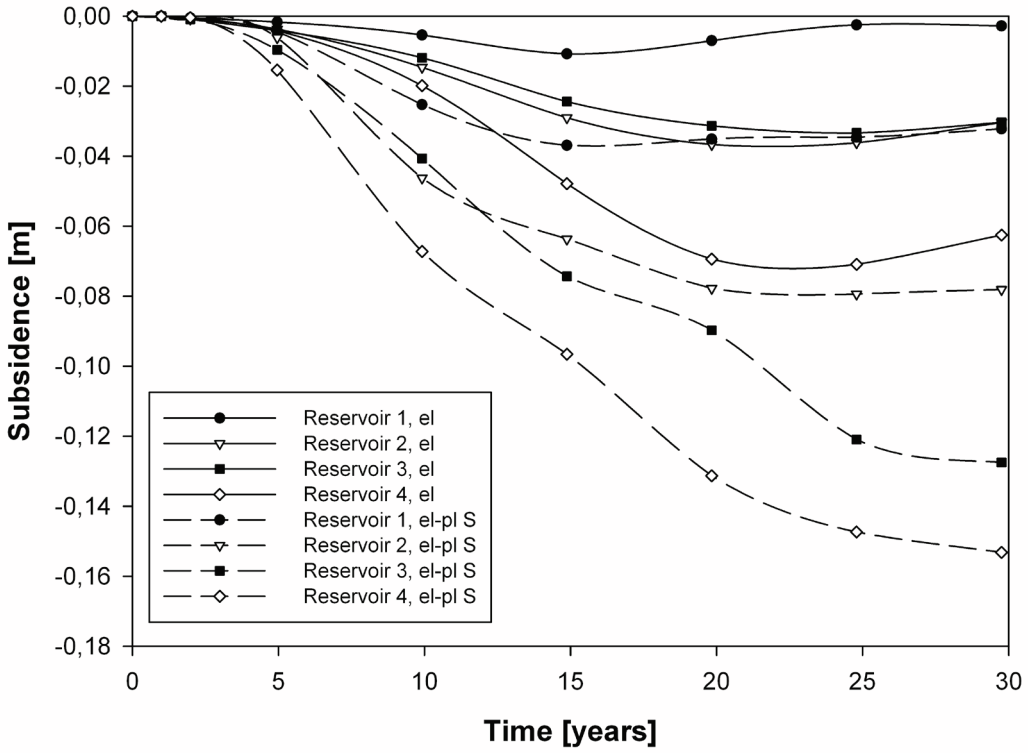

Figure 39 - History of surface subsidence above the reservoirs.

The subsidence bowl is depicted in Figure 40 and Figure 41, referring to the evolution of surface subsidence of Section A-A, Figure 36; apart from repeating the general trend shown in Figure 39, they evidence a subsidence bowl which appears, independently on time, to be slightly wider when elasto-plasticity is accounted for. It is to be underlined that the time scales involved, as well as the orders of magnitude for the resulting subsidence, agree well with what evidenced by [46] and [47] (the latter referring to linear elasticity only), with similar (or equal, as in the latter case) cumulative gas production histories and geological/geomechanical subsoil configurations.

In order to check the robustness of the model, two additional meshes have been considered (see Figure 42 and Figure 43); the results refer to unconventional plasticity analyses only: 4907 nodes and 980 20-node isoparametric elements (M1) and 13978 nodes and 2940 20-node isoparametric elements (M2), with 5 d.o.f. (u_i, i = 1-3, p, T) per node as for the first mesh (M0) of Figure 37.

The results are depicted in Figure 44 in terms of surface subsidence only: mesh independency is evidenced, with a maximum error (taking as reference the values from M2) of about 10%, Figure 45: the error tends to decrease in time, suggesting the ability of the model to perform long-term predictive subsidence analyses.

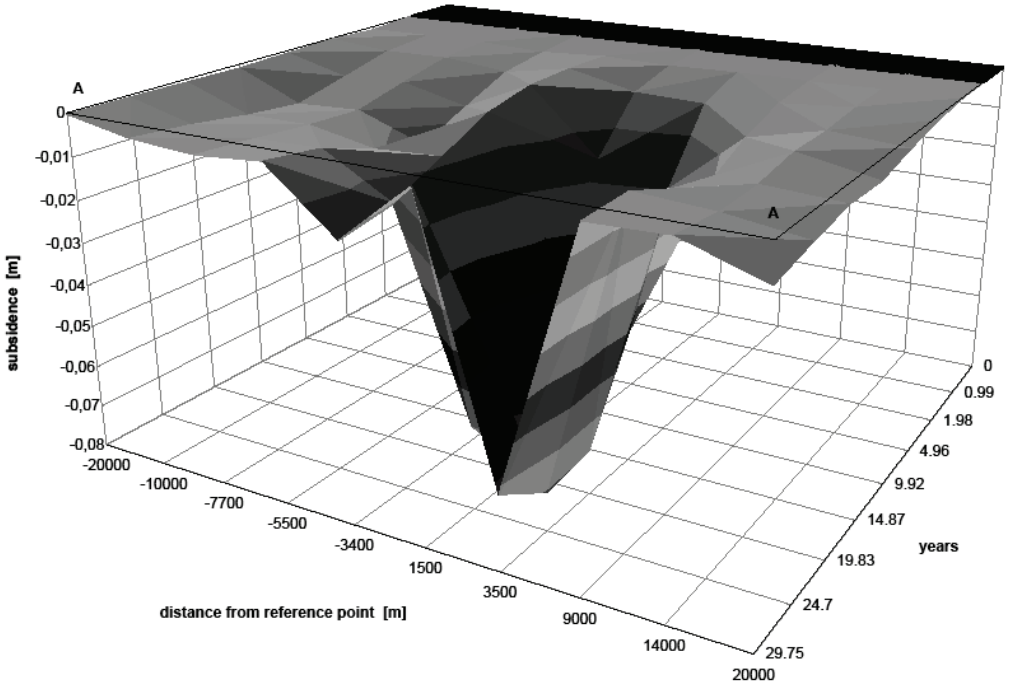

Figure 40 - Subsidence bowl, linear elastic case.

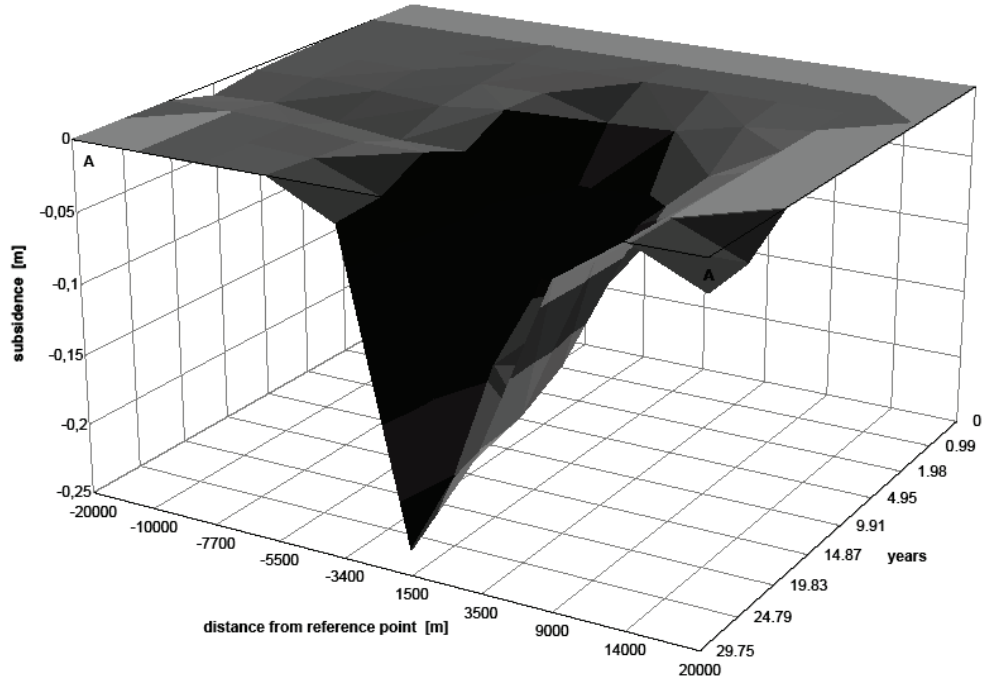

Figure 41 – Subsidence bowl, elasto-plastic case (S).

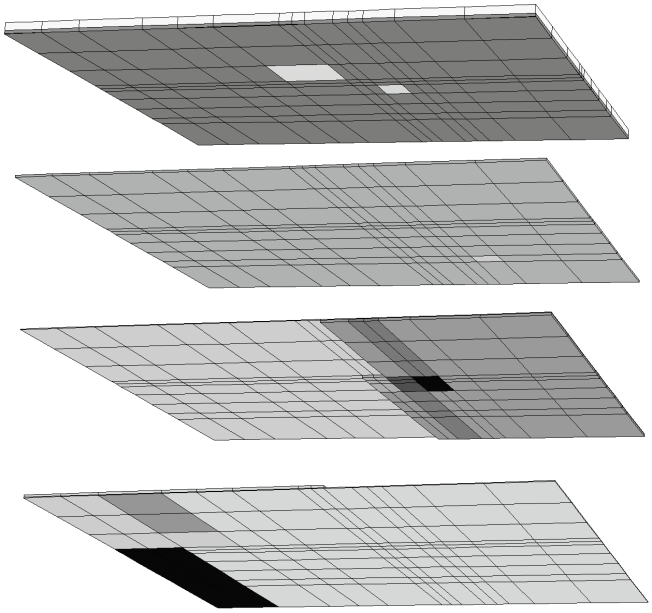

Figure 42- Mesh M1, referring to the same sketch of **Figure 37**.

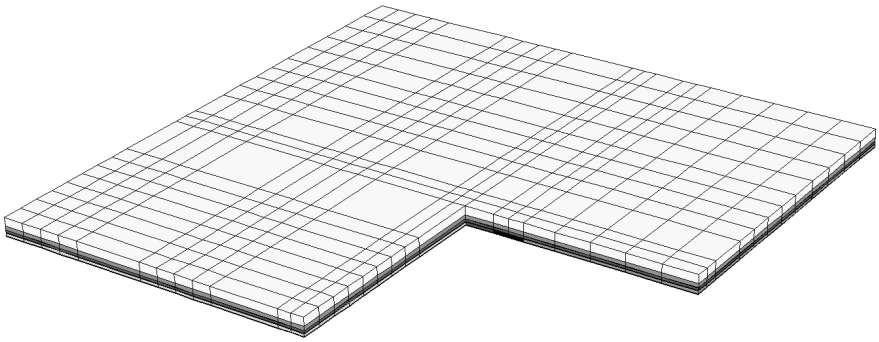

Figure 43 - Mesh M2 (portion).

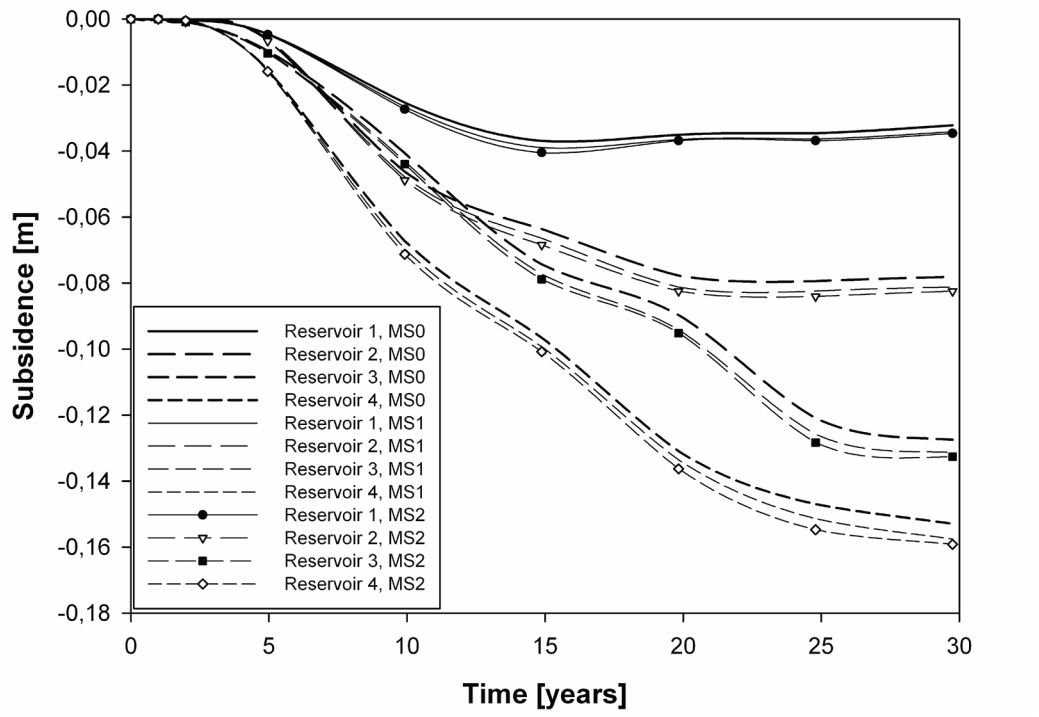

Figure 44 - Surface subsidence above the reservoirs, unconventional elasto-plasticity analyses; mesh sizes M0, M1, M2.

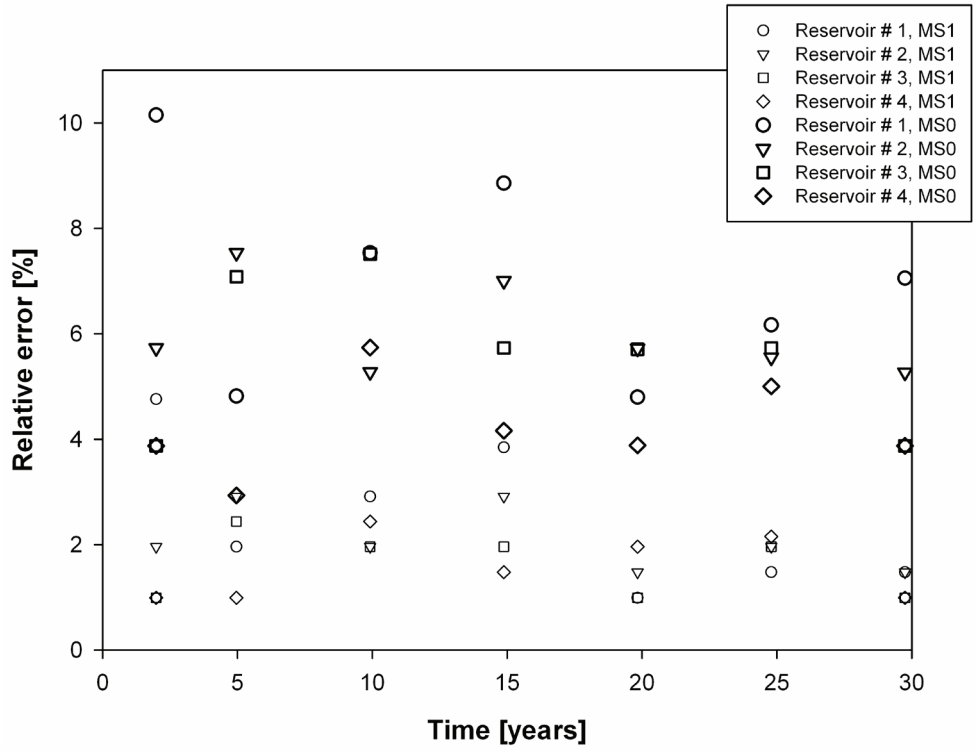

Figure 45 - Percentage error when calculating surface subsidence with mesh sizes M0 and M1.

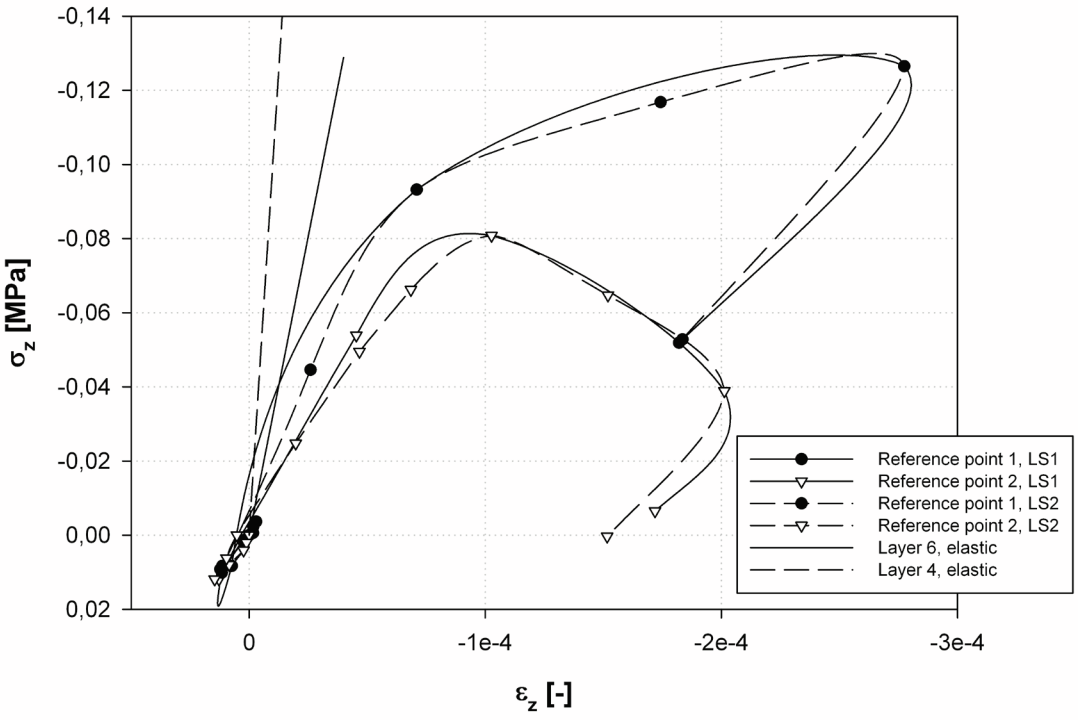

Figure 46 - Stress-strain curves for RP1 and RP2**.**

Further, two reference points (RP1 close to the deepest rigid underburden, belonging to layer 4 -see Table 5-, and RP2, at about 1100 m depth and at the conjunction of layers 6-9 and under layer 12, both in proximity of Reservoir # 1) have been considered for representing stress-strain curves (Figure 46): after a short expansion phase, the soils evidence either hardening or softening, depending on material characteristics and depth; the smoothness and shape of the elasto-plastic curves (subloading model) recalls the one reported in [30]. It is to be noticed that the unloading phases do not occur simultaneously with pressure recovery (of e.g. Reservoir # 1) but they are delayed in time. The mechanisms are strongly differentiated depending on the considered points, but they can give a general estimate of the complexity of the subsoil behaviour and they can provide for a first explanation of observed delayed surface settlements.

5.2. Return mapping implementation

This section deals with the implementation of the *cutting plane return mapping* algorithm [48] for a simple subloading surface model. At first a simple one-dimensional algorithm has been implemented showing how, with a small number of macro iterations, the solution is stable, then analyses for a three dimensional program have been carried out on a single quadrature point (i.e. *Gauss point)*. Here some errors connected with the normal vector to the plastic surface arise showing some difficulties on convergence to the correct solution. Finally an application to F.E. code PLASCON 3D is reported.

5.1.3. One dimensional implementation

The one dimensional case is limited to simple compression of the material considering a monotonic loading (i.e. the update of the return mapping technique in the *extended subloading surface* equations hasn't been implemented yet, so no loading-unloading test has been carried out).

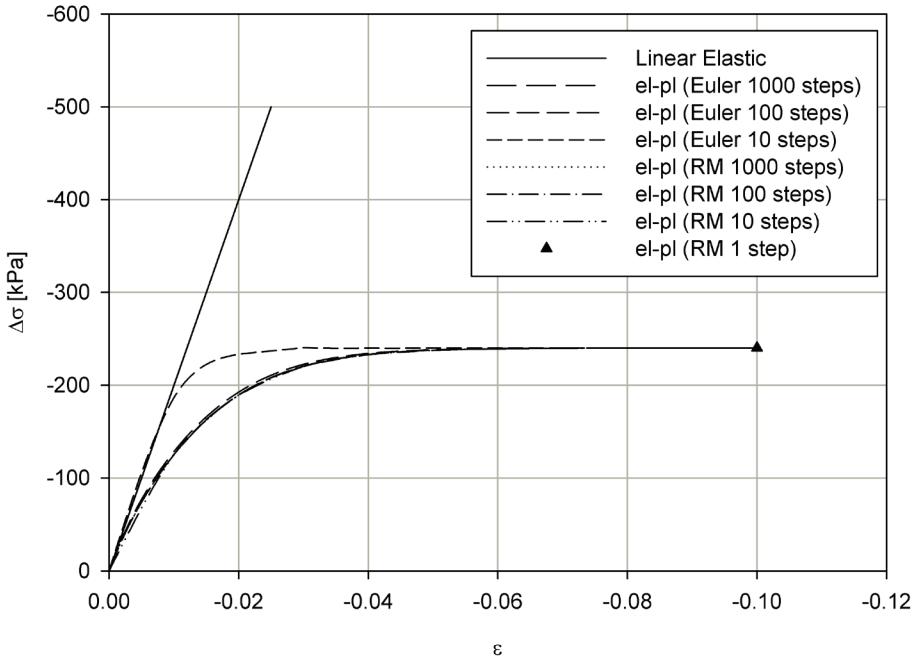

Figure 47 - One dimensional Euler Method Vs. Return Mapping (perfect plasticity).

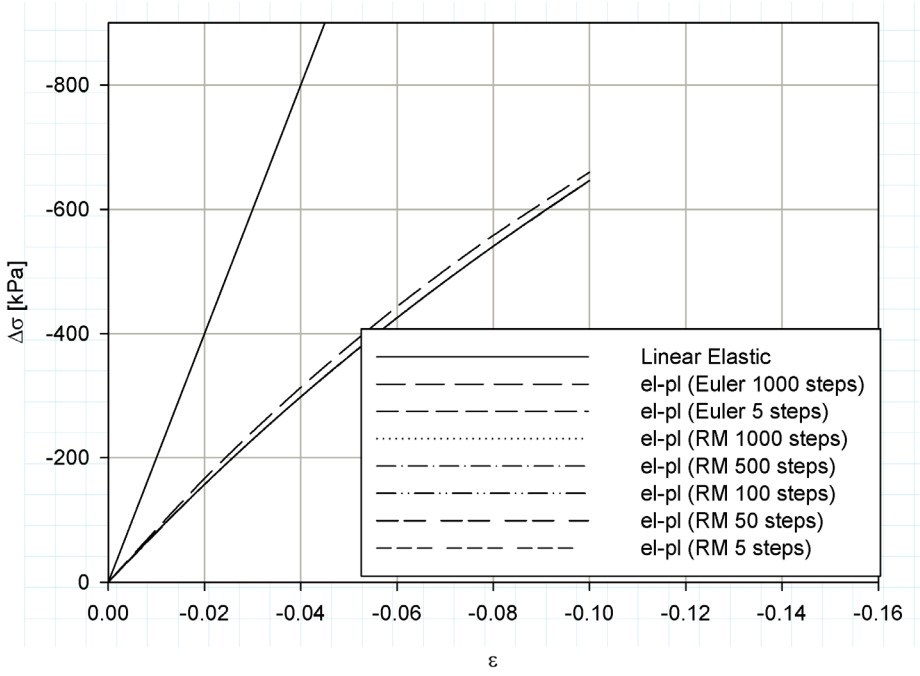

Figure 48 - One dimensional Euler Method Vs. Return Mapping (hardening case).

As it can be seen both for the perfect plasticity and the hardening cases (Figure 47 and Figure 48) the convergence on the correct elastoplastic curve is guarantee for a large steps computation (even for 10 steps or less).

The Euler method starts to commits some errors directly related to the step size: in the perfect plasticity case the inaccuracy of the solution for a number of steps smaller than 100 is quite evident.

For sake of completeness some of the subloading surface parameters have been investigated in the analysis. Figure 49 reports the evolution of the plastic modulus which tends to null value when the stress state reaches the plastic surface in full agreement with the theory. The same behaviour can be obviously observed in Figure 50 for the elastoplastic modulus that has already been defined by eq. (3.22).

On the other hand the evolution of the similarity ratio is described in Figure 51 showing a decreasing tendency of function *U* when the stress approaches to the normal-yield surface. Once *R* = 1 has been reached the material starts to deform under a constant stress level and the subloading surface can be regarded as a conventional plasticity model.

For one macro step a certain number of substeps is necessary for the convergence on the correct point to satisfy the accuracy imposed by the user.

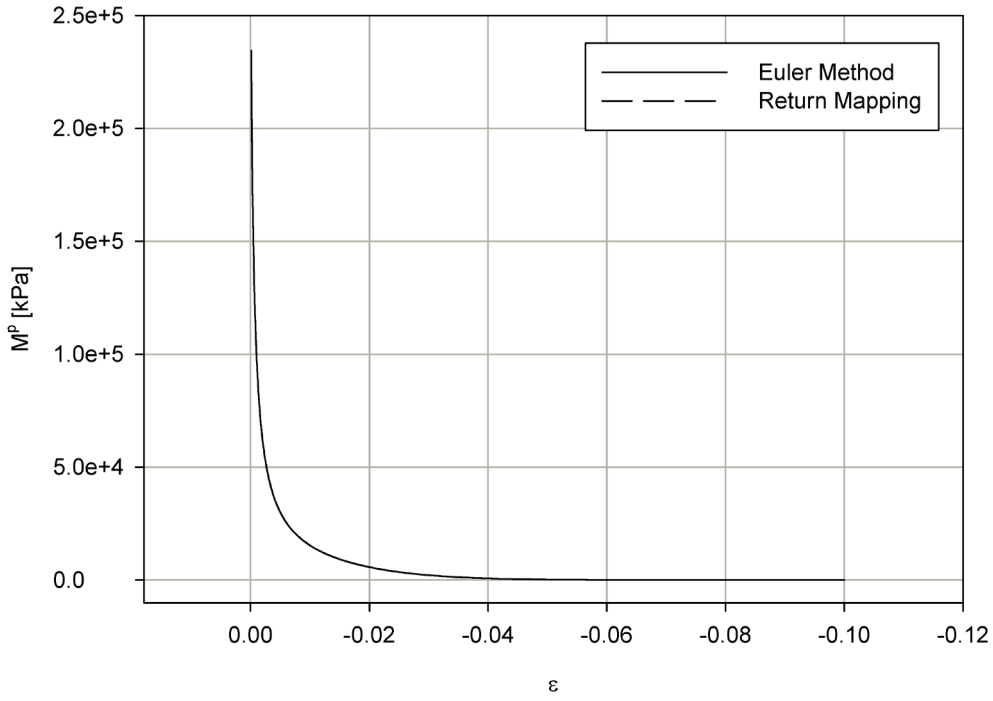

Figure 49 - Plastic Modulus vs. total strain for perfect plasticity and hardening cases.

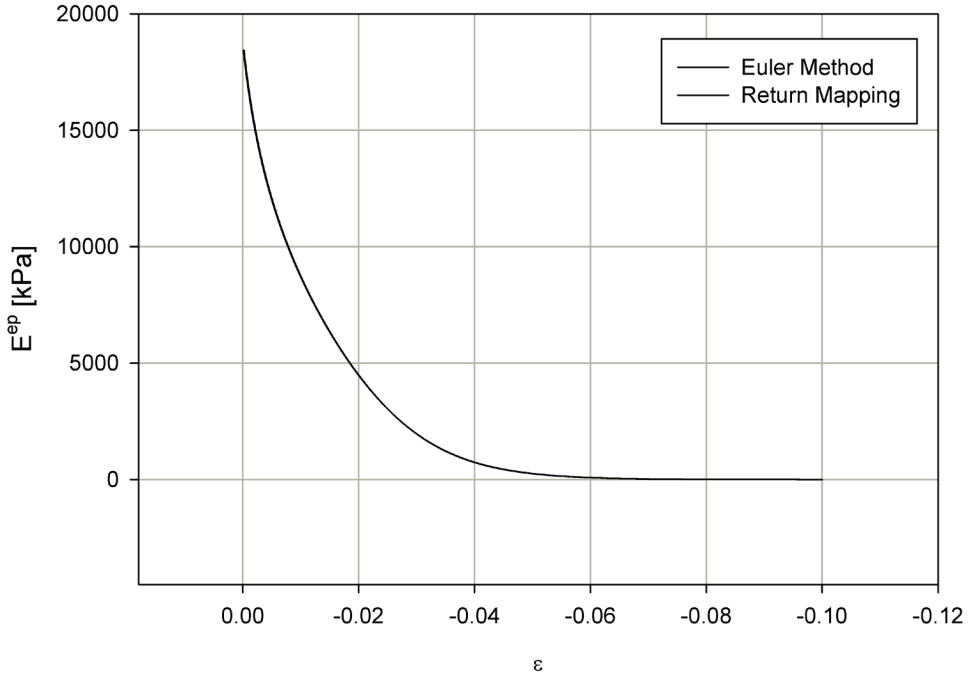

Figure 50 - Elastoplastic Modulus for a perfect plasticity case.

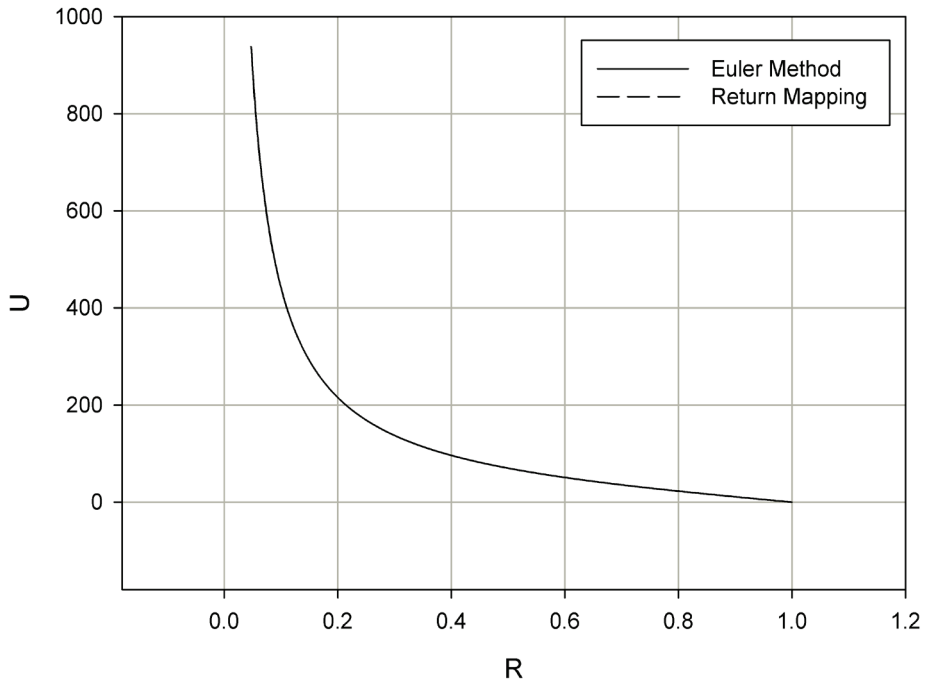

Figure 51 - U function vs. similarity ratio evolution for perfect plasticity case.

The following graph reports the convergence rate of the residual, computed as shown in paragraph 3.2.4, against the number of iterations required to get the fulfilment of eq. (3.90). The tolerance in the

diagram has been imposed under a threshold of 10^{-6}. As soon as the difference between the stress point, corrected by the plastic relaxation, and the one on the updated plastic surface is smaller that tolerance the DO cycle stops and the algorithm passes to the subsequent macro step.

The last two graphs of Figure 53 and Figure 54 deal with the application of the cutting plane method on metals. The main difference with the previous case for soil lies on the expression for the hardening function and its evolution (in the uniaxial case in fact the normal-yield surface coincides with a point so the difference between a soil and a metal depends on a scalar value)

$$F = F_0\left[1 + h_1\left\{1 - e^{(-h_2 H)}\right\}\right] \tag{4.15}$$

$$F' = F_0\, h_1\, h_2\, e^{(-h_2 H)} \tag{4.16}$$

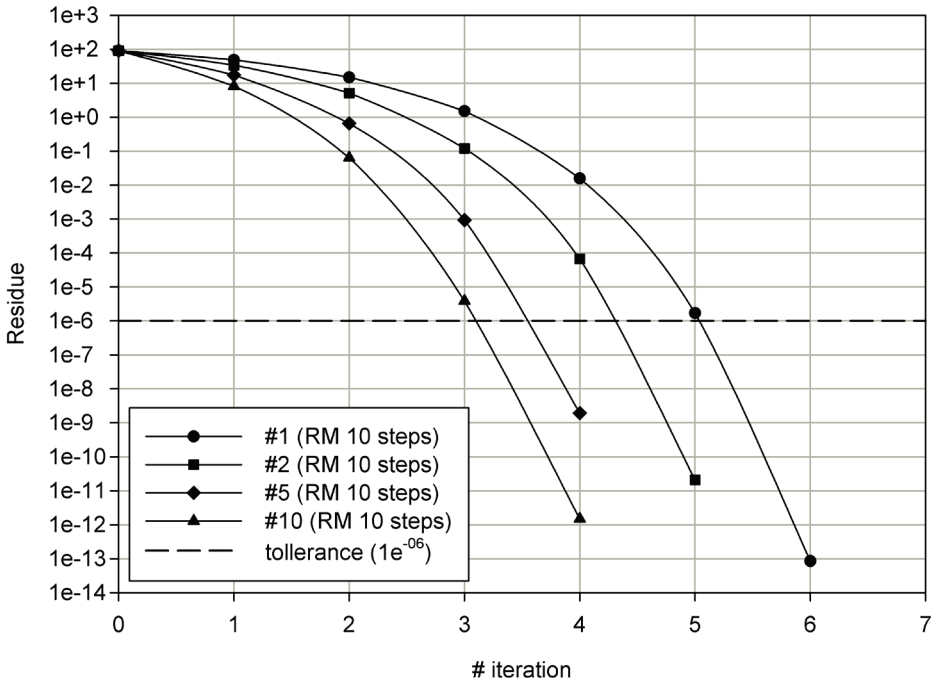

Figure 52 - Convergence rate for the 10 steps perfect plasticity case (soil).

As it can be seen the results are as good as the previous ones proving the robustness of the code. The investigations on metals have been carried out as a preparation for the more complicated 3D research code due to some problems encountered when dealing with soils as it will be clarified in the next pages.

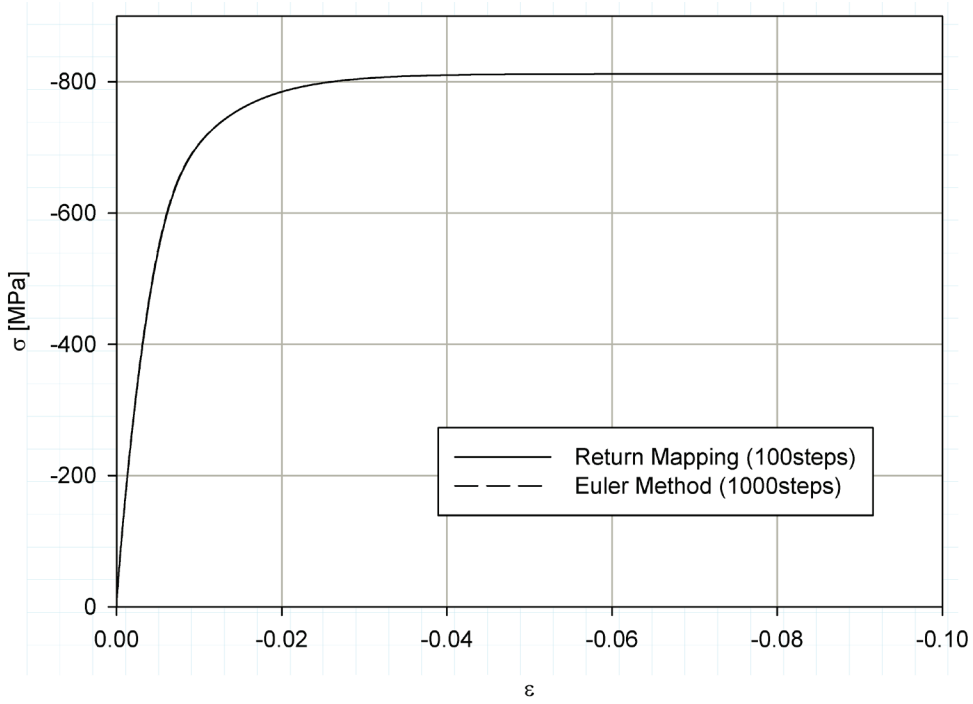

Figure 53 – Return mapping algorithm for metals.

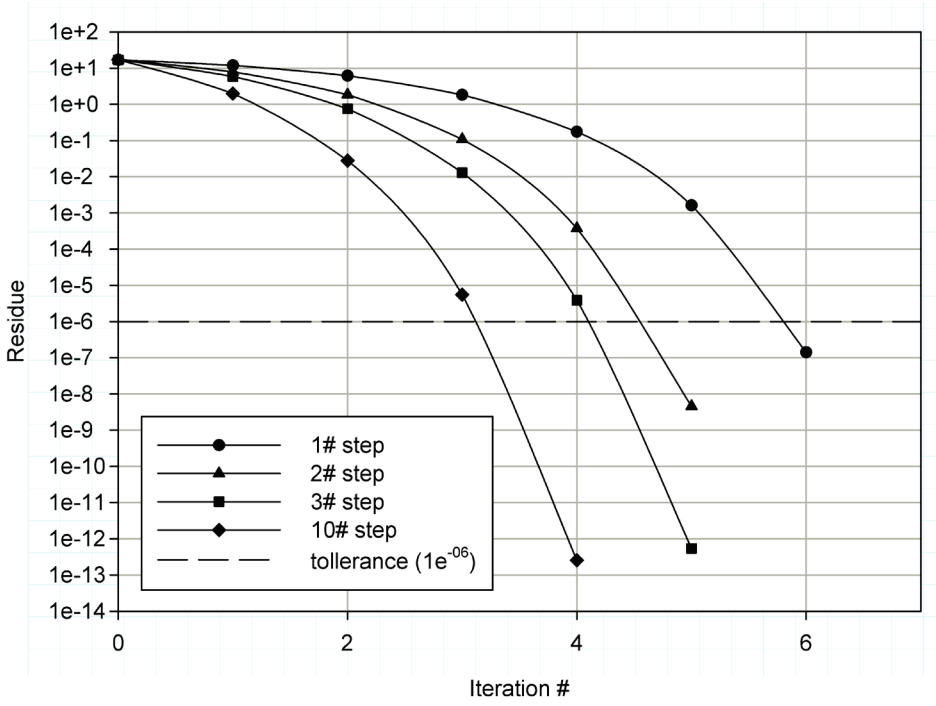

Figure 54 – Convergence rate for the 10 steps case (metal).

5.1.4. Three dimensional implementation

In the three dimensional implementation of the return mapping a neat distinction between the three dimensional single Gauss point problem and the implementation on the F.E. code should be underlined.

In the first case a difference between a fully strain input condition and on a mixed stress-strain input condition has to be pointed out. In the latter a global convergence algorithm for the balance of the external and internal forces should be taken into account. Starting with order at first the results for the single Gauss point problem will be presented and commented and then some considerations about the finite elements implementation will be described.

The formulation of the return mapping algorithm, as presented in the paragraph 3.2.4, is a fully strain driven problem, meaning that it requires the introduction of only strain increments as input. However in a single Gauss problem is not always possible to insert all strain rates input, for instance when a triaxial drained test should be simulated. In this case the input is composed by the lateral containing pressures and the strain rate for the compression or extension from the top of the sample as shown in Figure 55a.

When a sub-iteration of the return mapping algorithm converges the point found doesn't satisfy the correct mechanical equilibrium because the return mapping algorithm affects the stress state correcting also the components where the stress condition has been fixed as an external boundary condition. Thus the results deviate from the correct stress path, which for a triaxial drained test, should be function of the only input conditions. The problem can be avoided by performing an elastic correction Figure 56, which will not affect the plastic surface and plastic internal variables, and corrects the lateral components of the stress state to bring the point back to the stress path. Subsequently return mapping is performed again for the same macro step and a new equilibrium point is found. This procedure is implemented until the point both satisfied the equilibrium, derived by the application of the return mapping, and lies at the same time on the correct stress path. Figure 57 explains graphically the numerical procedure just described. After the trial elastic, the first correction of the stress state deviates from the stress path (*1# RM*), so it is necessary to adjust the boundary conditions (*1# Elastic correction*), once again return mapping is performed again to find the point *2#RM* and the zigzag evolution proceeds until the fulfilments of the equilibrium.

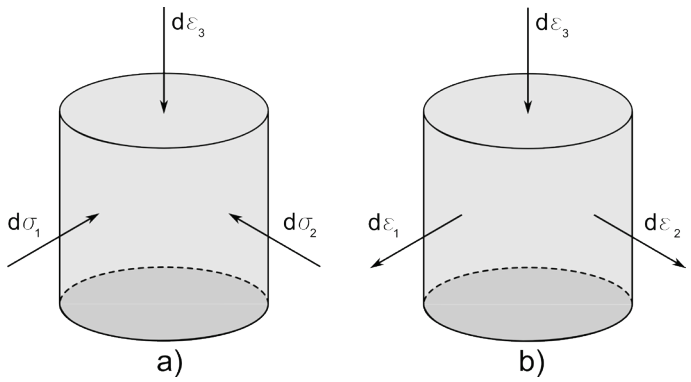

Figure 55 – Stress-strain rates input conditions for: **a)** triaxial drained test, **b)** triaxial undrained test.

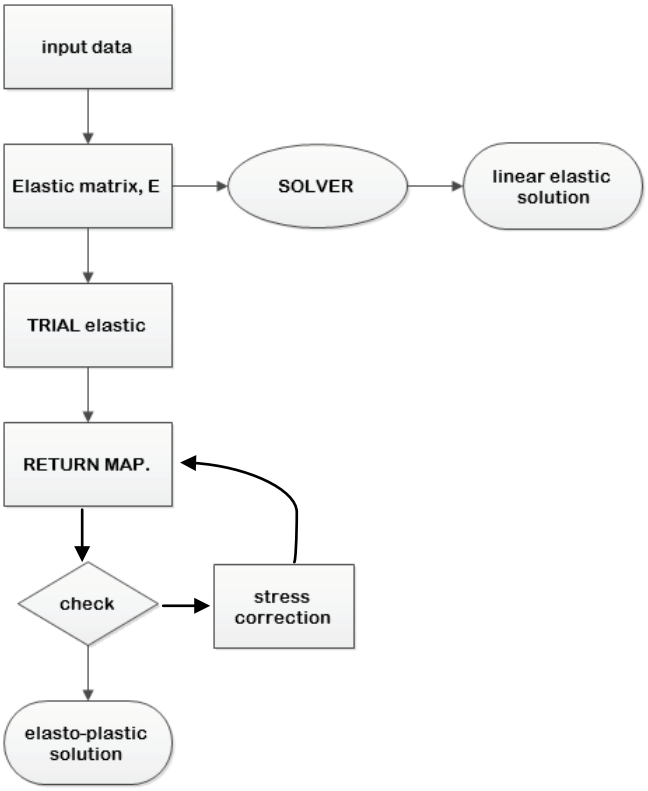

Figure 56 - Flow chart of the correction stress algorithm.

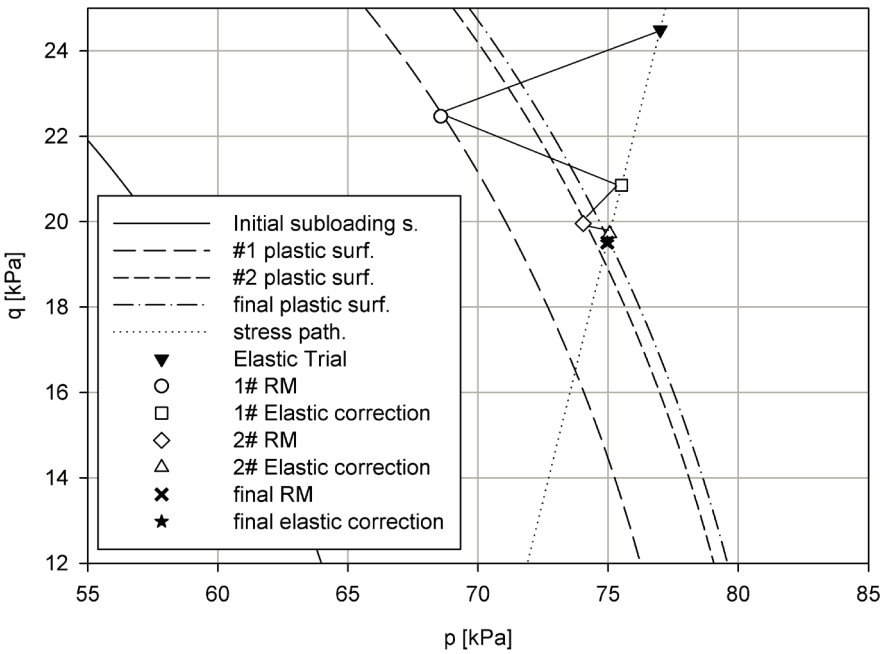

Figure 57 - Example of the stress correction algorithm for a mixed stress-strain rate input.

This kind of strategy is not necessary of course for the undrained triaxial test (Figure 55b) or in general for a full strain rate input case because the correction of the trial elastic state will be performed

correctly in all the components. In the finite elements problems the application of the cutting plane method is performed after the solution of system (2.21), implying that the strain rates for the actual step have already been computed and available to be used as input conditions.

During the implementation of the return mapping algorithm, both in the drained and undrained triaxial tests, some errors in the computation of the correct stress-strain curve arise. This fact is due to the continuous change of direction of the outward normal vector in the ongoing of the simulation, leading to the incorrect update of the plastic variables and deviating the solution from the correct one. The problem is less evident when a small steps analysis is carried out because from one step to another the change of direction is not so big and the error is relatively small as been proved by the analyses carried out.

One strategy adopted to corrects this aspect is that of reducing the differences of direction that arise in a large time steps simulation by using a combination of the outward normal vector to the plastic surface at the generic *n* step and at the *n+1* step. In detail three different cases have been investigated in this work: one using the $\mathbf{N}_n$ vector, another the $\mathbf{N}_{n+1}$, and the last applying the average of the two. Figure 58, Figure 59 and Figure 60 numerically reproduce the data measured by Skempton and Brown in [49] and which parameters are reported in Table 6.

ρ'	0.045
γ	0.002
mc	1.2
u	33
F0 [N/mm^2]	330

Table 6 – subloading surface parameters for the triaxial drained test.

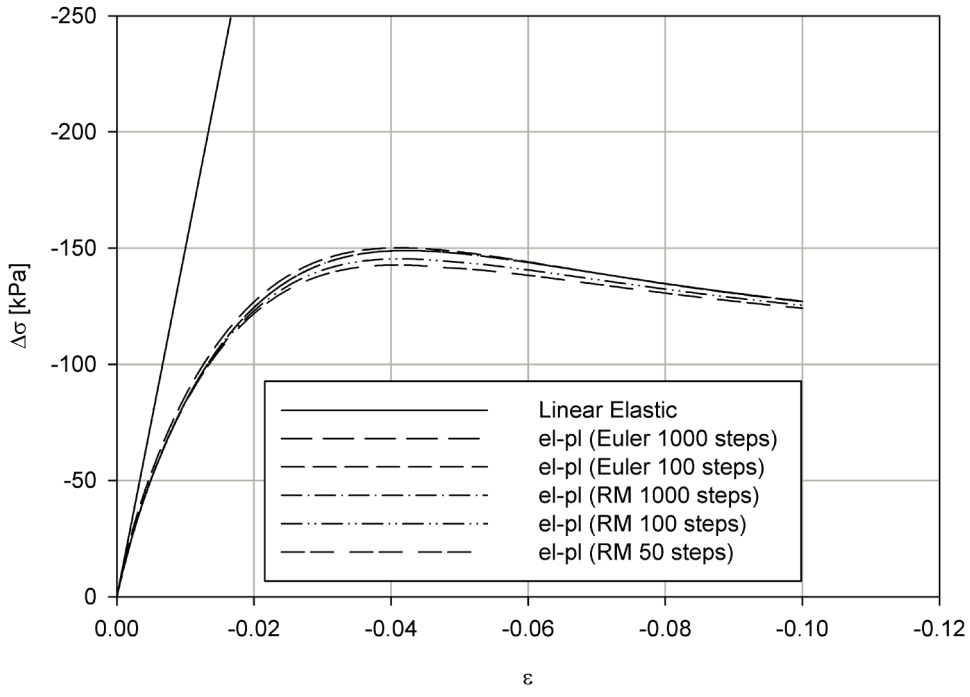

Figure 58 - Triaxial drained test (current normal vector).

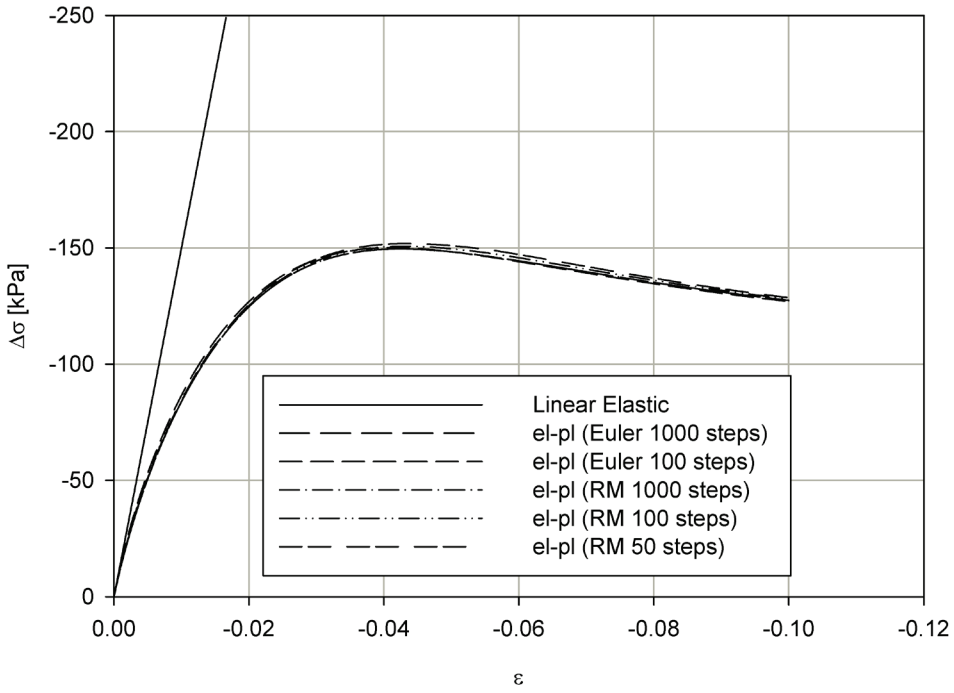

Figure 59 - Triaxial drained test (past normal vector).

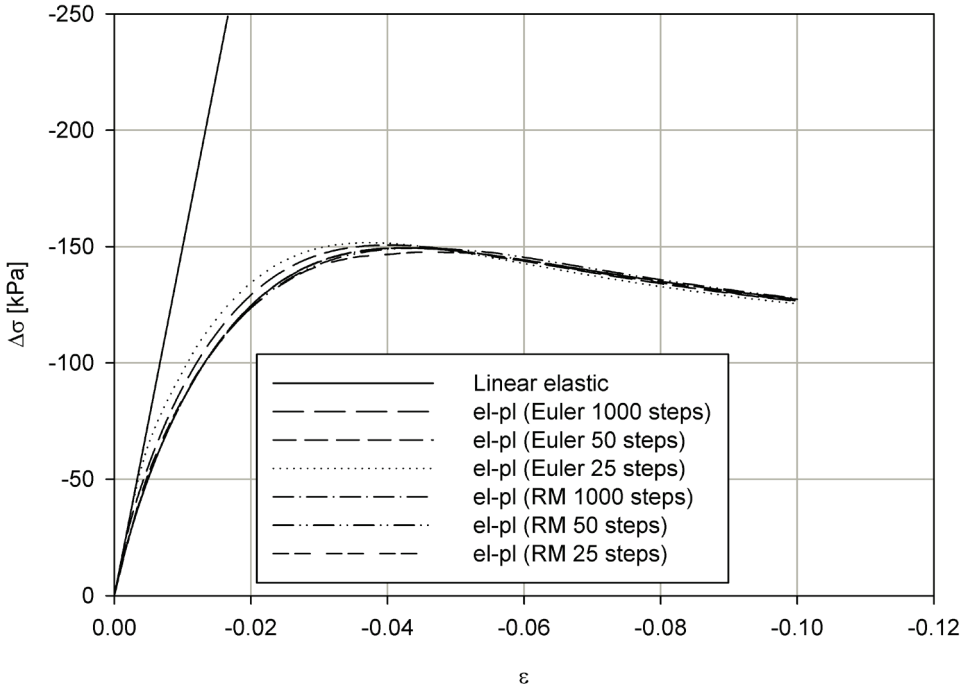

Figure 60 - Triaxial drained test (average normal vector).

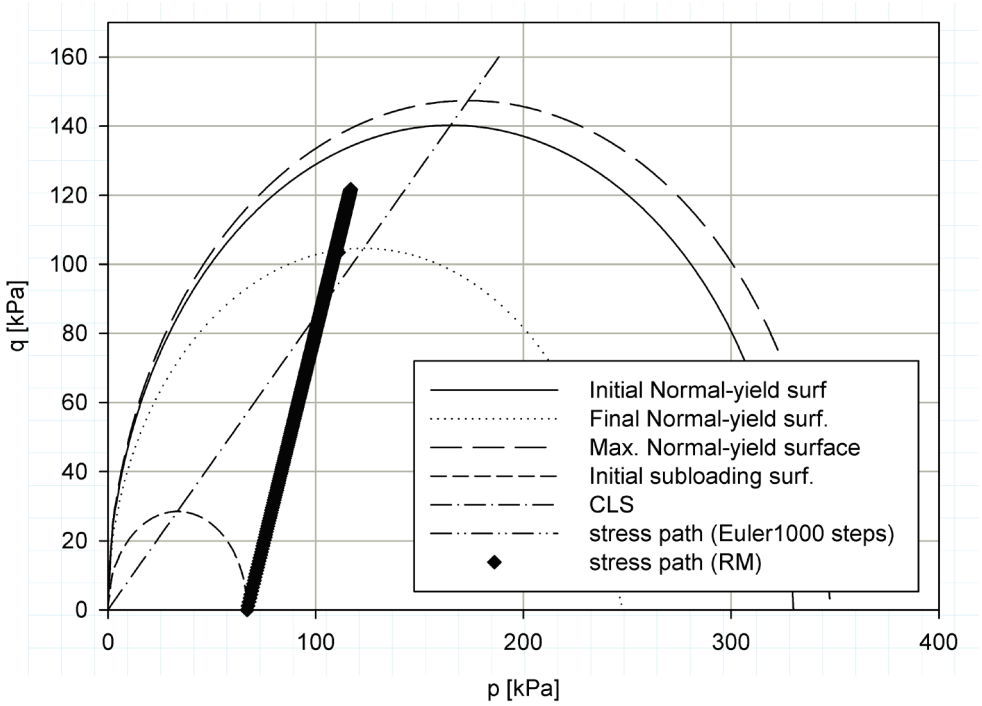

Figure 61 - Stress path for the drained triaxial test (average normal vector).

As it can be seen the solution of averaging the normal vector is quite satisfying showing a stable solution even with a reduced number of iterations, whereas the stress-strain curves obtained with the Euler method decreases the accuracy when the size of the steps increases. Additionally the stress path for the simulation can be seen in Figure 61.

Unfortunately the averaging process is not sufficient in the undrained triaxial test due to a extreme variation of the outward normal vector on the deviatoric-idrostatic plane. The input parameters have been taken from the measurement done by Bishop *et al*. [50] and reported in Table 7.

ρ'	0.022
γ	0.0063
mc	0.82
u	70
F0 [N/mm^2]	1700

Table 7 – subloading surface parameters for the undrained triaxial test.

Stress-strain curves are depicted in Figure 62, Figure 63 and Figure 64 respectively for the current normal vector, the past one and the average of the previous two. Differently from the triaxial drained case the averaging strategy doesn't seem to be effective for improving the goodness of the solution, in fact the stress regime is a little underestimated when reaches the critical state line. On the other hand a more stable condition is obtained by using the past vector.

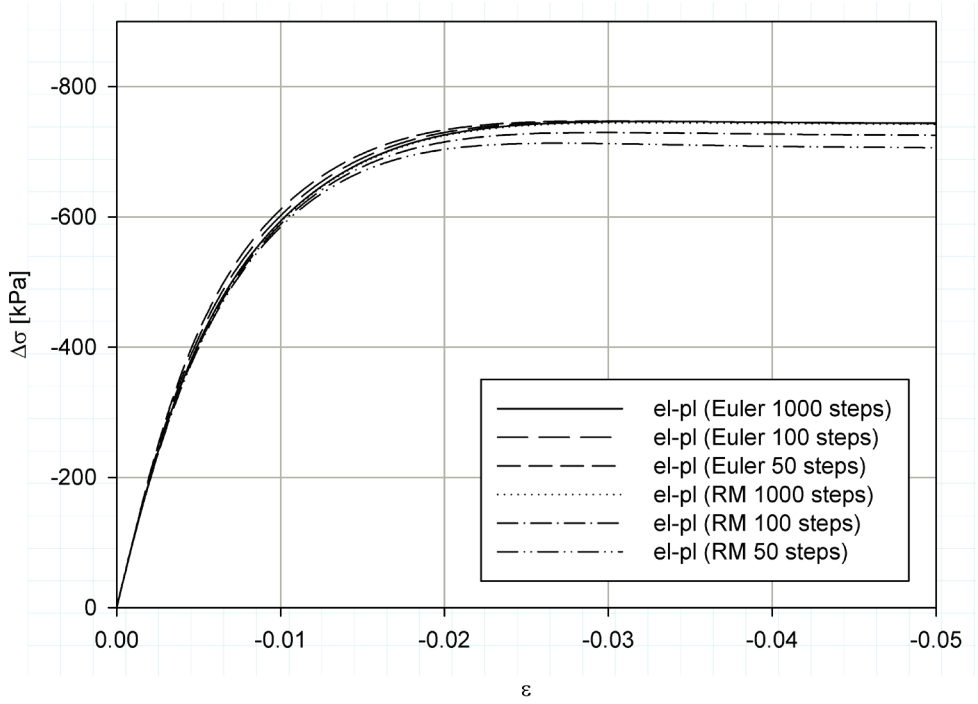

Figure 62 - Triaxial undrained test (current normal vector).

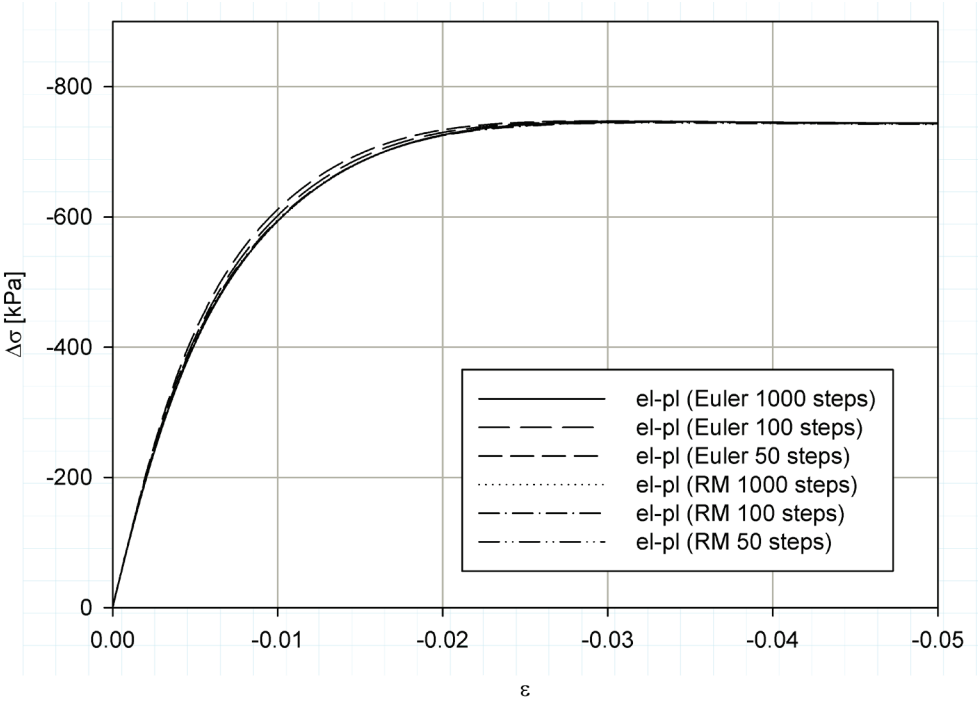

Figure 63 - Triaxial undrained test (past normal vector).

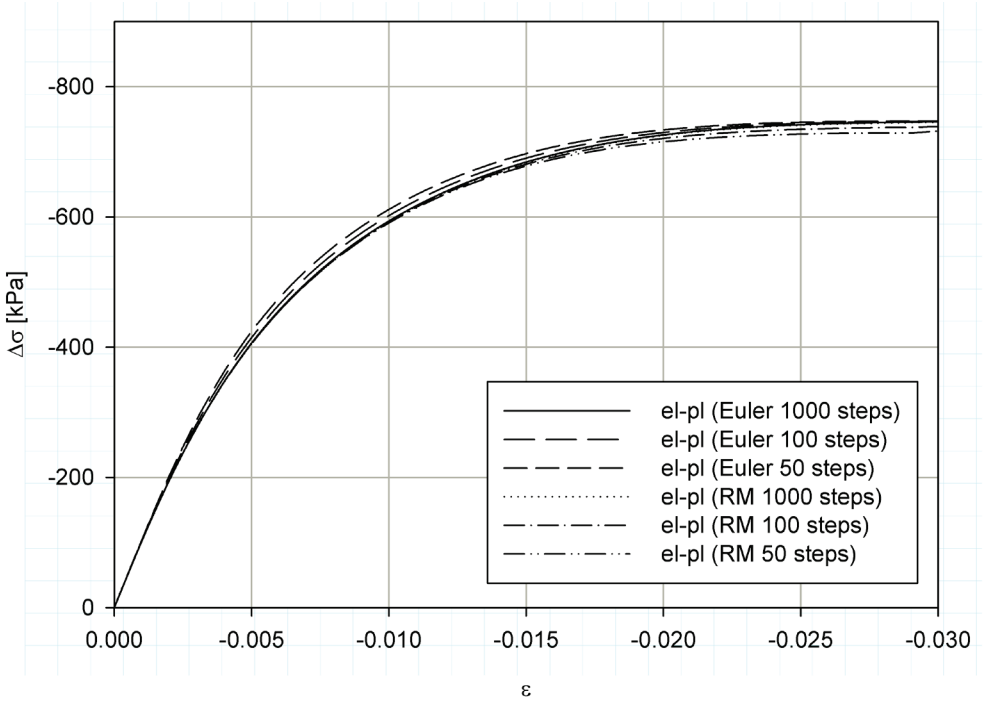

Figure 64 - Triaxial undrained test (average normal vector).

The role of the direction of the outward normal vector is then relevant on the results obtained. To verify the correct implementation of the model it has been chosen to carried out an idrostatic compression test (e.g. Figure 65) because it's a simple case where the direction of the normal vector doesn't varies in the stress space.

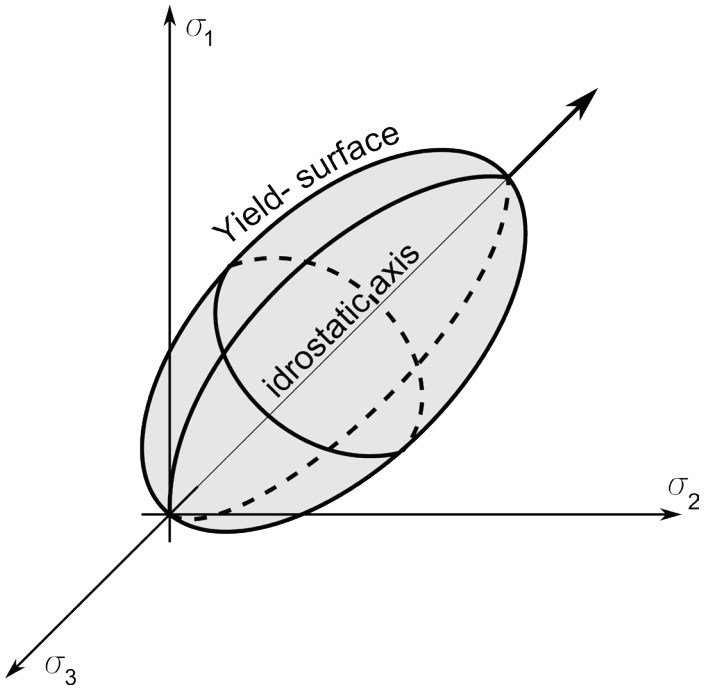

Figure 65 – sketch of the normal-yield surface in the stress space for the idrostatic analysis.

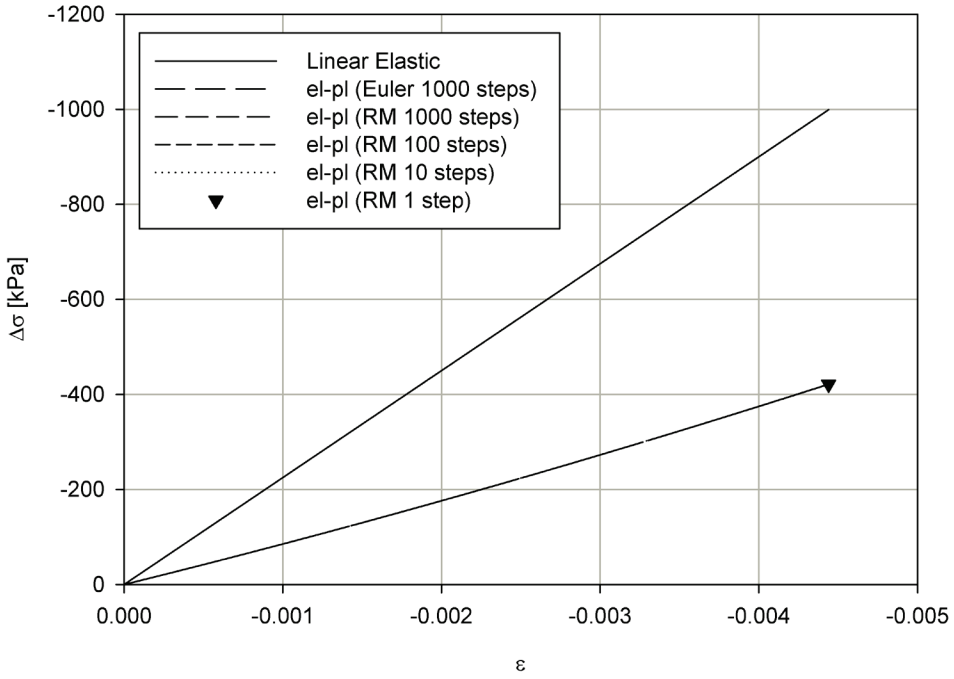

Figure 66 – Stress-strain curve for an idrostatic compression test.

As it can be seen in Figure 66 the convergence of the return mapping algorithm is guarantee on the correct point even in a single step simulation when the normal vector doesn't vary direction. The residual converge very fast (see Table 8) under the imposed tolerance according to the theoretical formulation of the algorithm.

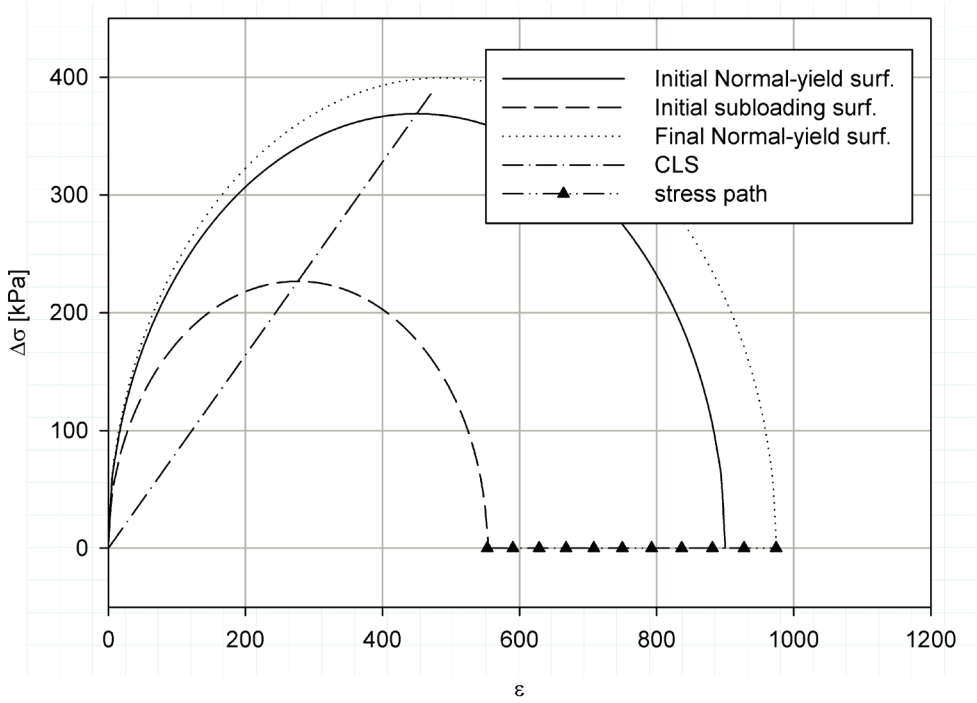

Figure 67 - Stress path in the idrostatic compression case.

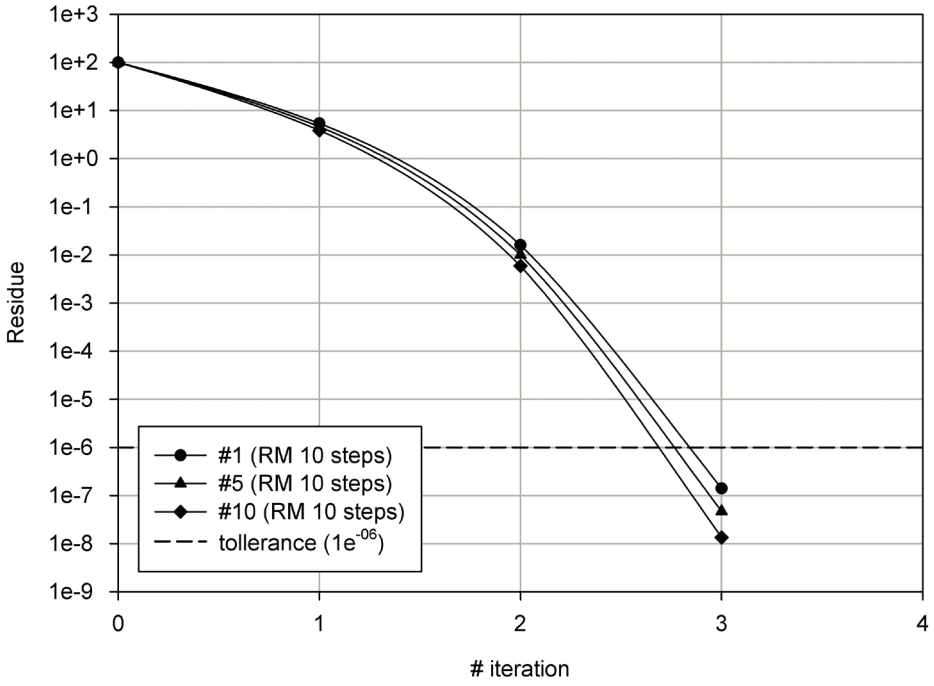

Figure 68 - Residual evolution for the 10 steps Return Mapping analysis.

MAIN step 1	
iteration	**residue**
0	9.9900e+01
1	5.3953e-00
2	1.5949e-02
3	1.3949e-07
MAIN step 5	
iteration	**residue**
0	9.9900e+01
1	4.6198e-00
2	9.9754e-03
3	4.6532e-08
MAIN step 10	
iteration	**residue**
0	9.9900e+01
1	3.8734e-00
2	5.8550e-03
3	1.3881e-08

Table 8 – Residue for the 10 steps idrostatic compression analysis.

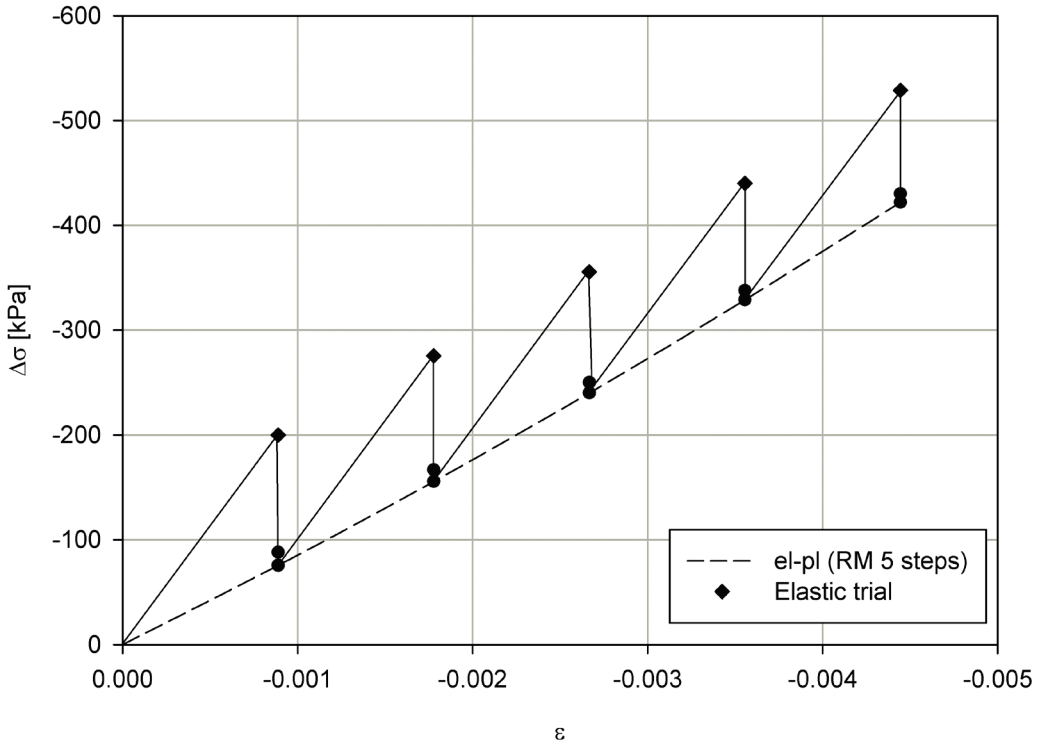

Figure 69 - Iterative convergence procedure for the 5 steps analysis.

Figure 69 describes the iterative procedure for the convergence on the correct point explicated by the return mapping algorithm. According to the theory the final stress is the projection on the trial elastic state in the plastic surface. Furthermore the plastic correction is more relevant in the first sub-step where the distance between the stress state and the correspondent plastic surface is maximum.

The accuracy of the algorithm has been investigated creating some iso-error maps according to [48]. Such graphs have been realized comparing the numerical solution and analytical one (i.e. numerical solution obtained with a really large number of steps) inducing a variation on the input strain rate component alternatively and fixing the other. The results show that if the number of steps decreases the errors between two steps increases considerably. The data are obtained using eq. (4.17).

$$\delta = \frac{\sqrt{\left(\sigma_{exact} - \sigma_{num}\right) : \left(\sigma_{exact} - \sigma_{num}\right)}}{\sqrt{\left(\sigma_{exact} - \sigma_{exact}\right)}} \tag{4.17}$$

Figure 70, Figure 71 and Figure 72 have been created by choosing a point of symmetry, respect to the principal directions 1 and 2 (the third one has been fixed), leading to a symmetrical distribution of the errors. As it can be seen the errors vary from the minimum value of 0.02 % for the 1000 vs. 100 iterations to the maximum of some percentage in Figure 72. In accordance to [48] the algorithm cannot be considered reliable for an error bigger than the 5% between two consecutive step.

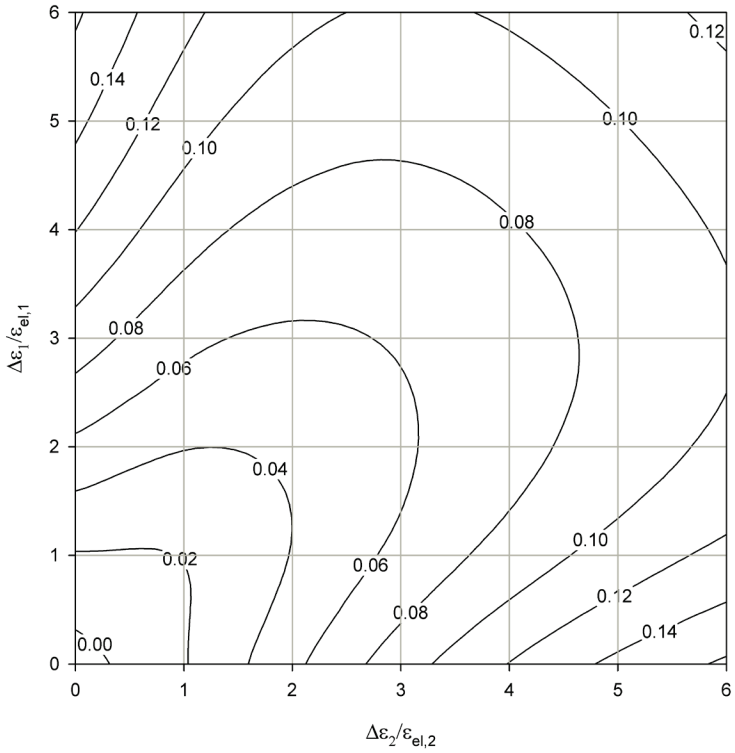

Figure 70 – iso-error map (%), 1000 vs. 100 iterations.

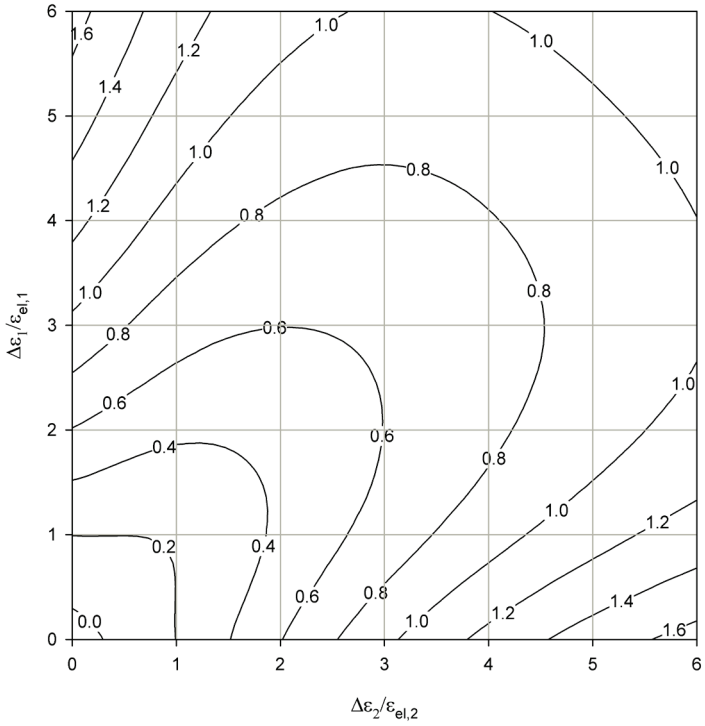

Figure 71 - iso-error map (%), 1000 vs. 10 iterations.

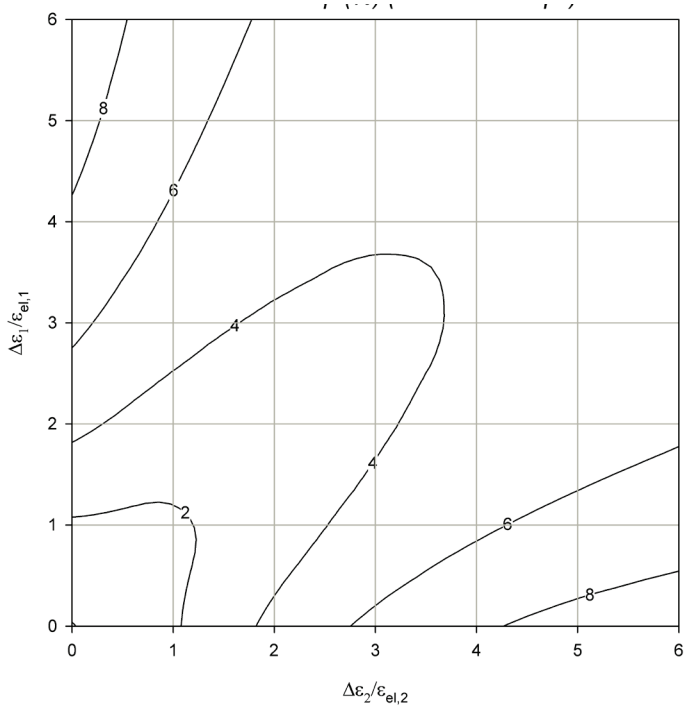

Figure 72 - iso-error map (%), 1000 vs. 1 iterations.

5.1.5. F.E. implementation

The previous paragraph 4.3 described the global procedure for the implementation of the return mapping procedure in the F.E. code that can be easily understood by observing Figure 24.

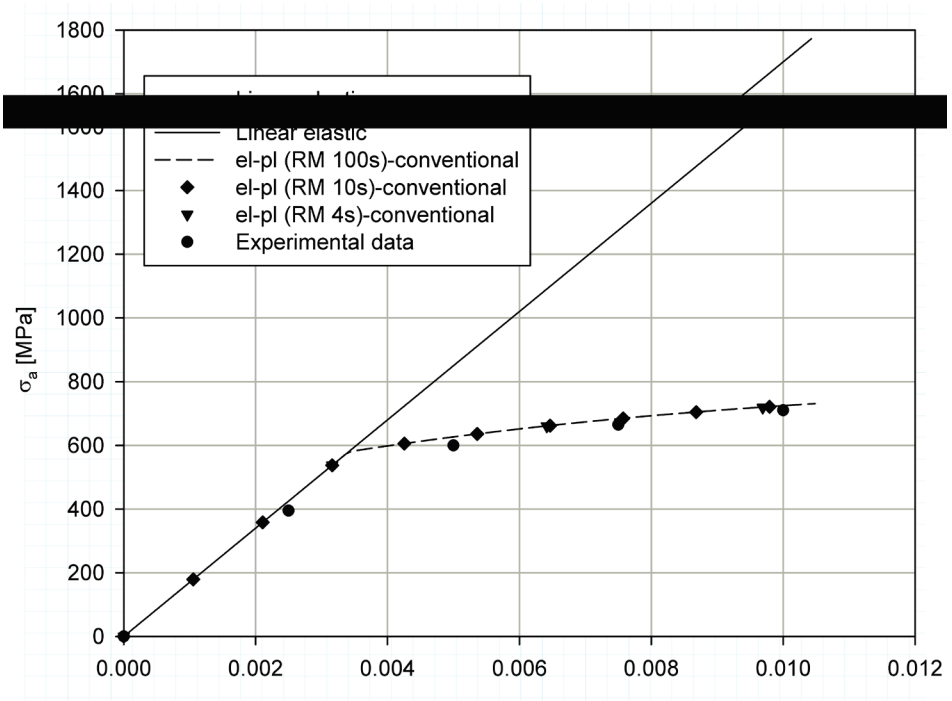

Figure 73 – stress-strain curve for conventional plasticity in uniaxial traction test.

The simulation carried out here deals with a uniaxial deformation for a steel which properties are reported in Table 9 (references can be found at [51]). The choice of metal rather than soil is due to the problems explained before connected with the normal vector to the plastic surface. Here a classical Von Mises yield condition has been assumed, so the outward normalized normal keeps the same orientation in the stress space as well as the plastic relaxation direction.

E [MPa]	170000
υ	0.3
$\mathbf{h_1}$	0.4
$\mathbf{h_2}$	170
$\mathbf{R_e}$	0.1
u	500
$\mathbf{F_0}$ [MPa]	580
$\boldsymbol{\sigma_0}$ [MPa]	0

Table 9 – subloading surface parameters for uniaxial traction analysis.

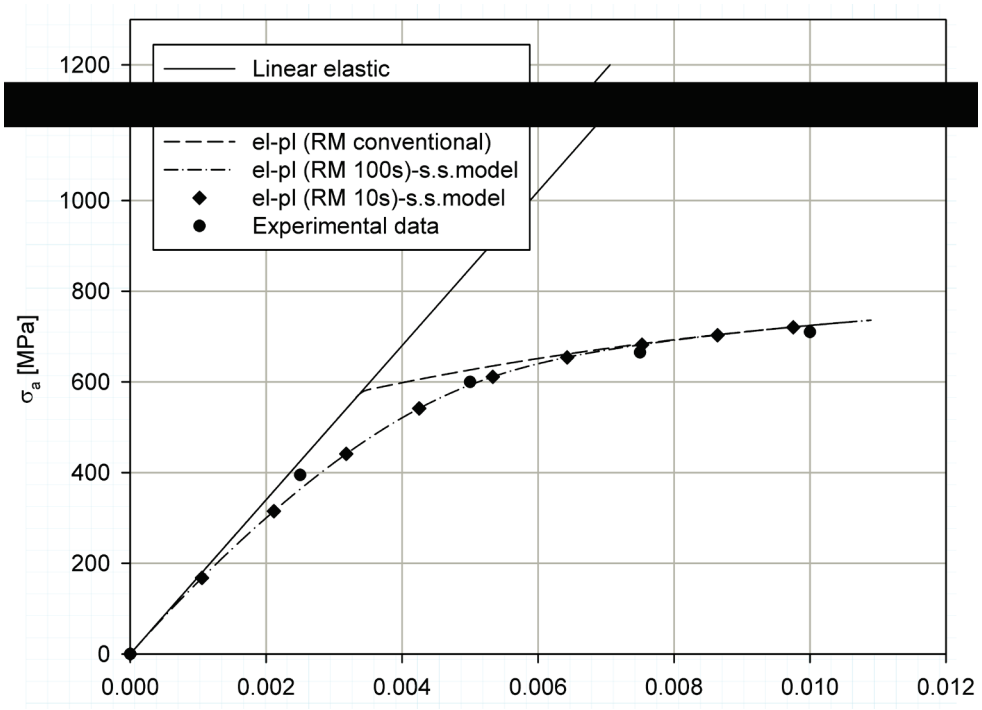

Figure 74 – subloading surface in uniaxial traction test for steel.

Figure 73 and Figure 74 respectively show the results of the implementation of the cutting plane algorithm for a conventional plasticity model and for the subloading surface one. The former slightly overestimate the stress level around the neck (i.e. the transition zone between the elastic and plastic domains), on the contrary the fulfilment of the smoothness and continuity conditions by the latter leads to a more realistic response of the model.

The model has been realized using 360 20-nodes brick isoparametric elements with quadratic shape functions. The solution is quite stable even with few steps (i.e.10) allowing to reduce computational time respect to the application of the Euler method.

5.3. Soil tensile strength

A yield condition for the extension to the negative pressure (i.e. tensile stress) for soil has been implemented by Prof. Hashiguchi [52] using a shift of the surface on the p-q plane. The implementation has been carried out for a three dimensional single Gauss point problem and then reproduced in the F.E. model PLASCON 3D.

As benchmark for the evaluation of the correct implementation of the algorithm a cemented-sand material has been chosen, which parameters have been reported in the following Table 10 and [53]. The meaning of the parameters has been already presented in the previous paragraphs so they will not be explained again.

$\mathbf{P_e}$ [kPa]	1200
ν	0.25
P	0.01
γ	0.00035
ϕ_c	28°
ξ	0.25
ζ	0.08
u	1200
$\mathbf{F_0}$ [N/m^2]	4200

Table 10 – subloading surface parameter in soil tensile strength investigation.

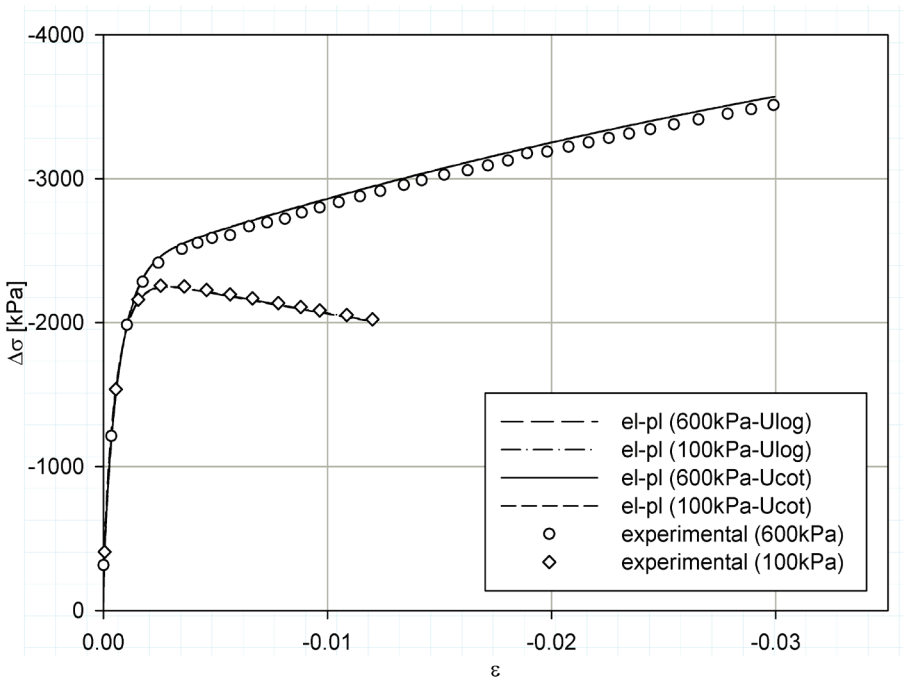

Figure 75 - Compression case for the two confining pressures.

The test has been carried out with the same material at two different lateral containing pressures respectively of -100 kPa and -600 kPa and inducing a displacement driven analysis both for extension and compression. The results are quite overlapped on the experimental data (e.g. Figure 75 and Figure 76).

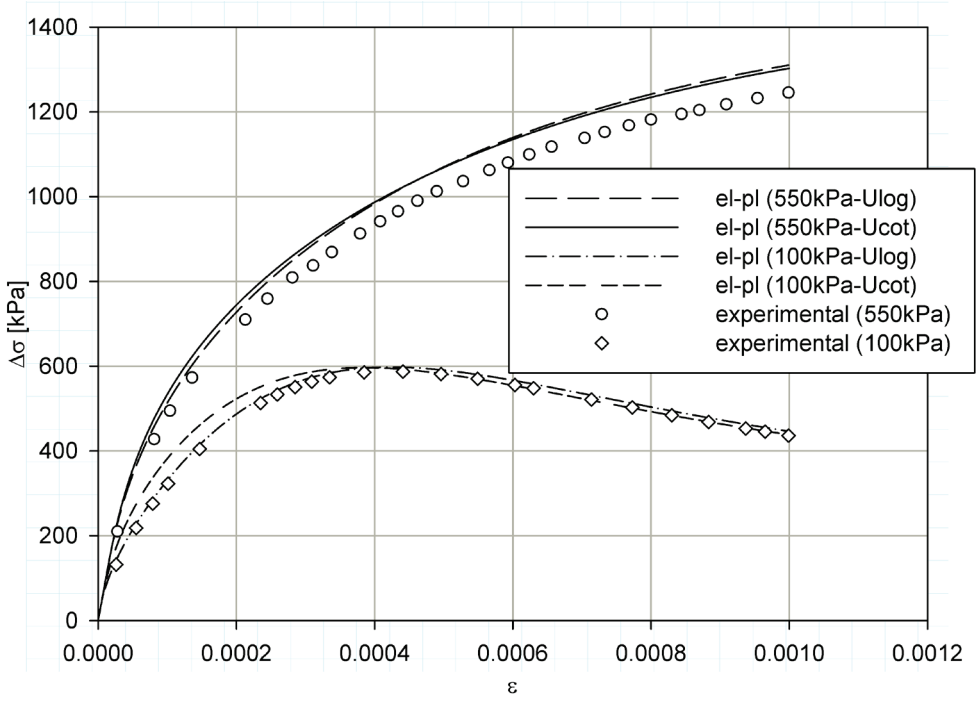

Figure 76 - Extension case for the two confining pressures.

The numerical curves have been evaluated with two different evolution law of the *U* function: one using the logarithm of the similarity ratio (no more used because of integrability issue) and the other with the cotangent function (i.e. eq. (3.63)). Obviously the small *u* parameter has been changed in the two cases.

It is quite interesting to observe the behaviour of the model in the deviatoric-idrostatic plane, considering the stress path and the evolution of the subloading and the normal-yield surfaces under different loading conditions. As it can be seen the stress path is straight as expected for a triaxial input conditions (i.e. it has been imagined to input the direct triaxial conditions on the single Gauss point problem which means a fixed lateral constrained pressure of respectively -100kPa and -600kPa and to give an incremental strain on the third component of -1^{-4} for the compression case and $+1^{-5}$ for the extension case).

The different input conditions generate a different response in the q-p plane. The results for the -600 kPa confining pressure case has not been reported here for sake of brevity and the attention has been focused on the -100 kPa lateral constrain test. In the compression case the stress path intersected the critical state line generating a softening response as appears in the stress-strain curve of Figure 77.

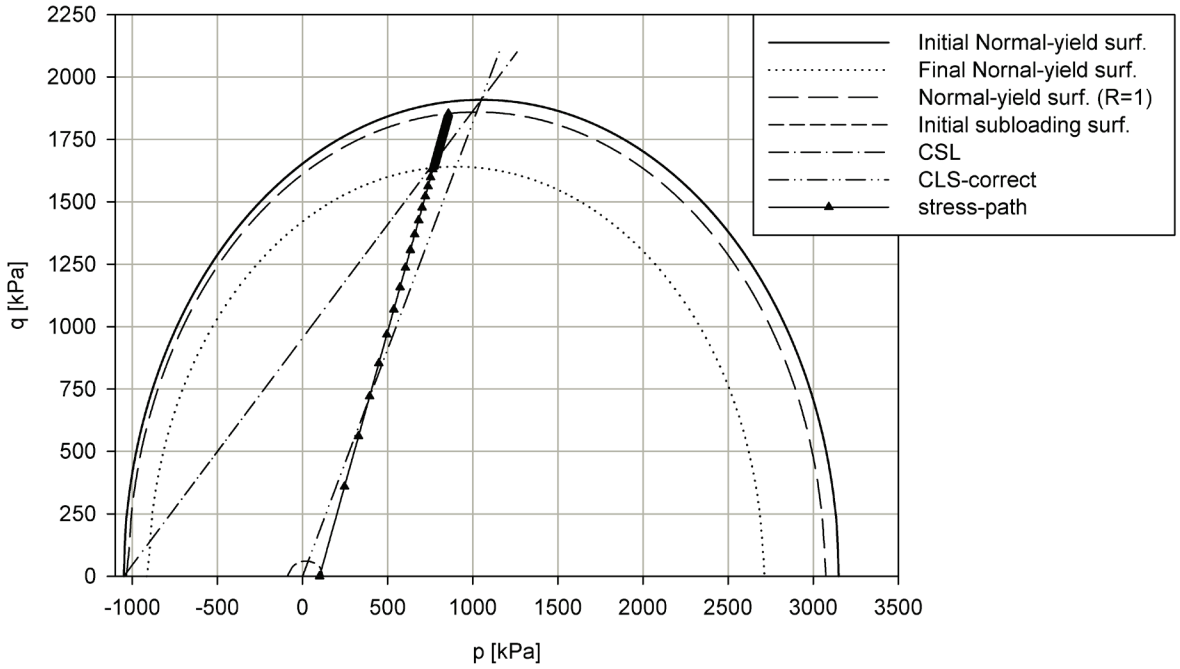

Figure 77 - Stress path for the compression case and -100kPa lateral stress.

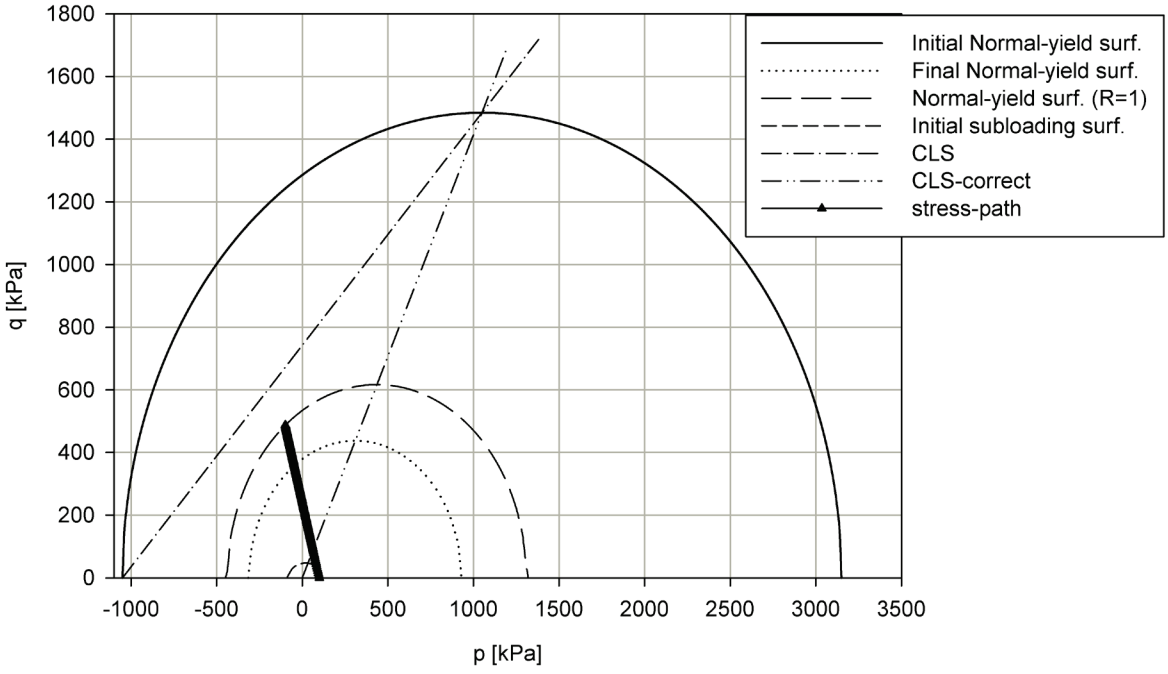

Figure 78 - Stress path for the extension case and -100kPa lateral stress.

The plastic volumetric strain (i.e. the first term of eq. (3.138)) affects the hardening/softening of soil in the positive (compression) idrostatic regime, while the deviatoric strain would induce a notable softening in the negative (tensile) one as described in Figure 76 and Figure 78.

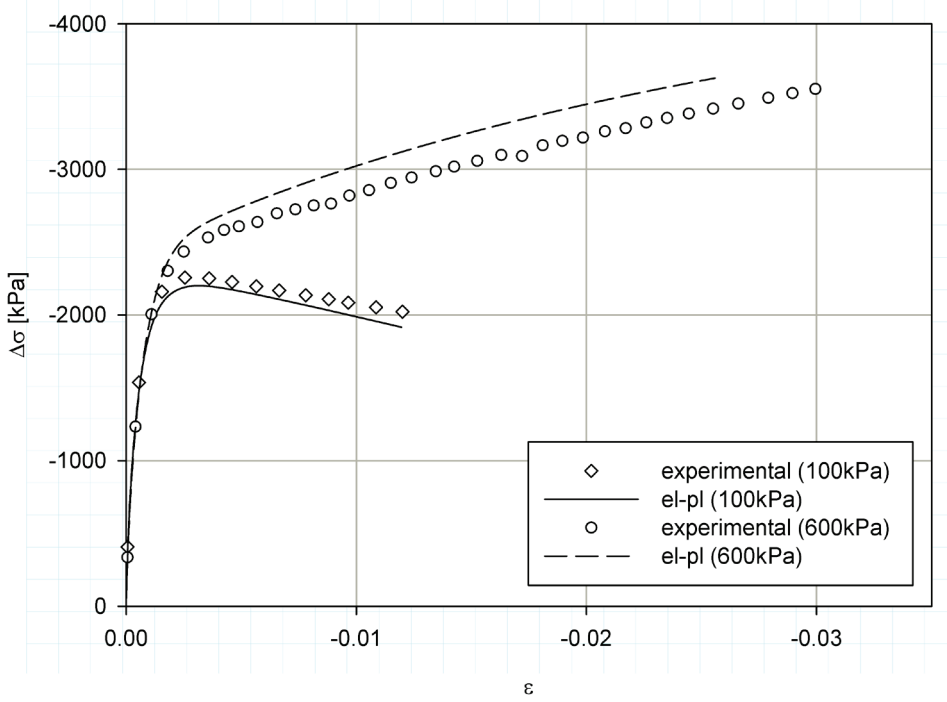

Figure 79 - Compression case for the F.E. simulation.

Subsequently the same analyses has been implemented again in a boundary value problem (i.e. finite elements simulation) creating a cylinder sample of the same dimension of the standard triaxial one using 20-node isoparametric elements seen in the previous analyses.

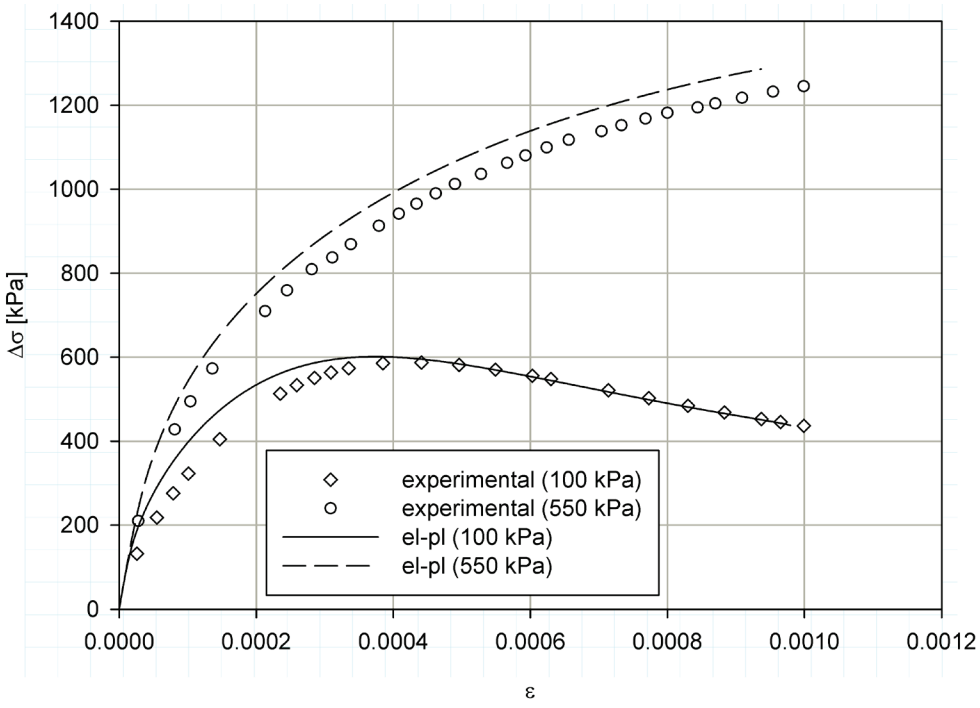

Figure 80 - Extension case for the F.E. simulation.

Here (i.e. Figure 79) there is a little overestimation of the curve for the -600 kPa lateral stress and a little underestimation for the -100kPa test but this inconvenience is due to the rough mesh used. Perfect triaxial conditions are not properly realized because a small number of elements has been involved and also because the boundary conditions have to be insert as displacements and forces on the mesh nodes and not directly as stress and strain on the Gauss points.

The extension case has been described in Figure 80 showing a good accordance between experimental data and numerical simulation.

5.4. Extended subloading surface

The extended subloading surface model has been realized with the purpose of investigate the answer of the soils under cyclic load. This unconventional algorithm has been developed at first in a one dimensional case and compared in a simulation analysis with the simple subloading theory (for a hardening and not hardening cases). The constitutive equations has then been implemented in a three dimensional single Gauss algorithm for the investigation of a more complete response and also for the evaluation of the reloading curve explained in the previous paragraph.

Finally, once the routines have been tested, a simulation on few elements has been carried out on the finite elements program to check the reliability of the answer.

5.1.6. One dimensional implementation

This simple case has been implemented for a soil under cyclic analysis in a load and unload case, comparing the answer in terms of stress-strain curve for the simple subloading surface with isotropic hardening and not hardening state and finally for the extended subloading surface with hardening.

Figure 81 and Figure 82 describe the simple subloading surface model in a cyclic analysis showing both hardening and not hardening answer. Intuitively the amplitude in the latter case keeps constant magnitude in each load-unload cycle because there is no contraction or expansion of the normal-yield surface (i.e. the yield stress traces a horizontal line in Figure 82) and so the elastoplastic modulus evolves in the same way over and over. The update of the internal variables in the former case makes the slope more stiff each repetition of the loading-unloading cycle due to the expansion of the normal-yield surface.

The simple subloading surface model is thus unable to predict the correct accumulation of plastic strains so the passage to the extended subloading surface is necessary for a numerical model capable to catch the real behaviour of a material under this loading conditions.

As it can be seen from Figure 83 the magnitude of the plastic deformations is considerably reduced thanks to the introduction of a similarity centre which translates inside the normal-yield surface following the plastic strain flow. The continuous line represents the stress-strain response obtained by means of the extended algorithm where the movement of the similarity centre creates close loops of increasing size at each repetition of the loading-unloading cycle. Furthermore it plays a key role in the

calculation of the plastic modulus (e.g. eq. (3.119)), in fact the total strains in the dashed and continuous lines are different even in the first loading curve. It is clear that the correct definition of the initial similarity centre position and of the parameters which govern its evolution are fundamental for the correct model response.

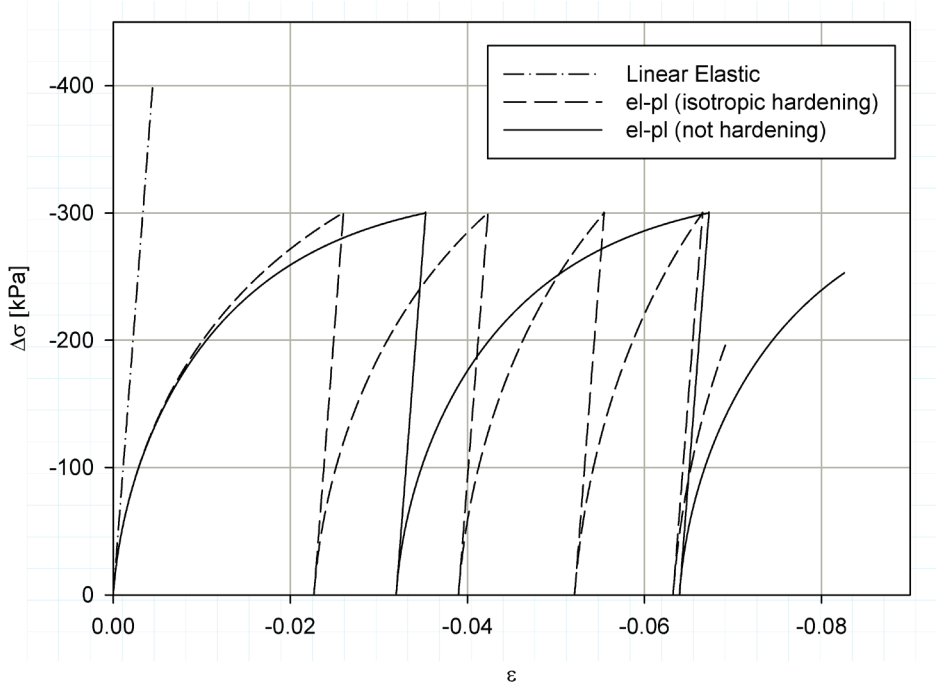

Figure 81 - Simple subloading surface model for a cyclic loading condition (hardening and not hardening cases).

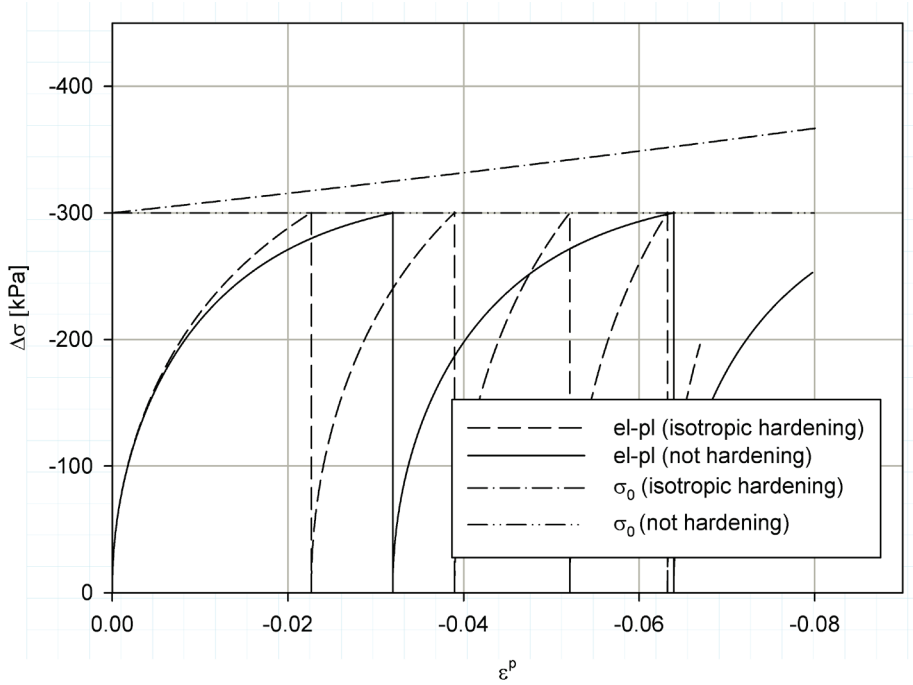

Figure 82 - Stress vs. plastic strains and normal-yield evolution.

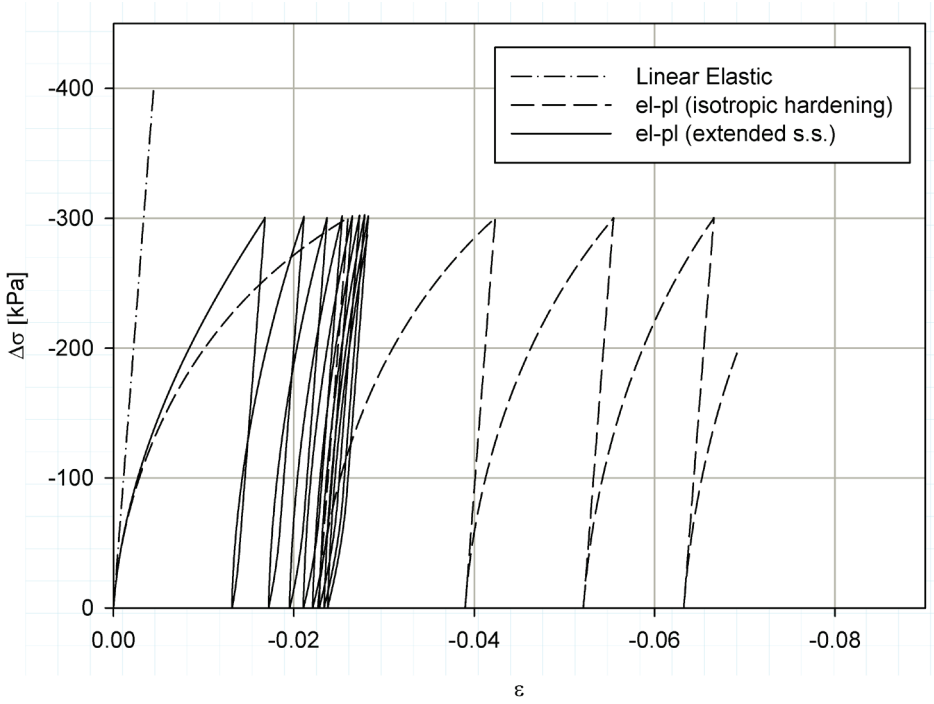

Figure 83 - Extended subloading surface vs. simple subloading surface.

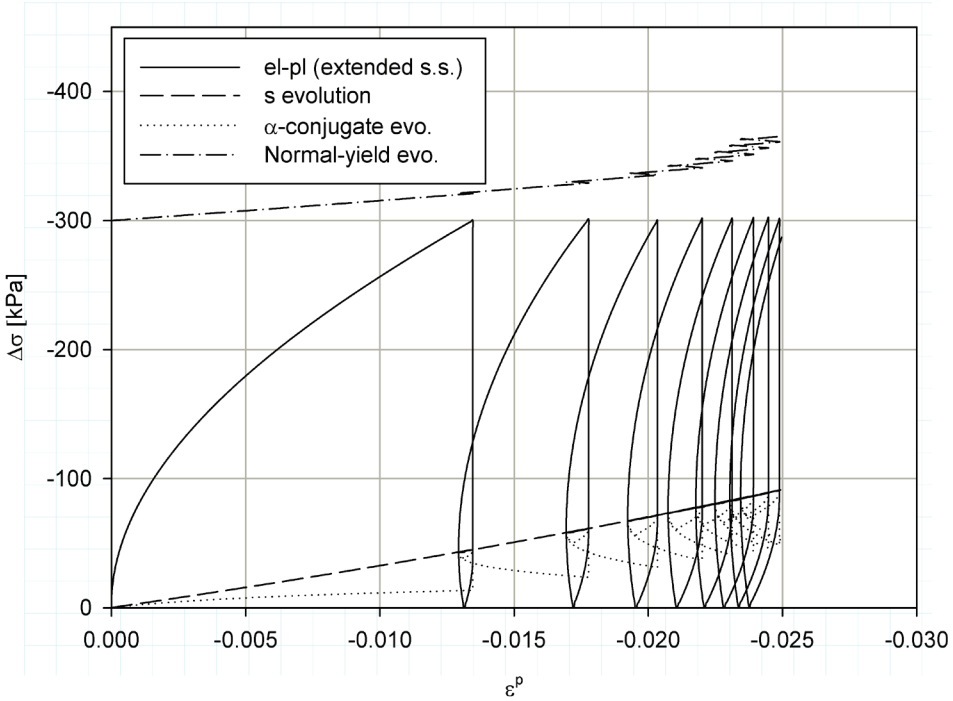

Figure 84 - Extended subloading surface parameters evolution.

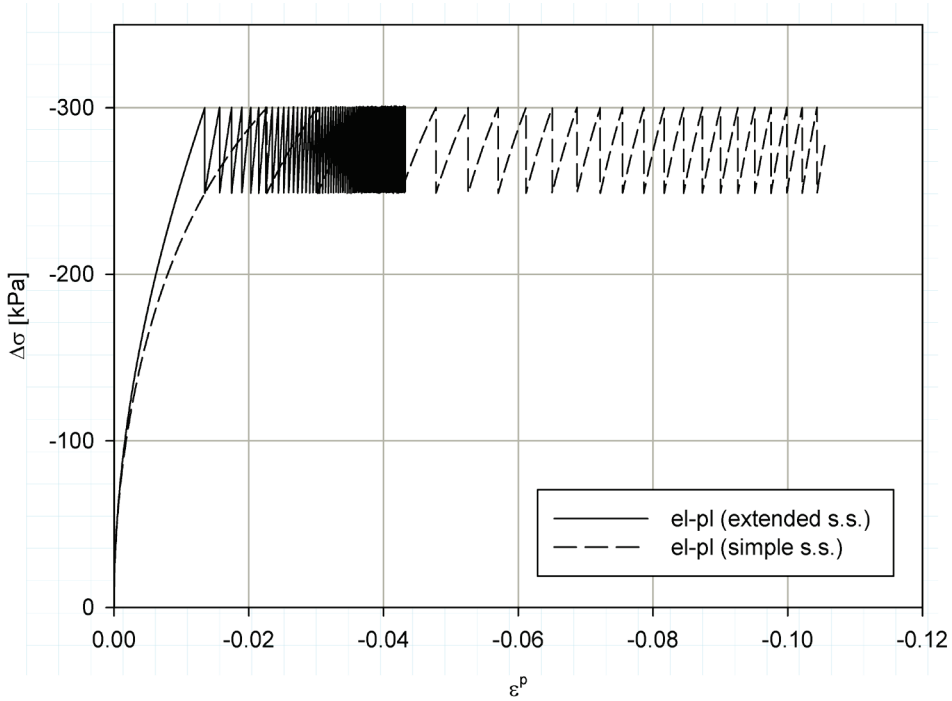

Figure 85 - Small amplitude analysis.

Figure 84 describes the movement of the similarity centre, of the conjugate *back-stress* and of the normal-yield evolution respect to the plastic strains. The plastic surface doesn't vary in the unloading path until the stress crosses the similarity centre, as already explained in paragraph 3.2.5, and then expands again in the subsequent reload.

The last case investigated for a one-dimensional algorithm is the small amplitude analysis. In conventional plasticity theories, even if a small perturbation on the stress state is induced, plastic deformations cannot be created because the point from the yield surface immediately comes back into the elastic domain. Situations of oscillation of the stress state are quite common in reality due, for instance, to small vibrations of machineries, earthquakes, or repeated loads on a soil embankment due to the passages of cars or trucks etc.

The simple subloading surface with a small number of cycles produces an incredible overestimation of the plastic deformations which is adjusted in a more realistic way by using the extended subloading surface. In this case no close loop is created until the stress crosses the similarity centre, anyhow the plastic modulus becomes more stiff decreasing the production of plastic strains.

5.1.7. Three dimensional implementation

Once tested the algorithm in a simple one-dimensional code the analyses have been extended on a three dimensional simulation, with a particular interest on the evolution of the *u* parameter, which has been taken into account according to the formulation expressed in the paragraph 3.2.5.2. The material parameters are quite almost the same used for the previous example with just some slight change

which can be appreciate in a more clear evolution of the similarity and of the conjugate back-stress variables.

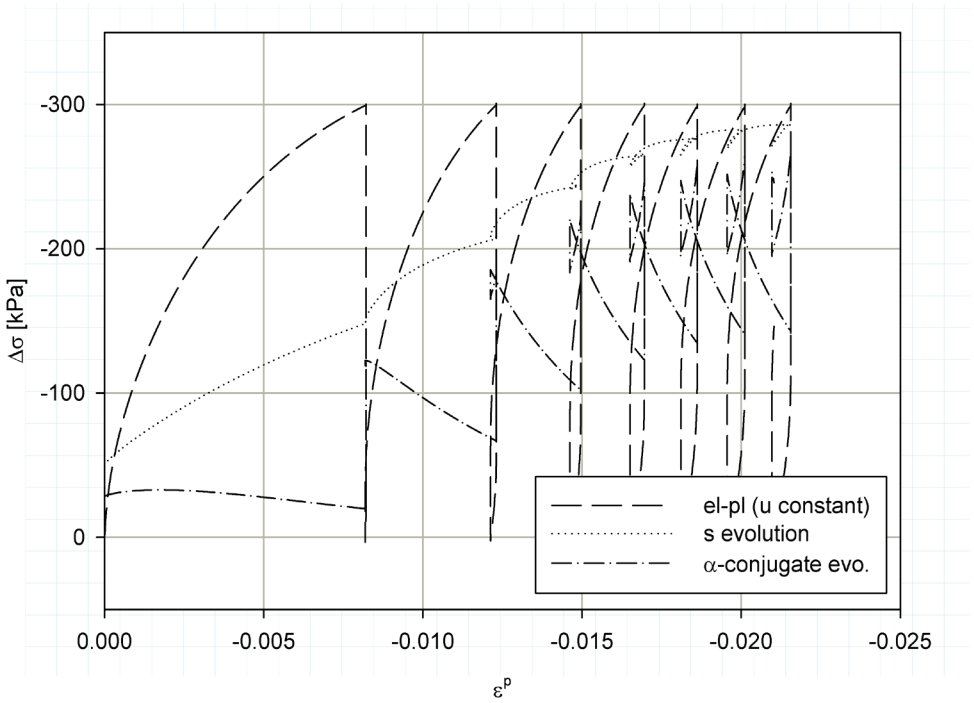

Figure 86 - No evolution of the *u* parameter.

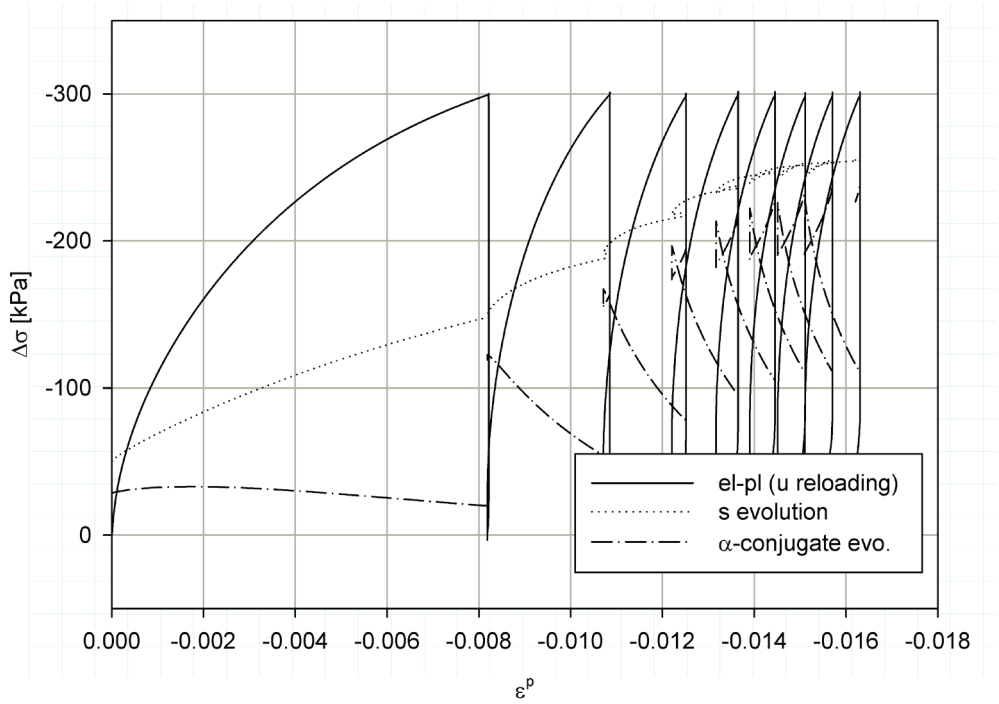

Figure 87 - No evolution of the *u* parameter.

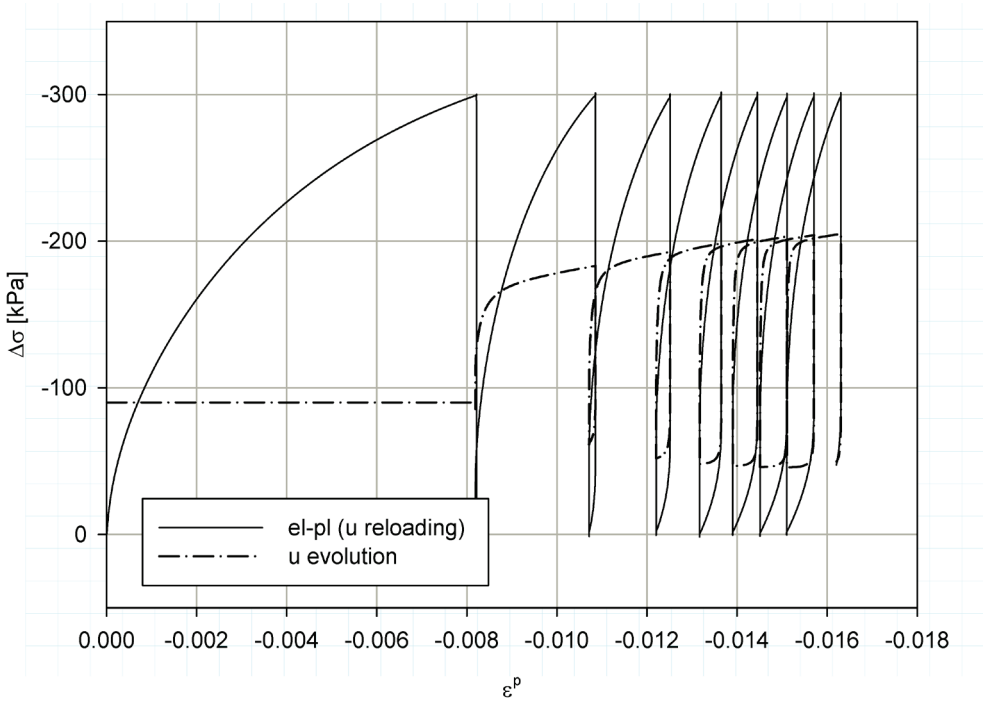

Figure 88 - Evolution of the small *u* parameter vs. plastic strain.

Figure 86 and Figure 87 report respectively the same test carried out with a fixed *u* and variable *u* parameter. The entity of the total plastic strain is considerably different due to a more stiff stress-strain curve and to loops more pronounced in the second case as it was expected.

Finally Figure 88 shows the evolution of the *u* parameter, which increases in the loading phase inducing a more stiff response of the soil and decreases in the unloading phase for a more gentle curvature respecting the *Masing effect* which has been observed experimentally [54].

5.1.8. F.E. analyses

The model answer in the previous two cases is in fully accordance with the expectations, consequently the routines has been implemented in the F.E. program PLASCON 3D for a computation on a boundary value problem, which prepares the ground for the future use of the numerical code in real predictive simulations. The routines related to the extended subloading surface model presented in the flow chart of Figure 23 are responsible for the setting up of the local stiffness matrices of each element which are then assembled in the global ***K***.

Due to the preliminary evolution of the study the simulation has been carried out on a small number of elements in order to check the correct implementation and behaviour of the constitutive model.

Figure 90 underlines the differences among all these approaches. The simple subloading surface clearly overestimates the total deformation, which is reduced in the extended formulation with a fixed small *u* parameter and it is further adjusted when eq.(3.129) is considered. A detail of the last two

curves is offered in Figure 91 where can be better appreciate the strain entities when the modification of the reloading curve is taken into account. Moreover the same comparison has been made by considering stress vs. plastic axial strains (Figure 92).

For the reloading modification curve case the evolution of the similarity centre and the conjugate back stress are depicted in Figure 93. As seen for the other examples (i.e. one dimensional and three dimensional single Gauss point algorithm) the similarity centre translates in the stress space following the plastic flow while the subloading surface expands. During the unloading phase (i.e. shrink of the subloading surface) no irreversible deformation is induced until the stress intersects the similarity centre. Staring from that point plastic strains in the opposite direction are generated allowing the formation of a close loop together with the next loading phase.

Different behaviour can be described for the conjugate back stress. It decreases during the loading phase while instead increases in the unloading one as depicted in the graph.

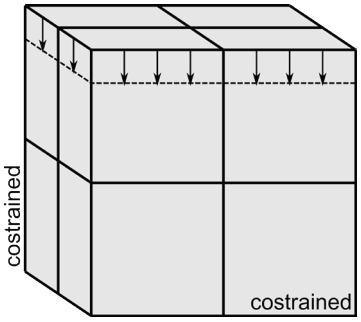

Figure 89 – sketch of the constrain and loading conditions.

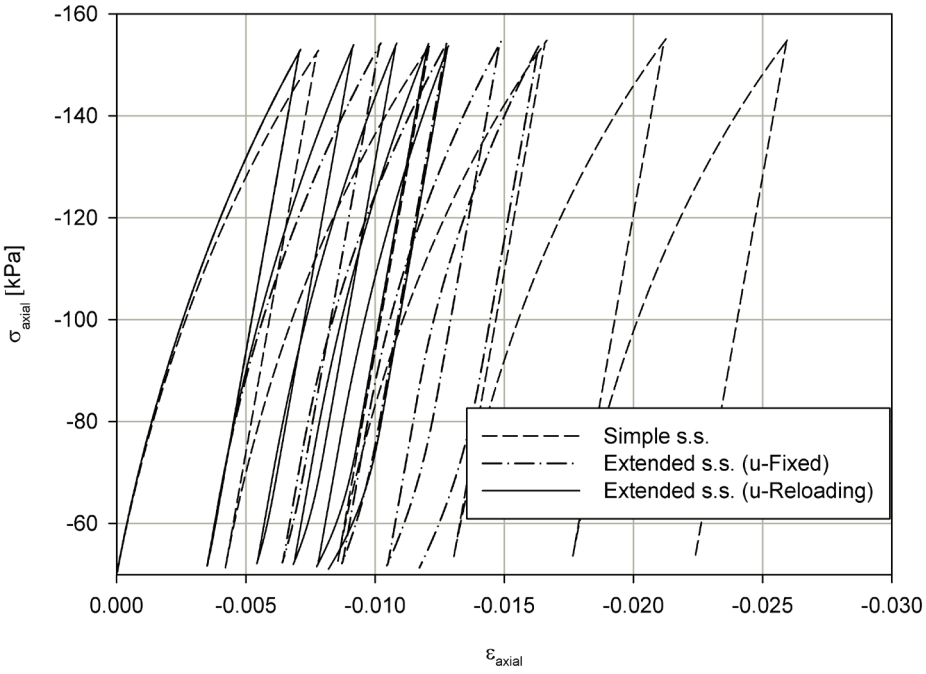

Figure 90 - Simple vs. extended subloading surface (with modification and not of the reloading curve).

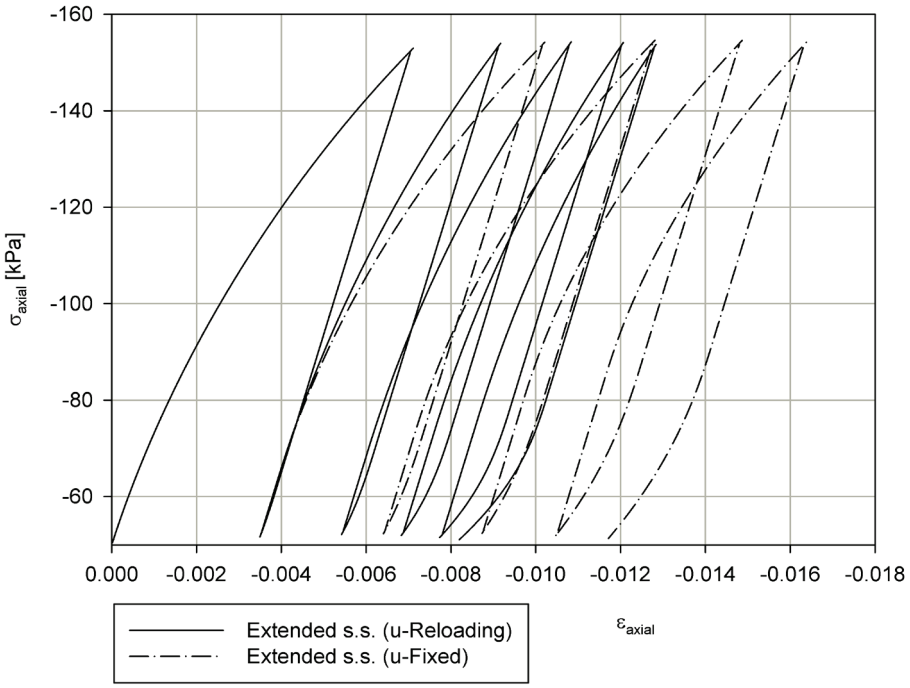

Figure 91 - extended subloading surface (with detail).

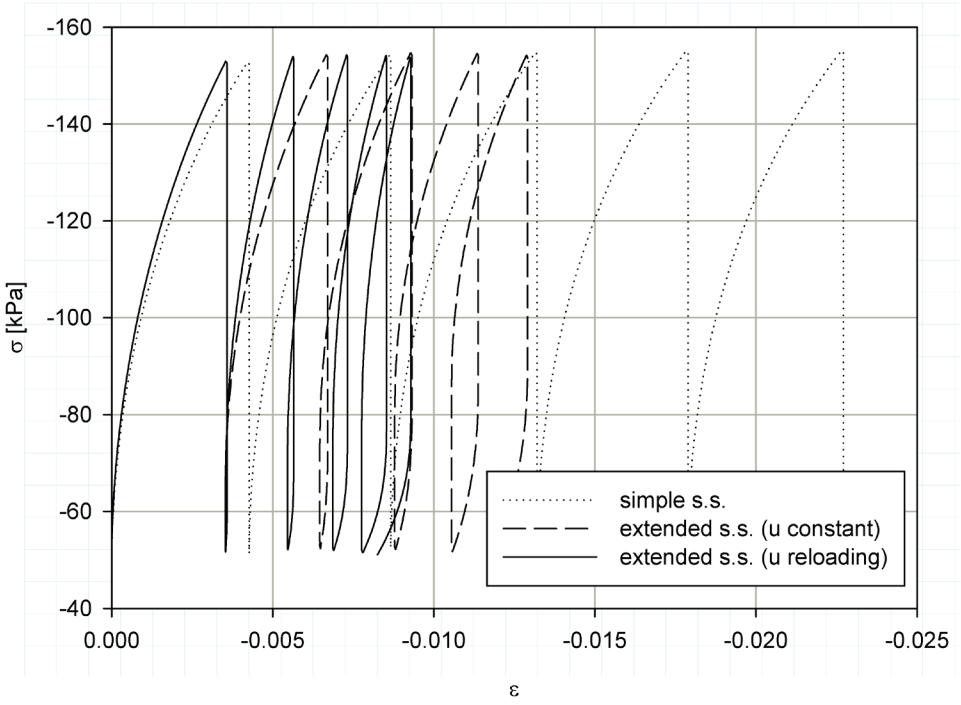

Figure 92 - Stress vs. plastic strain for the two models.

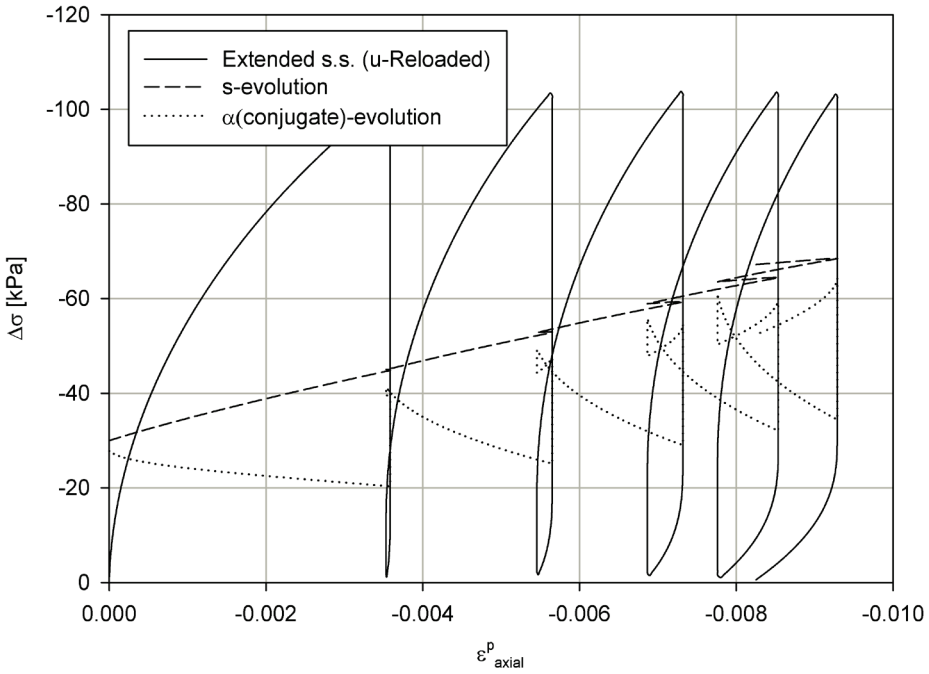

Figure 93 - Evolution of the similarity centre and the conjugate back stress vs. axial strain.

The same behaviour investigate in the three dimensional single Gauss point code, in Figure 88, is here found again for the modification of the reloading curve.

It has to be noticed that during the first loading unloading cycle no modification of the *u* parameter should be generated because the soil experiences for the first time a change in the stress state so the answer should be the one for an undisturbed material.

This can be observed comparing the stress strain curve for the algorithm with and without the modification of the reloading curve where there is a perfect overlap of the two lines and the first differences arise in the second cycle.

Last simulation presented in Figure 95 is a small stress amplitude analysis for the sample. As explained before this kind of analysis is quite relevant to analyze the plastic strains accumulation when a small perturbation of the stress state is created.

The graph compares the curves carried out with and without the modification of the reloading curve. In the next Figure 96 it is quite clear that similarity centre evolution is monotonically increasing since no intersection happens with the stress state in the unloading phase; it thus starts moving from the same point when the next load is applied without creating close loops.

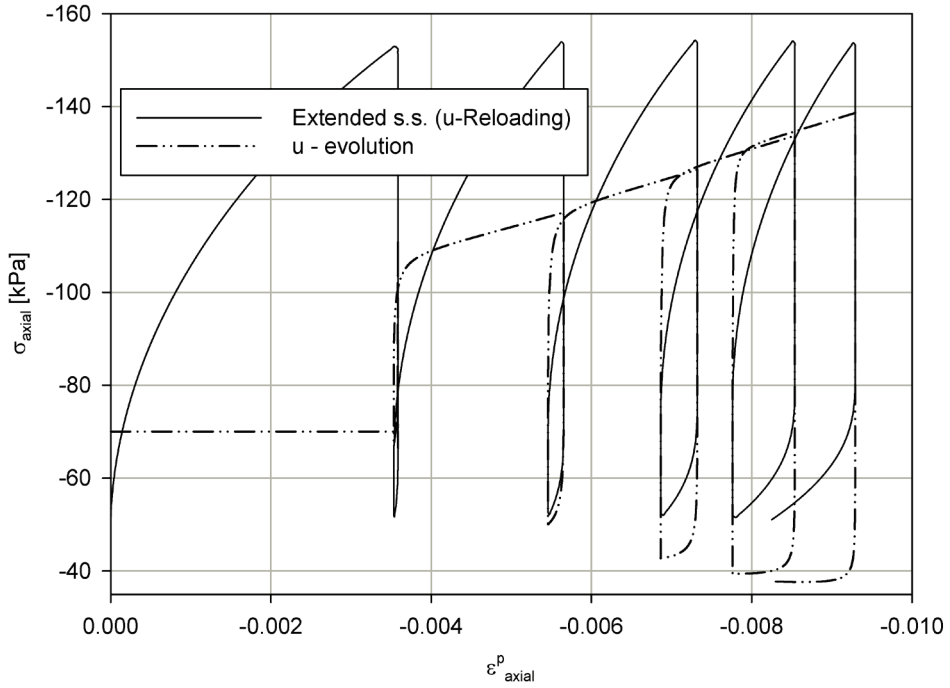

Figure 94 - *u* parameter evolution.

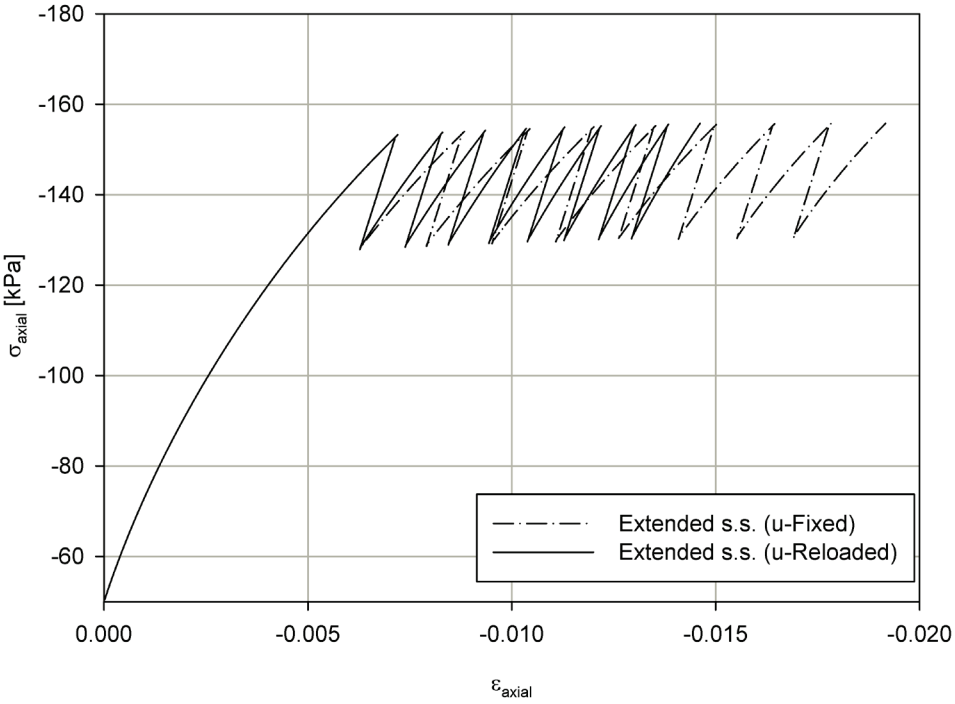

Figure 95 - Small amplitude analysis in a F.E. code.

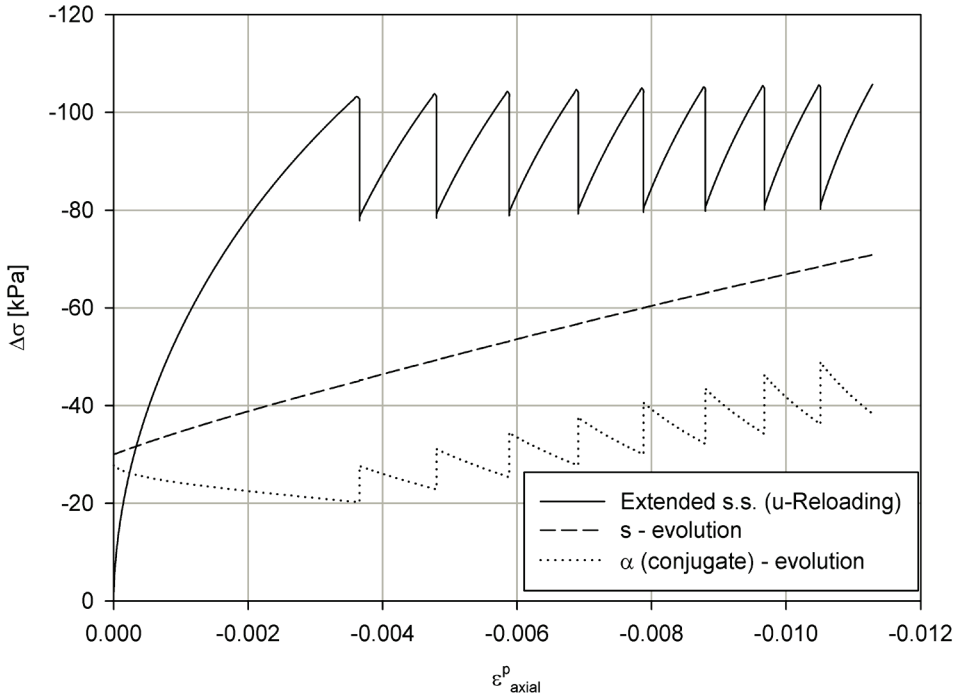

Figure 96 - Similarity centre and conjugate back stress evolution in the F.E. code.

References

[1] Siriwardane H.J., Desai C.S. (1981), "Two numerical schemes for non linear consolidation", *Int. Num. Meth. Eng.*, **17**, pp. 405-426.

[2] Poland J (Ed.)., (1984), "Guidebook to Studies of Land Subsidence due to Groundwater withdrawal", UNESCO, Paris.

[3] Terzaghi K., (1923), „Die Berechnung der Durchlassigkeitsziffer des Tones aus dem Verlauf der hydrodynamischen Spannungserscheinungen", *Akademie der Wissenchaften in Wien, Sitzungsberichte, Mathematisch-naturwissenschaftliche Klasse*, Part Iia, 1923; **132**(3/4): 125-138.

[4] Bishop A.V.,(1959), "The principle of effective stress". *Teknisk Ukeblad*, 106(39): 859-863.

[5] Lewis R.W., Schrefler B.A., (1982), "A finite element simulation of the subsidence of gas reservoirs undergoing a waterdrive". In: RH Gallagher, DH Norrie, JT Oden, OC Zienkiewicz (Eds.), *Finite Element in Fluids*, Wiley: Chichester, **4**, 179-199.

[6] Nuth M., Laloui L., (2008), "Effective stress concept in unsaturated soils: Clarification and validation of a unified framework", *International Journal for Numerical and Analytical Methods in Geomechanic*, **32**, pp. 771-801. DOI:10.1002/nag.645.

[7] Alonso E.E., Gens A., Josa A., (1990), "A constitutive model for partially saturated soils", *Geotechnique*, 40(**3**), pp. 405-430.

[8] Wiborg R., Jewhurst J., (1986), "Ekofisk subsidence detailed and solution assessed. Technology", *Oil and Gas Journal*, 2(1), pp. 47-51.

[9] Delage P., Schroeder C., Cui Y.J., (1996), "Subsidence and capillary effects in chalks". *Proceedings Eurock'96*, Balkema: Rotterdam, pp. 1291-1298.

[10] Chin L.Y., Nagel N.B., (2004), "Modeling of Subsidence and Reservoir Compaction under Waterflood Operations", *International Journal of Geomechanics*, 4(1), pp. 28-34.

[11] Collin F., Cui Y.J., Schroeder C., Charlier R., (2003), "Mechanical behaviour of chalk reservoir: Numerical modeling of water sensitivity and time dependence effects", *Proceedings ISRM 2003-Technology roadmap for rock mechanics*, South African Institute of Mining and Metallurgy, pp. 219-224.

[12] Eurock98, (1998), *Proceedings SPE/ISRM Rock Mechanics in Petroleum Engineering*, Trondheim, Norway, July 8-10, 1/2.

[13] Proceedings SPE/ISRM Rock Mechanics Conference. Irving, TX, USA, October 20-23, 2002.

[14] Kohler R., Hofstetter G., (2008), "A cap model for partially saturated soils", *Int. J. for Num. Anal. Meth. in Geomech.*, 32, pp. 981-1004. DOI:10.1002/nag.658.

[15] Schrefler B.A., Bolzon G., Salomoni V., Simoni L., (1997), "On compaction in gas reservoirs", *Atti dell'Accademia Nazionale dei Lincei* - Rendiconti Lincei: Scienze Fisiche e Naturali, s. IX, VIII(4): 235-248.

[16] Simoni L., Salomoni V., Schrefler B.A., (1999), "Elastoplastic subsidence models with and without capillary effects", *Comp. Meth. in App. Mech. and Eng.*, 171(3-4), pp. 491-502.

[17] Menin A., Salomoni V.A., Santagiuliana R., Simoni L., Gens A., Schrefler B.A., (2008), "A mechanism contributing to subsidence above gas reservoirs", Int. J. for Comp. Meth. in Eng. Sci. & Mech., 9(5), pp. 270-287. DOI: 10.1080/15502280802225234.

[18] Yale D.P., (2002), "Coupled geomechanics-fluid flow modelling: effects of plasticity and permeability alteration", *SPE/ISRM Rock Mechanics Conference*, Irving, TX, USA, October 20-23, SPE/ISRM 78202, 10 pp.

[19] Needleman A., (1988), "Material rate dependence and mesh sensitivity in localization problems", *Comp. Meth. App. Mech. Eng.*, **67**, pp. 69-86.

[20] Garikipati K., Hughes T.J.R., (1998), "A study of strain localization in a multiple scale framework - the one dimensional problem", *Comp. Meth. App. Mech. and Eng.*, **159**, pp.193-222.

[21] Zhou H., Randolph M.F., (2007), "Computational Techniques and Shear Band Development for Cylindrical and Spherical Penetrometers in Strain-Softening Clay", Int. J. of Geomech., **7**(4), pp. 287-295.

[22] Pietruszczak S., Mroz Z., (1981), "Finite element analysis of deformation of strain softening materials", *Int. J. for Num. Meth. in Eng.*, **17**, pp. 327-334.

[23] Willam K., (1984), "Experimental and computational aspects of concrete failure". In: F. Damjanic (Ed.), *Computer Aided Analysis and Design of Concrete Failure*. Pineridge Press: Swansea, pp. 33-70.

[24] Grammatikopoulou A., Zdravkovic L., Potts D.M., (2006), "General Formulation of Two Kinematic Hardening Constitutive Models with a Smooth Elastoplastic Transition", *Int. J. of Geomech.*, **6**(5), pp. 291-302.

[25] Eringen A.C., (1965), "Theory of micropolar continuum", *Proceedings 9th Midwestern Mechanical Conference*, University of Wisconsin, Madison, Wisconsin, pp. 23-40.

[26] Kroner E., (1967), "Elasticity theory of material with long-range cohesive forces", Int. J. of Solid and Struct., **3**, pp. 731-742.

[27] Bažant Z.P., Cedolin L., (1991), "Stability of Structures". *Oxford University Press*: NY.

[28] Marotti de Sciarra F., (2008), "A general theory for nonlocal softening plasticity of integral-type", Int. J. of Plast., **24**, pp. 1411-1439.

[29] Yamakawa Y., Hashiguchi K., Ikeda K., (2010), "Implicit stress-update algorithm for isotropic Cam-clay model based on the subloading surface concept at finite strains", Int. J. of Plast., **26**(5), pp. 634-658.

[30] Hashiguchi K., Saitoh K., Okayasu T., Tsutsumi S., (2002), "Evaluation of typical conventional and unconventional plasticity models for prediction of softening behaviour of soils". *Geotechnique*, **52**(8), pp. 561-578.

[31] Terzaghi K., Peck R.B., (1951) "Soil mechanics in engineering practice", *Wiley Inc.*, NY USA.

[32] Taylor D.W., (1948), *"Fundamental of soil mechanics*", *John Wiley and Sons*, NY USA 1948.

[33] Salomoni V.A., Schrefler B.A., (2005), "A CBS-type stabilizing algorithm fort the consolidation of saturated porous media", *International Journal for Numerical Methods in Engineering*, **63**, pp. 502-527.

[34] Gibson R.E., Schiffman R.L., Pu S.L., (1970), "Plane strain and axially symmetric consolidation of a clay layer on a smooth impervious base", *Quarterly J. of Mech. and App. Math.*, **23**(4), pp. 505-20.

[35] Shandu R.S., Liu H., Singh K.J., (1977), "Numerical performance of some finite element schemes for analysis of seepage in porous elastic media", *Int. J. for Num. and Anal. Meth. in Geomech.*, **1**, pp. 177-194.

[36] Shafiqu Q.S.M., (2008), "Finite element analysis of consolidation problems in several types of cohesive soils using the bounding surface model", *ARPN J. of Eng. and App. Sci.*, **3**(6): pp. 51-57.

[37] Supangkat H., (1994), "On finite element analysis of nonlinear consolidation", *Master Thesis*, Massachusetts Institute of Technology, Dept. of Mechanical Engineering, 1994 (http://hdl.handle.net/1721.1/37795).

[38] Schrefler B.A., Lewis R.W., Majorana C.E., (1981), "Subsidence above volumetric and waterdrive gas reservoirs", *Int. J. for Num. Meth. in Fluids*, **1**(2), pp. 101-15.

[39] Lewis R.W., Schrefler B.A., (1987), "The finite element method in the deformation and consolidation of porous media", *Wiley*, Chichester.

[40] Lewis R.W., Schrefler B.A., (1998), "The finite element method in the static and dynamic deformation and consolidation of porous media", *Wiley*, Chichester.

[41] Schrefler B.A., Wang X., Salomoni V., Zuccolo G., (1999), "An efficient parallel algorithm for three-dimensional analysis of subsidence above gas reservoirs", *Int. J. for Num. Meth. in Fluids*, **31**(1): 247-60.

[42] Carbognin L., Gatto P., Mozzi G., Gambolati G., (1978), "Land subsidence of Ravenna and its similarities with the Venice case". In: *SK Saxena* (Ed.), Evaluation and Prediction of Subsidence. ASCE: NY, USA, pp. 254-266.

[43] Gambolati G., Ricceri G., Bertoni W., Brighenti G., Vuillermin E., (1991), "Mathematical simulation of the subsidence of Ravenna", *Water Resources Research*, **27**(11), pp. 2899-2918.

[44] Comerlati A., Ferronato M., Gambolati G., Putti M., Teatini P., (2003), "Fluid-dynamic and geomechanical effects of CO2 sequestration below the Venice Lagoon", *Environmental and Engineering Geoscience*, **XII**(3), pp. 211-226.

[45] Schlumberger-GeoQuest. Eclipse Simulator. Version 2003A. Technical Description, Houston, TX, USA, 2003.

[46] Baù D., Gambolati G., Teatini P., (2000), "Residual land subsidence near abandoned gas fields raises concern over Northern Adriatic coastland", *Eos*, **81**(22), pp. 245-249.

[47] AGIP. Progetto Alto Adriatico – Studio di impatto ambientale. AGIP, San Donato, Italy, 1996 (in Italian).

[48] Simo J.C., Huges T.J.R., (1998), "Computation Inelasticity", Springer, Heidelberg.

[49] Skempton A.W., Brown J.D., (1961), "A landslide in boulder clay at Selset, Yorkshire", *Geotecnique*, **11**, pp. 280-293.

[50] Bishop A.W., Webb D.L., Lewin P.I., (1965), "Undisturbed samples of London clay from the Ashford Common shaft: strength-effective stress relationships", *Geotecnique*, **15**, pp. 1-31.

[51] Jiang Y., Zhang J., (2008), "Benchmark experiments and characteristics of static friction of machine tool sideway", *Int. J. Plasticity*, **24**, pp. 1481-1515.

[52] Hashiguchi K., Mase T., (2007), "Extended yield condition of soils with tensile yield strength and rotational hardening", *Int. J. Plasticity*, **23**, pp. 1939-1956.

[53] Namikawa T., Mihara S., (2007), "Elasto-plastic model for cemented sand", *Int. J. Numer. Anal. Meth. Geomech.*, **31**, 71-107.

[54] Masing G., (1926), "Eigenspannungen und Verfestigung beim Messing", in: *Proc. 2nd Int. Congr. Appl. Mech.*, Zurich, pp. 332-335.

6. Conclusions

The present work furnished a framework of plasticity inserted in the a more general context of porous media. The constitutive equation for both conventional and unconventional plasticity are reported in Chapter 3 starting from the definition of the uniaxial bond to the more complicated three dimensional unconventional extended subloading surface model.

The use of the unconventional plasticity models is fundamental for the correct modelling of nonlinear materials. The ability of catching a smooth stress-strain evolution proper of the *subloading surface* and of the *extended subloading surface* models [1] allows to fulfill the smoothness and continuity conditions leading to a more realistic description of soils or metals. Nevertheless the simple and solid mathematical formulation, reported in the early chapters of this thesis, makes possible to reduce the computational effort without recurring to particular numerical techniques as for the conventional theories. The introduction of a mobile similarity centre enriches and enlarges the number of analyses that are possible to deal with this unconventional theory investigating the behaviour of the material under cyclic loading-unloading tests .

As it can be seen in Chapter 5 many analyses have been carried out . The *simple subloading surface* model have been used in a predictive scenario of ongoing subsidence due to gas extraction from submarine reservoirs after calibration and validation tests [2]. The results obtained are quite good and reflect the order of magnitude observed in a field test with the same geological configuration. Moreover the abilities to reproduce a realistic softening behaviour of soils can justify the ongoing settlements even after the closure of the extraction wells. A stable and robust calculation is provided by means of the formulation of the similarity ratio evolution law which allows to obtain solutions for large time steps speeding up the computation. In order to verify the stability of the algorithm and its implementation in the research 3D code PLASCON3D different mesh refinements and time discretizations have been investigated proving the reliability of the results.

A particular numerical algorithm known as *return mapping* [3] has been used in different simulations for increase the accuracy of the solution when a small number of time steps is required. This is due to the fact that in the subyield state no controlling function of the stress is provided both in the conventional and unconventional models inducing an error which is related to the size of the time discretization. The return mapping in the *cutting plane* form has been implemented in a one-dimensional, three dimensional quadrature point and F.E. programs to test the goodness of the results. In the first case the use of this numerical technique produces reliable results showing a perfect stability of the solution when reducing the number of time steps and the correct evolution of the model parameters. Some problems arise when a three dimensional model has taken into account due to the variability of the normalized normal vectors on the yield surface. When the time step size becomes considerably big the difference between the vector to the plastic surface in the actual position (n) and the one in the subsequent ($n+1$) induces some errors in the computation of the plastic relaxation. This effect cannot be seen in metals due to a simple shape of the yield surface which maintains constant the orientation of the normal vector. The *iso-error* map traced for soils is in agreement with the one formulated by [3].

A shift of the yield surface has been consider, in accordance with [4], to evaluate the soil tensile strenght by implementing the updated constitutive equation in a three dimensional single Gauss point program and then in the PLASCON 3D. Results have been compared with experimentation carried out by [5] revealing a good response of the model.

The last analyses carried out deal with the response of soil under a cyclic loading-unloading analysis [6]. It's quite clear that in this context conventional theories are not capable to catch the plastic cumulative deformations because of the neat distinction in two different domains: linear elastic and plastic. Once the yield surface has expanded the point immediately comes back into the elastic domain when the stress level decreases giving pure reversible strains. In reality when a repeated cycle of loading and unloading is realized (for example vibrations) irreversible contributes arise. The only way to describe this phenomena is that to introduce a moving similarity centre point into the subloading surface. According to the constitutive equations reported in paragraph 3.2.5 the algorithm has been updated and implemented in a uniaxial, three dimensional and finally in the F.E. codes as in the previous cases. Among all the cyclic plasticity models the *extended subloading* one appears to be the only with a solid mathematical formulation which respects all the mechanical requirements aimed to be a useful instrument in soil behaviour prediction [7].

Additionally the modification of the reloading curve has been investigated to fulfill the Masing effect and not to overestimate the model response. The analyses carried out deal with simple cases with few elements due to the preliminary study on this theory. However it must be point out that all the curves obtained and the graphs are in full agreement with the theory.

At least an innovative coupling between plasticity and visco-elasticity has been made for concrete using the subloading surface formulation together with the Maxwell-chain model assuming model B3 for the compliance function. Also in this case the number of elements in the analyses is not so relevant due to the preliminary level of the study but the numerical behaviour of the algorithm shows encouraging and promising results.

A lot of further future developments can be carried out starting from the work presented in this thesis. The investigation of the role of the temperature in the elastoplastic constitutive equations (especially for high temperature concrete), the change of permeability in the material response or the extension to the finite strains theory are just some of the possible fields of interest for this unconventional plasticity algorithm combined with the F.E. research code PLASCON 3D.

References

[1] Hashiguchi K.,(2009), “Elastoplasticity theory - Lecture notes in applied and computational mechanics”. In: F Pfeiffer, P Wriggers (Eds.), Springer, Berlin, **42**, 393 pp.

[2] Siriwardane H.J., Desai C.S. (1981), “Two numerical schemes for non linear consolidation“, *Int. Num. Meth. Eng*., **17**, pp. 405-426.

[3] Simo J.C., Huges T.J.R., (1998), “Computation Inelasticity”, Springer, Heidelberg.

[4] Hashiguchi K., Mase T., (2007), “Extended yield condition of soils with tensile yield strength and rotational hardening”, *Int. J. Plasticity*, **23**, pp. 1939-1956.

[5] Namikawa T., Mihara S., (2007), “Elasto-plastic model for cemented sand”, *Int. J. Numer. Anal. Meth. Geomech.*, **31**, 71-107.

[6] Hashiguchi K., (1993b), “Mechanical requirements and structures of cyclic plasticity model”, *Int. J. of Plasticity*, **9**, pp. 721-748.

[7] Hashiguchi K., Chen Z.P., (1998), “Elastoplastic constitutive equations of soils with the subloading surface and the rotational hardening”, *Int. J. Numer. Anal. Meth. Geomech.*, **22**, pp. 197-227

7. **Appendix** - visco elasticity and plasticity

The coupled hydro-(thermo-)mechanical state in geomaterials (specifically, concretes) is here evaluated making reference to the subloading surface model when referring to the material plastic response. Particularly, an upgraded version (VEP3D) of the F.E. research code NEWCON3D describing concrete as a porous medium has been developed so to innovatively couple creep (via the Maxwell-chain model assuming model B3 for the compliance function), shrinkage and damage (via the Mazars' damage model) with unconventional plasticity, the latter allowing for the abolition of the distinction between the elastic and plastic domain and for giving a smooth response in a smooth monotonic loading process. The approach has allowed for taking advantages of the main features of the subloading surface model, already evidenced when dealing with soils, and to successfully enrich the material constitutive law for reaching a more complete mathematical-numerical description of geomaterials behaviour at the macro-scale and at the meso-scale level as well.

7.1. Introduction

Concrete is here treated as a multiphase system where the voids of the skeleton are partly filled with liquid and partly with a gas phase [1], [2]. The liquid phase consists of bound water (or adsorbed water), which is present in the whole range of water contents of the medium, and capillary water (or free water), which appears when water content exceeds so-called solid saturation point, i.e. the upper limit of the hygroscopic region of moisture content. The gas phase, i.e. moist air, is a mixture of dry air and water vapour, and is assumed to behave as an ideal gas. The approach here is to start from a phenomenological model (see e.g. [3], [4]), originally developed by Bažant and co-authors, e.g. [5], [6], in which mass diffusion and heat convection-conduction equations are written in terms of relative humidity, appropriately modified to take into account different phases as well as high ranges of both pressure and temperature. The proposed model couples non-linear material with experimental relations. As regards the mechanical field, NEWCON3D couples shrinkage, creep (via Model B3 [7], [8]) and damage (via Mazars' damage model [9]) effects under medium and high temperature levels; particularly, the code has now been upgraded (version VEP3D) to take into account a plastic response by means of the subloading surface model (see e.g. [10], [11]) whose main features have been already evidenced when dealing with soils [12], [13], being particularly relevant its ability of predicting softening behaviour when considering over-consolidated states.

7.2. The mathematical-numerical model

The coupled system of differential equations for dealing with humidity diffusion and heat transport can be written in the form [8]

$$k\frac{\partial h}{\partial t}-\nabla^T\mathbf{C}\nabla h-\frac{\partial h_s}{\partial t}-K\frac{\partial T}{\partial t}+\bar{\alpha}\mathbf{m}^T\frac{\partial \boldsymbol{\varepsilon}}{\partial t}=0 \tag{5.1}$$

$$\rho C_q\frac{\partial T}{\partial t}-\nabla^T\boldsymbol{\Lambda}\nabla T-\frac{\partial Q_h}{\partial t}=0 \tag{5.2}$$

where k is the cotangent of the isotherm slope, **C** is the (relative humidity) diffusivity diagonal matrix, dh_s the self-dessication, K the hygrothermic coefficient, $\mathbf{m}=\{1\quad 1\quad 1\quad 0\quad 0\quad 0\}^T$, $\bar{\alpha}=\left(\frac{\partial \mathrm{h}}{\partial \boldsymbol{\varepsilon}_{\mathrm{v}}}\right)\Big|_{\mathrm{T,w}}$ equals the change in h due to unit change of volumetric strain ε_v at constant moisture content w and temperature T, ρC_q is the thermal capacity, $\boldsymbol{\Lambda}$ the thermal conductivity diagonal matrix and Q_h the outflow of heat per unit volume of solid. The last term in (5.1) represents the coupling term for connecting hygro-thermal and mechanical responses [14].

The linear momentum balance equation for the whole multiphase medium, neglecting inertial forces, is

$$\nabla\dot{\boldsymbol{\sigma}}=0 \tag{5.3}$$

where $\boldsymbol{\sigma}$ is the total stress tensor; no variable body forces are accounted for.

The mechanical behaviour of a three-dimensional viscoelastic body is fully described by two creep or relaxation functions. If $\nu(t,t')=\nu(t)$ (with $\nu(t,t')$ the generalized Poisson's ratio for viscoelastic materials, $\nu(t)$ the elastic Poisson's ratio at time t, t' referring to the time of loading), one relaxation or creep function only is sufficient to describe such a behaviour. In the following, $\nu(t,t')=\nu(t)$ = constant is assumed [15].

The constitutive relationship, accounting for the coupling between creep and damage (directly extending the superposition principle to our case and referring to the non-local Mazars' damage model) can be written as

$$\boldsymbol{\sigma}(t)=\left[1-D\left(\tilde{\varepsilon}^*(t)\right)\right]\int_0^t\mathbf{D}'\sum_{\mu=1}^{n}E_\mu(t'_e)e^{\left[y_\mu(t'_v)-y_\mu(t_v)\right]}\left[d\boldsymbol{\varepsilon}(t)-d\boldsymbol{\varepsilon}^p(t)-d\boldsymbol{\varepsilon}^0(t)\right] \tag{5.4}$$

in which the damage factor is simply considered as a stress multiplier, depending on the current strain only (precisely, on the strain dependent on stresses $\varepsilon^*(\bar{t})=\varepsilon(\bar{t})$, with t being fixed); $\boldsymbol{\varepsilon}^p$ is the plastic strain contribution and $\boldsymbol{\varepsilon}^0$ refers to imposed deformations, not related to stresses (e.g. due to effects of chemical nature). Particularly, in equation (5.4) the relaxation function (dual to the creep function J(t,t') [7], [8] taking the form –via model B3-

$$J(t,t')=q_1+C_0(t,t')+C_d(t,t',t_0) \tag{5.5}$$

with q_1 the instantaneous strain due to unit stress, $C_0(t,t')$ compliance function for basic creep and $C_d(t,t',t_0)$ additional compliance function due to drying, t_0 referring to the age at the start of drying) is

expressed via a degenerate form (in agreement with the Maxwell-Chain model) and it includes hydration, humidity and temperature effects on creep velocity via t_e, t_v (named equivalent times), being $y_\mu(t) = \left(t / \tau_\mu \right)^{q_\mu}$ reduced times (μ = 1, 2, ..., N) [[9]]; ***D***' is given by

As regards plasticity, the subloading surface model is here briefly recalled in its main features.

$$\mathbf{D}^{\bullet -1} = \begin{bmatrix} 1 & -\nu & -\nu & 0 & 0 & 0 \\ & 1 & -\nu & 0 & 0 & 0 \\ & & 1 & 0 & 0 & 0 \\ & & & 2(1+\nu) & 0 & 0 \\ & & & & 2(1+\nu) & 0 \\ & & & & & 2(1+\nu) \end{bmatrix} \tag{5.6}$$

The subloading surface model use the same set of equations presented in chapter 3 and, even in this case, affects only the stiffness matrix for the solid phase. The only difference is due to the fact that the computation is no longer incremental as seen before for the other numerical code.

The idea has been that to subdivide the main time-step in a series of sub-steps creating a *fake* incremental plastic problem easy to be solved. Once the correct plastic strain increment is computed, total plastic deformations are updated and added in the total visco-elastic and plastic problem. This is theoretically based on the fact that, by considering small strains, plastic effects can be seen as a coaction of the viscous one, so the former can be computed separately and then included within the latter. The whole procedure requires a certain amount of memory to allow the sub-steps to store the intermediate vectors solution and to recall them back when necessary to compute the stress and strain rate. Figure 97 graphically schematizes the different passages that will be explained in the next section.

The application, within the numerical code VEP3D, of a standard Finite Elements discretization in space of equations (5.1) and (5.2) results in

$$\begin{bmatrix} \mathbf{L}^T & \mathbf{S} & \mathbf{TH} \\ \mathbf{0} & \mathbf{0} & \mathbf{TS} \end{bmatrix} \begin{Bmatrix} \dot{\overline{\mathbf{u}}} \\ \dot{\overline{\mathbf{h}}} \\ \dot{\overline{\mathbf{T}}} \end{Bmatrix} + \begin{bmatrix} \mathbf{0} & \mathbf{Q} & \mathbf{0} \\ \mathbf{0} & \mathbf{0} & \mathbf{TR} \end{bmatrix} \begin{Bmatrix} \overline{\mathbf{u}} \\ \overline{\mathbf{h}} \\ \overline{\mathbf{T}} \end{Bmatrix} = \begin{Bmatrix} \dot{\mathbf{HG}} \\ \dot{\mathbf{TG}} \end{Bmatrix} \tag{5.7}$$

where $\overline{\mathbf{u}}$, $\overline{\mathbf{h}}$, $\overline{\mathbf{T}}$ are the nodal values of the main variables as seen in chapter 2, and the other term can be summarized as:

- $\mathbf{L}^T = \int_\Omega \mathbf{N}^T \mathbf{m}^T \bar{\alpha} \mathbf{B} d\Omega$ is the coupling matrix representing the influence of the solid deformation in the continuity equation;
- $\mathbf{S} = \int_\Omega \mathbf{N}^T k \mathbf{N} d\Omega$ the coupling matrix representing the effect of the sorption isotherm;

- $\mathbf{TH} = -\int_\Omega \mathbf{N}^T K \mathbf{N} d\Omega$ the coupling matrix accounting for the influence of temperature in the equation of humidity diffusion;
- $\mathbf{Q} = \int_\Omega (\nabla \mathbf{N})^T \mathbf{C} (\nabla \mathbf{N}) d\Omega$ the matrix of humidity diffusion;
- $\mathbf{TS} = \int_\Omega \mathbf{N}^T \rho C_q \mathbf{N} d\Omega$ the matrix of heat capacity;
- $\mathbf{TR} = -\int_\Omega (\nabla \mathbf{N})^T \mathbf{\Lambda} (\nabla \mathbf{N}) d\Omega$ the matrix of thermal transmission;
- $\mathbf{HG} = \int_\Omega \mathbf{N}^T h_s d\Omega$: $\partial \mathbf{HG}/\partial t$ represents the humidity variation due to self-desiccation;
- $\mathbf{TG} = \int_\Omega \mathbf{N}^T Q_h \mathbf{N} d\Omega$: $\partial \mathbf{TG}/\partial t$ represents the variation in heat flux.

By posing

$$\bar{\mathbf{B}} = \begin{bmatrix} \mathbf{L}^T & \mathbf{S} & \mathbf{TH} \\ \mathbf{0} & \mathbf{0} & \mathbf{TS} \end{bmatrix}, \quad \bar{\mathbf{C}} = \begin{bmatrix} \mathbf{0} & \mathbf{Q} & \mathbf{0} \\ \mathbf{0} & \mathbf{0} & \mathbf{TR} \end{bmatrix}, \quad \bar{\mathbf{x}} = \begin{Bmatrix} \bar{\mathbf{u}} \\ \bar{\mathbf{h}} \\ \bar{\mathbf{T}} \end{Bmatrix}, \quad \bar{\mathbf{F}} = \begin{Bmatrix} \dot{\mathbf{HG}} \\ \dot{\mathbf{TG}} \end{Bmatrix} \tag{5.8}$$

the coupled system (5.7) is written in a more concise form

$$\bar{\mathbf{B}} \frac{d\bar{\mathbf{x}}}{dt} + \bar{\mathbf{C}} \bar{\mathbf{x}} = \bar{\mathbf{F}} \tag{5.9}$$

Integration of equation (5.9) in the time domain by means of a two-point recurrence scheme produces the monolithic system of equations

$$\left[\bar{\mathbf{B}} + \theta \Delta t_n \bar{\mathbf{C}}\right]_{n,\theta} \bar{\mathbf{x}}^{t_{n+1}} = \left[\bar{\mathbf{B}} - \Delta t_n (1-\theta) \bar{\mathbf{C}}\right]_{n,\theta} \bar{\mathbf{x}}^{t_n} + \bar{\mathbf{F}}_{n,\theta} \Delta t_n; \quad \theta = \frac{t - t_n}{\Delta t_n}, \quad \Delta t_n = t_{n+1} - t_n \tag{5.10}$$

On the other side, the linear momentum balance equation (5.3) for the whole mixture has been substituted by an integral approach in the form of the virtual work principle; after time integration by means of a finite difference technique and introducing a spatial finite elements approximation [15], [16], one obtains

$$(\mathbf{K1} - \mathbf{K2}) \bar{\mathbf{u}}^{t_{n+1}} = \mathbf{F}(t_{n+1}) + \mathbf{F}_{ML} + \mathbf{F}_{TH} + \mathbf{F}_{MTH} \tag{5.11}$$

Hence, the final system of equations becomes

$$\begin{bmatrix} \mathbf{K1}-\mathbf{K2} & \mathbf{0} & \mathbf{0} \\ \mathbf{L}^T & \mathbf{S}+\theta\Delta t_n\mathbf{Q} & \mathbf{TH} \\ \mathbf{0} & \mathbf{0} & \mathbf{TS}+\theta\Delta t_n\mathbf{TR} \end{bmatrix} \mathbf{x}^{t_{n+1}} =$$

$$= \begin{bmatrix} \mathbf{0} & \mathbf{0} & \mathbf{0} \\ \mathbf{L}^T & \mathbf{S}-\Delta t_n(1-\theta)\mathbf{Q} & \mathbf{TH} \\ \mathbf{0} & \mathbf{0} & \mathbf{TS}-\Delta t_n(1-\theta)\mathbf{TR} \end{bmatrix} \mathbf{x}^{t_n} + \begin{Bmatrix} \mathbf{F}(t_{n+1})+\mathbf{F}_{ML}+\mathbf{F}_{TH}+\mathbf{F}_{MTH} \\ \dot{\mathbf{HG}}\Delta t_n \\ \dot{\mathbf{TG}}\Delta t_n \end{Bmatrix} \tag{5.12}$$

For a complete description of the model, the reader is referred to [8].

7.3. Constructing the VEP3D procedure

Each main time step has been divided into three sub-steps. As it can be seen in Figure 97, a solution between main step 1 and 2 is computed for every sub-step in a different way: the first one is purely linear-elastic, the second is elasto-plastic and the last one visco-elastic and plastic. In detail, supposing that main step 1 is the first of the analysis, it will be shown how this algorithm works:

❶ sub-step: this sub-step computes the solution in terms of displacements, strains and stresses using a total integral form from the beginning of the analysis. It has to be highlighted that the solution is purely linear elastic. At this point, by knowing the solution at the previous main time step, it is possible to compute the unknown increments (i.e. $\Delta\boldsymbol{\varepsilon}^e$, $\Delta\mathbf{R}1$) which are needed in the second sub-step, and store them in *ad-hoc* vectors. Here, since time at step 1 is zero, the first sub-step can be also regarded as a sort of incremental step, so the rate of the variables are the variables themselves; but for sake of completeness its description has been given in general terms.

❷ sub-step: it is a pure incremental elasto-plastic computation. $\Delta\mathbf{R}1$ is the incremental forces vector applied as boundary condition; thanks to $\Delta\boldsymbol{\varepsilon}^e$ it is possible to set up the elasto-plastic matrix and find the solution of the system. Particularly, the permanent deformations can be estimated by subtracting to the just computed $\Delta\boldsymbol{\varepsilon}^{e,p}$, for the plastic sub-step, the $\Delta\boldsymbol{\varepsilon}^e$ stored at the previous elastic one, so obtaining the $\Delta\boldsymbol{\varepsilon}^p$ vector. This vector contains the plastic strain rates derived by means of the subloading surface model at each Gauss point. Subsequently, this contribution is stored into a cumulative vector (allowing for maintaining memory of the total plastic deformation) so to be added in the next (total) sub-step as a coaction. The same is done for the $\Delta\boldsymbol{\sigma}^p$ term, which is cumulated in an *ad-hoc* vector ($\boldsymbol{\sigma}^p$) for the next sub-step.

❸ sub-step: this third sub-step is the total visco-elastic and plastic one. Here the visco-elastic solution is computed in its integral. Recalling $\boldsymbol{\varepsilon}^p$ vector, this term is introduced in an internal procedure which applies an additional *fake* external system of forces such to induce exactly this deformation. In this way the system of real forces is responsible for the visco-elastic part of the strains whereas the fake one for the plastic. Being the plastic contribution already known, this approach serves as a numerical expedient to consistently take it into account for solving the FE system. It is also to be pointed out that

the deformations derived from the displacements are exactly the sum of the visco-elastic term and the plastic one.

On the other hand, the stresses are treated in a different way, because the fake system of forces does not contribute to stresses computation. Recalling $\boldsymbol{\sigma}^{p}$ vector, which contains the total plastic stress for the actual step, it is possible to perform a stress redistribution modifying the $\boldsymbol{\sigma}^{v.e.p}$ state of stress already estimated in the present sub-step. This is necessary because it is assumed that plasticity governs the equilibrium for the sample: the response in fact is first plastic and then viscous. The procedure described above is repeated at each main step in the same way. For sake of completeness it is to be noticed that, at the first sub-step of the second main step, the strain rate $\Delta\boldsymbol{\varepsilon}^{e}$ and the external load $\Delta\mathbf{R}1$ can be calculated recalling the stored solution at the first sub-step of the previous main step as evident in the flow chart of Figure 97. The loading procedure will be discussed in detail in the next Section.

7.4. The loading procedure

One of the crucial points in the upgraded procedure is the setting up of the right terms of the resolving system (see equation (5.12)). In fact, depending on the different loading histories, the model behaves in a different way. The (unconventional) plastic model used in the analysis is not time dependent, i.e. under a constant load, creep only contributes to deformation. The code differentiates permanent from transient load terms, so that the latter only is introduced in the right hand side of the system above when accounting for the second pure incremental sub-step; in this way the procedure has been changed in agreement with the flow-chart depicted in Figure 98.

RI-LOAD vector contains the permanent load, which affects the viscoelastic deformation part only, whereas **RLOAD** is the transient load vector which is cumulated step by step in the total forces vector **R**. If the analysis starts from step 1, the term $\Delta\mathbf{R}1$, mentioned before, coincides exactly with the transient load vector **RLOAD①.** Thus, this is the right hand term of the system that is to be applied in the second purely incremental plastic sub-step. At this point a vector is to be stored, named **R1M1**, containing the whole forces system applied passing through main step 1 to main step 2 (i.e. **RI-LOAD + RLOAD①**). This allows for correctly estimating $\Delta\mathbf{R}1$ term that is to be used in the plastic sub-step of the second main step. In other words, the correct $\Delta\mathbf{R}1$ load vector in the second main step is exactly equal to **RLOAD②**, which can be obtained by subtracting the **R1M1** vector stored before from the total cumulative forces vector **R1** (= **RI-LOAD** + **RLOAD①** + **RLOAD②**). Hence it can be guaranteed that, if the transient load is null (**RLOAD**n = 0), i.e. the load is just maintained on the sample, **R**1 and **R1M1** coincide and so even $\Delta\mathbf{R}1$ is null and the plastic mechanism is not activated between two steps.

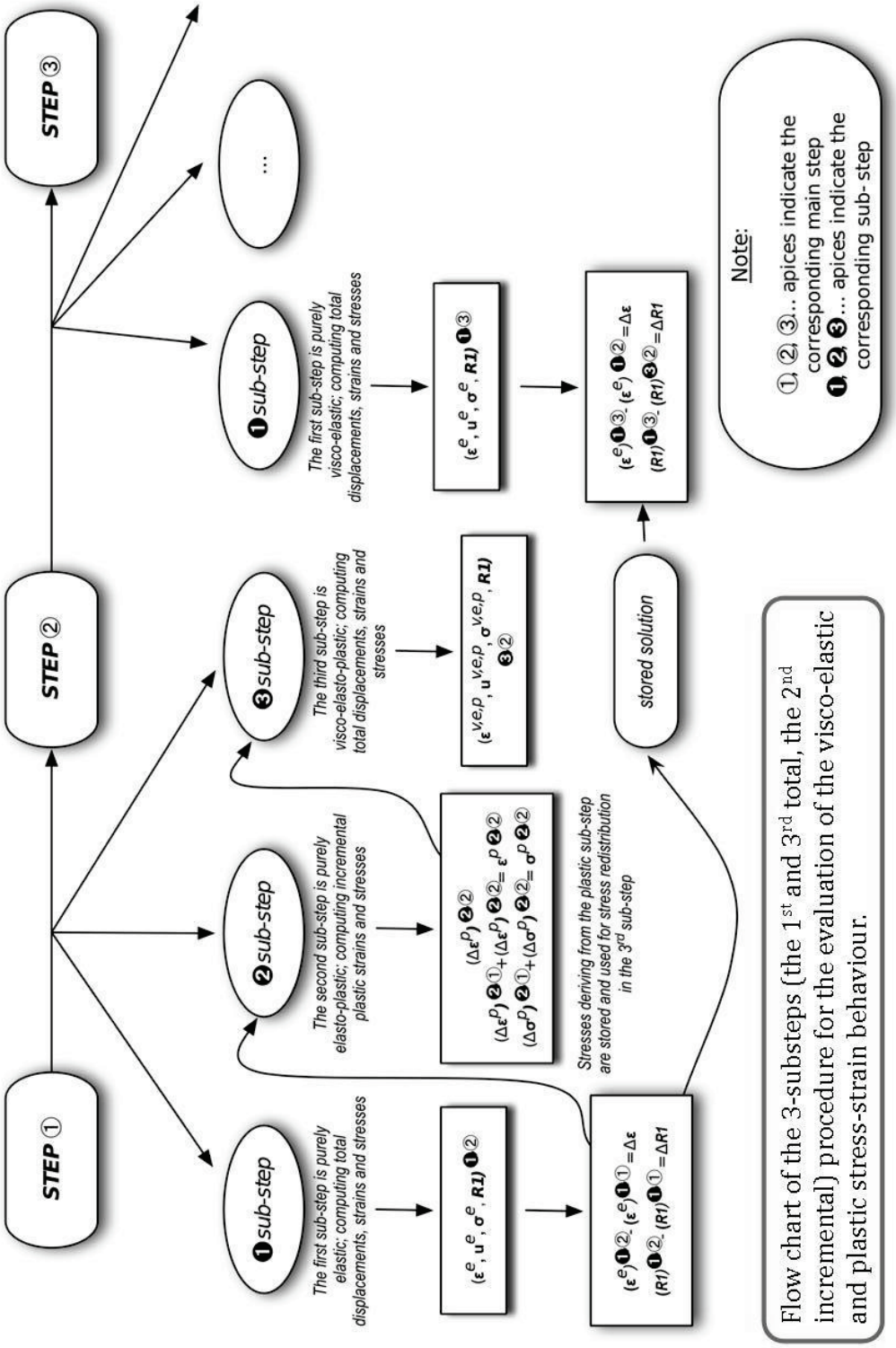

Figure 97 - Visco-elasto-plastic calculation, as implemented in VEP3D code.

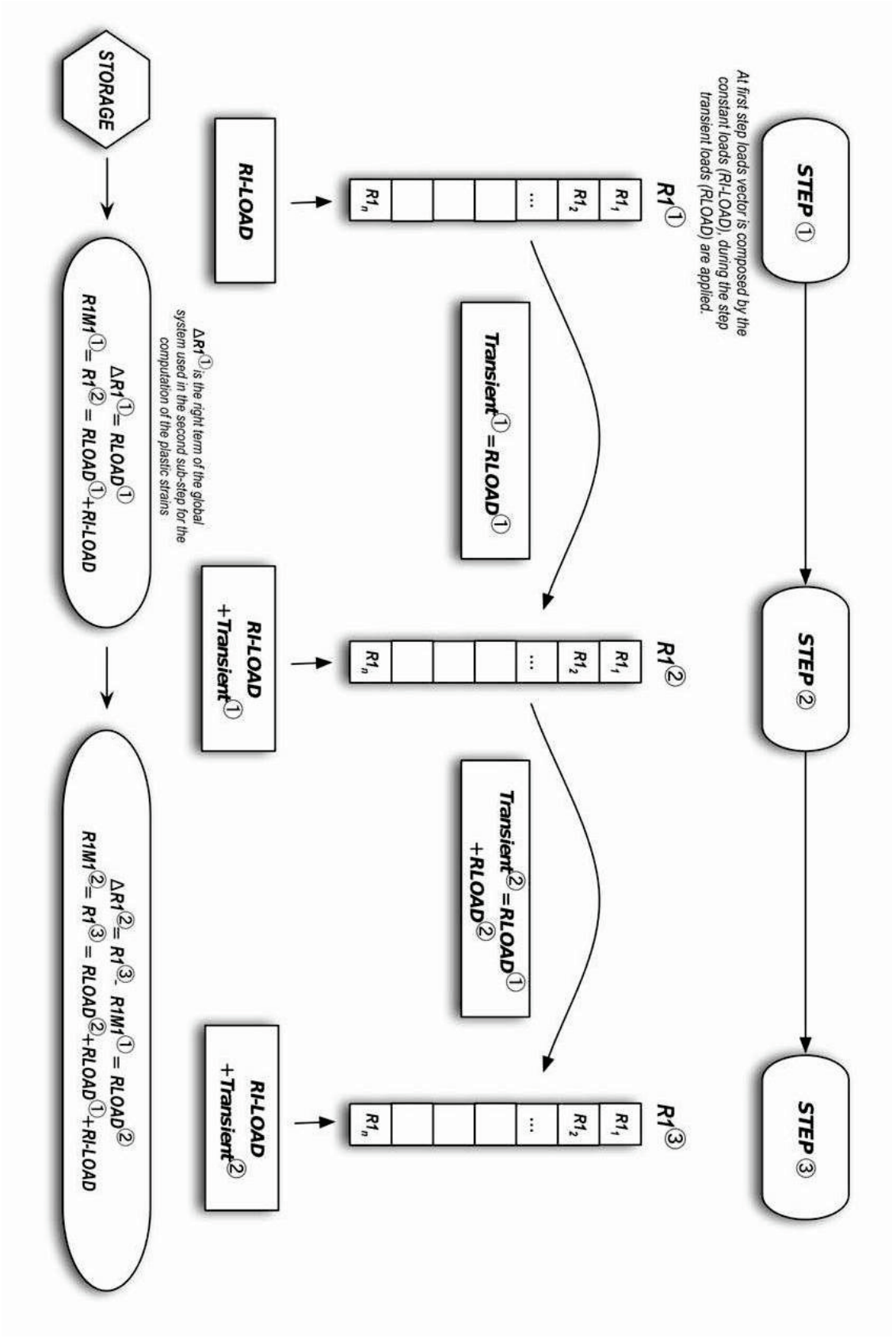

Figure 98- Loading procedure in VEP3D code.

7.5. Numerical analyses

The test sample is composed by 20-node brick elements (Figure 99), with a semi-infinite rigid layer on top to allow for uniformly distributing the applied load.. The block is constrained at the base only, whereas temperature and relative humidity variations are blocked, i.e. basic creep only can be activated.

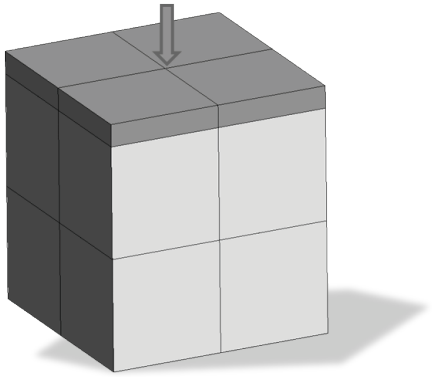

Figure 99 - Sketch of the sample used for the calibration analyses.

In order to calibrate the procedure, two different analyses, with different load conditions, have been carried out:

- ***Case A***: a load is applied from null value up to 400 kN, differentiating its time of application so to evidence the relations between the different elastic-viscous-plastic contributions;
- ***Case B***: the load reaches its maximum value (as before) in a fixed period of time (1 year), left constant for 1 year and then increased up to 800 kN; in this way the contribution of the plastic sub-step is evidenced (e.g. null under constant load).

In Table 11 and Table 12 the adopted material and subloading surface parameters are listed, respectively.

7.5.1. Case A

Figure 100 depicts the stress-strain curves for a typical point at different loading times differentiating the linear elastic (L.E.), the elasto-plastic (E.P.) and the visco-elasto-plastic (V.E.P.) responses: the contribution coming from creep is clearly evident and “stretches” the pure (time independent) E.P. curve towards higher deformation values.

Size [mm3]	200×200×200
v	0.18
Elastic Modulus [N/mm^2]	28522.1
Hydraulic Diffusivity [mm^2/d]	20
Thermal Conductivity [W/m·K]	1.67
Thermal Capacity [N/mm^2·K]	2.112
f_{cm28} [MPa]	36.3
Cement Content [kg/m^3]	350
Water Content [kg/m^3]	171.5
Aggregate-cement ratio	4.82
Age at the start of drying t_0 [d]	2
Age of loading t' [d]	7 - 28 - 90
Axial compressive stress [MPa]	9.07
Environmental Relative Humidity	50%
Environmental Temperature [°C]	20

Table 11 - Material parameters.

ρ'	0.10
γ	0.07
mc	0.82
u	25
F0 [N/mm^2]	62000

Table 12 - Subloading Surface parameters.

Two main observations can be pointed out: a) the stress level is governed by the plastic behaviour of the material, due to a stress re-distribution on the different Gauss points and b) the magnitude of the visco-elastic deformations decreases in time.

The gap between two consecutive curves (the only exception is for the last one which is computed for a very long period of time) decreases at increasing loading times, i.e. creep rates appear as being relevant at early ages whereas they tend to stabilize with concrete aging, as expected both experimentally and theoretically.

Additionally, if we particularly concentrate on the strain histories related to a 10-days and a 1-year loading time, creep effects can be more easily appreciated (Figure 101): for shorter loading times the final plastic deformations are bigger than the viscous ones, despite the fact that creep is stronger for most part of the analysis (in fact E.P. and V.E. curves intersect before the loading history is concluded); differently, for longer loading times the V.E. curve is always below the E.P. one (evidently, at the same load level creep contributions are stronger when longer loading times are accounted for). Moreover, the independence of the elasto-plastic part on time is clear.

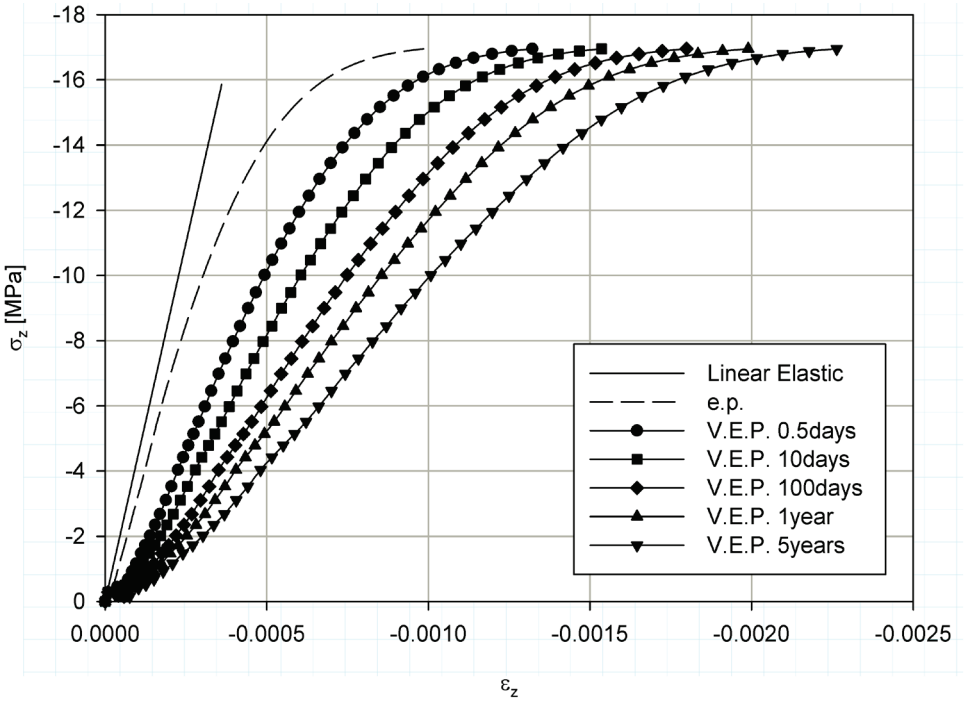

Figure 100 - Stress-strain curves at different loading times.

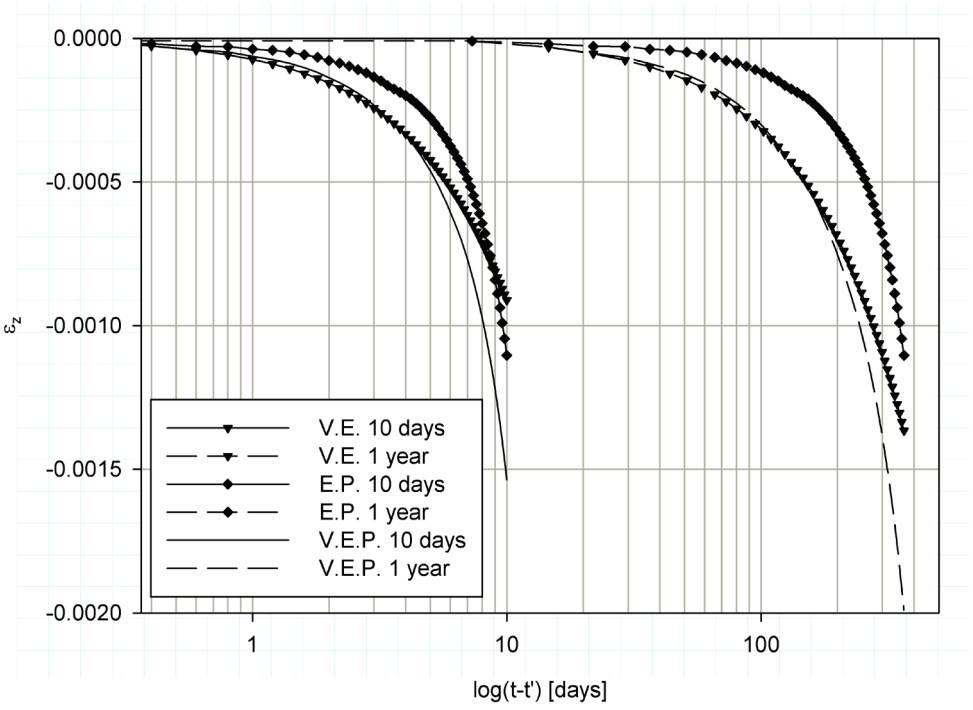

Figure 101 - Strain histories for two loading times.

7.5.2. Case B

In this analysis the same loading time (1 year) is maintained whereas the loading path has been changed so to newly verify the correctness of the implemented algorithms and particularly to check the null contribution of plasticity under constant loads.

A three-step loading path has been fixed, as previously stated, so obtaining the strain history curve of Figure 6: the purely E.P. deformations show, as expected, an horizontal plateau during the phase of constant load whereas pure viscous strains continue to develop; subsequently, during the last loading-step, E.P. deformations overcome V.E. ones.

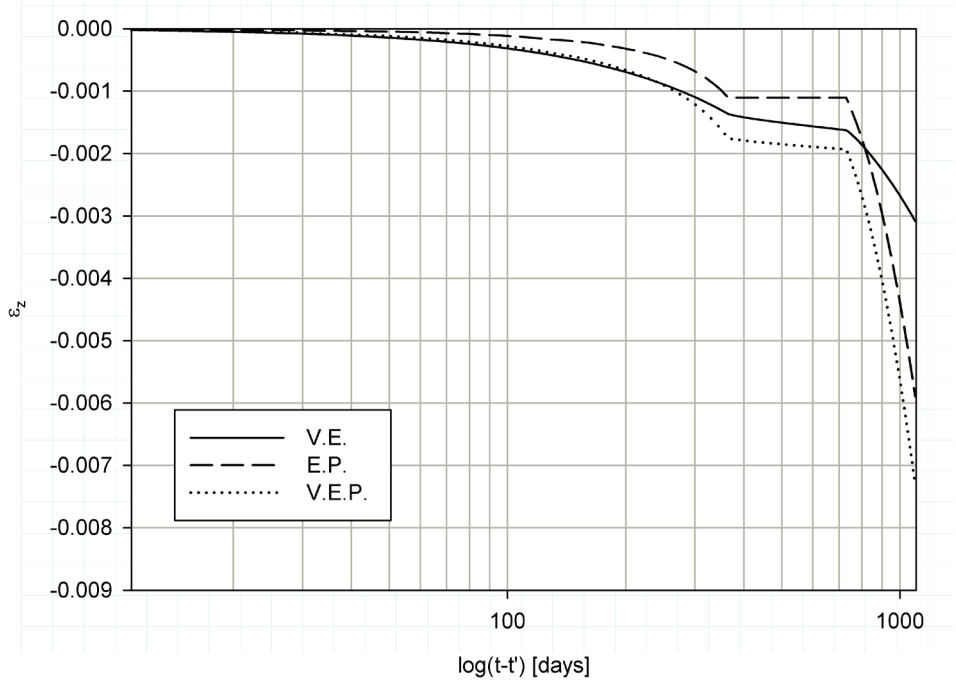

Figure 102 - Strain histories for the three-step loading path.

When considering the corresponding stress-strain law (Figure 103), the independence of the slopes of both the E.P. curve and of the V.E. straight line on the specific load path is shown, being the latter just shifted by a quantity correspondent to the strain value reached under constant load (darker area) whereas the former “frozen” at the same stress-strain point (dot) until reloading. The coupling between the two mechanisms leads to the light dotted V.E.P. curve, for which the stress plateau appears to be moved towards higher strain values (light area).

More importantly, it is to be noticed that apparently the addictive decomposition of strain is not respected, in the sense that total V.E.P. deformations are different from the sum between E.P. and V.E. ones; in reality V.E.P. analyses –for the specificity of the algorithm and as stated before- are driven by plasticity, i.e. the acceptable stress level is fixed by yielding and by the plasticity criterion and subsequently stresses are “relaxed” via creep. Additionally, pure E.P. and V.E. deformations,

referring to the same load, are related to different stress levels (as evident in Figure 103); consider in fact the stress levels relative to the same constant load). As a consequence, the addition of pure E.P. and V.E. strains do not give the V.E.P. ones and, particularly for the situation of constant load, the V.E.P. stress value is the one of E.P., maintained for a strain range fixed by the V.E. one.

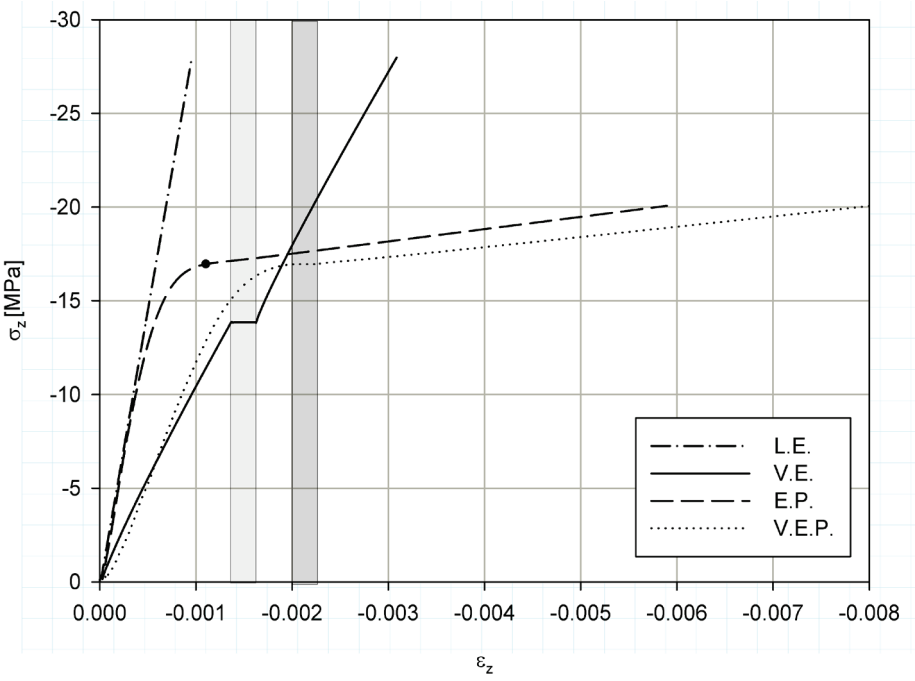

Figure 103 - Stress-strain curve for the three-step loading path.

References

[1] Baggio P., Majorana C.E., Schrefler B.A., (1995), "Thermo-hygro-mechanical analysis of concrete", *Int. J. Num. Meth. Fluids*, **20**, pp. 573-595.

[2] Gawin D., Majorana C.E., Schrefler B.A., (1999), "Numerical analysis of hygro-thermal behaviour and damage of concrete at high temperature", *Mech. Coh. Frict. Mat*., **4**, pp. 37-74.

[3] Gawin D., Majorana C.E., Schrefler B.A., (1999), "Numerical analysis of hygro-thermal behaviour and damage of concrete at high temperature", *Mech. Coh. Frict. Mat.*, **4**, 37-74.

[4] Salomoni V.A., Mazzucco G., Majorana C.E., (2007), "Mechanical and Durability Behaviour of Growing Concrete Structures", *Engrg. Com*., **24**(5), pp. 536-561.

[5] Salomoni V.A., Majorana C.E., Giannuzzi G.M., Miliozzi A., (2008), "Thermal-fluid flow within innovative heat storage concrete systems for solar power plants", *Int. J. Num. Meth. Heat and Fluid Flow*, **18**(7/8), pp. 969-999.

[6] Bažant Z.P., Thonguthai W., (1979), "Pore pressure in heated concrete walls: theoretical predictions", *Mag. Con. Res.*, **31**(107), pp. 67-76.

[7] Bažant Z.P. (Editor), (1988), "Mathematical Modelling of creep and shrinkage of concrete*", J. Wiley & Sons*, NY, USA.

[8] Bažant Z.P., Baweja S., (2000), "Creep and shrinkage prediction model for analysis and deign of concrete structures: Model B3", in Adam Neville Sym.: *Creep and Shrinkage – Structural Design Effects*, ACI SP – 194, pp. 1-83.

[9] Xotta G., Salomoni V.A., Majorana C.E., (2012), "Thermo-hygro-mechanical meso-scale analysis of concrete as a viscoelastic-damaged material", *Engineering Computations* (in press).

[10] Pijaudier-Cabot G., Mazars J., Pulikowski J., (1991), "Steel-concrete bond analysis with non local continuous damage", *J. Str. Engrg.,* **117**(3), pp. 862-882.

[11] Hashiguchi K., Saitoh K., Okayasu T., Tsutsumi S., (2002), "Evaluation of typical conventional and unconventional plasticity models for prediction of softening behaviour of soils", *Geotech.*, **52**(8), pp. 561-578.

[12] Hashiguchi K., (2009), "Elastoplasticity theory", in Lecture notes in applied and computational mechanics, *Pfeiffer- Wriggers Eds*., **42**, Springer, Berlin.

[13] Salomoni V.A., Fincato R., (2011), "3D subsidence analyses above gas reservoirs accounting for an unconventional plasticity model", *Int. J. for Num. and Analy. Meth. in Geomech.*, **36**, pp. 959-976.

[14] Salomoni V.A., Fincato R., (2012), "Subloading surface plasticity model algorithm for 3D subsidence analyses above gas reservoirs", *Int. J. of Geomech.*, **12**(4), pp. 414-427.

[15] Schrefler B.A., Simoni L., Majorana C.E., (1989), "A general model for the mechanics of saturated-unsaturated porous materials", Mat. Str., **22**, pp. 323-334.

[16] Majorana C.E., Salomoni V., Schrefler B.A., (1998), “Hygrothermal and mechanical model of concrete at high temperature”, Mat. Str., 31(210), pp. 378-386.

[17] Majorana, C.E. (1989), “Influence of damage on the mechanical and thermo-hygrometric response of continua”, Giornale del Genio Civile, Voll. July-August-September, pp. 211-236 (in Italian).